

BROKEN-SYMMETRY PHASES OF MATTER AND THEIR EFFECTS ON
ELECTRONIC AND MAGNETIC PROPERTIES

by

Sean Fahlman Peterson

A dissertation submitted in partial fulfillment
of the requirements for the degree

of

Doctor of Philosophy

in

Physics

MONTANA STATE UNIVERSITY
Bozeman, Montana

December 2023

©COPYRIGHT

by

Sean Fahlman Peterson

2023

All Rights Reserved

DEDICATION

I dedicate this to my father, who passed his curiosity for the world onto me. Growing up with a science teacher for a dad taught me to look at things and ask: why? And to my mother, who's supported me through so much, even when I wanted to quit. None of this would have been possible without my family, thanks for all the support.

ACKNOWLEDGEMENTS

I would like to acknowledge my advisor, Yves Idzerda for supporting my research through graduate school and teaching me many things along the way. I'd also like to thank Collin Crites and Frank Schooner, for many useful discussions. This work was supported by the National Science Foundation through Grant No. 1809846 and the NSF MonArk Quantum Foundry, which is supported from the NSF Q-AMASE-I program Award No. DMR1906383.

TABLE OF CONTENTS

1. INTRODUCTION	1
Broken-Symmetry	1
Phase Transitions	1
Order Parameters	4
Goldstone Bosons	5
Ferromagnetism	6
Landau Theory of Magnetism	6
Spin Precession	7
Microscopic Models of Magnetism	8
Magnons and Spin Waves	9
Hubbard Model	12
Magnetic Domains & Domain Walls	13
Magnetic Anisotropy	14
Magnetic Hysteresis	19
Stoner-Wohlfarth Model	19
Antiferromagnetism	21
Types of Antiferromagnetism	21
Exchange Bias	22
Spin Density Waves	22
Electronic Nematic Phase	26
Electronic Origin of Nematic Phase	27
Structural Transition	29
Fermi Surface Distortion	29
Superconductivity	32
Conventional Superconductivity	32
Unconventional Superconductivity	33
Phase Diagram with Broken-Symmetry Phases	33
2. THEORY	37
Stoner-Wohlfarth Model	37
Superconductivity	38
Mean-field Hamiltonian	38
Bogoliubov Eigenstates	39
Nematicity	42
Mean-field Hamiltonian	42
Nematic Mean-Field Order Parameter	43
Coexistence of Nematicity and Superconductivity	44
Mean-field Hamiltonian	44

TABLE OF CONTENTS – CONTINUED

Eigenstates	45
Δ and Φ Mean-field order Parameter Calculation	47
Spin Density Waves	49
Mean-field Hamiltonian	49
Eigenstates	49
Coexistence of Spin Density Waves and Superconductivity	52
Mean-field Hamiltonian	52
Eigenstates	55
Δ and M Mean-field Order Parameter Calculation	62
Impurity Scattering	65
Weak Scattering Limit	65
Strong Scattering Limit	70
Boltzmann Thermal Conductivity	74
3. NUMERICAL METHODS	78
k-space Integration Grids	78
Normal and Anomalous Self-energy Calculations	92
4. DETERMINATION OF ANISOTROPY CONSTANTS VIA FITTING OF MAGNETIC HYSTERESIS TO NUMERICAL CALCULATION OF STONER-WOHLFARTH MODEL	95
Contribution of Authors and Co-Authors	95
Manuscript Information	96
5. THERMAL TRANSPORT IN TWO-DIMENSIONAL NEMATIC SU- PERCONDUCTORS	101
Contribution of Authors and Co-Authors	101
Manuscript Information	102
6. ANISOTROPIC THERMAL TRANSPORT IN SUPERCONDUCTORS WITH COEXISTING SPIN DENSITY WAVES	116
Contribution of Authors and Co-Authors	116
Manuscript Information	117
7. CONCLUSION	131
Cubic Anisotropy Constants	131

TABLE OF CONTENTS – CONTINUED

Thermal Transport in Nematic Superconductors	133
Thermal Transport in Symmetry-broken Antiferromagnetic Superconductors.....	136
REFERENCES CITED.....	140
APPENDIX : Github Repositories	147

LIST OF TABLES

Table	Page
1.1 Broken-symmetries across selected phase transitions.....	2
7.1 Cubic anisotropy constants, $K_{\text{cubic}}^{(1)}$ from fitting Stoner-Wohlfarth model hysteresis loops to VSM measured hysteresis loops of bcc $\text{Fe}_x\text{Co}_y\text{Mn}_z$ films.	132
A.1 Github repositories of code used in this work.	148

LIST OF FIGURES

Figure	Page
1.1 Rod-shaped molecules commonly found in liquid crystals forming a nematic phase where a majority of the molecules are aligned in a single direction.	4
1.2 (a) Free energy of a ferromagnet in the Landau model as a function of magnetization when $T > T_C$ (red), $T = T_C$ (green), and $T < T_C$ (blue). (b) Magnetization that minimizes the free energy of a ferromagnet in the Landau model as a function of temperature.	7
1.3 Magnon dispersion relation E_k , for a one-dimensional ferromagnetic chain of spins. It can be seen that zero-energy magnon excitations exist at $k = 0$, these are known as Goldstone bosons.	10
1.4 Spin wave on a line of precessing spins (a) perspective view (b) top view. Figure originally published in <i>Magnetism in Condensed Matter</i> , S. Blundell[4].....	11
1.5 (a) Bloch domain wall where the magnetic moments rotate in a plane parallel to the domain wall. (b) Néel domain wall where the magnetic moments rotate in a plane perpendicular to the domain wall. Figure originally published in <i>Magnetism in Condensed Matter</i> , S. Blundell[4].....	13
1.6 (a) How a magnetic material with two domains resists magnetizing parallel to an applied magnetic field due to the demagnetizing field. (b) The changing demagnetizing factor causes the M - H loop to be less than linear in the external field. Figure originally published in <i>Modern Magnetic Materials Principles and Application</i> , Robert C. O’Handley[49].	15

LIST OF FIGURES – CONTINUED

Figure	Page
1.7 Topologies of the five d -wave orbitals, separated into e_g and t_{2g} symmetry, are shown at the top. Symmetry of the octahedral and tetrahedral sites are shown in the center. Splitting of the crystal field for $3d^4$ and $3d^9$ levels in octahedral and tetrahedral site symmetry are shown at the bottom. Figure originally published in <i>Modern Magnetic Materials Principles and Applications</i> , Robert C. O’Handley[49].....	16
1.8 Cubic anisotropy free energy surface plot when $K_{\text{cubic}}^{(2)} = 0$ (a) and $K_{\text{cubic}}^{(1)} > 0$ and the easy axes are oriented along the $[\pm 1, 0, 0]$, $[0, \pm 1, 0]$, and $[0, 0, \pm 1]$ directions (b) and $K_{\text{cubic}}^{(1)} < 0$ and the easy axes are oriented along the $[\pm 1, \pm 1, \pm 1]$ directions.....	18
1.9 Hysteresis loops for a sample with uniaxial anisotropy when a magnetic field is applied at an angle (a) $\theta_a = \pi/2$ relative to the easy axis, also known as the hard axis and (b) $\theta_a = \pi/6$ relative to the easy axis. Energy surface as a function of normalized applied magnetic field h and magnetization direction ϕ with the minima overlayed when (a) $\theta_a = \pi/2$ relative to the easy axis and (b) $\theta_a = \pi/6$ relative to the easy axis. Figure originally published in <i>Magnetism in Condensed Matter</i> , S. Blundell[4].....	20
1.10 Four types of antiferromagnetic order that occur on simple cubic lattices. Figure originally published in <i>Fundamentals of Magnetism</i> , Mathias Getzlaff[24].	21
1.11 Effect of exchange coupling on magnetic hysteresis loop for a material with an antiferromagnetic layer and a soft ferromagnetic layer. Figure originally published in <i>Modern Magnetic Materials</i> , Robert C. O’Handley[49].....	22

LIST OF FIGURES – CONTINUED

Figure	Page
1.12 (a)-(c) Square lattice of magnetic atoms (red points) where black arrows are on-site magnetization in $\pm\hat{z}$ direction, blue dashed lines are crystalline unit cell, and black dashed lines are magnetic unit cell for SDW state when: (a) $\mathbf{Q} = (\pi, \pi)$, (b) $\mathbf{Q} = (\pi/2, \pi/2)$, and (c) $\mathbf{Q} = (\pi, 0)$. (d)-(e) Fermi Surface (solid black curve) constructed to allow for FS nesting with FS translated by \mathbf{Q} (solid red curves) at the edges of the Reduced Brillouin Zone (dashed black lines) for SDW with nesting vector: (d) $\mathbf{Q} = (\pi, \pi)$, (e) $\mathbf{Q} = (\pi/2, \pi/2)$, and (f) $\mathbf{Q} = (\pi, 0)$	24
1.13 (a) Schematic of AFM2 (or type C AFM) magnetic structure with highly anisotropic nearest-neighbor hopping due to orbital ordering. (b),(c) Kinetic energy ΔE in the ferro-orbital and staggered-orbital structures. t and U denote the hopping parameter and intraorbital Coulomb repulsion, while U' and J_H denote the interorbital repulsion and Hund's exchange, respectively. Figure originally published in <i>Phys. Rev. Lett.</i> , 103(26):267001, 2009[41].	27
1.14 Two mechanisms for producing an electronic nematic phase: the melting of a striped phase which restores translational symmetry but preserves the reduced rotational symmetry, and a Fermi fluid developing nematic order through a distortion of the FS due to a Pomeranchuk instability. Figure originally published in <i>Annu. Rev. Condens. Matter Phys.</i> , 1:153–178, 2010[21].	28
1.15 In-plane schematic diagram of the structural transition from a tetragonal lattice, where $a = b$ to an orthorhombic lattice $a \neq b$. Figure originally published in <i>Nat. Phys.</i> , 10:97–104, Feb 2014[20].	30

LIST OF FIGURES – CONTINUED

Figure	Page
1.16 (a) Density of states in the nematic state normalized by the DOS at the Fermi level (N_F) in the normal state plotted versus the electron energy in the nematic state $\tilde{\xi}$ normalized by the temperature at which the structural transition driving the nematic transition took place. It can be seen that van Hove singularities occur in the DOS at $\tilde{\xi}_{\mathbf{k}}^{vH} = -\mu + 4t_2 \pm 2\Phi$. (b) Nematic state FS as Φ increases from 0 to $1.34T_s$ and the relevant saddle points in the normal state dispersion at $(\pm\pi, 0)$ and $(0, \pm\pi)$ are shown as blue points.	31
1.17 (a) Alternate stacking of deformed FSs due to nematicity in each CuO_2 plane. \tilde{t}_x and \tilde{t}_y are the effective in-plane electron hopping integrals along the x - and y -directions respectively; \tilde{t}_z is the effective hopping along the z -direction. (b) The resulting bulk FSs which become two-dimensional and consist of inner (black) and outer (purple) FSs. Figure originally published in <i>Nat. Commun.</i> , 12:2223, 2021[71].	32
1.18 Schematic phase diagram of hole- and electron-doped iron pnictides of the family BaFe_2As_2 . The blue region denotes orthorhombic stripe magnetism. The red region denotes orthorhombic nematic paramagnetic order (dark red denotes strong nematic order). The yellow region denotes superconductivity. The green region denotes a phase which preserves $C(4)$ rotational symmetry. Dotted lines illustrate nematic and Néel temperatures inside superconducting dome. Insets show temperature-dependence of nematic (Φ) and AFM (M) order parameters. Figure originally published in <i>Nat. Phys.</i> , 10:97–104, Feb 2014[20].....	34
1.19 (a) Typical superconducting cuprate open FS, which can be well modelled with the tight-binding model. (b) Reconstructed FS due to FS nesting by a $\mathbf{Q} = (\pi, \pi)$ SDW state inside the reduced Brillouin Zone (dashed lines). Figure originally published in <i>Phys. Rev. Lett.</i> , 103(15):157002, 2009[27].	35

LIST OF FIGURES – CONTINUED

Figure	Page
1.20 (a) Schematic diagram of the Fermi surfaces of the iron pnictides, where the blue pockets located at the M points of the FBZ are electron-like and the red pockets at the Γ point of the FBZ are hole-like. Figure originally published in <i>Annu. Rev. Condens. Matter Phys.</i> , 2:121, 2011, 2009[70].	36
2.1 Normalized energy surface Γ plotted as a function of the unitless applied magnetic field, h , and polar angle between the magnetization and applied magnetic field $\phi - \theta$. $\phi(h)$ when $\frac{\partial \Gamma}{\partial \phi} = 0$ is plotted along the bottom plane and shaded as a function of $\frac{\partial^2 \Gamma}{\partial \phi^2}$, where energy minima are shaded in blue and energy maxima are shaded in red.	38
2.2 Magnetic hysteresis of a thin-film ferromagnet with an in-plane cubic anisotropy and a two-step hysteresis calculated from the Stoner-Wohlfarth model.	39
2.3 (a) Normal state electron (solid blue) and hole (solid red) bands for a free-electron model $\xi_{\mathbf{k}} = \frac{\hbar^2 k^2}{2m} - \mu$ and the Bogoliubov quasiparticle (dashed blue) and Bogoliubov quasihole (dashed red) bands for s -wave superconductivity. (b) Bogoliubov transformation coefficients $ u_{\mathbf{k}} ^2$ and $ v_{\mathbf{k}} ^2$ which show that the Bogoliubov quasiparticles below the Fermi level are mostly hole-like and the ones above the Fermi level are mostly electron-like. This figure was inspired by Carsten Timm's <i>Theory of Superconductivity</i> [67].	42
2.4 Qualitative illustration of the superconducting gap amplitude for varying values of r along the nematically distorted FS. When $r > 0$ (cyan curves) the SC gap maximum is anti-aligned with the FS elongation. When $r < 0$ (cyan curves) the SC gap maximum is aligned with the FS elongation.	45

LIST OF FIGURES – CONTINUED

Figure	Page
2.5 Nematic order parameter, Φ , (solid curves) plotted as a function of temperature in the absence of superconductivity (black), coexisting with s - + d - wave superconductivity when $r = 0.2$ and $T_c^0 = .4T_S$ (cyan), and coexisting with s - + d - wave superconductivity when $r = -0.2$ and $T_c^0 = .4T_S$ (orange). The superconducting order parameter (dashed curves) is also shown when $r = 0.2$ (cyan) and $r = -0.2$ (orange).....	48
2.6 (a) & (b) Normal state electron $\xi_{\mathbf{k}}$ (solid blue) and $\xi_{\mathbf{k}+\mathbf{Q}}$ (solid red) bands for a tight-binding model $\xi_{\mathbf{k}} = \mu - t_1 \cos(2k_x a) - t_1 \cos(2k_y a) - t_2 \cos(2k_x a) \cos(2k_y a)$ and the $E_{\mathbf{k}}^{(\alpha)}$ SDW quasiparticle (dashed blue) and $E_{\mathbf{k}}^{(\beta)}$ SDW quasiparticle (dashed red) bands for the $\mathbf{Q} = (\pi/2, \pi/2)$ SDW state. It should be noted that, in general, $E_{\mathbf{k}}^{(\beta)} \neq -E_{\mathbf{k}}^{(\alpha)}$ despite their similarities in this illustration (c) & (d) SDW quasiparticle transformation coefficients $ u_{\mathbf{k}}^{\text{SDW}} ^2$ and $ v_{\mathbf{k}}^{\text{SDW}} ^2$ which show that the SDW quasiparticle bands are a result of the hybridization of the $\xi_{\mathbf{k}}$ and $\xi_{\mathbf{k}+\mathbf{Q}}$ normal state electron bands.....	53
2.7 Qualitative illustration of the amplitude and sign of the superconducting gap along the normal state tight-binding FSs (band parameters $t_1 = 100T_N$ and $t_2 = 10T_N$) to show the symmetry of the SC gap under translations of the \mathbf{Q} -vector. (a) $d_{x^2-y^2}$ SC pairing on the $\xi_{\mathbf{k}}^{(1)}$ FS (b) d_{xy} pairing on the $\xi_{\mathbf{k}}^{(1)}$ FS (c) $d_{x^2-y^2}$ SC pairing on the $\xi_{\mathbf{k}}^{(2)}$ FS (d) d_{xy} pairing on the $\xi_{\mathbf{k}}^{(2)}$ FS.....	54
2.8 FSs reconstructed by SDW ordering (solid black curves) when $M = 2T_N$ for the nesting vectors (a) $\mathbf{Q} = (\pi/2, \pi/2)$ and (b) $\mathbf{Q} = (\pi, 0)$. The d -wave nodal lines are represented with dotted cyan and orange lines for $d_{x^2-y^2}$ and d_{xy} respectively. Cyan and orange points represent the locations of the $d_{x^2-y^2}$ and d_{xy} nodes respectively when their nodal lines cross the reconstructed FS. Red X's show the locations of additional mixing nodes that occur only when the SC gap is even under translations of \mathbf{Q} ($\Delta_{\mathbf{k}+\mathbf{Q}} = \Delta_{\mathbf{k}}$).....	55

LIST OF FIGURES – CONTINUED

Figure	Page
2.9 (a) $(E_{\mathbf{k}}^{(\alpha)})^{(1)}$ (dashed blue curve) and $(E_{\mathbf{k}}^{(\beta)})^{(1)}$ (dashed red curve) first-order perturbation bands when the $\mathbf{Q} = (\pi/2, \pi/2)$ SDW state coexists with a $d^{(O)}$ -wave SC gap. (b) $(E_{\mathbf{k}}^{(\alpha)})^{(1)}$ (dashed blue curve) and $(E_{\mathbf{k}}^{(\beta)})^{(1)}$ (dashed red curve) first-order perturbation bands when the $\mathbf{Q} = (\pi/2, \pi/2)$ SDW state coexists with a $d^{(E)}$ -wave SC gap. (c) $E_{\mathbf{k}}^{(1;E)}$ (dashed blue curve) and $E_{\mathbf{k}}^{(2;E)}$ (dashed red curve) bands when the $\mathbf{Q} = (\pi/2, \pi/2)$ SDW state coexists with a $d^{(O)}$ -wave SC gap. (d) $E_{\mathbf{k}}^{(1;E)}$ (dashed blue curve) and $E_{\mathbf{k}}^{(2;E)}$ (dashed red curve) bands when the $\mathbf{Q} = (\pi/2, \pi/2)$ SDW state coexists with a $d^{(E)}$ -wave SC gap.	59
2.10 (a) SDW quasiparticle bands $E_{\mathbf{k}}^{(\alpha)}$ (dashed blue) and $E_{\mathbf{k}}^{(\beta)}$ (dashed red) and SDW + $d^{(O)}$ -wave SC coexistence bands $E_{\mathbf{k}}^{(1;O)}$ (solid blue) and $E_{\mathbf{k}}^{(2;O)}$ (solid red) plotted to show the hybridization between the $E_{\mathbf{k}}^{(\beta)}$ and $-E_{\mathbf{k}}^{(\beta)}$ bands which results in a band avoidance at the Fermi level. (b) Degree of hybridization between the SDW bands in order to create the coexistence bands when SDW coexists with $d^{(O)}$ -wave SC.	61
2.11 Self-consistently calculated M and Δ order parameters in the absence of superconductivity (black), when spin density waves coexist with a d -wave SC gap which is odd under translations of \mathbf{Q} (cyan), and when spin density waves coexist with a d -wave SC gap which is even under translations of \mathbf{Q} (orange).....	63

LIST OF FIGURES – CONTINUED

Figure	Page
2.12 Probability for a quasiparticle of momentum \mathbf{k} to scatter to another state in \mathbf{k} -space with momentum \mathbf{k}' . (a) Probability for a quasiparticle occupying a pure d_{xy} SC state where $\xi_{\mathbf{k}} > 0$ to scatter to another pure SC state of momentum \mathbf{k}' near the normal state FS. (b) Probability for a quasiparticle occupying a pure d_{xy} SC state where $\xi_{\mathbf{k}} < 0$ to scatter to another pure SC state of momentum \mathbf{k}' near the normal state FS. (c) Probability for a quasiparticle occupying a pure $\mathbf{Q} = (\pi/2, \pi/2)$ SDW state where $E_{\mathbf{k}}^{\beta} > 0$ to scatter to another pure SDW state of momentum \mathbf{k}' near the reconstructed FS. (d) Probability for a quasiparticle occupying a pure $\mathbf{Q} = (\pi/2, \pi/2)$ SDW state where $E_{\mathbf{k}}^{\beta} < 0$ to scatter to another pure SDW state of momentum \mathbf{k}' near the reconstructed FS. (e) Probability for a quasiparticle occupying a coexistence $\mathbf{Q} = (\pi/2, \pi/2)$ SDW + d_{xy} SC state where $E_{\mathbf{k}}^{\beta} > 0$ to scatter to another pure SDW state of momentum \mathbf{k}' near the reconstructed FS. (f) Probability for a quasiparticle occupying a coexistence $\mathbf{Q} = (\pi/2, \pi/2)$ SDW + d_{xy} SC state where $E_{\mathbf{k}}^{\beta} > 0$ to scatter to another coexistence state of momentum \mathbf{k}' near the reconstructed FS.	67
3.1 Heatmaps of $\frac{\partial f_{\mathbf{k}}^0}{\partial E}$ when $T = .5T_N$ plotted on integration grids for the $\xi_{\mathbf{k}}^{(1)}$ FS when $t_1 = 100T_N$, $t_2 = 10T_N$, and $E_c = 7.5T_N$. (a) $(\xi, \theta_{\mathbf{k}})$ -grid where $N_{\xi} = 3$ and $N_{\theta_{\mathbf{k}}} = 100$, so the total number of \mathbf{k} -points in the grid is $N_{grid} = 300$. (b) (k_x, k_y) -grid where $N_x = 100$ and $N_y = 50$, however a majority of the grid points were cutoff due to being below E_c leaving $N_{grid} = 330$ \mathbf{k} -points in this grid. It should be noted that these are purely for illustration and only grids like those in (a), albeit with a larger N_{ξ} , were used in calculations.	80
3.2 Convergence of the κ^n integral on the $(\xi, \theta_{\mathbf{k}})$ -grid (blue) and the (k_x, k_y) -grid (red), where it can be seen that given the same number of points the $(\xi, \theta_{\mathbf{k}})$ -grid tends to be an order of magnitude more accurate for this simple calculation.	81

LIST OF FIGURES – CONTINUED

Figure	Page
3.3 Heatmaps of $\frac{\partial f_{\mathbf{k}}^0}{\partial E}$ when $T = .2T_S$ plotted on integration grids for the $\xi_{\mathbf{k}}^{(3)}$ FS distorted by a nematic phase when $\mu = -4.8T_S$, $t_1 = 6T_S$, $t_2 = -1T_S$, $\Phi = 1.38T_S$, and $E_c = 8T_S$. (a) (\tilde{x}_i, k_x) -grid where $N_\xi = 3$ and $N_{\theta_{\mathbf{k}}} = 50$, so the total number of \mathbf{k} -points in the grid is $N_{grid} = 150$. (b) (k_x, k_y) -grid where $N_x = 100$ and $N_y = 50$, however a majority of the grid points were cutoff due to being below E_c leaving $N_{grid} = 168$ \mathbf{k} -points in this grid. It should be noted that these are purely for illustration and only grids like those in (a), albeit with a larger N_ξ , were used in calculations.	82
3.4 Convergence of the κ^N integral on the $(\tilde{\xi}, k_x)$ -grid (blue) and the (k_x, k_y) -grid (red), where it can be seen that given the same number of points the $(\tilde{\xi}, k_x)$ -grid tends to be nearly an order of magnitude more accurate for this calculation.	84
3.5 Heatmaps of $\frac{\partial f_{\mathbf{k}}^0}{\partial E}$ when $T = .25T_N$ plotted on integration grids for the $E_{\mathbf{k}}^{(2)}$ reconstructed FS when $\mathbf{Q} = (\pi/2, \pi/2)$ and $M = 2T_N$ for the $\xi_{\mathbf{k}}^{(1)}$ normal state dispersion with band parameters $t_1 = 100T_N$, $t_2 = 10T_N$, and $E_c = 3.25T_N$. (a) $(E^{(\beta)}, \theta_{\mathbf{k}})$ -grid where $N_E = 3$ and $N_{\theta_{\mathbf{k}}} = 100$, and the total number of \mathbf{k} -points in the grid is $N_{grid} = 250$ ($N_{grid} \neq N_E N_{\theta_{\mathbf{k}}}$ since not every $(E^{(\beta)}, \theta_{\mathbf{k}})$ combination has a solution). (b) $(\xi, \theta_{\mathbf{k}})$ -grid where $N_\xi = 3$ and $N_{\theta_{\mathbf{k}}} = 100$, so $N_{grid} = 300$. It should be noted that these are purely for illustration and much higher grid densities were used for actual calculations.	85
3.6 Convergence of the κ_{xy}^{SDW} integral at $T = 0.02T_N$ on the $(E, \theta_{\mathbf{k}})$ -grid (blue) and the $(\xi, \theta_{\mathbf{k}})$ -grid (red), where it can be seen that given the same number of points the $(E, \theta_{\mathbf{k}})$ -grid is a slight, but noticeable improvement over the $(\xi, \theta_{\mathbf{k}})$ -grid.	86

LIST OF FIGURES – CONTINUED

Figure	Page
3.7 Heatmaps of $\frac{\partial f_{\mathbf{k}}^0}{\partial E}$ when $T = .02T_N$ plotted on the integration grid for the $E_{\mathbf{k}}^{(2)}$ reconstructed FS when the $\mathbf{Q} = (\pi/2, \pi/2)$ SDW state coexists with d_{xy} superconductivity. Due to the fact that this is a $d^{(E)}$ -wave SC state, additional mixing nodes besides the typical d -wave symmetry nodes appear in the region of the FS reconstruction. (a) The $(E^{(\alpha,\beta)}, \theta_{\mathbf{k}})$ -grid combined with the $(E^{(2;E)}, \theta_{\mathbf{k}})$ -grid in order to properly capture the behavior of the additional mixing nodes, as just the $(E^{(\alpha,\beta)}, \theta_{\mathbf{k}})$ -grid tends to miss these points at low- T . (b) Zoomed in plot of the $(E^{(2;E)}, \theta_{\mathbf{k}})$ -grid at one of the mixing nodes.	88
3.8 Convergence of the $\kappa_{xy}^{d^{(E)}}$ integral at $T = 0.02T_N$ on the $(E^{(2;E)}, \theta_{\mathbf{k}})$ -grid (blue) and the $(E^{(\alpha,\beta)}, \theta_{\mathbf{k}})$ -grid (red), where it can be seen that given the same number of points the $(E^{(2;E)}, \theta_{\mathbf{k}})$ -grid is a noticeable improvement over the $(E, \theta_{\mathbf{k}})$ -grid due to actually picking up the mixing nodes properly.....	90
3.9 Time taken to calculate all the quasiparticle lifetimes $\tau_{\mathbf{k}}$ in the SC + SDW coexistence phase when run on a GPU (Nvidia GeForce RTX 2060 Mobile) and a CPU (Intel i7-10750H).....	91
3.10 Convergence of $ g(E_{\mathbf{k}}) ^2$ calculated on the nematically deformed $\xi_{\mathbf{k}}^{(3)}$ FS when $\mu = -4.8T_S$, $t_1 = 6T_S$, $t_2 = -T_S$, $\Phi = 1.34T_S$, $\Delta = 0.18T_S$, $r = 0.6$, and $E_{\mathbf{k}} = .015T_S$, chosen to ensure that both $k_x^{(1)}$ and $k_x^{(2)}$ are well defined and the integrand of $g(E_{\mathbf{k}})$ has three separate regions.....	94
7.1 (a) Stoner-Wohlfarth Model best fit (blue curve) to FeCoMn magnetic hysteresis data measured by VSM (red curve), (b) enlarged to visualize hysteresis in the raw data which has a coercive applied magnetic field value of around 1mT.	131
7.2 Heat conductivity components ($\kappa_{ij}^N(T)$) of the nematically deformed closed FS with band parameters $t_1 = 6T_S$, $t_2 = -T_S$, and $\mu = -4.8T_S$ in the absence of SC order. $\kappa_{ij}^N(T)$ is normalized by the conductivity ($\kappa^n(T)$) of the normal state (original FS, $\Phi = 0$). The normal state conductivity is T -linear, $\kappa^n(T) = \text{constant} \times T$	134

LIST OF FIGURES – CONTINUED

Figure	Page
7.3 Thermal conductivity components (κ_{xx} and κ_{yy}) in the co-existence phase in both the Born (blue curves) and Unitary (red curves) limits normalized by the $\kappa_{yy}^N(T)$ component in the pure nematic phase when (a) $r = 0.2$ with $T_c = 0.211T_N$, (b) $r = 0.45$ with $T_c = 0.158T_N$, (c) $r = 0.6$ with $T_c = 0.140T_N$, (d) $r = -0.2$ with $T_c = 0.317T_N$, (e) $r = -0.55$ with $T_c = 0.332T_N$, and (f) $r = -0.7$ with $T_c = 0.323T_N$. The parameters used are $\mu = -4.8T_N$, $t_1 = 6T_N$, $t_2 = -T_N$, and $\Phi = 1.34T_N$. The critical r -values are $r_c^+ \approx 0.52866$ and $r_c^- \approx -0.61447$	135
7.4 Diagonalized thermal conductivity tensor elements parallel (dashed curves) and perpendicular (dotted curves) to the SDW nesting vector \mathbf{Q} in the pure SDW state (black), SDW + d -wave SC state with odd translational symmetry (cyan), and SDW + d -wave SC state with even translational symmetry (orange). (a) $\kappa(T)T_N/\kappa(T_N)T$ plotted to remove linear T -dependence and emphasize deviations from normal state conductivity. (b) $\kappa(T)/\kappa(T_N)$ plotted on a log-log scale to emphasize low- T linearity.	137

ABSTRACT

Physical symmetries inherent to a material are often reflected in its electronic and magnetic properties. The in-plane four-fold rotational symmetry of thin-film ferromagnets inherent to their tetragonal lattice is also exhibited by their cubic anisotropy. The magnetization as a function of applied magnetic field can be calculated via the Stoner-Wohlfarth model. These calculated hysteresis loops were fit to measured hysteresis loops to determine anisotropy constants consistent with known values. An electronic nematic state reduces the in-plane four-fold rotational symmetry of materials by inducing a structural transition from tetragonal to orthorhombic/monoclinic, with two-fold symmetry. This reduced symmetry persists in the electronic thermal transport. Nematicity enhances nearest-neighbor hopping along one axis and reduces it along the other. This results in a deformed Fermi surface compressed (elongated) along the axis of stronger (weaker) electron hopping. This drags van Hove singularities through the Fermi level, affecting quasiparticle lifetimes. Calculating conductivity from the Boltzmann kinetic equation, nematicity enhances thermal transport along one axis and diminishes it along the other. Additionally, *s*-wave superconductivity coexisting with nematicity creates a feedback on the superconducting gap with a *d*-wave instability, which can lead to gapless excitations. In the case of weak feedback, nematic superconductors behave like fully-gapped superconductors along both axes, where transport decreases exponentially with temperature. Once gapless excitations form, transport along both axes becomes *T*-linear at low-*T*. Similarly, striped antiferromagnetism (AFM2 and AFM3) reduces the rotational symmetry of a square unit cell to a larger two-fold symmetric magnetic cell. Modeling the band structure with a tight-binding model and considering a smaller periodicity in momentum-space, gaps the Fermi surface along one axis. Calculating conductivity reveals diminished transport along one axis and enhanced thermal transport along the other. Considering *d*-wave superconductivity in this model results in two cases. One has highly anisotropic transport with greatly enhanced *T*-linear transport along one axis and diminished transport decreasing exponentially with temperature along the other. The second has weakly anisotropic transport with diminished *T*-linear conductivity along both axes. The symmetry of a material's properties, such as magnetic anisotropy and thermal transport, are intrinsically linked to their crystalline, electronic, and magnetic symmetries.

INTRODUCTION

Broken-SymmetryPhase Transitions

Phase transitions are characterized by a drastic change in behavior driven by a broken-symmetry. One of the most common phase transitions that occurs in nature is freezing, wherein a material transitions from a liquid to a solid. Assuming the resulting solid forms a crystalline structure (i.e. water \rightarrow ice), a continuous translational and rotational symmetry is broken inherent to liquids where it is just as likely to find a molecule anywhere regardless of location within the liquid and the orientation of the liquid. However, once this liquid condenses and becomes a crystalline solid, the translational and rotational symmetries become discrete. In crystals, the probability of finding a lattice site is only symmetric under integer multiples of the lattice vectors and symmetric under discrete rotations (i.e. a cubic lattices such as: simple cubic, face-centered cubic, and body-centered cubic are symmetric under rotations of $\pi/2$ about any Cartesian axis). Phase transitions can be brought about by a few environmental changes (such as applied pressure), but in this work the main driver of phase transitions that will be considered is decreasing temperature.

Similar to the transition from liquid \rightarrow solid, ferromagnetism breaks the rotational symmetry inherent to paramagnetism when T is lowered below the Curie temperature. In the absence of an applied field, paramagnetic moments can point in every direction and the average magnetic moment goes to zero, thus preserving the discrete rotational symmetry of the crystal lattice. However, ferromagnetism breaks this symmetry by aligning the magnetic moments in a single direction (within a single domain), thus breaking this discrete rotational symmetry (except under rotations that return the ferromagnet to its original orientation).

Table 1.1: Broken-symmetries across selected phase transitions.

Phase	T	Symmetry
liquid	$T > T_{\text{melt}}$	continuous translational and rotational symmetry
crystalline solid	$T < T_{\text{melt}}$	discrete translational and rotational symmetry
Paramagnet	$T > T_{\text{Curie}}$	discrete rotational symmetry
Ferromagnet	$T < T_{\text{Curie}}$	trivial rotational symmetry
Paramagnet	$T > T_{\text{Néel}}$	discrete rotational symmetry
Antiferromagnet	$T < T_{\text{Néel}}$	$C(2)$ rotational symmetry about \perp axis
liquid	$T < T_{\text{Nematic}}$	continuous rotational symmetry
nematic liquid crystal	$T > T_{\text{Nematic}}$	$C(2)$ rotational symmetry about \perp axis
2D metal film	$T > T_S$	$C(4)$ rotational symmetry
2D nematic metal	$T < T_S$	$C(2)$ rotational symmetry
normal metal	$T > T_c$	gauge symmetry
Superconductivity	$T < T_c$	broken gauge symmetry

Antiferromagnetism is very similar to ferromagnetism in that it breaks the discrete rotational symmetry of the lattice preserved under paramagnetism below its critical temperature (in this case the Néel temperature). However, rather than trivializing the rotational symmetry, antiferromagnetism (for certain antiferromagnetic states) reduces the rotational symmetry of the lattice to a $C(2)$ rotational symmetry about the Cartesian axes. This is due to the fact that antiferromagnetically aligned moments are antiparallel to one another, so there are two preferred directions for magnetic moments to point (at least in the simplest case of the Heisenberg model).

Another interesting phase transition to consider is the onset of the nematic phase in liquid crystals. While not discussed in length in this work, it is the inspiration for the naming convention of the nematic electronic state observed in some metals, which is discussed in length. In the nematic liquid crystal phase below T_{Nematic} , the rod-like molecules of the liquid crystal tend to align along a particular axis, this phenomenon can be seen in Figure 1.1. This breaks the continuous rotational symmetry of the liquid and reduces it to a $C(2)$ rotational symmetry about an axis perpendicular to the long axis of the nematically ordered molecules.

In a two-dimensional metallic sample with a $C(4)$ rotational symmetry, the electronic nematic phase also reduces the rotational symmetry to $C(2)$, hence the namesake of the nematic phase. This broken-symmetry is the result of an unequal occupation of the electronic orbitals which ultimately affects the electron hopping between lattice sites. This results in an enhanced electron hopping along one crystalline axis and a diminished electron hopping along the other. This is often accompanied by a structural transition (hence T_S), from a tetragonal lattice with $C(4)$ symmetry to either an orthorhombic or monoclinic lattice with $C(2)$ symmetry, and an antiferromagnetic transition.

Superconductivity breaks gauge symmetry of the normal metal[47] below T_c . This is because upon the onset of superconductivity, states with different complex phases of

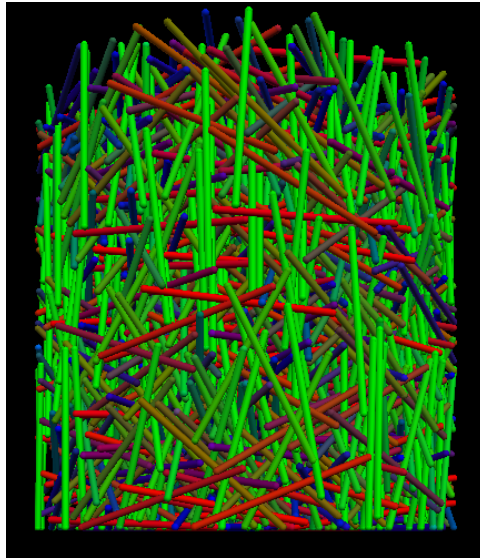


Figure 1.1: Rod-shaped molecules commonly found in liquid crystals forming a nematic phase where a majority of the molecules are aligned in a single direction.

the superconducting order parameter become distinguishable[47]. For certain types of superconducting states, other symmetries may be broken as well. For instance, in magnetic superconductors time-reversal symmetry is broken in order to allow for the spontaneous magnetization of Cooper pairs[47].

Order Parameters

Above the critical temperature of a broken-symmetry state there is some order parameter associated with the broken symmetry that is zero, which spontaneously becomes nonzero when the temperature is lowered below the critical temperature. For a first-order phase transition, the order parameter is discontinuous in its first derivative with respect to temperature. Therefore a "kink" appears in a plot of the order parameter plotted vs. temperature, but the order parameter goes to zero as $T \rightarrow T_{\text{critical}}$ continuously. For a second-order phase transition, the second derivative of the order parameter with respect to temperature is discontinuous at the critical temperature. This means that while the order

parameter goes to zero at the critical temperature, it does so with a discontinuity.

In crystalline materials, the Bragg peaks can be considered the order parameter as it is equal to a reciprocal lattice vector. For ferromagnets, the order parameter is much more straightforward, as it is simply the magnetization. Similarly, the order parameter for an antiferromagnet is also the magnetization, but since the total magnetization is zero for an antiferromagnet it is the magnetization of the sublattices. The order parameter of a nematic state for a liquid crystal is the second Legendre polynomial $S = \langle \frac{1}{2}(3 \cos^2 \theta - 1) \rangle$ averaged over all molecules in the liquid crystal and θ is the angle between the long axis of the molecules and the average direction the molecules are pointing[4]. The order parameter of an electronic nematic state is often written as Φ and depends on the electronic details of the nematically distorted metal, but it can be simply thought of as the amount that the nearest-neighbor hopping parameter is enhanced in one direction and diminished in the other. The order parameter in superconductors, is the momentum-dependent superconducting gap amplitude $\Delta_{\mathbf{k}}$, which can be complex in general, but was considered to only be real in this work.

Goldstone Bosons

A broken continuous global symmetry, as is the case when a liquid is frozen to create a crystal or the temperature of a paramagnet is lowered to create a ferromagnet, it is possible to create long-wavelength excitations in the order parameter for a vanishingly small energy cost. These excitations are known as Goldstone bosons[4]. For solids, the associated Goldstone bosons are vibrations in the crystal lattice known as phonons. In ferromagnets and antiferromagnets the Goldstone bosons associated with these broken symmetries are spin waves, the quantization of which are magnons. Magnons are a slight angular displacement between the precessing magnetic moments present in these permanent magnetic systems.

Ferromagnetism

Landau Theory of Magnetism

A convenient model to consider for ferromagnetism which produces a phase transition is the Landau Model. It is devised by writing down the free energy of the ferromagnet as a power series of the magnetization, M , where only even terms are nonzero due to the magnetization pointing in the \hat{z} and $-\hat{z}$ directions being equally favorable. Therefore, the free energy can be written as[4]:

$$E(M) = E_0 + a(T)M^2 + bM^4 \quad (1.1)$$

where E_0 and b ($b > 0$) are constants and $a(T)$ must change signs from positive to negative below the Curie temperature (the ferromagnetic transition temperature) to allow for a minimum in the free energy for a nonzero magnetization. The simplest case to consider is $a(T) = a_0(T - T_C)$. In order to solve for the magnetization which minimizes the free energy:

$$\frac{\partial F}{\partial M} = 0 \Rightarrow M = 0, \pm \sqrt{\frac{a(T_C - T)}{2b}} \quad (1.2)$$

where above T_C the only solution is $M = 0$, and below T_C the zero-magnetization solution is actually a local maximum in the free energy.

It can be seen from Figure 1.2(a), that when $T \geq T_C$ the only magnetization which minimizes the free energy is $M = 0$. However, when $T < T_C$ there exists a nonzero magnetization that minimizes the free energy. This magnetization represents the on-site magnetization of the ferromagnetic state and is shown as a function of T in Figure 1.2(b). Landau's approach to solving phase transitions in this way is known as a mean-field theory, which assumes that each spin in the ferromagnet interacts with the same average

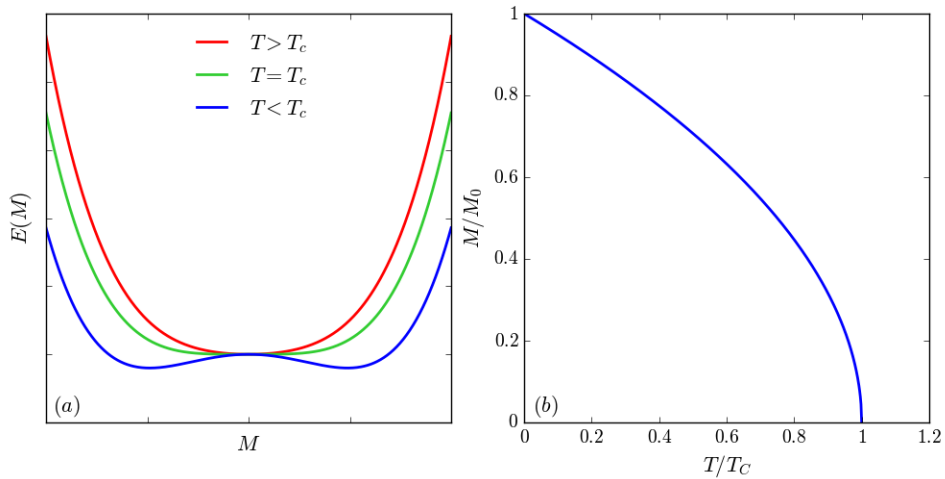


Figure 1.2: (a) Free energy of a ferromagnet in the Landau model as a function of magnetization when $T > T_C$ (red), $T = T_C$ (green), and $T < T_C$ (blue). (b) Magnetization that minimizes the free energy of a ferromagnet in the Landau model as a function of temperature.

magnetization produced by the other spins in the material. While mean-field theories can be easy to solve, they often miss order parameter fluctuations which become important near the transition temperature. Regardless, mean-field theories are widely used to approximate the order parameters of many broken-symmetry states such as ferromagnetism.

Spin Precession

In the presence of a magnetic field, a magnetic dipole with a magnetic moment of $e\hbar/2m_e c$ in cgs units has the Hamiltonian[58]:

$$\hat{\mathcal{H}} = -\frac{e}{m_e c} \hat{\mathbf{S}} \cdot \mathbf{B} = -\frac{eB}{m_e c} \hat{S}^z \quad (1.3)$$

where it can be assumed that $\mathbf{B} = B\hat{\mathbf{z}}$, which simplifies the Hamiltonian. Using the Heisenberg picture, one can derive the time-dependence of this magnetic dipole in an applied magnetic field:

$$\begin{aligned}
\frac{d\langle\hat{\mathbf{S}}(t)\rangle}{dt} &= -\frac{1}{i\hbar}\langle[\hat{\mathcal{H}},\hat{\mathbf{S}}(t)]\rangle + \frac{\partial\langle\hat{\mathbf{S}}(t)\rangle}{\partial t} \\
\frac{d\langle\hat{S}^x(t)\rangle}{dt} &= -\frac{eB}{i\hbar m_e c}\langle[\hat{S}^z(t),\hat{S}^x(t)]\rangle = \frac{eB}{m_e c}\langle\hat{S}^y(t)\rangle \\
\frac{d\langle\hat{S}^y(t)\rangle}{dt} &= -\frac{eB}{i\hbar m_e c}\langle[\hat{S}^z(t),\hat{S}^y(t)]\rangle = -\frac{eB}{m_e c}\langle\hat{S}^x(t)\rangle \\
\frac{d\langle\hat{S}^z(t)\rangle}{dt} &= -\frac{eB}{i\hbar m_e c}\langle[\hat{S}^z(t),\hat{S}^z(t)]\rangle = 0
\end{aligned} \tag{1.4}$$

where the commutation relation $[\hat{S}^l, \hat{S}^m] = i\hbar\epsilon_{lmn}\hat{S}^n$ was used to simplify these equations and obviously \hat{S}^z commutes with itself. In order to decouple these coupled first-order equations, the second-order differential equations can be considered:

$$\begin{aligned}
\frac{d^2\langle\hat{S}^x(t)\rangle}{dt^2} &= \frac{eB}{m_e c}\frac{d\langle\hat{S}^y(t)\rangle}{dt} = -\left(\frac{eB}{m_e c}\right)^2\langle\hat{S}^x(t)\rangle \\
\frac{d^2\langle\hat{S}^y(t)\rangle}{dt^2} &= -\frac{eB}{m_e c}\frac{d\langle\hat{S}^x(t)\rangle}{dt} = -\left(\frac{eB}{m_e c}\right)^2\langle\hat{S}^y(t)\rangle
\end{aligned} \tag{1.5}$$

which has the normal mode solutions with the frequency $\omega = eB/m_e c$, $\langle\hat{S}^x(t)\rangle = \langle\hat{S}^x(0)\rangle\cos\omega t - \langle\hat{S}^y(0)\rangle\sin\omega t$, and $\langle\hat{S}^y(t)\rangle = \langle\hat{S}^y(0)\rangle\cos\omega t + \langle\hat{S}^x(0)\rangle\sin\omega t$. Therefore, in the presence of an applied magnetic field, dipoles will precess around the applied field with frequency $\omega = eB/m_e c$.

Microscopic Models of Magnetism

The nearest-neighbor Heisenberg model is a common choice for understanding the magnetic interaction in solids, and is defined by the Hamiltonian:

$$\hat{\mathcal{H}}_{\text{Heisenberg}} = -\sum_{\langle ij \rangle} J\hat{\mathbf{S}}_i \cdot \hat{\mathbf{S}}_j \tag{1.6}$$

where $\sum_{\langle ij \rangle}$ is a sum over nearest-neighbor interactions, $\hat{\mathbf{S}}_i$ is the spin at the i^{th} lattice site, and J is the coupling constant. When $J > 0$, the Heisenberg Hamiltonian favors ferromagnetic ordering as parallel spins minimize the energy, whereas antiferromagnetic ordering is energetically favorable when $J < 0$. A simpler model to consider when modeling magnetic solids is the Ising model, which restricts the spins to pointing only in the $\pm\hat{z}$ -directions. The Ising model Hamiltonian is:

$$\hat{\mathcal{H}}_{\text{Ising}} = - \sum_{\langle ij \rangle} J \hat{S}_i^z \cdot \hat{S}_j^z \quad (1.7)$$

where \hat{S}_i^z is the z -component of the spin at the i^{th} lattice site.

Magnons and Spin Waves

Common to all broken-symmetry states, the ferromagnetic state has zero-energy excitations, or Goldstone modes, known as magnons. In order to discuss the magnon dispersion relation, the simple case of the one-dimensional nearest-neighbor Heisenberg Model can be considered:

$$\hat{\mathcal{H}}_{\text{Heisenberg}} = - \sum_{\langle ij \rangle} J \hat{\mathbf{S}}_i \cdot \hat{\mathbf{S}}_j = -2J \sum_i \hat{\mathbf{S}}_i \cdot \hat{\mathbf{S}}_{i+1} \quad (1.8)$$

From which the time-dependent spin operators can be found from the Heisenberg representation:

$$\frac{d\langle \hat{\mathbf{S}}_i(t) \rangle}{dt} = \frac{1}{i\hbar} \langle [\hat{\mathbf{S}}_i(t), \hat{\mathcal{H}}_{\text{Heisenberg}}] \rangle + \frac{\partial \langle \hat{\mathbf{S}}_i \rangle}{\partial t} = \frac{1}{i\hbar} \langle [\hat{\mathbf{S}}_i(t), -2J \sum_i \hat{\mathbf{S}}_i(t) \cdot \hat{\mathbf{S}}_{i+1}(t)] \rangle \quad (1.9)$$

where $\hat{\mathbf{S}}_i$ and $\hat{\mathbf{S}}_j$ commute when $i \neq j$, so only terms in $\hat{\mathcal{H}}_{\text{Heisenberg}}$ which contain $\hat{\mathbf{S}}_i$ are nonzero in this commutation relation.

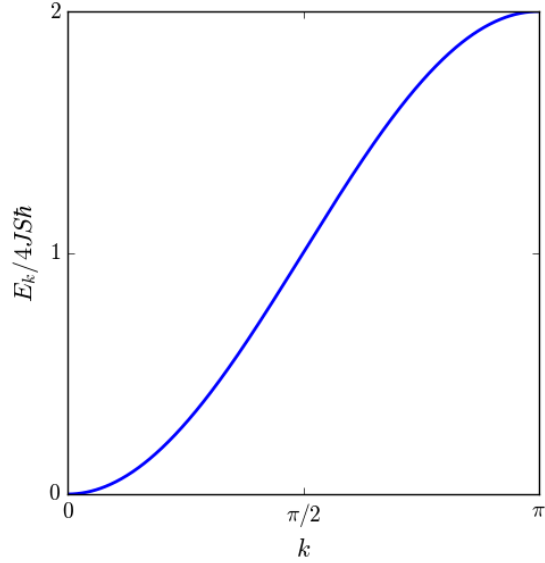


Figure 1.3: Magnon dispersion relation E_k , for a one-dimensional ferromagnetic chain of spins. It can be seen that zero-energy magnon excitations exist at $k = 0$, these are known as Goldstone bosons.

$$\frac{d\langle \hat{\mathbf{S}}_i(t) \rangle}{dt} = -\frac{2J}{i\hbar} \langle [\hat{\mathbf{S}}_i(t), \hat{\mathbf{S}}_{i-1}(t) \cdot \hat{\mathbf{S}}_i(t)] + [\hat{\mathbf{S}}_i(t), \hat{\mathbf{S}}_i(t) \cdot \hat{\mathbf{S}}_{i+1}(t)] \rangle \quad (1.10)$$

which can be simplified using the relations:

$$\begin{aligned} [\hat{\mathbf{S}}_i(t), \hat{\mathbf{S}}_{i-1}(t) \cdot \hat{\mathbf{S}}_i(t)] &= \sum_l \hat{\mathbf{r}}_l [\hat{S}_i^l(t), \sum_m \hat{S}_{i-1}^m(t) \hat{S}_i^m(t)] \\ &= \sum_l \sum_m \hat{\mathbf{r}}_l \hat{S}_{i-1}^m(t) [\hat{S}_i^l(t), \hat{S}_i^m(t)] \\ &= i\hbar \sum_l \sum_m \sum_n \epsilon_{lmn} \hat{\mathbf{r}}_l \hat{S}_{i-1}^m(t) \hat{S}_i^n(t) \\ &= i\hbar \hat{\mathbf{S}}_{i-1}(t) \times \hat{\mathbf{S}}_i(t) \end{aligned} \quad (1.11)$$

where $\hat{\mathbf{r}}_l$ is the unit vector in the l -direction. Similarly $[\hat{\mathbf{S}}_i(t), \hat{\mathbf{S}}_{i+1}(t) \cdot \hat{\mathbf{S}}_i(t)] = i\hbar \hat{\mathbf{S}}_{i+1}(t) \times \hat{\mathbf{S}}_i(t)$, therefore this equation can be simplified to:

$$\frac{d\langle\hat{\mathbf{S}}_i(t)\rangle}{dt} = 2J\langle\hat{\mathbf{S}}_i(t) \times (\hat{\mathbf{S}}_{i-1}(t) + \hat{\mathbf{S}}_{i+1}(t))\rangle \quad (1.12)$$

Treating the spins classically, and assuming the solution is close to the ferromagnetic ground state where all the spins are aligned along the \hat{z} -direction, it can be assumed that $S_i^z \approx S$, $S_i^x \ll S$, and $S_i^y \ll S$.

$$\begin{aligned} \frac{dS_i^x}{dt} &\approx 2JS(2S_i^y - S_{i-1}^y - S_{i+1}^y) \\ \frac{dS_i^y}{dt} &\approx -2JS(2S_i^x - S_{i-1}^x - S_{i+1}^x) \\ \frac{dS_i^z}{dt} &\approx 0 \end{aligned} \quad (1.13)$$

Assuming normal mode solutions, we arrive at the solutions where S_i^x and S_i^y are $\pi/2$ out of phase[4]:

$$S_j^x = Ae^{i(kja-\omega t)}, \quad S_j^y = -iAe^{i(kja-\omega t)} \quad (1.14)$$

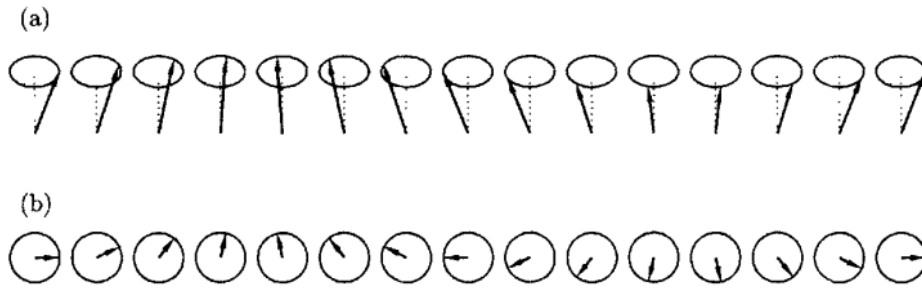


Figure 1.4: Spin wave on a line of precessing spins (a) perspective view (b) top view. Figure originally published in *Magnetism in Condensed Matter*, S. Blundell[4].

which yields the magnon dispersion relation for a one-dimensional ferromagnetic chain of spins:

$$E_k = 4JS\hbar(1 - \cos ka) \quad (1.15)$$

The magnon dispersion relation plotted as a function of the wavevector k for a one-dimensional chain of spins can be seen in Figure 1.3, where it can be seen that for $k = 0$ zero-energy excitations exist. These spin waves (magnons) affect the line of one-dimensional spins by causing them to precess slightly out of phase with their neighbors, as can be seen in Figure 1.4.

Hubbard Model

While the exchange term in the Heisenberg Hamiltonian is written in terms of the spin operators, the Hubbard Hamiltonian accounts for the interactions between electron spins in a different way[63]:

$$\hat{\mathcal{H}}_{\text{Hubbard}} = -t \sum_{\langle ij \rangle} \sum_{\sigma=\downarrow, \uparrow} (\hat{a}_{i,\sigma}^\dagger \hat{a}_{j,\sigma} + \hat{a}_{j,\sigma}^\dagger \hat{a}_{i,\sigma}) + U \sum_i n_{i,\uparrow} n_{i,\downarrow} \quad (1.16)$$

where t is the nearest-neighbor hopping energy and $\hat{a}_{i,\sigma}^\dagger$ is the creation operator for an electron on the i^{th} atom with spin σ , therefore the first term in the Hubbard Hamiltonian accounts for the the delocalized or band-like behavior of electrons where electrons of the same spin move between lattice sites. This term can be shown to be proportional to the kinetic energy. U is the Coulomb energy experienced by electrons of opposite spin on the same atom and $n_{i,\sigma} = \hat{a}_{i,\sigma}^\dagger \hat{a}_{i,\sigma}$ is the number operator for electrons on the i^{th} atom and spin σ , which favors the formation of localized moments. In contrast to the Heisenberg model, which allows for the flipping of localized spins exclusively, the Hubbard model allows for electrons, which preserve their spins, to move between lattice sites.

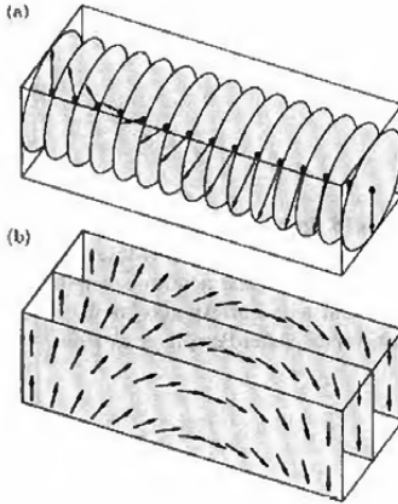


Figure 1.5: (a) Bloch domain wall where the magnetic moments rotate in a plane parallel to the domain wall. (b) Néel domain wall where the magnetic moments rotate in a plane perpendicular to the domain wall. Figure originally published in *Magnetism in Condensed Matter*, S. Blundell[4].

Magnetic Domains & Domain Walls

Ferromagnets in the absence of a strong magnetic field to align all magnetic moments parallel to each other and at finite temperatures have magnetic domains. Magnetic domains are regions of the magnetic material where all the moments are aligned (at least for a ferromagnet), which typically neighbor regions with their magnetic moments pointing in another direction. The boundary between neighboring magnetic domains such as these is commonly referred to as a domain wall. While one might imagine an abrupt change in the magnetic moments between these domains, it is actually more energetically favorable for this transition to occur over many lattice sites.

The most common types of domain wall are the Bloch domain wall, where the magnetic moments rotate in a plane parallel to the plane of the domain wall and can be seen in Figure 1.5(a), and the Néel domain wall, where the magnetic moments rotate in a plane perpendicular to the plane of the domain wall and can be seen in Figure 1.5(b). If we

consider the energy cost of these domain walls with the Heisenberg Hamiltonian discussed previously, it can be shown that the energy cost of these domain walls decreases drastically as the number of lattice sites involved in the domain wall increases ($E_{\text{domain}} \propto 1/N$). While one might expect the domain wall to therefore encompass the whole sample in order for $N \rightarrow 0$ and $E_{\text{domain}} \rightarrow \infty$, this isn't the only interaction competing to dictate the directions in which the magnetic moments point and the magnetic anisotropy ensures that this doesn't happen.

Magnetic Anisotropy

In magnetic materials it is observed that the magnetization has preferred directions in which to point, known as the easy axes, which are a combination of both intrinsic and extrinsic anisotropies. Intrinsic anisotropy comes from the lattice and its effect on the electronic orbitals. Whereas extrinsic anisotropy is the result of factors external to the lattice such as the physical geometry of the magnetic material which leads to a demagnetization field due to the magnetic reconnection of field lines from surface dipoles.

Shape anisotropy is the result of magnetic dipoles on the surface of a magnetic material coupling with other surface dipoles through the interaction energy[63]:

$$E_{\text{dipole-dipole}} = -\frac{1}{2\pi\mu_0} \sum_{i \neq j} \frac{1}{r_{ij}^3} \left(\mathbf{m}_i \cdot \mathbf{m}_j - 3 \frac{(\mathbf{r}_{ij} \cdot \mathbf{m}_i)(\mathbf{r}_{ij} \cdot \mathbf{m}_j)}{r_{ij}^2} \right) \quad (1.17)$$

where \mathbf{r}_{ij} is the displacement vector between the i^{th} and j^{th} magnetic moments and \mathbf{m}_i is the i^{th} atomic dipole moment. While dipoles coupling within the material do contribute to the anisotropy, they aren't associated with the shape anisotropy. Accordingly, the dipole-dipole interaction in bulk materials can be separated into three components:

$$E_{\text{dipole-dipole}} = E_S + E_L + E_D \quad (1.18)$$

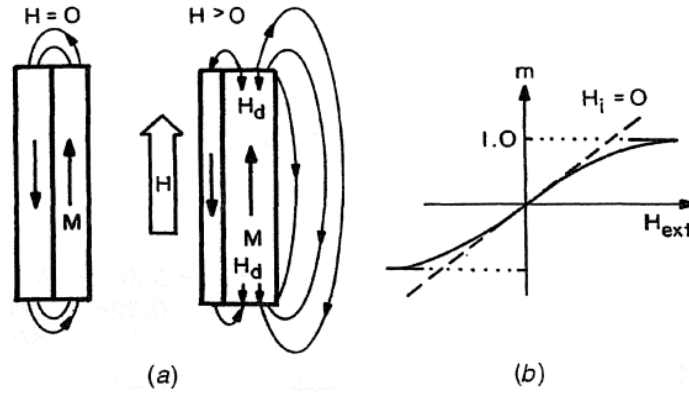


Figure 1.6: (a) How a magnetic material with two domains resists magnetizing parallel to an applied magnetic field due to the demagnetizing field. (b) The changing demagnetizing factor causes the M - H loop to be less than linear in the external field. Figure originally published in *Modern Magnetic Materials Principles and Application*, Robert C. O’Handley[49].

where E_S is a "microscopic" component coming from the atomic dipoles on the lattice sites within a spherical volume and E_L comes from magnetic pseudo-charges on the surface of that sphere. E_D is due to the demagnetizing field and is a "macroscopic" component coming from magnetic pseudo-charges on the external surface of the magnetic sample. The dominant term is E_D , which is due to the demagnetizing field and is responsible for the extrinsic anisotropy known as shape anisotropy. Thus, macroscopic shape anisotropy has its origins from dipole interactions between free dipoles at the surface which create fields external to the magnetic sample and reconnect with other free dipoles on the surface, a schematic diagram of this process can be seen in Figure 1.6(a).

Magnetocrystalline anisotropy is not simply due to the anisotropy of the dipole interaction, as is the case for the shape anisotropy, but rather due to more intrinsic interactions within the crystalline lattice. Crystalline anisotropy can be attributed to the spin part of the magnetic moment coupling to the electronic orbital shape and orientation, also known as spin-orbit coupling ($\xi \mathbf{L} \cdot \mathbf{S}$), as well as the chemical bonding of the atomic orbitals with their local environment, also known as the crystalline electric field. The strength of the

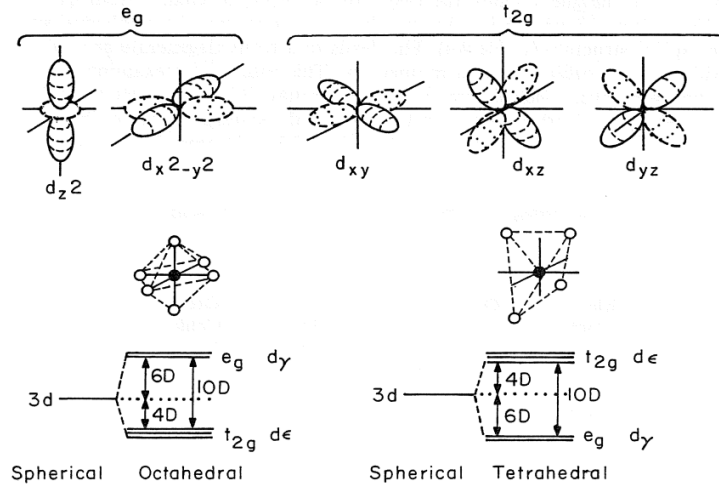


Figure 1.7: Topologies of the five d -wave orbitals, separated into e_g and t_{2g} symmetry, are shown at the top. Symmetry of the octahedral and tetrahedral sites are shown in the center. Splitting of the crystal field for $3d^4$ and $3d^9$ levels in octahedral and tetrahedral site symmetry are shown at the bottom. Figure originally published in *Modern Magnetic Materials Principles and Applications*, Robert C. O’Handley[49].

anisotropy of the crystalline electric field determines the strength of the magnetic anisotropy that an ion in that field can exhibit. For the transition metals, the anisotropy is often treated by examining the crystal field splitting of the valence states of the relevant magnetic ion and considering spin-orbit coupling as a perturbation. When a magnetic ion is considered in a crystal lattice, the typical degeneracy of the five electronic d -orbitals becomes lifted. The e_g orbitals, d_{z^2} and $d_{x^2-y^2}$ whose electronic wavefunctions point toward the six neighboring sites, and t_{2g} orbitals, d_{xy} , d_{xz} , and d_{yz} whose electronic wavefunctions point between neighboring sites, take on different energy levels. These orbitals can be seen in Figure 1.7. The electron occupation of the e_g and t_{2g} sites depends on the relative energies of the orbitals and the number of valence electrons. Fully occupied orbitals have no total angular momentum and don’t contribute to the crystalline anisotropy, only orbitals with a total angular momentum will determine which direction the material prefers to magnetize in (also known as the easy axis).

Materials with cubic lattices exhibit a magnetocrystalline anisotropy with the same cubic symmetry. A phenomenological approach to solving for the energy associated with the magnetic cubic anisotropy is to write it in terms of the direction cosines $\alpha_x = \sin \theta \cos \phi$, $\alpha_y = \sin \theta \sin \phi$, and $\alpha_z = \cos \theta$. Where the direction cosines represent the magnetization vector components normalized by the saturation magnetization $\alpha_i = m_i = M_i/M_S$. The energy associated with the cubic anisotropy can therefore be written as[53]:

$$E_{\text{cubic}} = \kappa_2(\alpha_x^2 + \alpha_y^2 + \alpha_z^2) + \kappa_4(\alpha_x^4 + \alpha_y^4 + \alpha_z^4) + \kappa_6(\alpha_x^6 + \alpha_y^6 + \alpha_z^6) + \dots \quad (1.19)$$

where it can be seen that only terms belonging to the cubic symmetry group have been considered. This can be shown to reduce to the more common form for cubic anisotropy:

$$E_{\text{cubic}} = E_0 + K_{\text{cubic}}^{(1)}(\alpha_x^2\alpha_y^2 + \alpha_x^2\alpha_z^2 + \alpha_y^2\alpha_z^2) + K_{\text{cubic}}^{(2)}\alpha_x^2\alpha_y^2\alpha_z^2 + \dots \quad (1.20)$$

where $E_0 = \kappa_2 + \kappa_4 + \kappa_6$ is a constant and is largely unimportant, $K_{\text{cubic}}^{(1)} = -2\kappa_4 - 4\kappa_6$ is the first-order cubic anisotropy constant, and $K_{\text{cubic}}^{(2)} = 6\kappa_6$ is the second-order cubic anisotropy constant. In practice the magnitude of the cubic anisotropy constants decreases with increasing order, because of this only the first two terms are typically considered. When $K_{\text{cubic}}^{(1)} > 0$, the easy axes are oriented along the $[\pm 1, 0, 0]$, $[0, \pm 1, 0]$, and $[0, 0, \pm 1]$ directions, and the hard axes are oriented along the $[\pm 1, \pm 1, \pm 1]$ directions. This can be seen in Figure 1.8(a), where the energy minima occur along the $[\pm 1, 0, 0]$, $[0, \pm 1, 0]$, and $[0, 0, \pm 1]$ directions. However, when $K_{\text{cubic}}^{(1)} < 0$, the easy and hard axes become switched. Which can be seen in Figure 1.8(b) where the energy is minimized along the $[\pm 1, \pm 1, \pm 1]$ directions.

Common materials with cubic anisotropies are bcc Fe (which has $K_{\text{cubic}}^{(1)} > 0$) and fcc Co (which has $K_{\text{cubic}}^{(1)} < 0$)[53]. While bulk materials exhibit cubic anisotropy with six easy axes, a strong shape anisotropy in magnetic thin films forces the magnetization to remain

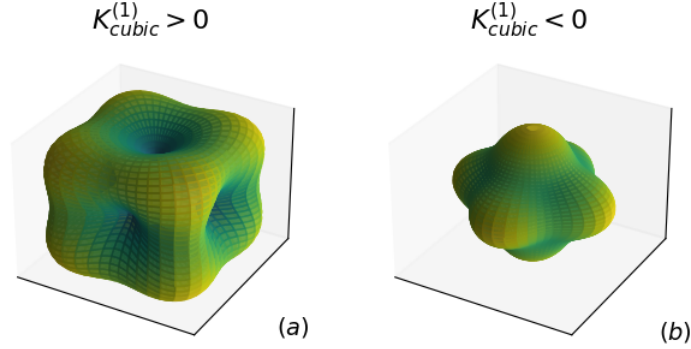


Figure 1.8: Cubic anisotropy free energy surface plot when $K_{\text{cubic}}^{(2)} = 0$ (a) and $K_{\text{cubic}}^{(1)} > 0$ and the easy axes are oriented along the $[\pm 1, 0, 0]$, $[0, \pm 1, 0]$, and $[0, 0, \pm 1]$ directions (b) and $K_{\text{cubic}}^{(1)} < 0$ and the easy axes are oriented along the $[\pm 1, \pm 1, \pm 1]$ directions.

in the film plane. Thus, $\theta = \pi/2$ and $\alpha_x = \cos \phi$, $\alpha_y = \sin \phi$, $\alpha_z = 0$. This reduces the cubic anisotropy energy to:

$$E_{\text{cubic}} = E_0 + K_{\text{cubic}}^{(1)} \sin^2 \phi \cos^2 \phi \quad (1.21)$$

A tetragonal distortion, which breaks the cubic symmetry ($c \neq a = b$) of the lattice can result in a uniaxial magnetocrystalline anisotropy. The free energy of a uniaxial anisotropy can be written as[49]:

$$E_u = E_0 + K_u^{(1)} \sin^2 \theta + K_u^{(2)} \sin^4 \theta + \dots \quad (1.22)$$

where $K_u^{(1)}$ and $K_u^{(2)}$ are the first- and second-order uniaxial anisotropy constants respectively. When $K_u^{(1)} > 0$ the easy axis lies along the c -axis, and when $K_u^{(1)} < 0$ the easy axes lie along the a - and b -axes.

Magnetic Hysteresis

One effect of magnetic anisotropy is the magnetic hysteresis loop. Hysteresis loops are the result of an applied magnetic field overcoming the energy minima associated with the magnetization pointing along one of the easy axes of the magnetic sample. If a magnetic field is applied parallel to an easy axis, the flipping of the magnetic moment is rather abrupt as the magnetic anisotropy favors the moment pointing in that direction. A calculated hysteresis loop with an applied magnetic field somewhat near an easy axis can be seen in Figure 1.9(c). However, if a magnetic field is applied along a hard axis it is quite difficult for the applied field to overcome the magnetic anisotropy. This results in no magnetic hysteresis, which can be seen in Figure 1.9(a) due to the fact that the magnetization along the hard axis will always be zero without an applied magnetic field as it is an energetically unfavorable direction for the magnetization to point.

Stoner-Wohlfarth Model

If one assumes that an entire ferromagnetic sample consists of a single domain, and thus a single magnetic moment (this is known as the macroscopic spin approximation), the magnetic hysteresis loop can be quite simply derived via the Stoner-Wohlfarth model. This approximation works quite well for ferromagnets which were previously magnetized in a strong magnetic field. The Stoner-Wohlfarth model begins by subtracting the Zeeman coupling term between the applied magnetic field (\mathbf{H}) and the sample magnetization (\mathbf{M}) from the anisotropic free energy:

$$E = E_{\text{anis}} - \mu_0 \mathbf{H} \cdot \mathbf{M} \quad (1.23)$$

where E_{anis} can be the anisotropic free energy (neglecting the constant E_0) for any symmetry in general, but here only cubic and uniaxial symmetries will be considered. In order to simplify the problem, the second-order anisotropy constants $K_{\text{cubic}}^{(2)}$ and $K_u^{(2)}$ will be ignored,

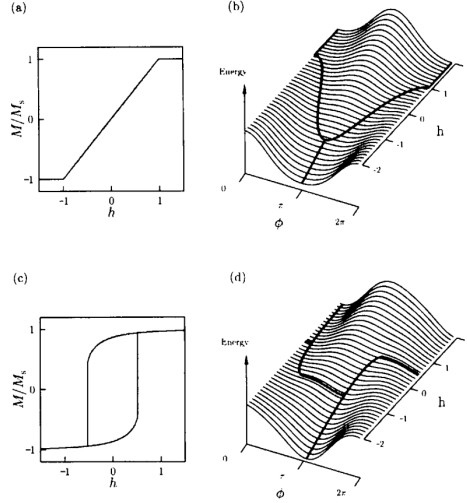


Figure 1.9: Hysteresis loops for a sample with uniaxial anisotropy when a magnetic field is applied at an angle (a) $\theta_a = \pi/2$ relative to the easy axis, also known as the hard axis and (b) $\theta_a = \pi/6$ relative to the easy axis. Energy surface as a function of normalized applied magnetic field h and magnetization direction ϕ with the minima overlayed when (a) $\theta_a = \pi/2$ relative to the easy axis and (b) $\theta_a = \pi/6$ relative to the easy axis. Figure originally published in *Magnetism in Condensed Matter*, S. Blundell[4].

noting that these tend to be an order of magnitude smaller than the first-order terms. The free energy can be normalized by the first-order anisotropy constant in order to reduce the parameters by defining the reduced energy Γ [37]:

$$\Gamma = E_{\text{anis}}^{(1)}/K_i^{(1)} - 2\mathbf{h} \cdot \mathbf{M}/M_S \quad (1.24)$$

where $\mathbf{h} = \frac{\mathbf{H}}{H_K}$, $H_K = \frac{2K_i^{(1)}}{\mu_0 M_S}$, $K_i^{(1)}$ is the first-order cubic or uniaxial anisotropy constant, and M_S is the saturation magnetization. Minimizing this free energy as a function of the magnetization direction, ϕ or θ , can be used to find the magnetization (\mathbf{M}) as a function of applied magnetic field (\mathbf{H}), also known as the magnetic hysteresis loop. This process is rather simply illustrated in Figure 1.9 for a uniaxial anisotropy.

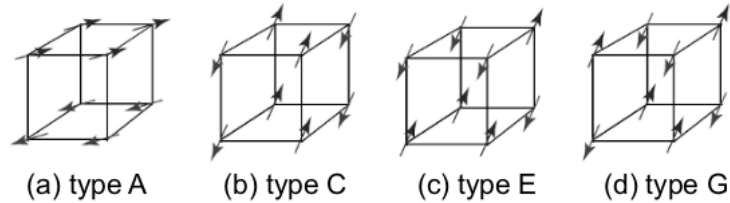


Figure 1.10: Four types of antiferromagnetic order that occur on simple cubic lattices. Figure originally published in *Fundamentals of Magnetism*, Mathias Getzlaff[24].

Antiferromagnetism

If the exchange interaction between neighboring magnetic moments, J (from the Heisenberg/Ising Hamiltonian), is negative it becomes energetically favorable for the magnetic moments to be antiparallel with each other. Such an interaction results in antiferromagnetic behavior. Antiferromagnets can be described with two ferromagnetic sublattices whose magnetizations are aligned antiparallel to each other, resulting in a zero net magnetization.

Types of Antiferromagnetism

There are many ways to arrange an equal number of up and down spins on a lattice. G-type antiferromagnetism is one of the more common antiferromagnetic states on simple cubic lattices because all nearest-neighbor lattice sites have anti-aligned magnetic moments, which can be seen in Figure 1.10(d). A-type antiferromagnets form ferromagnetic layers which are antiferromagnetically coupled, as can be seen in Figure 1.10(a). B-type antiferromagnets result in chain-like ferromagnetic ordering which are antiferromagnetically coupled to neighboring chains, as can be seen in Figure 1.10(b).

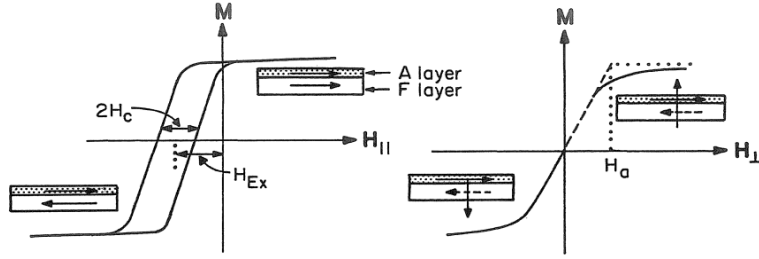


Figure 1.11: Effect of exchange coupling on magnetic hysteresis loop for a material with an antiferromagnetic layer and a soft ferromagnetic layer. Figure originally published in *Modern Magnetic Materials*, Robert C. O’Handley[49].

Exchange Bias

If an antiferromagnetic layer is grown on a ferromagnetic layer (or vice-versa), the antiferromagnetic layer can exert an exchange magnetic field (\mathbf{H}_{Ex}) which picks a preferred direction, not just a preferred axis for the ferromagnet to magnetize in. This effect can be understood through a shift in the hysteresis loop measured along the easy axis by an amount equal to the exchange field, which can be seen in Figure 1.11.

In order to model ferromagnets with an antiferromagnetic exchange layer, the energy that was considered in the Stoner-Wohlfarth model can be modified to include the exchange field[37]:

$$E = E_{\text{anis}} - \mu_0(\mathbf{H} + \mathbf{H}_{\text{Ex}}) \cdot \mathbf{M} \quad (1.25)$$

which behaves as expected within the Stoner-Wohlfarth model, that is it shifts the magnetic hysteresis by \mathbf{H}_{Ex} .

Spin Density Waves

Antiferromagnetic stripe ordering[68] can lead to the formation of a spin density wave (SDW) state with a sinusoidal spatial magnetization of the form $\mathbf{M}(\mathbf{r}) = M\hat{\mathbf{z}} \cos \mathbf{Q} \cdot \mathbf{r}$, where M is the magnetization of the antiferromagnetic sublattice and \mathbf{Q} is the SDW nesting

vector. The spin density wave state can either be commensurate or incommensurate with the underlying crystal lattice. Some common commensurate SDW nesting vectors in two-dimensions are $\mathbf{Q} = (\pi, \pi)$, $\mathbf{Q} = (\pi, 0)$, and $\mathbf{Q} = (\pi/2, \pi/2)$. The $\mathbf{Q} = (\pi, \pi)$ SDW state, most commonly seen in the cuprates[12, 68] is also referred to as the AFM1[17] state and is similar to the G-type antiferromagnets previously mentioned where the nearest-neighbor spins all display antiferromagnetic alignments. The magnetizations of an AFM1 system can be seen in Figure 1.12(a), along with its magnetic unit cell seen as a dashed black curve. A spin density wave phase can lead to a FS reconstruction[27, 39] which gaps sections of the FS due to nesting. This nesting occurs because AFM reduces the periodicity of the lattice by resulting in a larger magnetic unit cell than the $a \times a$ unit cell of the lattice leading to a smaller Reduced Brillouin Zone (RBZ) than the $\frac{2\pi}{a} \times \frac{2\pi}{a}$ First Brillouin Zone (FBZ). The AFM1 state has magnetic lattice vectors $\mathbf{a}^{\text{AFM1}} = a(\hat{\mathbf{x}} + \hat{\mathbf{y}})$ and $\mathbf{b}^{\text{AFM1}} = a(\hat{\mathbf{y}} - \hat{\mathbf{x}})$, which results in the magnetic unit cell seen as the black dashed curve in Figure 1.12 (a). This results in the reciprocal magnetic lattice vectors of $\mathbf{a}_{\mathbf{k}}^{\text{AFM1}} = \frac{\pi}{a}(\hat{\mathbf{x}} + \hat{\mathbf{y}})$ and $\mathbf{b}_{\mathbf{k}}^{\text{AFM1}} = \frac{\pi}{a}(\hat{\mathbf{y}} - \hat{\mathbf{x}})$, which results in the RBZ seen as the black dashed curve in Figure 1.12 (d). This Reduced Brillouin Zone supports Fermi Surface nesting both parallel and perpendicular to the nesting vector \mathbf{Q} when the Spin Density Waves are commensurate with the lattice. Specifically, this occurs for a tight-binding model electron dispersion of:

$$\xi_{\mathbf{k}}^{(0)} = \mu - t_1 \cos k_x a - t_1 \cos k_y a - t_2 \cos k_x a \cos k_y a \quad (1.26)$$

where μ is the chemical potential and was set to 0, t_1 is the nearest-neighbor hopping parameter, and t_2 is the next-nearest neighbor hopping parameter. This can also be seen from the intersection of the black ($\xi_{\mathbf{k}}^{(0)} = 0$ FS) and red ($\xi_{\mathbf{k}+\mathbf{Q}}^{(0)} = 0$ FS translated by \mathbf{Q}) curves in Figure 1.12 (d) along all four edges of the RBZ. This gaps the FS where these overlaps occur, known as a FS reconstruction. This is the result of a band hybridization of

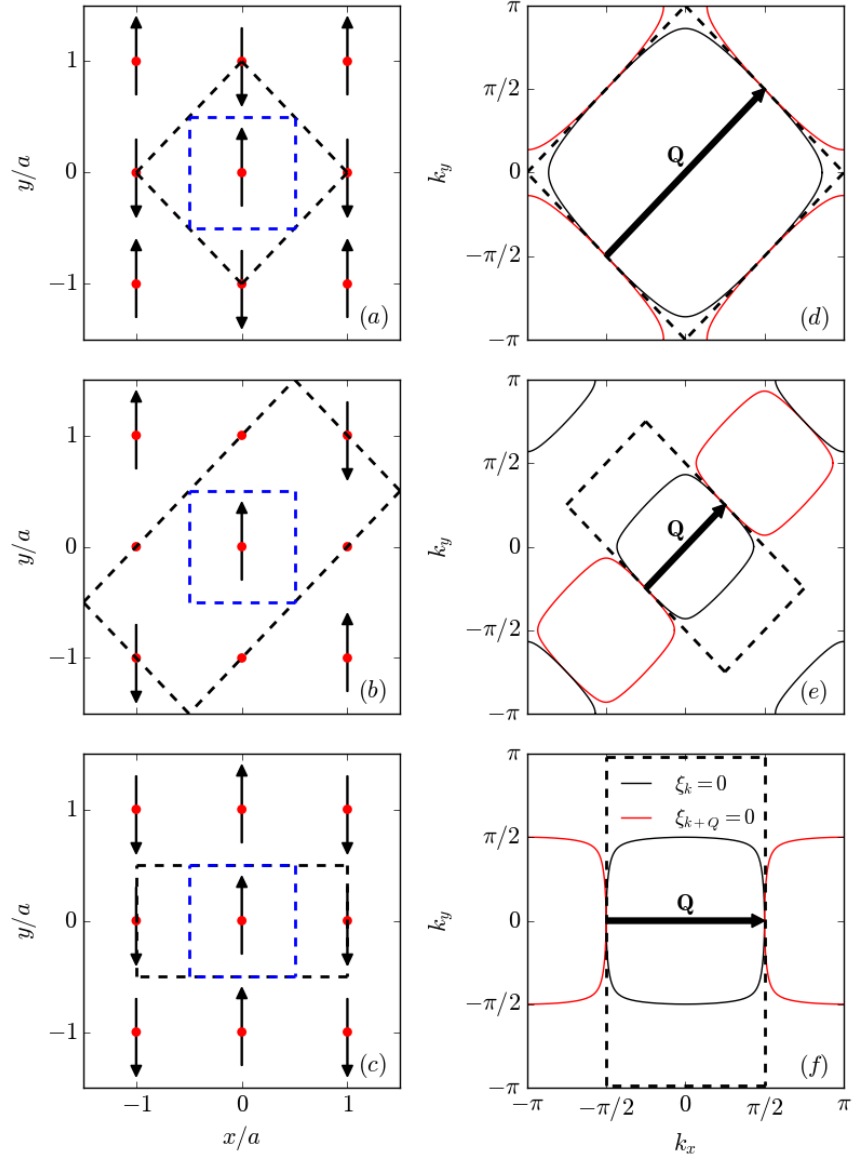


Figure 1.12: (a)-(c) Square lattice of magnetic atoms (red points) where black arrows are on-site magnetization in $\pm \hat{z}$ direction, blue dashed lines are crystalline unit cell, and black dashed lines are magnetic unit cell for SDW state when: (a) $\mathbf{Q} = (\pi, \pi)$, (b) $\mathbf{Q} = (\pi/2, \pi/2)$, and (c) $\mathbf{Q} = (\pi, 0)$. (d)-(e) Fermi Surface (solid black curve) constructed to allow for FS nesting with FS translated by \mathbf{Q} (solid red curves) at the edges of the Reduced Brillouin Zone (dashed black lines) for SDW with nesting vector: (d) $\mathbf{Q} = (\pi, \pi)$, (e) $\mathbf{Q} = (\pi/2, \pi/2)$, and (f) $\mathbf{Q} = (\pi, 0)$.

the $\xi_{\mathbf{k}}$ and $\xi_{\mathbf{k}+\mathbf{Q}}$ bands, which will be discussed in greater detail later.

The $\mathbf{Q} = (\pi, 0)$ SDW state is also referred to as the AFM2 state[17] is common to the iron pnictide materials[15, 30] and is a two-dimensional analogue to the C-type antiferromagnets where ferromagnetically coupled chains of spins are antiferromagnetically coupled to one another. The magnetization of an AFM2 state on a two-dimensional square lattice can be seen in Figure 1.12(c) and the resulting magnetic unit cell is again seen as a black dashed curve. This results in the magnetic lattice vectors $\mathbf{a}^{\text{AFM2}} = 2a\hat{\mathbf{x}}$ and $\mathbf{b}^{\text{AFM2}} = a\hat{\mathbf{y}}$. This reduces the $C(4)$ rotational symmetry of the crystal lattice to a $C(2)$ rotational symmetry similar the AF3 state. Furthermore, the reciprocal lattice vectors of the AFM2 state are $\mathbf{a}_{\mathbf{k}}^{\text{AFM2}} = \frac{\pi}{a}\hat{\mathbf{x}}$ and $\mathbf{b}_{\mathbf{k}}^{\text{AFM2}} = \frac{2\pi}{a}\hat{\mathbf{y}}$, which also results in a RBZ with a $C(2)$ rotational symmetry and can be seen from the black dashed lines in Figure 1.12 (f). the AFM2 state results is commensurate with the lattice when the normal state tight-binding electron dispersion is:

$$\xi_{\mathbf{k}}^{(2)} = \mu - t_1 \cos((k_x - k_y)a) - t_1 \cos((k_x + k_y)a) - t_2 \cos((k_x - k_y)a) \cos((k_x + k_y)a) \quad (1.27)$$

where again the tight-binding parameters are the same as those for $\xi_{\mathbf{k}}^{(0)}$. Which only supports FS nesting parallel to \mathbf{Q} which reconstructs the FS, and preserves the normal state FS perpendicular to \mathbf{Q} .

The $\mathbf{Q} = (\pi/2, \pi/2)$ SDW state is seen in the iron chalcogenides[42], this phase is also known as the AFM3 state[17]. The AFM3 state has the magnetic lattice vectors $\mathbf{a}^{\text{AFM3}} = 2a(\hat{\mathbf{x}} + \hat{\mathbf{y}})$ and $\mathbf{b}^{\text{AFM3}} = a(\hat{\mathbf{y}} - \hat{\mathbf{x}})$ which results in the magnetic unit cell seen as the black dashed curve in Figure 1.12 (b). The antiferromagnetic ordering of the AFM3 state reduces the $C(4)$ rotational symmetry inherent to the lattice to the $C(2)$ rotational symmetry of the magnetic unit cell, similar to the AFM2 state (in fact these AFM states have many

similarities). The reciprocal magnetic lattice vectors of the AFM3 state are $\mathbf{a}_{\mathbf{k}}^{\text{AFM3}} = \frac{\pi}{2a}(\hat{\mathbf{x}} + \hat{\mathbf{y}})$ and $\mathbf{b}_{\mathbf{k}}^{\text{AFM3}} = \frac{\pi}{a}(\hat{\mathbf{y}} - \hat{\mathbf{x}})$, which results in a RBZ that also has a reduced $C(2)$ rotational symmetry and can be seen as the black dashed curve in Figure 1.12 (e). Due to the $C(2)$ symmetry inherent to the AFM3 RBZ, FS nesting is only supported parallel to \mathbf{Q} and not perpendicular to \mathbf{Q} when the SDW is commensurate with the lattice. This nesting occurs when the tight-binding electron dispersion is:

$$\xi_{\mathbf{k}}^{(1)} = \mu - t_1 \cos 2k_x a - t_1 \cos 2k_y a - t_2 \cos 2k_x a \cos 2k_y a \quad (1.28)$$

where the tight-binding parameters are the same as those for $\xi_{\mathbf{k}}^{(0)}$ and $\xi_{\mathbf{k}}^{(2)}$. This results in a FS reconstruction parallel to \mathbf{Q} , but preserves the normal state FS perpendicular to \mathbf{Q} .

Electronic Nematic Phase

The electronic nematic phase is used to denote an electron fluid which spontaneously breaks a symmetry of the underlying Hamiltonian, the interchange of two axes of the lattice[21]. A simple case to consider is that of a crystal with a $C(4)$ rotational symmetry, which nematicity reduces to a $C(2)$ rotational symmetry. However, in some instances where the crystal field is weak, the nematic state breaks a continuous rotational symmetry, $C(\infty)$, and reduces it to a $C(2)$ rotational symmetry for a two-dimensional (or quasi-two-dimensional) system. A nematic phase such as this is often referred to as a XY-nematic phase. It is also possible to consider more complex rotational symmetries as a result of a nematic phase, for instance a $C(\infty)$ rotational symmetry can be reduced to a hexagonal $C(6)$ rotational symmetry due to a nematic phase.

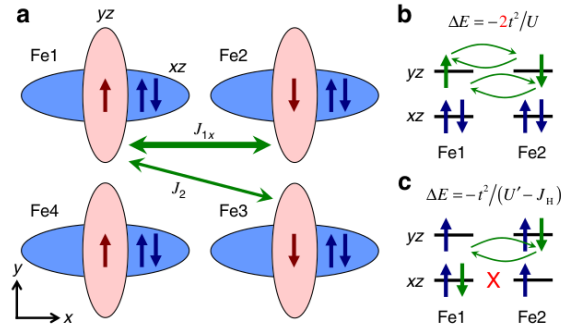


Figure 1.13: (a) Schematic of AFM2 (or type C AFM) magnetic structure with highly anisotropic nearest-neighbor hopping due to orbital ordering. (b),(c) Kinetic energy ΔE in the ferro-orbital and staggered-orbital structures. t and U denote the hopping parameter and intraorbital Coulomb repulsion, while U' and J_H denote the interorbital repulsion and Hund's exchange, respectively. Figure originally published in *Phys. Rev. Lett.*, 103(26):267001, 2009[41].

Electronic Origin of Nematic Phase

While the onset of the $C(2)$ electronic nematic state is often accompanied by a structural transition from a tetragonal lattice with $C(4)$ in-plane rotational symmetry to an orthorhombic or monoclinic lattice, which have $C(2)$ in-plane rotational symmetry and an antiferromagnetic spin-stripe phase, such as the AFM2 phase previously discussed which has a $C(2)$ rotational symmetry, the nematic phase is largely attributed to an unequal electronic orbital occupation. The relevant orbitals (at least in the Fe-based materials like the Fe pnictides) are the $3d_{xz}$ and $3d_{yz}$ orbitals[20] which have t_{2g} symmetry. These orbitals form two pockets with mostly d_{xz} and d_{yz} weight around the center of the Brillouin zone and two electron pockets at the zone corners with mostly d_{xy} characteristics[43]. The broken $C(4)$ tetragonal symmetry can be attributed to an unequal occupation of the d_{xz}/d_{yz} orbitals, arising from the coupled spin-orbital physics, which leads to anisotropic nearest-neighbor hopping integrals[41] (a schematic of which can be seen in Figure 1.13).

An electronic nematic state can arise from the melting of a striped, or smectic phase to one in which the translational symmetry is restored, but the rotational symmetry remains

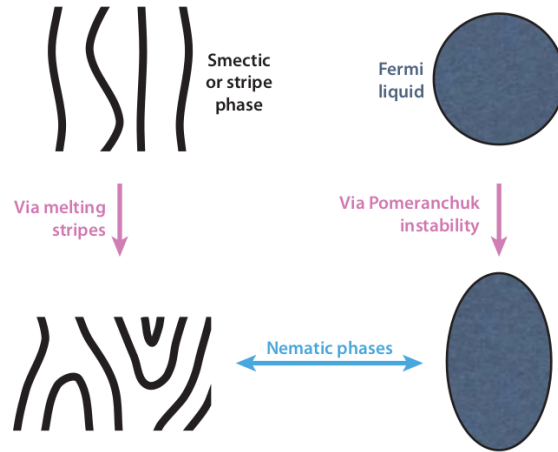


Figure 1.14: Two mechanisms for producing an electronic nematic phase: the melting of a striped phase which restores translational symmetry but preserves the reduced rotational symmetry, and a Fermi fluid developing nematic order through a distortion of the FS due to a Pomeranchuk instability. Figure originally published in *Annu. Rev. Condens. Matter Phys.*, 1:153–178, 2010[21].

broken. A schematic diagram of this process can be seen on the left side of Figure 1.14. The resulting nematic phase is typically an anisotropic metal since the underlying degrees of freedom are electrons which form these stripe segments.

A Fermi liquid can also develop an electronic nematic phase from a metallic state with a FS, whose symmetries reflect those of the underlying lattice, and well-defined quasiparticles. The nematic transition is due to a thermal (Pomeranchuk) instability in which the symmetries of the Fermi liquid state are lowered. If this instability occurs in the spin-singlet channel, the result is that the FS spontaneously distorts. In its most basic form, the Pomeranchuk instability is a quantum phase transition which distorts the circular FS of a metal into an elliptical FS, which can be seen on the right side of Figure 1.14. For a circular FS, the complex FS distortion can be defined from the anomalous expectation value of a Fermion bilinear in the particle-hole channel and a particular angular momentum channel as[21]:

$$\Phi_l = \sum_{\mathbf{k}} \langle \hat{a}_{\mathbf{k}}^\dagger \hat{a}_{\mathbf{k}} \rangle e^{il\phi_{\mathbf{k}}} \quad (1.29)$$

where $\langle \hat{a}_{\mathbf{k}}^\dagger \hat{a}_{\mathbf{k}} \rangle = f_{\mathbf{k}}^0$, is the number operator whose expectation value is equivalent to the Fermi distribution function and $\phi_{\mathbf{k}}$ is the polar angle in \mathbf{k} -space. The typical $C(2)$ nematic phase order parameter corresponds to the $l = 2$ component. This can be understood to have a d -wave symmetry. Additionally, the $l = 6$ component corresponds to the hexagonal Pomeranchuk phase briefly mentioned earlier. In the nematic phase, the anisotropic nature of the nematic ground state is also reflected in the transport properties[9, 19] which becomes stronger as the FS distortion grows.

Structural Transition

Upon the onset of the electronic nematic phase, the lattice either undergoes a simultaneous[20] or is preceded[33] by (as $T \rightarrow 0$) a structural transition. This structural transition shares the same reduced rotational symmetry of the nematic state, which has a $C(2)$ rotational symmetry, where the lattice typically transitions from a tetragonal lattice with an in-plane $C(4)$ rotational symmetry to an orthorhombic (see Figure 1.15) or a monoclinic lattice. This structural distortion is often attributed[18] to the antiferromagnetic spin-stripe state (or AFM2 state) commonly associated with the anisotropic orbital occupation in the nematic phase, which can be seen in Figure 1.13. Anisotropies in the electronic and spin degrees of freedom are inevitably connected to the crystal field of the lattice, which reflects these very same anisotropies.

Fermi Surface Distortion

As previously discussed, the simplest FS distortion to consider due to the electronic nematic state is on a circular FS which becomes distorted into an ellipse as can be seen in Figure 1.14. However, a more realistic FS (at least for the cuprates), is the tight-binding

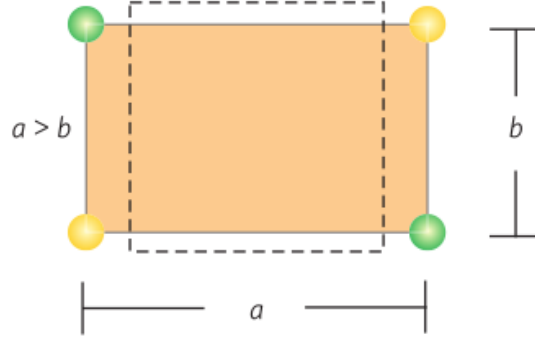


Figure 1.15: In-plane schematic diagram of the structural transition from a tetragonal lattice, where $a = b$ to an orthorhombic lattice $a \neq b$. Figure originally published in Nat. Phys., 10:97–104, Feb 2014[20].

FS. The tight-binding electron dispersion considered here was:

$$\xi_{\mathbf{k}}^{(3)} = -\mu - 2t_1 \cos k_x a - 2t_1 \cos k_y a - 4t_2 \cos k_x a \cos k_y a \quad (1.30)$$

with the band parameters $\mu = -4.8T_S$, $t_1 = 6T_S$, and $t_2 = -T_S$. The nematic state modifies the normal state electron dispersion by $\tilde{\xi}_{\mathbf{k}} = \xi_{\mathbf{k}} + \Phi f_{\mathbf{k}}$, where Φ is the mean-field nematic order parameter and $f_{\mathbf{k}} = \cos k_x a - \cos k_y a$, which breaks the $C(4)$ rotational symmetry inherent to the electron dispersion and reduces it to a $C(2)$ rotational symmetry inherent to a nematic state. The nematic transition temperature, T_S , is associated with a structural transition from a lattice with an in-plane $C(4)$ rotational symmetry, like a tetragonal lattice, to one with a $C(2)$ rotational symmetry, like an orthorhombic or monoclinic lattice. The nematic state can be thought of as enhancing the nearest-neighbor hopping in the $\hat{\mathbf{y}}$ -direction and diminishing the nearest-neighbor hopping in the $\hat{\mathbf{x}}$ -direction[72]:

$$\tilde{\xi}_{\mathbf{k}} = -\mu - (2t_1 - \Phi) \cos k_x a - (2t_1 + \Phi) \cos k_y a - 4t_2 \cos k_x a \cos k_y a \quad (1.31)$$

Due to this, the nematic state elongates the FS in the $\hat{\mathbf{x}}$ -direction and compresses the FS in

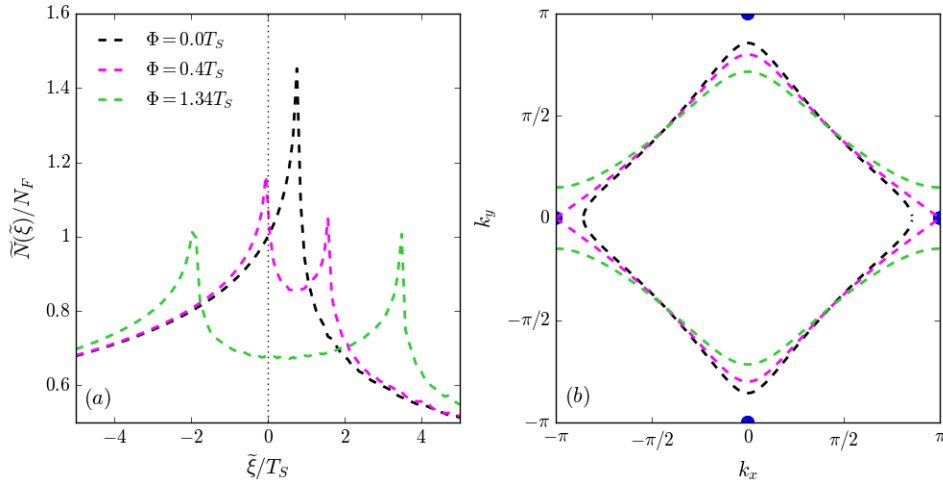


Figure 1.16: (a) Density of states in the nematic state normalized by the DOS at the Fermi level (N_F) in the normal state plotted versus the electron energy in the nematic state $\tilde{\xi}$ normalized by the temperature at which the structural transition driving the nematic transition took place. It can be seen that van Hove singularities occur in the DOS at $\tilde{\xi}_{\mathbf{k}}^{vH} = -\mu + 4t_2 \pm 2\Phi$. (b) Nematic state FS as Φ increases from 0 to $1.34T_s$ and the relevant saddle points in the normal state dispersion at $(\pm\pi, 0)$ and $(0, \pm\pi)$ are shown as blue points.

the \hat{y} -direction, which can be seen in Figure 1.16(b).

This leads to a distorted FS which has quasiparticle states with enhanced quasiparticle velocities in the \hat{y} -direction and diminished velocities in the \hat{x} -direction relative to the normal state FS. This modification to the quasiparticle velocities on the FS results in enhanced electron transport in the \hat{y} -direction and diminishes electron transport in the \hat{x} -direction.

Another effect of nematicity breaking the $C(4)$ rotational symmetry of the electronic state and elongating the FS is that it can drag the FS through regions of \mathbf{k} -space where the electron velocities are zero (saddle points). This causes a singularity in the local DOS and leads to van Hove singularities in the total DOS, which can be seen in Figure 1.16 (a) when the DOS is discontinuous in the first derivative in $\tilde{\xi}$. The saddle points in \mathbf{k} -space occur near the bare FS at $(k_x, k_y) = (\pm\pi, 0), (0, \pm\pi)$. However, as the nematic order parameter increases the FS when $k_x = 0$ retreats from these saddle points, whereas the FS when $k_y = 0$ is dragged through these saddle points. The energy at which these van Hove singularities

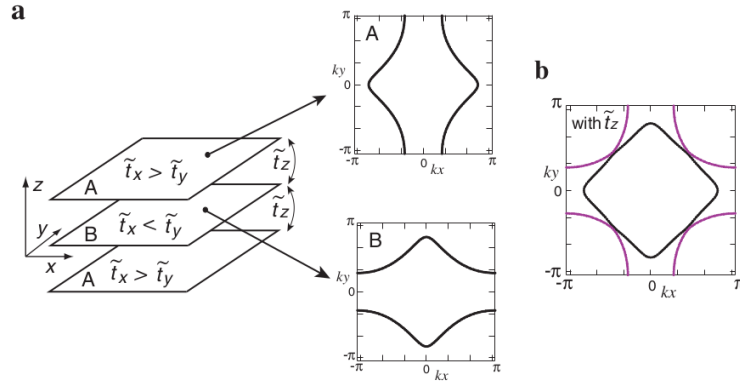


Figure 1.17: (a) Alternate stacking of deformed FSs due to nematicity in each CuO_2 plane. \tilde{t}_x and \tilde{t}_y are the effective in-plane electron hopping integrals along the x - and y -directions respectively; \tilde{t}_z is the effective hopping along the z -direction. (b) The resulting bulk FSs which become two-dimensional and consist of inner (black) and outer (purple) FSs. Figure originally published in Nat. Commun., 12:2223, 2021[71].

occur at can be shown to be $\xi_{\mathbf{k}}^{vH} = -\mu + 4t_2 \pm 2\Phi$, where the energy at the $(\pm\pi, 0)$ saddle points is lowered by 2Φ and the energy at the $(0, \pm\pi)$ saddle points is raised by 2Φ .

In bulk materials these FS distortions can align perpendicular to one another[71], thus restoring the $C(4)$ rotational symmetry of the material when many quasi-two-dimensional layers are considered. This can be seen in Figure 1.17. Thus, to measure anisotropic transport properties from an electronic nematic phase, one must produce monolayer materials to ensure that the $C(4)$ rotational symmetry isn't restored over many layers.

Superconductivity

Conventional Superconductivity

Superconductivity is marked by the complete disappearance of dc resistivity in a material and has been found in many metals at sufficiently low-temperature[47]. Bardeen-Cooper-Schrieffer (BCS) theory is based on the instability of an electron gas ground state with an arbitrarily small attractive potential between its particles against the formation

of bound state electron pairs. In conventional superconductors, electron interactions with phonons generate a small amount of excess charge around the electrons which creates an attractive potential stronger than their Coulomb repulsion. This interaction is nearly isotropic and the Cooper pairs form a s -wave state with zero orbital angular momentum[47]. Conventional s -wave superconductors tend to have extremely low critical temperatures due to weak electron-phonon coupling constants, it has been predicted to be less than $1K$ [70], and so aren't very viable in commercial applications.

Unconventional Superconductivity

Some of the more commonly studied high-temperature superconductors are the cuprates[65], iron pnictides[70], and iron chalcogenides[28]. A common feature of these families of materials is the quasi-two-dimensional nature of their crystalline structure, where they feature sheets of square-lattice transition metals (Cu or Fe) separated by insulating layers[70]. Because of this, these materials tend to have cylindrical Fermi surfaces[40, 61] (FSs), which are largely k_z -independent and can therefore be modelled accurately in two-dimensions[75]. The quasi-two-dimensional nature of these materials allows for the growth of single superconducting layers[5, 23, 73] on a substrate which preserves the essential physics of these materials, demonstrating that superconductivity in the cuprates and iron-based materials is an inherently two-dimensional phenomenon. Superconductivity in these materials also tends to be unconventional in nature and often results in an extended s -wave[10] SC gap for the iron-based materials or a d -wave[14] SC gap for the cuprates. Unconventional superconductors such as these can be mediated by antiferromagnetic spin fluctuations.

Phase Diagram with Broken-Symmetry Phases

Unconventional superconductors, such as the iron pnictides and cuprates, often have a complicated phase diagram where superconductivity coexists with other broken-symmetry

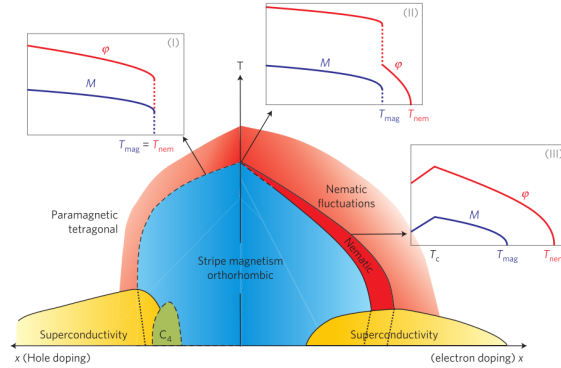


Figure 1.18: Schematic phase diagram of hole- and electron-doped iron pnictides of the family BaFe_2As_2 . The blue region denotes orthorhombic stripe magnetism. The red region denotes orthorhombic nematic paramagnetic order (dark red denotes strong nematic order). The yellow region denotes superconductivity. The green region denotes a phase which preserves $C(4)$ rotational symmetry. Dotted lines illustrate nematic and Néel temperatures inside superconducting dome. Insets show temperature-dependence of nematic (Φ) and AFM (M) order parameters. Figure originally published in *Nat. Phys.*, 10:97–104, Feb 2014[20].

phases, dependent on material properties such as dopant concentration[3, 57]. One of the more common broken-symmetry states that unconventional superconductivity coexists with is antiferromagnetism. Specifically, a striped antiferromagnetic state which couples electron states in the Brillouin zone by a nesting vector \mathbf{Q} , known as a spin density wave (SDW) state[16, 26, 38, 66], or more commonly stripe magnetism[20]. This striped magnetic phase will often be preceded by or simultaneously appear alongside an electronic nematic phase which reduces the $C(4)$ in-plane rotational symmetry to a $C(2)$ rotational symmetry. The electronic nematic phase typically results in a structural change in the lattice from a tetragonal phase, which has $C(4)$ in-plane rotational symmetry, to an orthorhombic[46] or monoclinic[15] lattice, both of which have $C(2)$ rotational symmetry.

Cuprate superconductors with d -wave superconductivity commonly arise out of a commensurate spin density wave state with the nesting vector $\mathbf{Q} = (\pi, \pi)$ [16, 38]. This SDW state reconstructs the metallic FS, seen in Figure 1.19(a), with quasiparticle pockets located at the M points in the FBZ and preserves the d -wave SC symmetry nodes, which are the

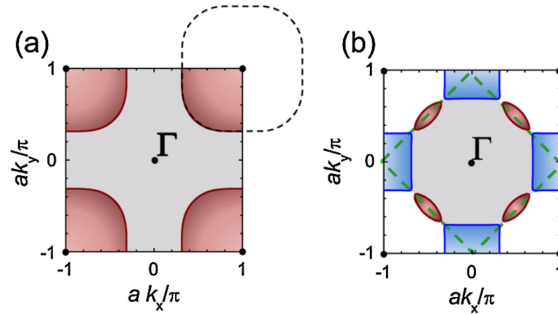


Figure 1.19: (a) Typical superconducting cuprate open FS, which can be well modelled with the tight-binding model. (b) Reconstructed FS due to FS nesting by a $\mathbf{Q} = (\pi, \pi)$ SDW state inside the reduced Brillouin Zone (dashed lines). Figure originally published in *Phys. Rev. Lett.*, 103(15):157002, 2009[27].

main contributors to quasiparticle transport[6]. This commensurate SDW nesting vector can however be modified through hole-doping[68] to result in an incommensurate SDW state with nesting vector $\mathbf{Q} = (\pi - 2\pi\epsilon, \pi - 2\pi\epsilon)$ and $C(2)$ rotational symmetry. Additionally, through Hubbard model calculations the d -wave SC state in the cuprates was found to coexist with a $\mathbf{Q} = (\pi, 0)$ SDW state[75]. The cuprate superconductors were also measured to undergo an electronic nematic phase transition[71], which distorted the quasi-two-dimensional FSs in the layered SC as can be seen in Figure 1.17. However, it was found that the FS distortion due to nematicity was rotated by $\pi/2$ between adjacent layers along the \hat{z} -axis in bulk, thus averaging out any broken symmetries between the in-plane directions.

Iron pnictide superconductors are multi-band[70] unlike the cuprate superconductors, which are well modelled as single-band superconductors. This results in the iron pnictides having multiple Fermi surfaces, some of which are hole-like (located around the Γ point of the FBZ) and some of which are electron-like (located around the M points in the FBZ). These Fermi surfaces are represented in Figure 1.20. The iron pnictide superconductors have an extended s -wave or s^\pm SC gap, which is constant for a particular band but multiple SC gaps exist for each band (and consequently each FS) some of which are negative. This extended s -wave gap in the pnictides often arises out of a commensurate SDW state with the nesting

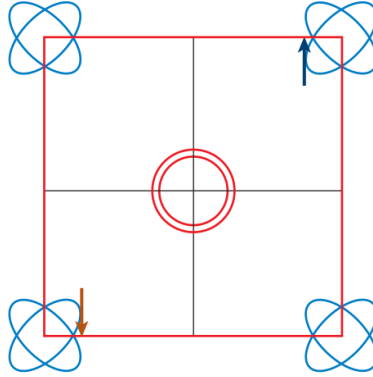


Figure 1.20: (a) Schematic diagram of the Fermi surfaces of the iron pnictides, where the blue pockets located at the M points of the FBZ are electron-like and the red pockets at the Γ point of the FBZ are hole-like. Figure originally published in *Annu. Rev. Condens. Matter Phys.*, 2:121, 2011, 2009[70].

vector $\mathbf{Q} = (\pi, 0)$ [8, 15, 30, 36, 74], resulting in the striped magnetic phase seen in the phase diagram in Figure 1.18.

The iron chalcogenides lack an antiferromagnetic state in the bulk phase due to magnetic frustration[48]. However, this frustration can be lifted in monolayer iron chalcogenides grown on SrTiO_3 substrates which apply an epitaxial strain on the lattice and increase the spacing between the iron atoms[66]. Iron chalcogenide monolayers with epitaxial strain to induce antiferromagnetic behavior has been found to greatly enhance the superconducting transition temperature[23] compared to those measured in bulk[28]. This enhanced superconducting transition temperature is likely the result of the antiferromagnetic state enhancing superconductivity[66] through a spin fluctuation (magnon) mediated pairing interaction as opposed to the weaker more conventional phonon mediated pairing. Furthermore, one of the antiferromagnetic states observed in the iron chalcogenides is the $\mathbf{Q} = (\pi/2, \pi/2)$ SDW state[42, 54]. Additionally, superconductivity in the iron chalcogenides also coexists alongside an electronic nematic phase[29].

THEORY

Stoner-Wohlfarth Model

Considering the cubic anisotropy energy within the Stoner-Wohlfarth model yields the equation:

$$E_{\text{cubic}} = K_{\text{cubic}}^{(1)} \sin^2 \phi \cos^2 \phi - \mu_0 \mathbf{H} \cdot \mathbf{M} \quad (2.1)$$

where $K_{\text{cubic}}^{(1)}$ is the first-order cubic anisotropy constant, \mathbf{M} is the sample magnetization (assuming the macroscopic spin approximation), ϕ is the in-plane polar angle of the sample magnetization, and \mathbf{H} is the applied magnetic field. This can be normalized by $K_{\text{cubic}}^{(1)}$ to get the reduced energy:

$$\Gamma_{\text{cubic}} = \sin^2 \phi \cos^2 \phi - 2\mathbf{h} \cdot \mathbf{M}/M_S \quad (2.2)$$

where $\mathbf{h} = \frac{\mathbf{H}}{H_K^{\text{cubic}}}$, $H_K^{\text{cubic}} = \frac{2K_{\text{cubic}}^{(1)}}{\mu_0 M_S}$, M_S is the saturation magnetization, and $\hat{\mathbf{h}} \cdot \mathbf{M}/M_S = \cos(\phi - \theta)$. The reduced energy can be minimized as a function of ϕ in order to determine the most energetically favorable direction for the magnetization to point. The favored direction for the magnetization to point in as a function of the reduced applied field can be seen as the blue curves in Figure 2.1. In order to find the magnetic hysteresis from these minima, the cosine of the difference between the magnetization direction and the applied field direction, $\cos(\phi - \theta)$. This model results in a minor hysteresis loop indicative of a two-step hysteresis, which is an effect that was measured experimentally by Daboo[13]. Minor loops such as these were also theoretically treated by Usov[69] for bulk materials with three equivalent crystallographic directions (and therefore had two minor loops), whereas the materials considered here only have two equivalent directions due to a tetragonal distortion and a thin-film shape anisotropy (thus resulting in only a single minor loop). The resulting

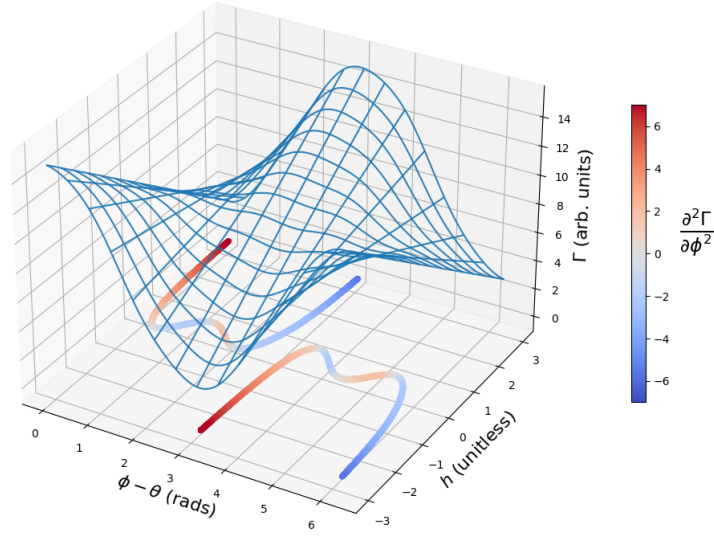


Figure 2.1: Normalized energy surface Γ plotted as a function of the unitless applied magnetic field, h , and polar angle between the magnetization and applied magnetic field $\phi - \theta$. $\phi(h)$ when $\frac{\partial \Gamma}{\partial \phi} = 0$ is plotted along the bottom plane and shaded as a function of $\frac{\partial^2 \Gamma}{\partial \phi^2}$, where energy minima are shaded in blue and energy maxima are shaded in red.

magnetic hysteresis loop as a function of applied magnetic field for a thin-film magnet with cubic anisotropy can be seen in Figure 2.2. This calculated hysteresis loop can be used with a least-squares fitting algorithm (after removing the minor hysteresis loop from the model calculation) in order to measure first-order cubic anisotropy constants from experimentally measured hysteresis loops. This same process can be repeated for other forms of anisotropy, such as uniaxial anisotropy.

Superconductivity

Mean-field Hamiltonian

The mean-field BCS Hamiltonian, ignoring constants, can be written as[47]:

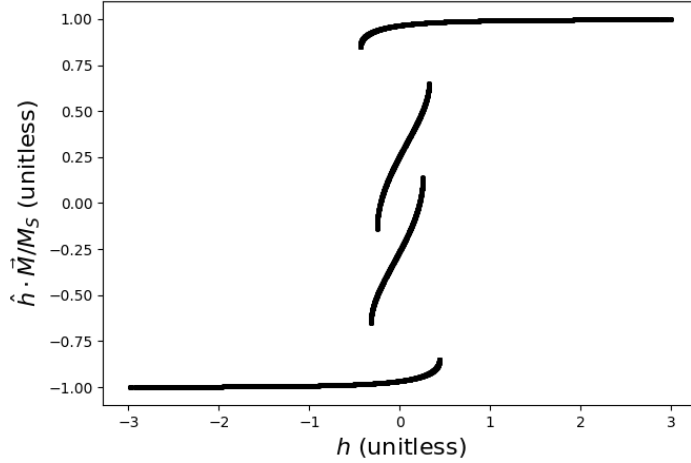


Figure 2.2: Magnetic hysteresis of a thin-film ferromagnet with an in-plane cubic anisotropy and a two-step hysteresis calculated from the Stoner-Wohlfarth model.

$$H_0 + H_{SC} = \frac{1}{2} \sum_{\mathbf{k}, \sigma} (\xi_{\mathbf{k}} \hat{a}_{\mathbf{k}, \sigma}^\dagger \hat{a}_{\mathbf{k}, \sigma} - \xi_{\mathbf{k}} \hat{a}_{-\mathbf{k}, \sigma} \hat{a}_{-\mathbf{k}, \sigma}^\dagger + \Delta_{\mathbf{k}} \hat{a}_{\mathbf{k}, \sigma}^\dagger \hat{a}_{-\mathbf{k}, -\sigma}^\dagger + \Delta_{\mathbf{k}} \hat{a}_{-\mathbf{k}, -\sigma} \hat{a}_{\mathbf{k}, \sigma}) \quad (2.3)$$

where $\sum_{\mathbf{k}, \sigma}$ is a sum over $\mathbf{k} \in \text{FBZ}$ and $\sigma = \uparrow, \downarrow$, $\xi_{\mathbf{k}}$ is the inversion symmetric ($\xi_{-\mathbf{k}} = \xi_{\mathbf{k}}$) normal state electron dispersion relation, $\hat{a}_{\mathbf{k}, \sigma}^\dagger$ is the creation operator for an electron with momentum \mathbf{k} and spin σ , and $\Delta_{\mathbf{k}}$ is the mean-field superconducting gap.

Bogoliubov Eigenstates

This Hamiltonian can be rewritten with the Nambu state vectors as:

$$H_0 + H_{SC} = \frac{1}{2} \sum_{\mathbf{k}, \sigma} \hat{\Psi}_{\mathbf{k}}^\dagger \mathcal{H}_{\mathbf{k}}^{\text{BCS}} \hat{\Psi}_{\mathbf{k}}, \quad \mathcal{H}_{\mathbf{k}}^{\text{BCS}} = \begin{pmatrix} \xi_{\mathbf{k}} & \Delta_{\mathbf{k}} \\ \Delta_{\mathbf{k}} & -\xi_{\mathbf{k}} \end{pmatrix} \quad (2.4)$$

where $\hat{\Psi}_{\mathbf{k}}^\dagger = (\hat{a}_{\mathbf{k}, \sigma}^\dagger, \hat{a}_{-\mathbf{k}, -\sigma})$ is the Nambu vector. This Hamiltonian can be diagonalized by introducing new Fermionic operators, which are a superposition of the electron creation (\hat{a}^\dagger)

and annihilation (\hat{a}) operators, this is known as the Bogoliubov transformation:

$$\hat{\mathbf{B}}_{\mathbf{k}} = \begin{pmatrix} \hat{b}_{\mathbf{k},\sigma} \\ \hat{b}_{-\mathbf{k},-\sigma}^\dagger \end{pmatrix} = \begin{pmatrix} u_{\mathbf{k}} & -v_{\mathbf{k}} \\ v_{\mathbf{k}} & u_{\mathbf{k}} \end{pmatrix} \begin{pmatrix} \hat{a}_{\mathbf{k},\sigma} \\ \hat{a}_{-\mathbf{k},-\sigma}^\dagger \end{pmatrix} \quad (2.5)$$

where \hat{b}^\dagger and \hat{b} are the creation and annihilation operators respectively for Bogoliubov quasiparticles. The coefficients of the Bogoliubov transformation, $u_{\mathbf{k}}$ and $v_{\mathbf{k}}$, can be found by enforcing that \hat{b} follows the Fermionic commutation relation $\{\hat{b}_{\mathbf{k},\sigma}, \hat{b}_{\mathbf{k},\sigma}^\dagger\} = 1$ and ensuring that this transformation does indeed diagonalize the Hamiltonian. By doing this, it can be shown that[67]:

$$u_{\mathbf{k}} = \frac{E_{\mathbf{k}}^{\text{SC}} + \xi_{\mathbf{k}}}{\sqrt{2E_{\mathbf{k}}^{\text{SC}}(E_{\mathbf{k}}^{\text{SC}} + \xi_{\mathbf{k}})}} = \sqrt{\frac{1}{2} \left(1 + \frac{\xi_{\mathbf{k}}}{E_{\mathbf{k}}^{\text{SC}}} \right)} \quad (2.6)$$

$$v_{\mathbf{k}} = \frac{\Delta_{\mathbf{k}}}{\sqrt{2E_{\mathbf{k}}^{\text{SC}}(E_{\mathbf{k}}^{\text{SC}} + \xi_{\mathbf{k}})}} = \sqrt{\frac{1}{2} \left(1 - \frac{\xi_{\mathbf{k}}}{E_{\mathbf{k}}^{\text{SC}}} \right)} \quad (2.7)$$

Furthermore, applying this transformation to the BCS Hamiltonian yields:

$$H_0 + H_{SC} = \frac{1}{2} \sum_{\mathbf{k},\sigma} E_{\mathbf{k}}^{\text{SC}} \hat{b}_{\mathbf{k},\sigma}^\dagger \hat{b}_{\mathbf{k},\sigma} - \frac{1}{2} \sum_{\mathbf{k},\sigma} E_{\mathbf{k}}^{\text{SC}} \hat{b}_{-\mathbf{k},\sigma} \hat{b}_{-\mathbf{k},\sigma}^\dagger = \frac{1}{2} \sum_{\mathbf{k},\sigma} \hat{\mathbf{B}}_{\mathbf{k}}^\dagger \begin{pmatrix} E_{\mathbf{k}}^{\text{SC}} & 0 \\ 0 & -E_{\mathbf{k}}^{\text{SC}} \end{pmatrix} \hat{\mathbf{B}}_{\mathbf{k}} \quad (2.8)$$

where $\pm E_{\mathbf{k}}^{\text{SC}} = \pm \sqrt{\xi_{\mathbf{k}}^2 + \Delta_{\mathbf{k}}^2}$ are the eigenvalues of $\hat{\mathcal{H}}_{\mathbf{k}}^{\text{BCS}}$ and subsequently are the quasiparticle and quasihole bands of the superconducting state respectively. The eigenstates of $\hat{\mathcal{H}}_{\mathbf{k}}^{\text{BCS}}$ can be written as $|E_{\mathbf{k}}^{\text{SC}}\rangle = \hat{b}_{\mathbf{k},\sigma}^\dagger |0\rangle$ and $|-E_{\mathbf{k}}^{\text{SC}}\rangle = \hat{b}_{-\mathbf{k},-\sigma} |0\rangle$, where $|0\rangle$ denotes the ground state of the system where all states below the Fermi level are occupied by electrons and all states above the Fermi level are unoccupied (this is also known as the vacuum state for Bogoliubov quasiparticles). The state $|E_{\mathbf{k}}^{\text{SC}}\rangle = \hat{b}_{\mathbf{k},\sigma}^\dagger |0\rangle$ represents the creation of a Bogoliubov quasiparticle which couples an electron and hole of opposite momentum (\mathbf{k})

and spin (σ) and excites them above the Fermi sea. When a Bogoliubov quasiparticle is created above the Fermi sea, a Bogoliubov quasihole is created below the Fermi level in the $-E_{\mathbf{k}}^{\text{SC}}$ band, this is what the $|-E_{\mathbf{k}}^{\text{SC}}\rangle = \hat{b}_{-\mathbf{k},-\sigma}|0\rangle$ state represents. These quasiholes are created due to the fact that the electron-hole pair which are involved in the creation of Bogoliubov quasiparticles leave vacant states below the Fermi level when they become coupled. These same eigenstates can also be written in terms of the electron creation and annihilation operators as:

$$\begin{aligned} |E_{\mathbf{k}}^{\text{SC}}\rangle &= (u_{\mathbf{k}}\hat{a}_{\mathbf{k},\sigma}^{\dagger} + v_{\mathbf{k}}\hat{a}_{-\mathbf{k},-\sigma})|0\rangle := \begin{pmatrix} u_{\mathbf{k}} \\ v_{\mathbf{k}} \end{pmatrix} \\ |-E_{\mathbf{k}}^{\text{SC}}\rangle &= (-v_{\mathbf{k}}\hat{a}_{\mathbf{k},\sigma}^{\dagger} + u_{\mathbf{k}}\hat{a}_{-\mathbf{k},-\sigma})|0\rangle := \begin{pmatrix} -v_{\mathbf{k}} \\ u_{\mathbf{k}} \end{pmatrix} \end{aligned} \quad (2.9)$$

where the eigenstates can be represented as eigenvectors in the basis of the electron creation and annihilation operators $\hat{a}_{\mathbf{k},\sigma}^{\dagger}$ and $\hat{a}_{-\mathbf{k},-\sigma}$, which is the same basis that $\hat{\mathcal{H}}_{\mathbf{k}}^{\text{BCS}}$ is constructed in.

The superconducting quasiparticle band ($E_{\mathbf{k}}^{\text{SC}}$) is the result of a hybridization of both the normal state electron and hole bands, and is mostly hole-like when $\xi_{\mathbf{k}} \ll 0$ and mostly electron-like when $\xi_{\mathbf{k}} \gg 0$. Near the Fermi level this mixing of the normal state particle and hole bands becomes more complicated as the bands become degenerate and the superconducting quasiparticle band becomes a superposition of both the particle and hole bands, which is demonstrated in Figure 2.3.

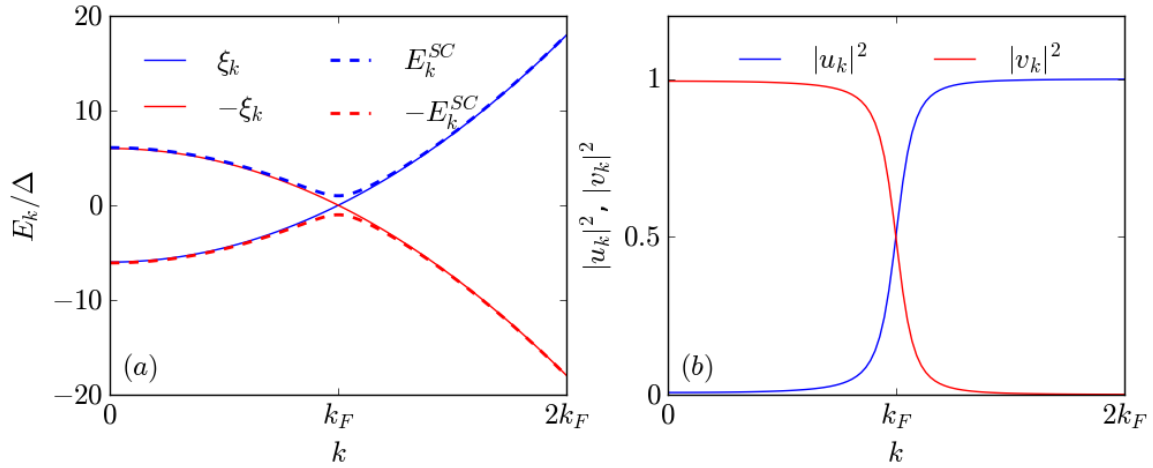


Figure 2.3: (a) Normal state electron (solid blue) and hole (solid red) bands for a free-electron model $\xi_{\mathbf{k}} = \frac{\hbar^2 k^2}{2m} - \mu$ and the Bogoliubov quasiparticle (dashed blue) and Bogoliubov quasihole (dashed red) bands for s -wave superconductivity. (b) Bogoliubov transformation coefficients $|u_{\mathbf{k}}|^2$ and $|v_{\mathbf{k}}|^2$ which show that the Bogoliubov quasiparticles below the Fermi level are mostly hole-like and the ones above the Fermi level are mostly electron-like. This figure was inspired by Carsten Timm's *Theory of Superconductivity*[67].

Nematicity

Mean-field Hamiltonian

The nematic state can be modelled through a mean-field modification to the normal state electronic Hamiltonian H_0 :

$$H_0 + H_{\text{Nem}} = \frac{1}{2} \sum_{\mathbf{k}, \sigma} (\xi_{\mathbf{k}} \hat{a}_{\mathbf{k}, \sigma}^\dagger \hat{a}_{\mathbf{k}, \sigma} - \xi_{\mathbf{k}} \hat{a}_{-\mathbf{k}, -\sigma} \hat{a}_{-\mathbf{k}, -\sigma}^\dagger + \Phi f_{\mathbf{k}} \hat{a}_{\mathbf{k}, \sigma}^\dagger \hat{a}_{\mathbf{k}, \sigma} - \Phi f_{\mathbf{k}} \hat{a}_{-\mathbf{k}, -\sigma} \hat{a}_{-\mathbf{k}, -\sigma}^\dagger) \quad (2.10)$$

where Φ is the mean-field nematic order parameter and $f_{\mathbf{k}} = \cos k_x a - \cos k_y a$. The Hamiltonian can be rewritten in the Nambu basis as:

$$H_0 + H_{\text{Nem}} = \frac{1}{2} \sum_{\mathbf{k}, \sigma} \hat{\Psi}_{\mathbf{k}}^\dagger \hat{\mathcal{H}}_{\mathbf{k}}^{\text{Nem}} \hat{\Psi}_{\mathbf{k}}, \quad \hat{\mathcal{H}}_{\mathbf{k}}^{\text{Nem}} = \begin{pmatrix} \xi_{\mathbf{k}} + \Phi f_{\mathbf{k}} & 0 \\ 0 & -\xi_{\mathbf{k}} - \Phi f_{\mathbf{k}} \end{pmatrix} \quad (2.11)$$

where $\hat{\Psi}_{\mathbf{k}}^\dagger = (\hat{a}_{\mathbf{k}, \sigma}^\dagger, \hat{a}_{-\mathbf{k}, -\sigma})$ is the Nambu state vector. From this representation it is clear to see that nematicity doesn't hybridize the electron and hole bands, and therefore doesn't require new Fermionic creation and annihilation operators since $\hat{\mathcal{H}}_{\mathbf{k}}^{\text{Nem}}$ is already diagonal in the Nambu basis. In fact, nematicity can be thought of as a modification the nearest neighbor hopping for a tight-binding electron dispersion where it enhances t_{1y} and reduces t_{1x} by Φ .

Nematic Mean-Field Order Parameter

The mean-field Nematic order parameter, Φ is defined by:

$$\Phi = -V_{\text{Nem}} \sum_{\mathbf{k}} f_{\mathbf{k}} \langle \hat{a}_{\mathbf{k}}^\dagger \hat{a}_{\mathbf{k}} \rangle \quad (2.12)$$

where $\hat{a}_{\mathbf{k}}^\dagger$ is the creation operator for an electron of momentum \mathbf{k} and $\hat{a}_{\mathbf{k}}^\dagger \hat{a}_{\mathbf{k}}$ is also commonly referred to as the number operator. At equilibrium, the number operator for electrons is the Fermi-Dirac distribution function, $\langle \hat{a}_{\mathbf{k}}^\dagger \hat{a}_{\mathbf{k}} \rangle = 1/(e^{(\xi_{\mathbf{k}} + \Phi f_{\mathbf{k}})/T} + 1)$, where $\xi_{\mathbf{k}} + \Phi f_{\mathbf{k}}$ is the electron dispersion relation distorted by nematicity and can be shown to reduce to:

$$\Phi = V_{\text{Nem}} \sum_{\mathbf{k}} \frac{f_{\mathbf{k}}}{2} \left(\tanh \frac{\xi_{\mathbf{k}} + \Phi f_{\mathbf{k}}}{2T} - 1 \right) \quad (2.13)$$

as $T \rightarrow T_S$ and $\Phi \rightarrow 0$, this equation becomes[7]:

$$\Phi = \frac{V_{\text{Nem}} \Phi}{2} \sum_{\mathbf{k}} \frac{f_{\mathbf{k}}^2}{2T_S} \text{sech}^2 \frac{\xi_{\mathbf{k}}}{2T_S} \quad (2.14)$$

which leads to the self-consistency equation that can be used to solve for the mean-field nematic order parameter Φ :

$$0 = \sum_{\mathbf{k}} f_{\mathbf{k}} \left(\tanh \frac{\xi_{\mathbf{k}} + \Phi f_{\mathbf{k}}}{2T} - 1 \right) - \Phi \sum_{\mathbf{k}} \frac{f_{\mathbf{k}}^2}{2T_S} \operatorname{sech}^2 \frac{\xi_{\mathbf{k}}}{2T_S} \quad (2.15)$$

The solution to this equation as a function of temperature can be seen in Figure 2.5 as the black curve.

Coexistence of Nematicity and Superconductivity

Mean-field Hamiltonian

When superconductivity coexists with a nematic state, the mean-field Hamiltonian can be written as:

$$\begin{aligned} H_0 + H_{\text{Nem}} + H_{\text{SC}} = & \frac{1}{2} \sum_{\mathbf{k}, \sigma} (\xi_{\mathbf{k}} \hat{a}_{\mathbf{k}, \sigma}^\dagger \hat{a}_{\mathbf{k}, \sigma} - \xi_{\mathbf{k}} \hat{a}_{-\mathbf{k}, -\sigma} \hat{a}_{-\mathbf{k}, -\sigma}^\dagger + \Phi f_{\mathbf{k}} \hat{a}_{\mathbf{k}, \sigma}^\dagger \hat{a}_{\mathbf{k}, \sigma} \\ & - \Phi f_{\mathbf{k}} \hat{a}_{-\mathbf{k}, -\sigma} \hat{a}_{-\mathbf{k}, -\sigma}^\dagger + \Delta_{\mathbf{k}} \hat{a}_{\mathbf{k}, \sigma}^\dagger \hat{a}_{-\mathbf{k}, -\sigma}^\dagger + \Delta_{\mathbf{k}} \hat{a}_{-\mathbf{k}, -\sigma} \hat{a}_{\mathbf{k}, \sigma}) \end{aligned} \quad (2.16)$$

Nematicity coexisting with s -wave superconductivity can result in a d -wave feedback from the symmetry-broken nematic state on the superconducting order. This can be modelled by defining:

$$\Delta_{\mathbf{k}} = \Delta \mathcal{Y}_{\mathbf{k}} = \frac{\Delta}{\sqrt{1+r^2}} (1 + r \cos k_x a - r \cos k_y a) \quad (2.17)$$

where $\mathcal{Y}_{\mathbf{k}}$ is normalized by $\sqrt{1+r^2}$ to ensure that $\int \frac{d^2k}{(2\pi)^2} |\mathcal{Y}_{\mathbf{k}}|^2 = 1$ and r is the anisotropy parameter that describes the degree of the nematic feedback on the s -wave SC state. While the anisotropy parameter r should be proportional to Φ , it also depends on the details of the electronic structure[7] and was beyond the scope of this work. Therefore, r was treated

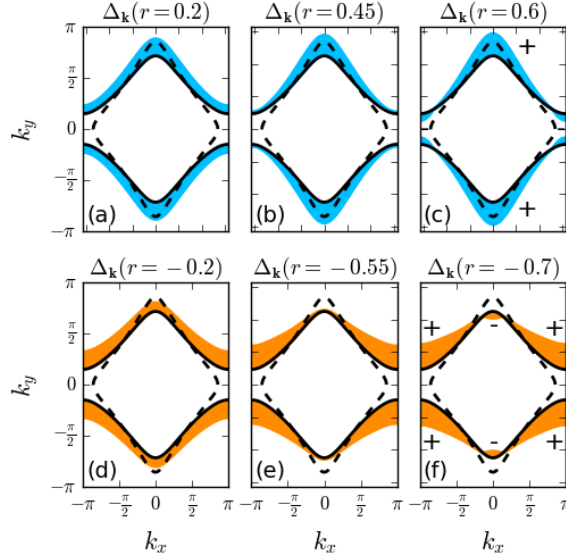


Figure 2.4: Qualitative illustration of the superconducting gap amplitude for varying values of r along the nematically distorted FS. When $r > 0$ (cyan curves) the SC gap maximum is anti-aligned with the FS elongation. When $r < 0$ (cyan curves) the SC gap maximum is aligned with the FS elongation.

as a phenomenological constant where $-1 < r < 1$.

A qualitative plot of the s - and d -wave SC mixing can be seen in Figure 2.4 for various values of r . When $|r|$ is small, the SC gap is essentially still an s -wave SC gap. However as $|r|$ increases, two nodes appear on the nematically distorted FS. The critical r -value at which nodes appear is different depending on the sign of r .

$$r_c^+ = -\frac{2t_1t_2 + t_2\Phi - 4t_2^2}{4t_2^2 + t_2\mu - 4t_1t_2}, \quad r_c^- = -\frac{2t_1t_2 + t_2\Phi + 4t_2^2}{4t_2^2 + t_2\mu + 4t_1t_2} \quad (2.18)$$

When $r > 0$, nodal quasiparticle states appear on the distorted FS near the edge of the FBZ, whereas the nodal quasiparticle states appear near the center of the FS when $r < 0$.

Eigenstates

The SC + nematicity coexistence Hamiltonian can be rewritten in the Nambu basis to derive the eigenstates as:

$$H_0 + H_{\text{Nem}} + H_{\text{SC}} = \frac{1}{2} \sum_{\mathbf{k}, \sigma} \hat{\Psi}_{\mathbf{k}}^\dagger \hat{\mathcal{H}}_{\mathbf{k}}^{(\text{SC} + \text{Nem})} \hat{\Psi}_{\mathbf{k}}, \quad \hat{\mathcal{H}}_{\mathbf{k}}^{(\text{SC} + \text{Nem})} = \begin{pmatrix} \tilde{\xi}_{\mathbf{k}} & \Delta_{\mathbf{k}} \\ \Delta_{\mathbf{k}} & -\tilde{\xi}_{\mathbf{k}} \end{pmatrix} \quad (2.19)$$

where the Nambu state vector is $\hat{\Psi}_{\mathbf{k}}^\dagger = (\hat{a}_{\mathbf{k}, \sigma}^\dagger, \hat{a}_{-\mathbf{k}, -\sigma})$ and $\tilde{\xi}_{\mathbf{k}} = \xi_{\mathbf{k}} + \Phi f_{\mathbf{k}}$ is the normal state electron tight-binding dispersion modified by nematicity. This Hamiltonian has the eigenvalues $\pm E_{\mathbf{k}}^{(\text{SC} + \text{Nem})} = \pm \sqrt{\tilde{\xi}_{\mathbf{k}}^2 + \Delta_{\mathbf{k}}^2}$ and is diagonalized by the modified Bogoliubov eigenstates:

$$\begin{aligned} |E_{\mathbf{k}}^{(\text{SC} + \text{Nem})}\rangle &= \hat{b}_{\mathbf{k}, \sigma}^\dagger |0\rangle = (\tilde{u}_{\mathbf{k}} \hat{a}_{\mathbf{k}, \sigma}^\dagger + \tilde{v}_{\mathbf{k}} \hat{a}_{-\mathbf{k}, -\sigma}) |0\rangle := \begin{pmatrix} \tilde{u}_{\mathbf{k}} \\ \tilde{v}_{\mathbf{k}} \end{pmatrix} \\ | -E_{\mathbf{k}}^{(\text{SC} + \text{Nem})}\rangle &= \hat{b}_{-\mathbf{k}, -\sigma} |0\rangle = (-\tilde{v}_{\mathbf{k}} \hat{a}_{\mathbf{k}, \sigma}^\dagger + \tilde{u}_{\mathbf{k}} \hat{a}_{-\mathbf{k}, -\sigma}) |0\rangle := \begin{pmatrix} -\tilde{v}_{\mathbf{k}} \\ \tilde{u}_{\mathbf{k}} \end{pmatrix} \end{aligned} \quad (2.20)$$

where

$$\tilde{u}_{\mathbf{k}} = \frac{E_{\mathbf{k}}^{(\text{SC} + \text{Nem})} + \tilde{\xi}_{\mathbf{k}}}{\sqrt{2E_{\mathbf{k}}^{(\text{SC} + \text{Nem})}(E_{\mathbf{k}}^{(\text{SC} + \text{Nem})} + \tilde{\xi}_{\mathbf{k}})}} = \sqrt{\frac{1}{2} \left(1 + \frac{\tilde{\xi}_{\mathbf{k}}}{E_{\mathbf{k}}^{(\text{SC} + \text{Nem})}} \right)} \quad (2.21)$$

$$\tilde{v}_{\mathbf{k}} = \frac{\Delta_{\mathbf{k}}}{\sqrt{2E_{\mathbf{k}}^{(\text{SC} + \text{Nem})}(E_{\mathbf{k}}^{(\text{SC} + \text{Nem})} + \tilde{\xi}_{\mathbf{k}})}} = \sqrt{\frac{1}{2} \left(1 - \frac{\tilde{\xi}_{\mathbf{k}}}{E_{\mathbf{k}}^{(\text{SC} + \text{Nem})}} \right)} \quad (2.22)$$

The coexistence of superconductivity and nematicity is effectively the typical superconducting state, but with a modified electronic state. However, nematicity does affect the superconducting gap structure beyond the nematic feedback on the singlet superconducting channel.

Δ and Φ Mean-field order Parameter Calculation

The mean-field definition for Φ when it coexists with superconductivity is the same as in the absence of superconductivity defined in Equation (2.12). However, $\langle \hat{a}_{\mathbf{k}}^\dagger \hat{a}_{\mathbf{k}} \rangle = |u_{\mathbf{k}}|^2 f(E_{\mathbf{k}}^{(\text{SC+Nem})}) + |v_{\mathbf{k}}|^2 (1 - f(E_{\mathbf{k}}^{(\text{SC+Nem})}))$ since Bogoliubov quasiparticles are a superposition of electrons (with probability $|u_{\mathbf{k}}|^2$) and holes (with probability $|v_{\mathbf{k}}|^2$). This can be shown to reduce to:

$$\Phi = V_{\text{Nem}} \sum_{\mathbf{k}} f_{\mathbf{k}} \left(\frac{\xi_{\mathbf{k}} + \Phi f_{\mathbf{k}}}{E_{\mathbf{k}}^{(\text{SC+Nem})}} \tanh \frac{E_{\mathbf{k}}^{(\text{SC+Nem})}}{2T} - 1 \right) \quad (2.23)$$

where V_{Nem} can be eliminated in favor of T_S by subtracting Equation (2.14) from Equation (2.23) to result in the self-consistency equation for Φ in the presence of superconductivity:

$$0 = \sum_{\mathbf{k}} f_{\mathbf{k}} \left(\frac{\xi_{\mathbf{k}} + \Phi f_{\mathbf{k}}}{E_{\mathbf{k}}^{(\text{SC+Nem})}} \tanh \frac{E_{\mathbf{k}}^{(\text{SC+Nem})}}{2T} - 1 \right) - \Phi \sum_{\mathbf{k}} \frac{f_{\mathbf{k}}^2}{2T_S} \text{sech}^2 \frac{\xi_{\mathbf{k}}}{2T_S} \quad (2.24)$$

This self-consistency equation must be simultaneously satisfied along with the self-consistency equation for the SC gap, Δ , which can be derived from its mean-field definition[47]:

$$\Delta = -V_{\text{SC}} \sum_{\mathbf{k}} \mathcal{Y}_{\mathbf{k}} \langle \hat{a}_{-\mathbf{k},\downarrow} \hat{a}_{\mathbf{k},\uparrow} \rangle \quad (2.25)$$

where this can be converted from the electron creation/annihilation operators to the Bogoliubov quasiparticle creation/annihilation operators: $\langle \hat{a}_{-\mathbf{k},\downarrow} \hat{a}_{\mathbf{k},\uparrow} \rangle = \langle (u_{\mathbf{k}} \hat{b}_{-\mathbf{k},\downarrow} + v_{\mathbf{k}} \hat{b}_{\mathbf{k},\uparrow}^\dagger) (u_{\mathbf{k}} \hat{b}_{\mathbf{k},\uparrow} - v_{\mathbf{k}} \hat{b}_{-\mathbf{k},\downarrow}^\dagger) \rangle$. This can be further simplified using the relations: $\langle \hat{b}_{-\mathbf{k},\downarrow} \hat{b}_{\mathbf{k},\uparrow} \rangle = \langle \hat{b}_{\mathbf{k},\uparrow}^\dagger \hat{b}_{-\mathbf{k},\downarrow}^\dagger \rangle = 0$ and $\langle \hat{b}_{\mathbf{k},\uparrow}^\dagger \hat{b}_{\mathbf{k},\uparrow} \rangle = 1 - \langle \hat{b}_{-\mathbf{k},\downarrow} \hat{b}_{-\mathbf{k},\downarrow}^\dagger \rangle = f(E_{\mathbf{k}}^{(\text{SC+Nem})})$, where $f(E_{\mathbf{k}}^{(\text{SC+Nem})})$ is the Fermi distribution function for the Bogoliubov quasiparticles. From these relations it can be shown that:

$$\langle \hat{a}_{-\mathbf{k},\downarrow} \hat{a}_{\mathbf{k},\uparrow} \rangle = \frac{\Delta \mathcal{Y}_{\mathbf{k}}}{2E_{\mathbf{k}}^{(\text{SC+Nem})}} \tanh \frac{E_{\mathbf{k}}^{(\text{SC+Nem})}}{2T}.$$

$$\Delta = -V_{\text{SC}} \Delta \sum_{\mathbf{k}} \frac{\mathcal{Y}_{\mathbf{k}}^2}{2E_{\mathbf{k}}^{(\text{SC+Nem})}} \tanh \frac{E_{\mathbf{k}}^{(\text{SC+Nem})}}{2T} \quad (2.26)$$

This equation can be further simplified to aid in the convergence of numerical integration by converting $\frac{1}{x} \tanh \frac{x}{2}$ to the Matsubara sum $\sum_{n=0}^{\infty} \frac{4}{x^2 + \pi^2(2n+1)^2}$, to derive the final equation:

$$\Delta = -V_{\text{SC}} \sum_{\mathbf{k}} \frac{\mathcal{Y}_{\mathbf{k}}^2}{2T} \sum_{n=0}^{\infty} \frac{4T}{(E_{\mathbf{k}}^{(\text{SC+Nem})})^2 + \omega_n^2} \quad (2.27)$$

where $\omega_n = 2\pi(n + \frac{1}{2})T$ is the Matsubara frequency. The unknown V_{SC} can be eliminated in favor of T_c^0 , the superconducting transition temperature in the absence of nematicity, to arrive at the self-consistency equation:

$$0 = \sum_{\mathbf{k}} \frac{\mathcal{Y}_{\mathbf{k}}^2}{2} \sum_{n=0}^{\infty} \left(\frac{4T}{(E_{\mathbf{k}}^{(\text{SC+Nem})})^2 + \omega_n^2} - \frac{4T_c^0}{\xi_{\mathbf{k}}^2 + (\omega_n^0)^2} \right) \quad (2.28)$$

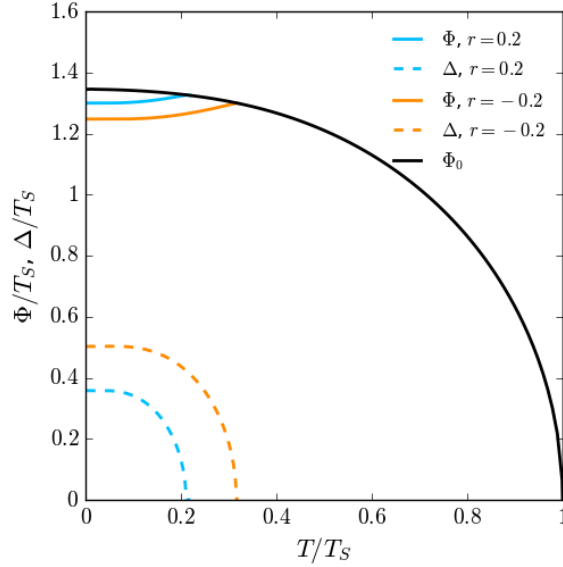


Figure 2.5: Nematic order parameter, Φ , (solid curves) plotted as a function of temperature in the absence of superconductivity (black), coexisting with s - + d - wave superconductivity when $r = 0.2$ and $T_c^0 = .4T_S$ (cyan), and coexisting with s - + d - wave superconductivity when $r = -0.2$ and $T_c^0 = .4T_S$ (orange). The superconducting order parameter (dashed curves) is also shown when $r = 0.2$ (cyan) and $r = -0.2$ (orange).

The results from simultaneously solving the Δ and Φ self-consistency equations are presented in Figure 2.5 for $r = 0.2$ (cyan) and $r = -0.2$ (orange). It can be seen that in both cases

investigated here that nematicity suppresses the superconducting transition temperature, however less so when the superconducting gap maximum is aligned with the FS elongation ($r < 0$).

Spin Density Waves

Mean-field Hamiltonian

The mean-field Hamiltonian for the SDW state can be written as:

$$\begin{aligned}
H_0 + H_{\text{SDW}} = & \frac{1}{4} \sum_{\mathbf{k}, \sigma} (\xi_{\mathbf{k}} \hat{a}_{\mathbf{k}, \sigma}^\dagger \hat{a}_{\mathbf{k}, \sigma} - \xi_{\mathbf{k}} \hat{a}_{-\mathbf{k}, \sigma} \hat{a}_{-\mathbf{k}, \sigma}^\dagger + \xi_{\mathbf{k}+\mathbf{Q}, \sigma} \hat{a}_{\mathbf{k}+\mathbf{Q}, \sigma}^\dagger \hat{a}_{\mathbf{k}+\mathbf{Q}, \sigma} \\
& - \xi_{\mathbf{k}+\mathbf{Q}, \sigma} \hat{a}_{-\mathbf{k}-\mathbf{Q}, \sigma} \hat{a}_{-\mathbf{k}-\mathbf{Q}, \sigma}^\dagger + M \hat{a}_{\mathbf{k}, \sigma}^\dagger \hat{a}_{\mathbf{k}+\mathbf{Q}, \sigma} + M \hat{a}_{\mathbf{k}+\mathbf{Q}, \sigma}^\dagger \hat{a}_{\mathbf{k}, \sigma} \\
& + M \hat{a}_{-\mathbf{k}, \sigma} \hat{a}_{-\mathbf{k}-\mathbf{Q}, \sigma}^\dagger + M \hat{a}_{-\mathbf{k}-\mathbf{Q}, \sigma} \hat{a}_{-\mathbf{k}, \sigma}^\dagger)
\end{aligned} \tag{2.29}$$

where it can be seen from this Hamiltonian that the SDW state connects electron (hole) states of momentum \mathbf{k} with electron (hole) states of parallel spin and momentum $\mathbf{k} + \mathbf{Q}$.

With the Nambu state vector, $\hat{\Psi}_{\mathbf{k}}^\dagger = (\hat{a}_{\mathbf{k}, \sigma}^\dagger, \hat{a}_{-\mathbf{k}, -\sigma}, \hat{a}_{\mathbf{k}+\mathbf{Q}, \sigma}^\dagger, \hat{a}_{-\mathbf{k}-\mathbf{Q}, -\sigma})$.

Eigenstates

This Hamiltonian can be rewritten in the Nambu basis as:

$$H_0 + H_{\text{SDW}} = \frac{1}{4} \sum_{\mathbf{k}, \sigma} \hat{\Psi}_{\mathbf{k}}^\dagger \hat{\mathcal{H}}_{\mathbf{k}}^{\text{SDW}} \hat{\Psi}_{\mathbf{k}}, \quad \hat{\mathcal{H}}_{\mathbf{k}}^{\text{SDW}} = \begin{pmatrix} \xi_{\mathbf{k}} & 0 & M & 0 \\ 0 & -\xi_{\mathbf{k}} & 0 & M \\ M & 0 & \xi_{\mathbf{k}+\mathbf{Q}} & 0 \\ 0 & M & 0 & -\xi_{\mathbf{k}+\mathbf{Q}} \end{pmatrix} \tag{2.30}$$

where the eigenvalues of $\hat{\mathcal{H}}_{\mathbf{k}}^{\text{SDW}}$ are the bands for the SDW state and were found to be:

$$\pm E_{\mathbf{k}}^{(\alpha)} = \pm \left(\xi_{\mathbf{k}}^+ + \sqrt{(\xi_{\mathbf{k}}^-)^2 + M^2} \right), \quad \pm E_{\mathbf{k}}^{(\beta)} = \pm \left(\xi_{\mathbf{k}}^+ - \sqrt{(\xi_{\mathbf{k}}^-)^2 + M^2} \right) \quad (2.31)$$

where $E_{\mathbf{k}}^{(\alpha)}$ and $E_{\mathbf{k}}^{(\beta)}$ represent SDW quasiparticle bands, while $-E_{\mathbf{k}}^{(\alpha)}$ and $-E_{\mathbf{k}}^{(\beta)}$ represent SDW quasihole bands. Furthermore, the eigenvectors of $\hat{\mathcal{H}}_{\mathbf{k}}^{\text{SDW}}$ can be found in order to construct a unitary transformation matrix which defines new Fermionic operators which represent the creation and annihilation operators for SDW quasiparticles in the $E_{\mathbf{k}}^{(\alpha)}$ and $E_{\mathbf{k}}^{(\beta)}$ quasiparticle bands or the $-E_{\mathbf{k}}^{(\alpha)}$ and $-E_{\mathbf{k}}^{(\beta)}$ quasihole bands:

$$\hat{\Psi}_{\mathbf{k}}^{\text{SDW}} = \hat{B}_{\mathbf{k}}^{\text{SDW}} \hat{\Psi}_{\mathbf{k}} = \begin{pmatrix} \hat{\alpha}_{\mathbf{k},\sigma} \\ \hat{\alpha}_{-\mathbf{k},-\sigma}^\dagger \\ \hat{\beta}_{\mathbf{k},\sigma} \\ \hat{\beta}_{-\mathbf{k},-\sigma}^\dagger \end{pmatrix} = \begin{pmatrix} u_{\mathbf{k}}^{\text{SDW}} & 0 & v_{\mathbf{k}}^{\text{SDW}} & 0 \\ 0 & u_{\mathbf{k}}^{\text{SDW}} & 0 & -v_{\mathbf{k}}^{\text{SDW}} \\ -v_{\mathbf{k}}^{\text{SDW}} & 0 & u_{\mathbf{k}}^{\text{SDW}} & 0 \\ 0 & v_{\mathbf{k}}^{\text{SDW}} & 0 & u_{\mathbf{k}}^{\text{SDW}} \end{pmatrix} \begin{pmatrix} \hat{a}_{\mathbf{k},\sigma} \\ \hat{a}_{-\mathbf{k},-\sigma}^\dagger \\ \hat{a}_{\mathbf{k}+\mathbf{Q},\sigma} \\ \hat{a}_{-\mathbf{k}-\mathbf{Q},-\sigma}^\dagger \end{pmatrix} \quad (2.32)$$

where:

$$u_{\mathbf{k}}^{\text{SDW}} = \frac{\xi_{\mathbf{k}}^- + \zeta_{\mathbf{k}}}{\sqrt{2\zeta_{\mathbf{k}}(\zeta_{\mathbf{k}} + \xi_{\mathbf{k}}^-)}} = \sqrt{\frac{1}{2} \left(1 + \frac{\xi_{\mathbf{k}}^-}{\zeta_{\mathbf{k}}} \right)} \quad (2.33)$$

$$v_{\mathbf{k}}^{\text{SDW}} = \frac{M}{\sqrt{2\zeta_{\mathbf{k}}(\zeta_{\mathbf{k}} + \xi_{\mathbf{k}}^-)}} = \sqrt{\frac{1}{2} \left(1 - \frac{\xi_{\mathbf{k}}^-}{\zeta_{\mathbf{k}}} \right)}$$

where $\zeta_{\mathbf{k}} = \sqrt{(\xi_{\mathbf{k}}^-)^2 + M^2}$. The eigenstate $|E_{\mathbf{k}}^{(\alpha)}\rangle = \hat{\alpha}_{\mathbf{k},\sigma}^\dagger |0\rangle$ represents the creation of a SDW quasiparticle of momentum \mathbf{k} and spin σ in the $E_{\mathbf{k}}^{(\alpha)}$ band. When a SDW quasiparticle is created in the $E_{\mathbf{k}}^{(\alpha)}$ band. A corresponding SDW quasihole is created in the $-E_{\mathbf{k}}^{(\alpha)}$ band due to the vacancies in the Fermi sea left by the coupled electrons associated with the creation

of the SDW quasiparticle, this is represented with the eigenstate $\left| -E_{\mathbf{k}}^{(\alpha)} \right\rangle = \hat{\alpha}_{-\mathbf{k},-\sigma} |0\rangle$. Similarly, the eigenstate $\left| E_{\mathbf{k}}^{(\beta)} \right\rangle = \hat{\beta}_{\mathbf{k},\sigma}^\dagger |0\rangle$ represents the creation of a SDW quasiparticle of momentum \mathbf{k} and spin σ in the $E_{\mathbf{k}}^{(\beta)}$ band. This also creates a corresponding quasihole in the $-E_{\mathbf{k}}^{(\beta)}$ band, represented by the eigenstate $\left| -E_{\mathbf{k}}^{(\beta)} \right\rangle = \hat{\beta}_{-\mathbf{k},-\sigma} |0\rangle$. These eigenstates can be written in terms of the electron creation and annihilation operators, and also be represented in the Nambu basis as:

$$\begin{aligned}
\left| E_{\mathbf{k}}^{(\alpha)} \right\rangle &= \hat{\alpha}_{\mathbf{k},\sigma}^\dagger |0\rangle = (u_{\mathbf{k}}^{\text{SDW}} \hat{a}_{\mathbf{k},\sigma}^\dagger + v_{\mathbf{k}}^{\text{SDW}} \hat{a}_{\mathbf{k}+\mathbf{Q},\sigma}^\dagger) |0\rangle := \begin{pmatrix} u_{\mathbf{k}}^{\text{SDW}} \\ 0 \\ v_{\mathbf{k}}^{\text{SDW}} \\ 0 \end{pmatrix} \\
\left| -E_{\mathbf{k}}^{(\alpha)} \right\rangle &= \hat{\alpha}_{-\mathbf{k},-\sigma} |0\rangle = (u_{\mathbf{k}}^{\text{SDW}} \hat{a}_{-\mathbf{k},-\sigma} - v_{\mathbf{k}}^{\text{SDW}} \hat{a}_{-\mathbf{k}-\mathbf{Q},-\sigma}) |0\rangle := \begin{pmatrix} 0 \\ u_{\mathbf{k}}^{\text{SDW}} \\ 0 \\ -v_{\mathbf{k}}^{\text{SDW}} \end{pmatrix} \\
\left| E_{\mathbf{k}}^{(\beta)} \right\rangle &= \hat{\beta}_{\mathbf{k},\sigma}^\dagger |0\rangle = (-v_{\mathbf{k}}^{\text{SDW}} \hat{a}_{\mathbf{k},\sigma}^\dagger + u_{\mathbf{k}}^{\text{SDW}} \hat{a}_{\mathbf{k}+\mathbf{Q},\sigma}^\dagger) |0\rangle := \begin{pmatrix} -v_{\mathbf{k}}^{\text{SDW}} \\ 0 \\ u_{\mathbf{k}}^{\text{SDW}} \\ 0 \end{pmatrix} \\
\left| -E_{\mathbf{k}}^{(\beta)} \right\rangle &= \hat{\beta}_{-\mathbf{k},-\sigma} |0\rangle = (v_{\mathbf{k}}^{\text{SDW}} \hat{a}_{-\mathbf{k},-\sigma} + u_{\mathbf{k}}^{\text{SDW}} \hat{a}_{-\mathbf{k}-\mathbf{Q},-\sigma}) |0\rangle := \begin{pmatrix} 0 \\ v_{\mathbf{k}}^{\text{SDW}} \\ 0 \\ u_{\mathbf{k}}^{\text{SDW}} \end{pmatrix}
\end{aligned} \tag{2.34}$$

From these eigenvectors it can be plain to see that the SDW state hybridizes the normal

state $\xi_{\mathbf{k}}$ and $\xi_{\mathbf{k}+\mathbf{Q}}$ electron bands to create the $E_{\mathbf{k}}^{(\alpha)}$ and $E_{\mathbf{k}}^{(\beta)}$ SDW quasiparticle bands and the normal state $-\xi_{\mathbf{k}}$ and $-\xi_{\mathbf{k}+\mathbf{Q}}$ hole bands to create the $-E_{\mathbf{k}}^{(\alpha)}$ and $-E_{\mathbf{k}}^{(\beta)}$ SDW quasihole bands.

While the band hybridization between the normal state $\xi_{\mathbf{k}}$ and $\xi_{\mathbf{k}+\mathbf{Q}}$ electron bands seen in Figure 2.6 (a) & (c) looks very similar to that of the Bogoliubov transformation, it is important to note that this is a hybridization between two electron bands instead of a hybridization between an electron and a hole band which has profoundly different properties when examining impurity scattering probabilities. Furthermore, it is also worth noting that in general $E_{\mathbf{k}}^{(\beta)} \neq -E_{\mathbf{k}}^{(\alpha)}$. It can also be seen from Figure 2.6 (b) & (d) that along the edge of the RBZ (when $(k_x, k_y) = (\pi/4, \pi/4) \rightarrow (\pi/2, 0)$) that the $\xi_{\mathbf{k}}$ and $\xi_{\mathbf{k}+\mathbf{Q}}$ normal state bands are degenerate, which results in band avoidance between the $E_{\mathbf{k}}^{(\alpha)}$ and $E_{\mathbf{k}}^{(\beta)}$ SDW quasiparticle bands. This also results in the $\hat{a}_{\mathbf{k},\sigma}^\dagger |0\rangle$ and $\hat{\beta}_{\mathbf{k},\sigma}^\dagger |0\rangle$ eigenstates having equal magnitude components of $\hat{a}_{\mathbf{k},\sigma}^\dagger$ and $\hat{a}_{\mathbf{k}+\mathbf{Q},\sigma}^\dagger$ (e.g. $|u_{\mathbf{k}}^{\text{SDW}}|^2 = |v_{\mathbf{k}}^{\text{SDW}}|^2 = 1/2$).

Coexistence of Spin Density Waves and Superconductivity

Mean-field Hamiltonian

When superconductivity coexists with spin density waves, the mean-field Hamiltonian can be written as:

$$\begin{aligned}
H_0 + H_{\text{SDW}} + H_{\text{SC}} = & \frac{1}{2} \sum_{\mathbf{k},\sigma} \left(\xi_{\mathbf{k}} \hat{a}_{\mathbf{k},\sigma}^\dagger \hat{a}_{\mathbf{k},\sigma} - \xi_{\mathbf{k}} \hat{a}_{-\mathbf{k},\sigma} \hat{a}_{-\mathbf{k},\sigma}^\dagger + \xi_{\mathbf{k}+\mathbf{Q},\sigma} \hat{a}_{\mathbf{k}+\mathbf{Q},\sigma}^\dagger \hat{a}_{\mathbf{k}+\mathbf{Q},\sigma} \right. \\
& - \xi_{\mathbf{k}+\mathbf{Q},\sigma} \hat{a}_{-\mathbf{k}-\mathbf{Q},\sigma} \hat{a}_{-\mathbf{k}-\mathbf{Q},\sigma}^\dagger + M \hat{a}_{\mathbf{k},\sigma}^\dagger \hat{a}_{\mathbf{k}+\mathbf{Q},\sigma} + M \hat{a}_{\mathbf{k}+\mathbf{Q},\sigma}^\dagger \hat{a}_{\mathbf{k},\sigma} \\
& + M \hat{a}_{-\mathbf{k},\sigma} \hat{a}_{-\mathbf{k}-\mathbf{Q},\sigma}^\dagger + M \hat{a}_{-\mathbf{k}-\mathbf{Q},\sigma} \hat{a}_{-\mathbf{k},\sigma}^\dagger + \Delta_{\mathbf{k}} \hat{a}_{\mathbf{k},\sigma}^\dagger \hat{a}_{-\mathbf{k},-\sigma} \\
& + \Delta_{\mathbf{k}} \hat{a}_{-\mathbf{k},-\sigma} \hat{a}_{\mathbf{k},\sigma} + \Delta_{\mathbf{k}+\mathbf{Q}} \hat{a}_{\mathbf{k}+\mathbf{Q},\sigma}^\dagger \hat{a}_{-\mathbf{k}-\mathbf{Q},-\sigma} \\
& \left. + \Delta_{\mathbf{k}+\mathbf{Q}} \hat{a}_{-\mathbf{k}-\mathbf{Q},-\sigma} \hat{a}_{\mathbf{k}+\mathbf{Q},\sigma} \right)
\end{aligned} \tag{2.35}$$

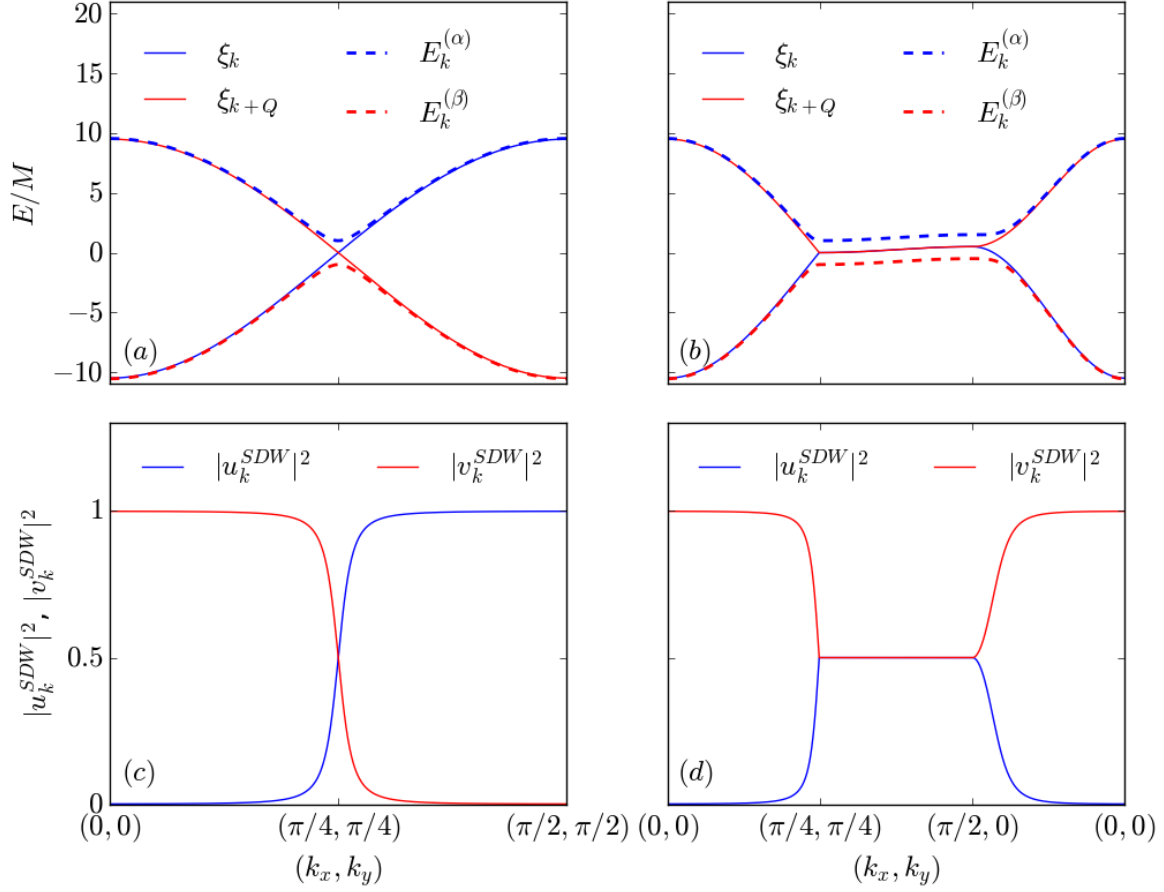


Figure 2.6: (a) & (b) Normal state electron $\xi_{\mathbf{k}}$ (solid blue) and $\xi_{\mathbf{k}+\mathbf{Q}}$ (solid red) bands for a tight-binding model $\xi_{\mathbf{k}} = \mu - t_1 \cos(2k_x a) - t_1 \cos(2k_y a) - t_2 \cos(2k_x a) \cos(2k_y a)$ and the $E_{\mathbf{k}}^{(\alpha)}$ SDW quasiparticle (dashed blue) and $E_{\mathbf{k}}^{(\beta)}$ SDW quasiparticle (dashed red) bands for the $\mathbf{Q} = (\pi/2, \pi/2)$ SDW state. It should be noted that, in general, $E_{\mathbf{k}}^{(\beta)} \neq -E_{\mathbf{k}}^{(\alpha)}$ despite their similarities in this illustration (c) & (d) SDW quasiparticle transformation coefficients $|u_{\mathbf{k}}^{SDW}|^2$ and $|v_{\mathbf{k}}^{SDW}|^2$ which show that the SDW quasiparticle bands are a result of the hybridization of the $\xi_{\mathbf{k}}$ and $\xi_{\mathbf{k}+\mathbf{Q}}$ normal state electron bands.

d -wave superconductivity coexisting with a symmetry-broken spin density wave state with an in-plane $C(2)$ rotational symmetry results in either a superconducting gap which is odd ($d^{(O)}$ -wave) or even ($d^{(E)}$ -wave) under translations of \mathbf{Q} . As can be seen in Figure 2.7 (a) and (d), a $d_{x^2-y^2}$ SC gap coexisting with a $\mathbf{Q} = (\pi/2, \pi/2)$ SDW state and a d_{xy} SC gap coexisting with a $\mathbf{Q} = (\pi, 0)$ SDW state are odd under translations of \mathbf{Q} . Alternatively, as can be seen in Figure 2.7 (b) and (c), a d_{xy} SC gap coexisting with a $\mathbf{Q} = (\pi/2, \pi/2)$ SDW state and a $d_{x^2-y^2}$ SC gap coexisting with a $\mathbf{Q} = (\pi, 0)$ SDW state are even under translations of \mathbf{Q} . The symmetry class of these SC + SDW coexistence states are vital to the nature of the low-energy quasiparticle excitations.

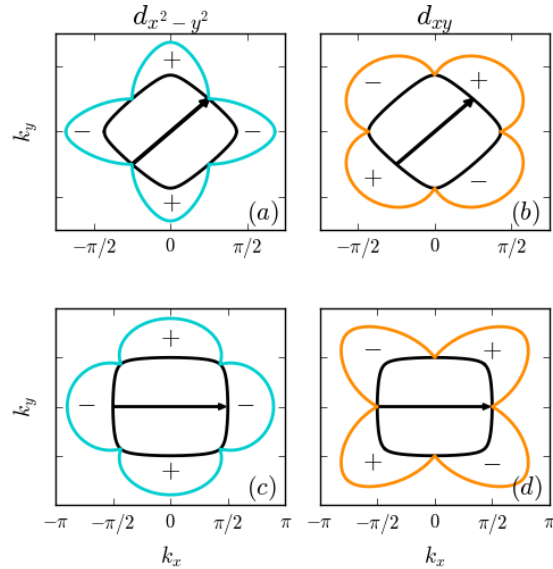


Figure 2.7: Qualitative illustration of the amplitude and sign of the superconducting gap along the normal state tight-binding FSs (band parameters $t_1 = 100T_N$ and $t_2 = 10T_N$) to show the symmetry of the SC gap under translations of the \mathbf{Q} -vector. (a) $d_{x^2-y^2}$ SC pairing on the $\xi_{\mathbf{k}}^{(1)}$ FS (b) d_{xy} pairing on the $\xi_{\mathbf{k}}^{(1)}$ FS (c) $d_{x^2-y^2}$ SC pairing on the $\xi_{\mathbf{k}}^{(2)}$ FS (d) d_{xy} pairing on the $\xi_{\mathbf{k}}^{(2)}$ FS.

When the superconducting gap is odd under translations of \mathbf{Q} , the FS reconstruction gaps two of the d -wave symmetry nodes which are parallel to \mathbf{Q} , which can be seen in Figure 2.8. However, when the superconducting gap is even under translations of \mathbf{Q} not only are none of

the d -wave symmetry nodes gapped by the FS reconstruction, but additional mixing nodes appear near the edges of the FS reconstruction as can be seen by the red X's in Figure 2.8.

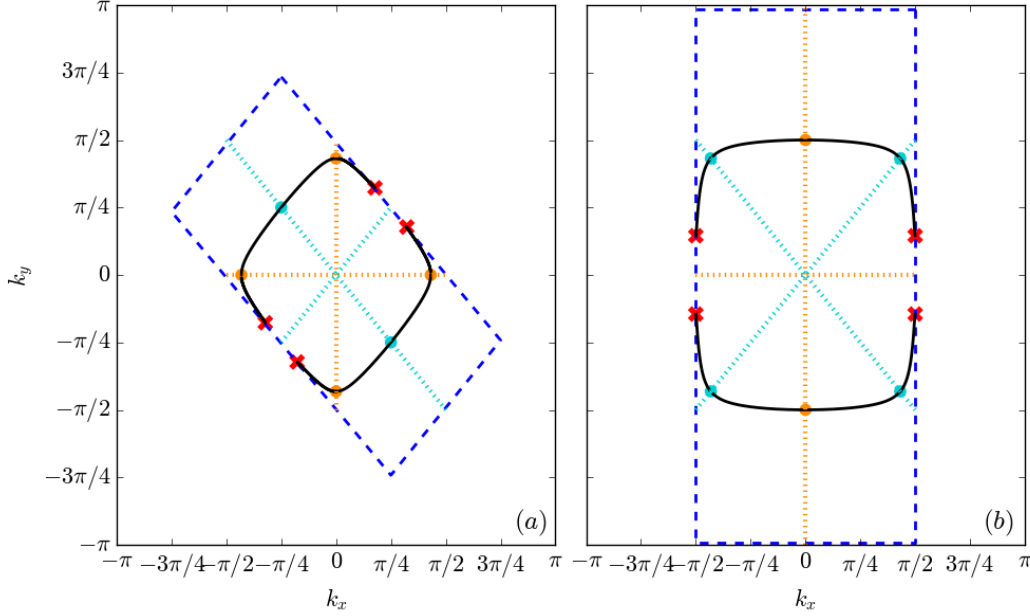


Figure 2.8: FSs reconstructed by SDW ordering (solid black curves) when $M = 2T_N$ for the nesting vectors (a) $\mathbf{Q} = (\pi/2, \pi/2)$ and (b) $\mathbf{Q} = (\pi, 0)$. The d -wave nodal lines are represented with dotted cyan and orange lines for $d_{x^2-y^2}$ and d_{xy} respectively. Cyan and orange points represent the locations of the $d_{x^2-y^2}$ and d_{xy} nodes respectively when their nodal lines cross the reconstructed FS. Red X's show the locations of additional mixing nodes that occur only when the SC gap is even under translations of \mathbf{Q} ($\Delta_{\mathbf{k}+\mathbf{Q}} = \Delta_{\mathbf{k}}$).

Eigenstates

The Hamiltonian can be rewritten in the Nambu basis, where $\hat{\Psi}_{\mathbf{k}}^\dagger = (\hat{a}_{\mathbf{k},\sigma}^\dagger, \hat{a}_{-\mathbf{k},-\sigma}, \hat{a}_{\mathbf{k}+\mathbf{Q},\sigma}^\dagger, \hat{a}_{-\mathbf{k}-\mathbf{Q},-\sigma})$

$$H_0 + H_{\text{SDW}} + H_{\text{SC}} = \frac{1}{2} \sum_{\mathbf{k},\sigma} \hat{\Psi}_{\mathbf{k}}^\dagger \hat{\mathcal{H}}_{\mathbf{k}} \hat{\Psi}_{\mathbf{k}}, \quad \hat{\mathcal{H}}_{\mathbf{k}} = \begin{pmatrix} \xi_{\mathbf{k}} & \Delta_{\mathbf{k}} & M & 0 \\ \Delta_{\mathbf{k}} & -\xi_{\mathbf{k}} & 0 & M \\ M & 0 & \xi_{\mathbf{k}+\mathbf{Q}} & \Delta_{\mathbf{k}+\mathbf{Q}} \\ 0 & M & \Delta_{\mathbf{k}+\mathbf{Q}} & -\xi_{\mathbf{k}+\mathbf{Q}} \end{pmatrix} \quad (2.36)$$

Since the eigenvectors of $\hat{\mathcal{H}}_{\mathbf{k}}$ are difficult to obtain analytically in general, one might expect perturbation theory to provide good approximations to these eigenvectors. In this approach superconductivity was treated as a perturbation to the SDW state since superconductivity typically arises out of the SDW state ($T_c < T_N$) and the SC order parameter is smaller than the SDW order parameter ($\Delta \ll M$).

$$\hat{\mathcal{H}}_{\mathbf{k}} = \hat{\mathcal{H}}_{\mathbf{k}}^{\text{SDW}} + \hat{\mathcal{H}}_{\mathbf{k}}^{\Delta} = \begin{pmatrix} \xi_{\mathbf{k}} & 0 & M & 0 \\ 0 & -\xi_{\mathbf{k}} & 0 & M \\ M & 0 & \xi_{\mathbf{k}+\mathbf{Q}} & 0 \\ 0 & M & 0 & -\xi_{\mathbf{k}+\mathbf{Q}} \end{pmatrix} + \begin{pmatrix} 0 & \Delta_{\mathbf{k}} & 0 & 0 \\ \Delta_{\mathbf{k}} & 0 & 0 & 0 \\ 0 & 0 & 0 & \Delta_{\mathbf{k}+\mathbf{Q}} \\ 0 & 0 & \Delta_{\mathbf{k}+\mathbf{Q}} & 0 \end{pmatrix} \quad (2.37)$$

where the first-order corrections to the eigenvalues to be accurately described by:

$$(\pm E_{\mathbf{k}}^{(\alpha,\beta)})^{(1)} = \pm E_{\mathbf{k}}^{(\alpha,\beta)} + \sum_{E_{\mathbf{k}}^{(i)} = \pm E_{\mathbf{k}}^{(\alpha)}, \pm E_{\mathbf{k}}^{(\beta)}} \frac{\left| \langle E_{\mathbf{k}}^{(i)} | \hat{\mathcal{H}}_{\mathbf{k}}^{\Delta} | \pm E_{\mathbf{k}}^{(\alpha,\beta)} \rangle \right|^2}{\pm E_{\mathbf{k}}^{(\alpha,\beta)} - E_{\mathbf{k}}^{(i)}} \quad (2.38)$$

$$(\pm E_{\mathbf{k}}^{(\alpha)})^{(1)} = \pm \left(E_{\mathbf{k}}^{(\alpha)} + \frac{(\Delta_{\mathbf{k}} |u_{\mathbf{k}}^{\text{SDW}}|^2 - \Delta_{\mathbf{k}+\mathbf{Q}} |v_{\mathbf{k}}^{\text{SDW}}|^2)^2}{2E_{\mathbf{k}}^{(\alpha)}} + \frac{(2\Delta_{\mathbf{k}}^+ u_{\mathbf{k}}^{\text{SDW}} v_{\mathbf{k}}^{\text{SDW}})^2}{E_{\mathbf{k}}^{(\alpha)} + E_{\mathbf{k}}^{(\beta)}} \right) \quad (2.39)$$

$$(\pm E_{\mathbf{k}}^{(\beta)})^{(1)} = \pm \left(E_{\mathbf{k}}^{(\beta)} + \frac{(\Delta_{\mathbf{k}} |v_{\mathbf{k}}^{\text{SDW}}|^2 - \Delta_{\mathbf{k}+\mathbf{Q}} |u_{\mathbf{k}}^{\text{SDW}}|^2)^2}{2E_{\mathbf{k}}^{(\beta)}} + \frac{(2\Delta_{\mathbf{k}}^+ u_{\mathbf{k}}^{\text{SDW}} v_{\mathbf{k}}^{\text{SDW}})^2}{E_{\mathbf{k}}^{(\alpha)} + E_{\mathbf{k}}^{(\beta)}} \right) \quad (2.40)$$

and the first-order corrections to the eigenvectors are:

$$\left| \pm E_{\mathbf{k}}^{(\alpha, \beta)} \right\rangle^{(1)} = \left| \pm E_{\mathbf{k}}^{(\alpha, \beta)} \right\rangle + \sum_{E_{\mathbf{k}}^{(i)} = \pm E_{\mathbf{k}}^{(\alpha)}, \pm E_{\mathbf{k}}^{(\beta)}} \frac{\langle E_{\mathbf{k}}^{(i)} | \hat{\mathcal{H}}_{\mathbf{k}}^{\Delta} | \pm E_{\mathbf{k}}^{(\alpha, \beta)} \rangle}{\pm E_{\mathbf{k}}^{(\alpha, \beta)} - E_{\mathbf{k}}^{(i)}} \left| E_{\mathbf{k}}^{(i)} \right\rangle \quad (2.41)$$

$$\left| \pm E_{\mathbf{k}}^{(1)} \right\rangle = \left| \pm E_{\mathbf{k}}^{(\alpha)} \right\rangle \pm \frac{\Delta_{\mathbf{k}} |u_{\mathbf{k}}^{\text{SDW}}|^2 - \Delta_{\mathbf{k}+\mathbf{Q}} |v_{\mathbf{k}}^{\text{SDW}}|^2}{2E_{\mathbf{k}}^{(\alpha)}} \left| \mp E_{\mathbf{k}}^{(\alpha)} \right\rangle + \frac{2\Delta_{\mathbf{k}}^+ u_{\mathbf{k}}^{\text{SDW}} v_{\mathbf{k}}^{\text{SDW}}}{E_{\mathbf{k}}^{(\alpha)} + E_{\mathbf{k}}^{(\beta)}} \left| \mp E_{\mathbf{k}}^{(\beta)} \right\rangle \quad (2.42)$$

$$\left| \pm E_{\mathbf{k}}^{(2)} \right\rangle = \begin{cases} \left| \pm E_{\mathbf{k}}^{(\beta)} \right\rangle \mp \frac{\Delta_{\mathbf{k}} |u_{\mathbf{k}}^{\text{SDW}}|^2 - \Delta_{\mathbf{k}+\mathbf{Q}} |v_{\mathbf{k}}^{\text{SDW}}|^2}{2E_{\mathbf{k}}^{(\beta)}} \left| \mp E_{\mathbf{k}}^{(\beta)} \right\rangle - \frac{2\Delta_{\mathbf{k}}^+ u_{\mathbf{k}}^{\text{SDW}} v_{\mathbf{k}}^{\text{SDW}}}{E_{\mathbf{k}}^{(\alpha)} + E_{\mathbf{k}}^{(\beta)}} \left| \mp E_{\mathbf{k}}^{(\alpha)} \right\rangle & \text{if } E_{\mathbf{k}}^{(\beta)} > 0 \\ \left| \mp E_{\mathbf{k}}^{(\beta)} \right\rangle \pm \frac{\Delta_{\mathbf{k}} |u_{\mathbf{k}}^{\text{SDW}}|^2 - \Delta_{\mathbf{k}+\mathbf{Q}} |v_{\mathbf{k}}^{\text{SDW}}|^2}{2E_{\mathbf{k}}^{(\beta)}} \left| \pm E_{\mathbf{k}}^{(\beta)} \right\rangle - \frac{2\Delta_{\mathbf{k}}^+ u_{\mathbf{k}}^{\text{SDW}} v_{\mathbf{k}}^{\text{SDW}}}{E_{\mathbf{k}}^{(\alpha)} + E_{\mathbf{k}}^{(\beta)}} \left| \pm E_{\mathbf{k}}^{(\alpha)} \right\rangle & \text{if } E_{\mathbf{k}}^{(\beta)} < 0 \end{cases} \quad (2.43)$$

However, perturbation theory fails to accurately describe the mixing between the SDW quasiparticle and quasihole bands when superconductivity coexists with the SDW state, because superconductivity is an inherently non-perturbative effect. The simplest way to visualize this failure is by plotting the bands derived from the first-order corrections to the eigenvalues. These bands can be seen in Figure 2.9 (a) when the d -wave SC gap is odd under translations of \mathbf{Q} and in Figure 2.9 (b) when the d -wave SC gap is even under translations of \mathbf{Q} . It can be seen that the $(E_{\mathbf{k}}^{(\beta)})^{(1)}$ band diverges when the $E_{\mathbf{k}}^{(\beta)}$ SDW band goes to 0 due to a degeneracy between the $E_{\mathbf{k}}^{(\beta)}$ and $-E_{\mathbf{k}}^{(\beta)}$ bands. It can also be seen that both the $(E_{\mathbf{k}}^{(\alpha)})^{(1)}$ and $(E_{\mathbf{k}}^{(\beta)})^{(1)}$ bands diverge when the $\pm E_{\mathbf{k}}^{(\alpha)}$ and $\mp E_{\mathbf{k}}^{(\beta)}$ SDW bands are degenerate. Typically, this would be remedied by setting up a submatrix for only these degenerate bands, however this results in a discontinuous solution to the bands. In order to properly solve for the eigenvectors of the coexistence Hamiltonian $\hat{\mathcal{H}}_{\mathbf{k}}$, a two-step diagonalization method can be employed[31], which changes the basis of the coexistence Hamiltonian from the electron creation and annihilation operators ($\hat{\Psi}_{\mathbf{k}}$) to the SDW quasiparticle creation and annihilation

operators ($\hat{\Psi}_{\mathbf{k}}^{\text{SDW}}$).

$$H = \frac{1}{2} \sum_{\mathbf{k}} (\hat{\Psi}_{\mathbf{k}}^{\text{SDW}})^\dagger \hat{\mathcal{H}}'_{\mathbf{k}} \hat{\Psi}_{\mathbf{k}}^{\text{SDW}}, \quad \hat{\mathcal{H}}'_{\mathbf{k}} = \hat{B}_{\mathbf{k}}^{\text{SDW}} \hat{\mathcal{H}}'_{\mathbf{k}} (\hat{B}_{\mathbf{k}}^{\text{SDW}})^\dagger \quad (2.44)$$

$$\hat{\mathcal{H}}'_{\mathbf{k}} = \begin{pmatrix} \langle E_{\mathbf{k}}^{(\alpha)} | \hat{\mathcal{H}}_{\mathbf{k}} | E_{\mathbf{k}}^{(\alpha)} \rangle & \langle E_{\mathbf{k}}^{(\alpha)} | \hat{\mathcal{H}}_{\mathbf{k}} | -E_{\mathbf{k}}^{(\alpha)} \rangle & \langle E_{\mathbf{k}}^{(\alpha)} | \hat{\mathcal{H}}_{\mathbf{k}} | E_{\mathbf{k}}^{(\beta)} \rangle & \langle E_{\mathbf{k}}^{(\alpha)} | \hat{\mathcal{H}}_{\mathbf{k}} | -E_{\mathbf{k}}^{(\beta)} \rangle \\ \langle -E_{\mathbf{k}}^{(\alpha)} | \hat{\mathcal{H}}_{\mathbf{k}} | E_{\mathbf{k}}^{(\alpha)} \rangle & \langle -E_{\mathbf{k}}^{(\alpha)} | \hat{\mathcal{H}}_{\mathbf{k}} | -E_{\mathbf{k}}^{(\alpha)} \rangle & \langle -E_{\mathbf{k}}^{(\alpha)} | \hat{\mathcal{H}}_{\mathbf{k}} | E_{\mathbf{k}}^{(\beta)} \rangle & \langle -E_{\mathbf{k}}^{(\alpha)} | \hat{\mathcal{H}}_{\mathbf{k}} | -E_{\mathbf{k}}^{(\beta)} \rangle \\ \langle E_{\mathbf{k}}^{(\beta)} | \hat{\mathcal{H}}_{\mathbf{k}} | E_{\mathbf{k}}^{(\alpha)} \rangle & \langle E_{\mathbf{k}}^{(\beta)} | \hat{\mathcal{H}}_{\mathbf{k}} | -E_{\mathbf{k}}^{(\alpha)} \rangle & \langle E_{\mathbf{k}}^{(\beta)} | \hat{\mathcal{H}}_{\mathbf{k}} | E_{\mathbf{k}}^{(\beta)} \rangle & \langle E_{\mathbf{k}}^{(\beta)} | \hat{\mathcal{H}}_{\mathbf{k}} | -E_{\mathbf{k}}^{(\beta)} \rangle \\ \langle -E_{\mathbf{k}}^{(\beta)} | \hat{\mathcal{H}}_{\mathbf{k}} | E_{\mathbf{k}}^{(\alpha)} \rangle & \langle -E_{\mathbf{k}}^{(\beta)} | \hat{\mathcal{H}}_{\mathbf{k}} | -E_{\mathbf{k}}^{(\alpha)} \rangle & \langle -E_{\mathbf{k}}^{(\beta)} | \hat{\mathcal{H}}_{\mathbf{k}} | E_{\mathbf{k}}^{(\beta)} \rangle & \langle -E_{\mathbf{k}}^{(\beta)} | \hat{\mathcal{H}}_{\mathbf{k}} | -E_{\mathbf{k}}^{(\beta)} \rangle \end{pmatrix}$$

which can be shown to reduce to:

$$\hat{\mathcal{H}}'_{\mathbf{k}} = \begin{pmatrix} E_{\mathbf{k}}^{(\alpha)} & \Delta_{\mathbf{k}} |u_{\mathbf{k}}^{\text{SDW}}|^2 - \Delta_{\mathbf{k}+\mathbf{Q}} |v_{\mathbf{k}}^{\text{SDW}}|^2 & 0 & 2\Delta_{\mathbf{k}}^+ u_{\mathbf{k}}^{\text{SDW}} v_{\mathbf{k}}^{\text{SDW}} \\ \Delta_{\mathbf{k}} |u_{\mathbf{k}}^{\text{SDW}}|^2 - \Delta_{\mathbf{k}+\mathbf{Q}} |v_{\mathbf{k}}^{\text{SDW}}|^2 & -E_{\mathbf{k}}^{(\alpha)} & -2\Delta_{\mathbf{k}}^+ u_{\mathbf{k}}^{\text{SDW}} v_{\mathbf{k}}^{\text{SDW}} & 0 \\ 0 & -2\Delta_{\mathbf{k}}^+ u_{\mathbf{k}}^{\text{SDW}} v_{\mathbf{k}}^{\text{SDW}} & E_{\mathbf{k}}^{(\beta)} & -\Delta_{\mathbf{k}} |v_{\mathbf{k}}^{\text{SDW}}|^2 + \Delta_{\mathbf{k}+\mathbf{Q}} |u_{\mathbf{k}}^{\text{SDW}}|^2 \\ 2\Delta_{\mathbf{k}}^+ u_{\mathbf{k}}^{\text{SDW}} v_{\mathbf{k}}^{\text{SDW}} & 0 & -\Delta_{\mathbf{k}} |v_{\mathbf{k}}^{\text{SDW}}|^2 + \Delta_{\mathbf{k}+\mathbf{Q}} |u_{\mathbf{k}}^{\text{SDW}}|^2 & -E_{\mathbf{k}}^{(\beta)} \end{pmatrix}$$

This Hamiltonian can be further simplified in order to derive the coexistence eigenstates for the cases when the superconducting gap is even ($\Delta_{\mathbf{k}+\mathbf{Q}} = \Delta_{\mathbf{k}}$) and odd ($\Delta_{\mathbf{k}+\mathbf{Q}} = -\Delta_{\mathbf{k}}$) under translations of the SDW nesting vector.

When the SC gap is odd under translations of \mathbf{Q} , $\Delta_{\mathbf{k}+\mathbf{Q}} = -\Delta_{\mathbf{k}}$, and therefore $\Delta_{\mathbf{k}}^+ = 0$, thus, resulting in the interband coupling term going to zero. Furthermore, the intraband coupling term $\Delta_{\mathbf{k}} |u_{\mathbf{k}}^{\text{SDW}}|^2 - \Delta_{\mathbf{k}+\mathbf{Q}} |v_{\mathbf{k}}^{\text{SDW}}|^2$, can be reduced to: $\Delta_{\mathbf{k}} (|u_{\mathbf{k}}^{\text{SDW}}|^2 + |v_{\mathbf{k}}^{\text{SDW}}|^2) = \Delta_{\mathbf{k}}$ (which makes use of the normalization $|u_{\mathbf{k}}^{\text{SDW}}|^2 + |v_{\mathbf{k}}^{\text{SDW}}|^2 = 1$). Therefore $\hat{\mathcal{H}}'_{\mathbf{k}}$ can be even further reduced to:

$$\hat{\mathcal{H}}'_{\mathbf{k}} = \begin{pmatrix} E_{\mathbf{k}}^{(\alpha)} & \Delta_{\mathbf{k}} & 0 & 0 \\ \Delta_{\mathbf{k}} & -E_{\mathbf{k}}^{(\alpha)} & 0 & 0 \\ 0 & 0 & E_{\mathbf{k}}^{(\beta)} & -\Delta_{\mathbf{k}} \\ 0 & 0 & -\Delta_{\mathbf{k}} & -E_{\mathbf{k}}^{(\beta)} \end{pmatrix} \quad (2.45)$$

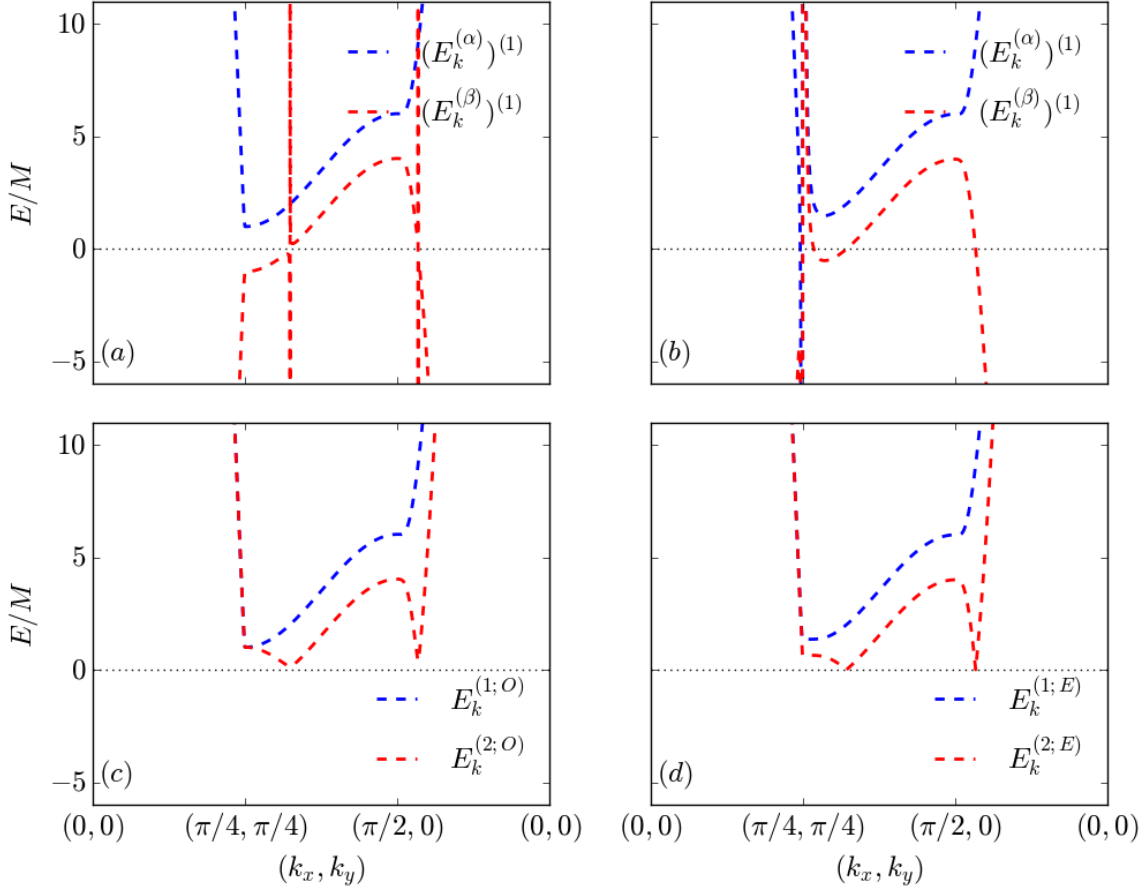


Figure 2.9: (a) $(E_{\mathbf{k}}^{(\alpha)})^{(1)}$ (dashed blue curve) and $(E_{\mathbf{k}}^{(\beta)})^{(1)}$ (dashed red curve) first-order perturbation bands when the $\mathbf{Q} = (\pi/2, \pi/2)$ SDW state coexists with a $d^{(O)}$ -wave SC gap. (b) $(E_{\mathbf{k}}^{(\alpha)})^{(1)}$ (dashed blue curve) and $(E_{\mathbf{k}}^{(\beta)})^{(1)}$ (dashed red curve) first-order perturbation bands when the $\mathbf{Q} = (\pi/2, \pi/2)$ SDW state coexists with a $d^{(E)}$ -wave SC gap. (c) $E_{\mathbf{k}}^{(1;O)}$ (dashed blue curve) and $E_{\mathbf{k}}^{(2;O)}$ (dashed red curve) bands when the $\mathbf{Q} = (\pi/2, \pi/2)$ SDW state coexists with a $d^{(O)}$ -wave SC gap. (d) $E_{\mathbf{k}}^{(1;E)}$ (dashed blue curve) and $E_{\mathbf{k}}^{(2;E)}$ (dashed red curve) bands when the $\mathbf{Q} = (\pi/2, \pi/2)$ SDW state coexists with a $d^{(E)}$ -wave SC gap.

which looks reminiscent of the pure SC Hamiltonian in the Nambu basis, but for the $\pm E_{\mathbf{k}}^{(\alpha)}$ and $\pm E_{\mathbf{k}}^{(\beta)}$ SDW bands. The submatrix therefore has the eigenvalues: $\pm \epsilon_{\mathbf{k}}^{(1;O)} = \pm \sqrt{(E_{\mathbf{k}}^{(\alpha)})^2 + \Delta_{\mathbf{k}}^2}$ and $\pm \epsilon_{\mathbf{k}}^{(2;O)} = \pm \sqrt{(E_{\mathbf{k}}^{(\beta)})^2 + \Delta_{\mathbf{k}}^2}$, which can be shown[60] to be equivalent to the $E_{\mathbf{k}}^{(1)}$ and $E_{\mathbf{k}}^{(2)}$ bands respectively. Therefore, the eigenvectors of the SC + SDW coexistence state when the SC gap is odd under translations of \mathbf{Q} can be shown to be similar to those of the Bogoliubov transform for the pure SC state:

$$\begin{aligned}
|E_{\mathbf{k}}^{(1)}\rangle &= u_{\mathbf{k}}^{(1;O)} |E_{\mathbf{k}}^{(\alpha)}\rangle + v_{\mathbf{k}}^{(1;O)} |-E_{\mathbf{k}}^{(\alpha)}\rangle = (u_{\mathbf{k}}^{(1;O)} \hat{\alpha}_{\mathbf{k},\sigma}^\dagger + v_{\mathbf{k}}^{(1;O)} \hat{\alpha}_{-\mathbf{k},-\sigma}) |0\rangle \\
|-E_{\mathbf{k}}^{(1)}\rangle &= -v_{\mathbf{k}}^{(1;O)} |E_{\mathbf{k}}^{(\alpha)}\rangle + u_{\mathbf{k}}^{(1;O)} |-E_{\mathbf{k}}^{(\alpha)}\rangle = (-v_{\mathbf{k}}^{(1;O)} \hat{\alpha}_{\mathbf{k},\sigma}^\dagger + u_{\mathbf{k}}^{(1;O)} \hat{\alpha}_{-\mathbf{k},-\sigma}) |0\rangle \\
|E_{\mathbf{k}}^{(2)}\rangle &= u_{\mathbf{k}}^{(2;O)} |E_{\mathbf{k}}^{(\beta)}\rangle - v_{\mathbf{k}}^{(2;O)} |-E_{\mathbf{k}}^{(\beta)}\rangle = (u_{\mathbf{k}}^{(2;O)} \hat{\beta}_{\mathbf{k},\sigma}^\dagger - v_{\mathbf{k}}^{(2;O)} \hat{\beta}_{-\mathbf{k},-\sigma}) |0\rangle \\
|-E_{\mathbf{k}}^{(2)}\rangle &= v_{\mathbf{k}}^{(2;O)} |E_{\mathbf{k}}^{(\beta)}\rangle + u_{\mathbf{k}}^{(2;O)} |-E_{\mathbf{k}}^{(\beta)}\rangle = (v_{\mathbf{k}}^{(2;O)} \hat{\beta}_{\mathbf{k},\sigma}^\dagger + u_{\mathbf{k}}^{(2;O)} \hat{\beta}_{-\mathbf{k},-\sigma}) |0\rangle
\end{aligned} \tag{2.46}$$

where:

$$u_{\mathbf{k}}^{(1,2;O)} = \frac{E_{\mathbf{k}}^{(1,2;O)} + E_{\mathbf{k}}^{(\alpha,\beta)}}{\sqrt{2E_{\mathbf{k}}^{(1,2;O)}(E_{\mathbf{k}}^{(1,2;O)} + E_{\mathbf{k}}^{(\alpha,\beta)})}} = \sqrt{\frac{1}{2} \left(1 + \frac{E_{\mathbf{k}}^{(\alpha,\beta)}}{E_{\mathbf{k}}^{(1,2;O)}} \right)} \tag{2.47}$$

$$v_{\mathbf{k}}^{(1,2;O)} = \frac{\Delta_{\mathbf{k}}}{\sqrt{2E_{\mathbf{k}}^{(1,2;O)}(E_{\mathbf{k}}^{(1,2;O)} + E_{\mathbf{k}}^{(\alpha,\beta)})}} = \sqrt{\frac{1}{2} \left(1 - \frac{E_{\mathbf{k}}^{(\alpha,\beta)}}{E_{\mathbf{k}}^{(1,2;O)}} \right)} \tag{2.48}$$

When the SC gap is odd under translations of \mathbf{Q} , it can be seen that the $E_{\mathbf{k}}^{(\alpha)}$ SDW quasiparticle and $-E_{\mathbf{k}}^{(\alpha)}$ SDW quasihole bands hybridize to create the $E_{\mathbf{k}}^{(1)}$ quasiparticle band. Similarly, the $E_{\mathbf{k}}^{(\beta)}$ and $-E_{\mathbf{k}}^{(\beta)}$ bands hybridize to create the $E_{\mathbf{k}}^{(2)}$ quasiparticle band. However, since the $E_{\mathbf{k}}^{(\beta)}$ and $-E_{\mathbf{k}}^{(\beta)}$ bands are degenerate at the Fermi level this band hybridization leads to a band avoidance characteristic of a fully-gapped SC, which can be seen in Figure 2.10 (a).

This is why the odd d -wave SC gap coexisting with a commensurate SDW state leads

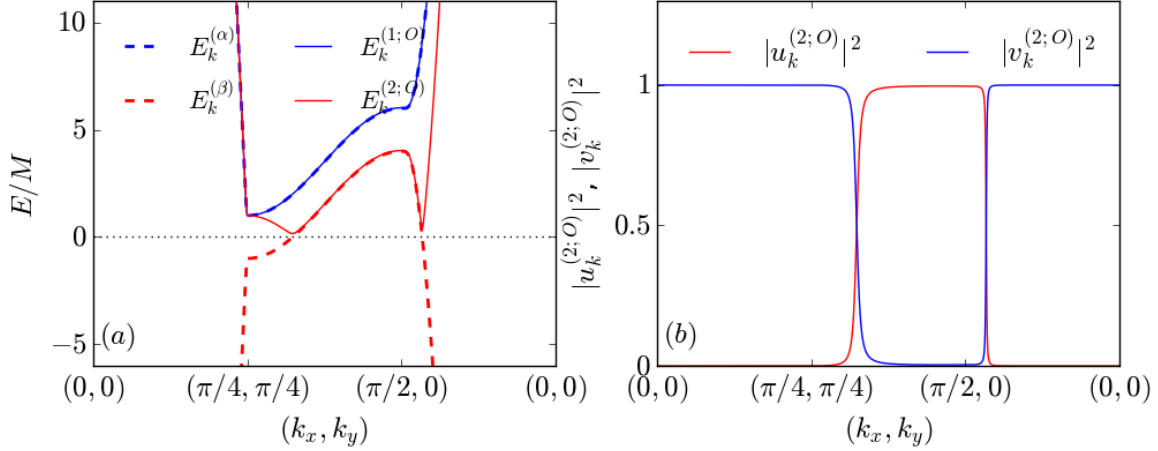


Figure 2.10: (a) SDW quasiparticle bands $E_{\mathbf{k}}^{(\alpha)}$ (dashed blue) and $E_{\mathbf{k}}^{(\beta)}$ (dashed red) and SDW + $d^{(O)}$ -wave SC coexistence bands $E_{\mathbf{k}}^{(1;O)}$ (solid blue) and $E_{\mathbf{k}}^{(2;O)}$ (solid red) plotted to show the hybridization between the $E_{\mathbf{k}}^{(\beta)}$ and $-E_{\mathbf{k}}^{(\beta)}$ bands which results in a band avoidance at the Fermi level. (b) Degree of hybridization between the SDW bands in order to create the coexistence bands when SDW coexists with $d^{(O)}$ -wave SC.

to no nodes in regions of \mathbf{k} -space where Δ and M are both nonzero. Similar to how the pure SC bands were hole-like when $\xi_{\mathbf{k}} < 0$ and electron-like when $\xi_{\mathbf{k}} > 0$, the $E_{\mathbf{k}}^{(2)}$ coexistence band is more $E_{\mathbf{k}}^{(\beta)}$ -like when $E_{\mathbf{k}}^{(\beta)} > 0$ and more $-E_{\mathbf{k}}^{(\beta)}$ -like when $E_{\mathbf{k}}^{(\beta)} < 0$, which can be seen in Figure 2.10 (b).

When the superconducting gap is even under translations of the SDW nesting vector, $\Delta_{\mathbf{k}+\mathbf{Q}} = \Delta_{\mathbf{k}}$ which simplifies $\hat{\mathcal{H}}'_{\mathbf{k}}$ to:

$$\hat{\mathcal{H}}'_{\mathbf{k}} = \begin{pmatrix} E_{\mathbf{k}}^{(\alpha)} & \Delta_{\mathbf{k}}(|u_{\mathbf{k}}^{\text{SDW}}|^2 - |v_{\mathbf{k}}^{\text{SDW}}|^2) & 0 & 2\Delta_{\mathbf{k}}u_{\mathbf{k}}^{\text{SDW}}v_{\mathbf{k}}^{\text{SDW}} \\ \Delta_{\mathbf{k}}(|u_{\mathbf{k}}^{\text{SDW}}|^2 - |v_{\mathbf{k}}^{\text{SDW}}|^2) & -E_{\mathbf{k}}^{(\alpha)} & -2\Delta_{\mathbf{k}}u_{\mathbf{k}}^{\text{SDW}}v_{\mathbf{k}}^{\text{SDW}} & 0 \\ 0 & -2\Delta_{\mathbf{k}}u_{\mathbf{k}}^{\text{SDW}}v_{\mathbf{k}}^{\text{SDW}} & E_{\mathbf{k}}^{(\beta)} & \Delta_{\mathbf{k}}(|u_{\mathbf{k}}^{\text{SDW}}|^2 - |v_{\mathbf{k}}^{\text{SDW}}|^2) \\ 2\Delta_{\mathbf{k}}u_{\mathbf{k}}^{\text{SDW}}v_{\mathbf{k}}^{\text{SDW}} & 0 & \Delta_{\mathbf{k}}(|u_{\mathbf{k}}^{\text{SDW}}|^2 - |v_{\mathbf{k}}^{\text{SDW}}|^2) & -E_{\mathbf{k}}^{(\beta)} \end{pmatrix}$$

which can't be solved beyond calculating the eigenvectors numerically from the equation: $(\hat{\mathcal{H}}'_{\mathbf{k}} - E_{\mathbf{k}}^{(i)}\hat{I})|E_{\mathbf{k}}^{(i)}\rangle = 0$, where $E_{\mathbf{k}}^{(i)} = \pm E_{\mathbf{k}}^{(1;E)}, \pm E_{\mathbf{k}}^{(2;E)}$. However, at both the symmetry and mixing nodes the intraband coupling term, $\Delta_{\mathbf{k}}(|u_{\mathbf{k}}^{\text{SDW}}|^2 - |v_{\mathbf{k}}^{\text{SDW}}|^2)$, goes to zero. This is due

to the fact that $\Delta_{\mathbf{k}} = 0$ at the symmetry nodes, and $|u_{\mathbf{k}}^{\text{SDW}}|^2 = |v_{\mathbf{k}}^{\text{SDW}}|^2 = \frac{1}{2}$ at the mixing nodes, allowing for the eigenvectors to be found analytically at the nodes. This results in the $E_{\mathbf{k}}^{(\beta)}$ and $-E_{\mathbf{k}}^{(\beta)}$ bands not hybridizing, so there is no band avoidance and the nodes survive. This results in the nodal eigenvectors:

$$\begin{aligned}
|E_{\mathbf{k}}^{(1)}\rangle &= u_{\mathbf{k}}^{(E)} |E_{\mathbf{k}}^{(\alpha)}\rangle + v_{\mathbf{k}}^{(E)} |-E_{\mathbf{k}}^{(\beta)}\rangle = (u_{\mathbf{k}}^{(E)} \hat{\alpha}_{\mathbf{k},\sigma}^\dagger + v_{\mathbf{k}}^{(E)} \hat{\beta}_{-\mathbf{k},-\sigma}) |0\rangle \\
|-E_{\mathbf{k}}^{(1)}\rangle &= u_{\mathbf{k}}^{(E)} |-E_{\mathbf{k}}^{(\alpha)}\rangle + v_{\mathbf{k}}^{(E)} |E_{\mathbf{k}}^{(\beta)}\rangle = (u_{\mathbf{k}}^{(E)} \hat{\alpha}_{-\mathbf{k},-\sigma} + v_{\mathbf{k}}^{(E)} \hat{\beta}_{\mathbf{k},\sigma}^\dagger) |0\rangle \\
|E_{\mathbf{k}}^{(2)}\rangle &= -v_{\mathbf{k}}^{(E)} |-E_{\mathbf{k}}^{(\alpha)}\rangle + u_{\mathbf{k}}^{(E)} |E_{\mathbf{k}}^{(\beta)}\rangle = (-v_{\mathbf{k}}^{(E)} \hat{\alpha}_{-\mathbf{k},-\sigma} + u_{\mathbf{k}}^{(E)} \hat{\beta}_{\mathbf{k},\sigma}^\dagger) |0\rangle \\
|-E_{\mathbf{k}}^{(2)}\rangle &= -v_{\mathbf{k}}^{(E)} |E_{\mathbf{k}}^{(\alpha)}\rangle + u_{\mathbf{k}}^{(E)} |-E_{\mathbf{k}}^{(\beta)}\rangle = (-v_{\mathbf{k}}^{(E)} \hat{\alpha}_{\mathbf{k},\sigma}^\dagger + u_{\mathbf{k}}^{(E)} \hat{\beta}_{-\mathbf{k},-\sigma}) |0\rangle
\end{aligned} \tag{2.49}$$

where:

$$u_{\mathbf{k}}^{(E)} = \frac{E_{\mathbf{k}}^{(\alpha)} + E_{\mathbf{k}}^{(\beta)} + \Xi_{\mathbf{k}}}{\sqrt{2\Xi_{\mathbf{k}}(\Xi_{\mathbf{k}} + E_{\mathbf{k}}^{(\alpha)} + E_{\mathbf{k}}^{(\beta)})}} = \sqrt{\frac{1}{2} \left(1 + \frac{E_{\mathbf{k}}^{(\alpha)} + E_{\mathbf{k}}^{(\beta)}}{\Xi_{\mathbf{k}}} \right)} \tag{2.50}$$

$$v_{\mathbf{k}}^{(E)} = \frac{4\Delta_{\mathbf{k}} u_{\mathbf{k}}^{\text{SDW}} v_{\mathbf{k}}^{\text{SDW}}}{\sqrt{2\Xi_{\mathbf{k}}(\Xi_{\mathbf{k}} + E_{\mathbf{k}}^{(\alpha)} + E_{\mathbf{k}}^{(\beta)})}} = \sqrt{\frac{1}{2} \left(1 + \frac{E_{\mathbf{k}}^{(\alpha)} - E_{\mathbf{k}}^{(\beta)}}{\Xi_{\mathbf{k}}} \right)} \tag{2.51}$$

and $\Xi_{\mathbf{k}} = \sqrt{(E_{\mathbf{k}}^{(\alpha)} + E_{\mathbf{k}}^{(\beta)})^2 + (4\Delta_{\mathbf{k}} u_{\mathbf{k}}^{\text{SDW}} v_{\mathbf{k}}^{\text{SDW}})^2}$. While these equations are only exact at the symmetry and mixing nodes, they can be used as an approximation in the vicinity of the nodes where either $\Delta_{\mathbf{k}} \approx 0$ or $|u_{\mathbf{k}}^{\text{SDW}}|^2 \approx |v_{\mathbf{k}}^{\text{SDW}}|^2 \approx \frac{1}{2}$, but in general aren't an accurate description of the eigenvectors.

Δ and M Mean-field Order Parameter Calculation

The mean field order parameters M and Δ can be self-consistently solved for from the Green's function method [34, 35, 44, 45, 60]. This can be obtained from the bare Matsubara

Green's function which can be found from the Dyson equation:

$$\hat{G}_{\mathbf{k}}(\omega_n) = (i\omega_n \hat{I} - \hat{\mathcal{H}}_{\mathbf{k}})^{-1} \quad (2.52)$$

where $\omega_n = 2\pi T(n + 1/2)$ is the Matsubara frequency. The relevant Green's functions for Δ are contained in the diagonal blocks, whereas the relevant Green's functions for M are contained in the off-diagonal blocks. Calculating the relevant Green's functions from the Dyson equation and substituting them into the definitions of the mean-field order parameters Δ and M yields two systems of equations for when the SC gap is odd or even under translations of \mathbf{Q} . When the SC gap is odd under translations of \mathbf{Q} , $1/V_{\text{SC}}$ and $1/V_{\text{SDW}}$ when Δ and M are nonzero can be written as:

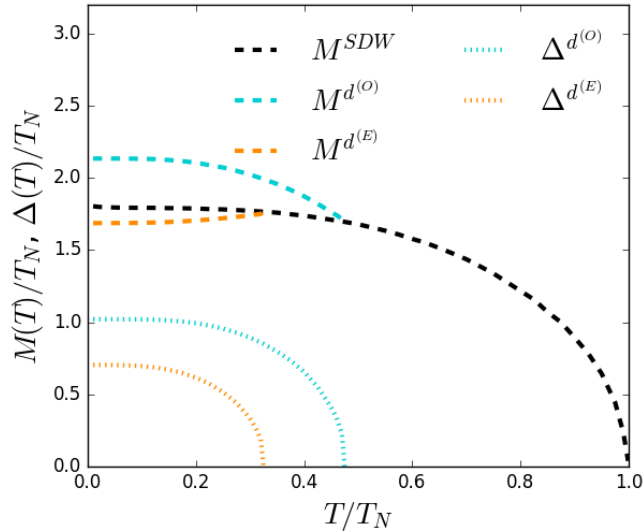


Figure 2.11: Self-consistently calculated M and Δ order parameters in the absence of superconductivity (black), when spin density waves coexist with a d -wave SC gap which is odd under translations of \mathbf{Q} (cyan), and when spin density waves coexist with a d -wave SC gap which is even under translations of \mathbf{Q} (orange).

$$\begin{aligned}
\frac{1}{V_{\text{SC}}} &= T \sum_{\omega_n} \sum_{\mathbf{k}} \frac{\mathcal{Y}_{\mathbf{k}}^2}{D_{\mathbf{k}}^{(O)}(\omega_n)} (\omega_n^2 + (\xi_{\mathbf{k}}^-)^2 + (\xi_{\mathbf{k}}^+)^2 + M^2 + \Delta_{\mathbf{k}}^2) \\
\frac{1}{V_{\text{SDW}}} &= T \sum_{\omega_n} \sum_{\mathbf{k}} \frac{1}{D_{\mathbf{k}}^{(O)}(\omega_n)} (\omega_n^2 + (\xi_{\mathbf{k}}^-)^2 - (\xi_{\mathbf{k}}^+)^2 + M^2 + \Delta_{\mathbf{k}}^2) \\
D_{\mathbf{k}}^{(O)} &= (\omega_n^2 + (\xi_{\mathbf{k}}^-)^2 + (\xi_{\mathbf{k}}^+)^2 + \Delta_{\mathbf{k}}^2 + M^2)^2 - 4(\xi_{\mathbf{k}}^+)^2((\xi_{\mathbf{k}}^-)^2 + M^2) \\
&= \left(\omega_n^2 + (E_{\mathbf{k}}^{(1;O)})^2 \right) \left(\omega_n^2 + (E_{\mathbf{k}}^{(2;O)})^2 \right)
\end{aligned} \tag{2.53}$$

and $1/V_{\text{SC}}$ and $1/V_{\text{SDW}}$ when the SC gap is even under translations of \mathbf{Q} when both Δ and M are nonzero can be written as:

$$\begin{aligned}
\frac{1}{V_{\text{SC}}} &= T \sum_{\omega_n} \sum_{\mathbf{k}} \frac{\mathcal{Y}_{\mathbf{k}}^2}{D_{\mathbf{k}}^{(E)}(\omega_n)} (\omega_n^2 + (\xi_{\mathbf{k}}^-)^2 + (\xi_{\mathbf{k}}^+)^2 - M^2 + \Delta_{\mathbf{k}}^2) \\
\frac{1}{V_{\text{SDW}}} &= T \sum_{\omega_n} \sum_{\mathbf{k}} \frac{1}{D_{\mathbf{k}}^{(E)}(\omega_n)} (\omega_n^2 + (\xi_{\mathbf{k}}^-)^2 - (\xi_{\mathbf{k}}^+)^2 + M^2 - \Delta_{\mathbf{k}}^2) \\
D_{\mathbf{k}}^{(E)} &= (\omega_n^2 + (\xi_{\mathbf{k}}^-)^2 + (\xi_{\mathbf{k}}^+)^2 + \Delta_{\mathbf{k}}^2 + M^2)^2 - 4(\xi_{\mathbf{k}}^+)^2((\xi_{\mathbf{k}}^-)^2 + M^2) - 4M^2\Delta_{\mathbf{k}}^2 \\
&= \left(\omega_n^2 + (E_{\mathbf{k}}^{(1;E)})^2 \right) \left(\omega_n^2 + (E_{\mathbf{k}}^{(2;E)})^2 \right)
\end{aligned} \tag{2.54}$$

where $E_c = 2\pi T(n_c + 1/2)$ and $E_B = 2\pi T(n_B + 1/2)$ are the cutoff energies for the SC and SDW Matsubara sums respectively; $n_c = 30T_N/T$ and $n_B = 175T_N/T$ were used in this work. The natural choice of energy scale for these equations is T_N , since T_c depends on the value of M . In order to self-consistently solve for the order parameters, Δ and M , the SC and SDW interaction potentials can be eliminated by subtracting Equation (2.55) from

Equation (2.53) or Equation (2.54).

$$\begin{aligned} \frac{1}{V_{\text{SC}}} &= T_c^0 \sum_{\omega_n}^{E_c} \frac{\mathcal{Y}_{\mathbf{k}}^2 (\omega_n^2 + (\xi_{\mathbf{k}}^-)^2 + (\xi_{\mathbf{k}}^+)^2)}{(\omega_n^2 + (\xi_{\mathbf{k}}^-)^2 + (\xi_{\mathbf{k}}^+)^2)^2 - 4(\xi_{\mathbf{k}}^- \xi_{\mathbf{k}}^+)^2} \\ \frac{1}{V_{\text{SDW}}} &= T_N \sum_{\omega_n}^{E_B} \frac{(\omega_n^2 + (\xi_{\mathbf{k}}^-)^2 + (\xi_{\mathbf{k}}^+)^2)}{(\omega_n^2 + (\xi_{\mathbf{k}}^-)^2 + (\xi_{\mathbf{k}}^+)^2)^2 - 4(\xi_{\mathbf{k}}^- \xi_{\mathbf{k}}^+)^2} \end{aligned} \quad (2.55)$$

and T_c^0 is the superconducting transition temperature in the absence of spin density waves. In this work $T_c^0 = .35T_N$ was used for both symmetry classes, but the actual superconducting transition temperatures were found to be $T_c^{(O)} = .47T_N$ and $T_c^{(E)} = .32T_N$ from self-consistency. The order parameters Δ and M can be seen as a function of temperature for both the odd and even symmetry classes in FIG. 2.11.

Impurity Scattering

Weak Scattering Limit

The quasiparticle scattering rates in the Born limit can be derived from Fermi's golden rule[47]:

$$w_{\mathbf{k},\mathbf{k}'} = \frac{2\pi}{\hbar} |\langle \mathbf{k}' | H_{\text{imp}} | \mathbf{k} \rangle|^2 \delta(E_{\mathbf{k}} - E_{\mathbf{k}'}) \quad (2.56)$$

where $w_{\mathbf{k},\mathbf{k}'}$ is the rate at which quasiparticles occupying a state $|\mathbf{k}\rangle$ with momentum \mathbf{k} and energy $E_{\mathbf{k}}$ scatter off impurities to a state $|\mathbf{k}'\rangle$ with momentum \mathbf{k}' and energy $E_{\mathbf{k}'}$ and H_{imp} is the impurity Hamiltonian. First, H_{imp} must be projected into the Nambu basis, as this is the basis that the superconducting eigenstates are represented in.

$$H_{\text{imp}} = \sum_{\mathbf{k},\mathbf{k}',\sigma} \hat{a}_{\mathbf{k}',\sigma}^\dagger \hat{a}_{\mathbf{k},\sigma} = V \sum_{\mathbf{k},\mathbf{k}'} \hat{\Psi}_{\mathbf{k}'}^\dagger \hat{\mathcal{H}}_{\mathbf{k}}^{\text{imp}} \hat{\Psi}_{\mathbf{k}} \quad (2.57)$$

where V is the isotropic scattering amplitude and $\hat{\mathcal{H}}_{\mathbf{k}}^{\text{imp}}$ is the impurity Hamiltonian in the Nambu basis and for a SC with a single electron and hole band can be written as:

$$\hat{\mathcal{H}}_{\mathbf{k}}^{\text{imp}} = \begin{pmatrix} 1 & 0 \\ 0 & -1 \end{pmatrix} \quad (2.58)$$

and the impurity Hamiltonian for a system with two electron bands and two hole bands, like the SDW state which has artificially doubled bands, can be written as:

$$\hat{\mathcal{H}}_{\mathbf{k}}^{\text{imp}} = \begin{pmatrix} 1 & 0 & 0 & 0 \\ 0 & -1 & 0 & 0 \\ 0 & 0 & 1 & 0 \\ 0 & 0 & 0 & -1 \end{pmatrix} \quad (2.59)$$

Furthermore, the so-called coherence factor, which is the probability for a quasiparticle occupying a state of momentum \mathbf{k} in the $E_{\mathbf{k}}^{(i)}$ band to scatter off an impurity to a state of momentum \mathbf{k}' in the $E_{\mathbf{k}'}^{(j)}$ band can be written as:

$$|C_{ij}(\mathbf{k}, \mathbf{k}')|^2 = \left| \langle E_{\mathbf{k}'}^{(j)} | \hat{\mathcal{H}}_{\mathbf{k}}^{\text{imp}} | E_{\mathbf{k}}^{(i)} \rangle \right|^2 \quad (2.60)$$

where $E_{\mathbf{k}}^{(i)}$ can represent the normal state electron and hole bands ($\pm\xi_{\mathbf{k}}$), the pure SC quasiparticle and quasihole bands ($\pm E_{\mathbf{k}}^{\text{SC}}$), the pure SDW quasiparticle and quasihole bands ($\pm E_{\mathbf{k}}^{(\alpha)}$, $\pm E_{\mathbf{k}}^{(\beta)}$), the SC + Nematicity coexistence bands ($\pm E_{\mathbf{k}}^{(\text{SC+Nem})}$), or the SC + SDW coexistence bands ($\pm E_{\mathbf{k}}^{(1)}$, $\pm E_{\mathbf{k}}^{(2)}$). Interestingly, due to the fact that the superconducting bands hybridize electron and hole bands, quasiparticles within the Fermi sea don't scatter to states outside of the Fermi sea, which can be seen in Figure 2.12 (a) & (b). This is due to the fact that superconducting quasiparticle states below the Fermi sea are mostly hole-like and quasiparticle states above the Fermi sea are mostly electron-like. The SDW bands are a result of a hybridization of two electron bands, and therefore quasiparticles occupying

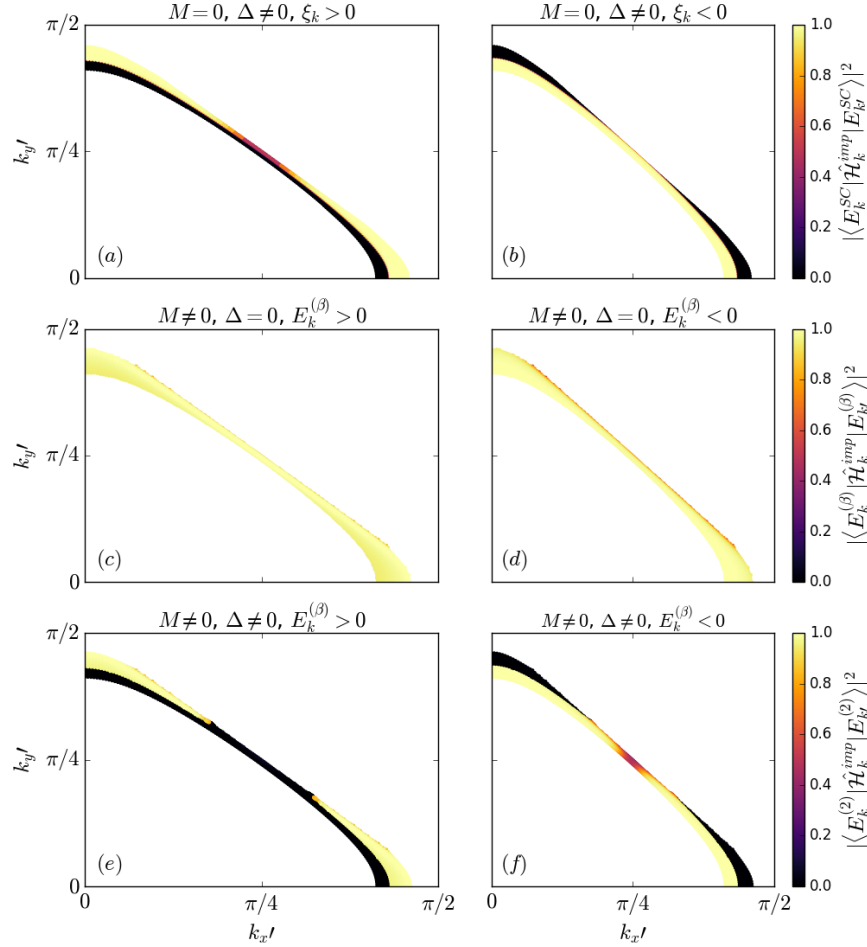


Figure 2.12: Probability for a quasiparticle of momentum \mathbf{k} to scatter to another state in \mathbf{k} -space with momentum \mathbf{k}' . (a) Probability for a quasiparticle occupying a pure d_{xy} SC state where $\xi_{\mathbf{k}} > 0$ to scatter to another pure SC state of momentum \mathbf{k}' near the normal state FS. (b) Probability for a quasiparticle occupying a pure d_{xy} SC state where $\xi_{\mathbf{k}} < 0$ to scatter to another pure SC state of momentum \mathbf{k}' near the normal state FS. (c) Probability for a quasiparticle occupying a pure $\mathbf{Q} = (\pi/2, \pi/2)$ SDW state where $E_{\mathbf{k}}^{\beta} > 0$ to scatter to another pure SDW state of momentum \mathbf{k}' near the reconstructed FS. (d) Probability for a quasiparticle occupying a pure $\mathbf{Q} = (\pi/2, \pi/2)$ SDW state where $E_{\mathbf{k}}^{\beta} < 0$ to scatter to another pure SDW state of momentum \mathbf{k}' near the reconstructed FS. (e) Probability for a quasiparticle occupying a coexistence $\mathbf{Q} = (\pi/2, \pi/2)$ SDW + d_{xy} SC state where $E_{\mathbf{k}}^{\beta} > 0$ to scatter to another pure SDW state of momentum \mathbf{k}' near the reconstructed FS. (f) Probability for a quasiparticle occupying a coexistence $\mathbf{Q} = (\pi/2, \pi/2)$ SDW + d_{xy} SC state where $E_{\mathbf{k}}^{\beta} < 0$ to scatter to another coexistence state of momentum \mathbf{k}' near the reconstructed FS.

states within the Fermi sea are able to scatter to states above the Fermi sea with nearly unit probability, which can be seen in Figure 2.12 (c) & (d). This is one of the reasons why the SDW state is considered a metallic state. Additionally, the coexistence state hybridizes the SDW quasiparticle and quasihole bands similar to the way pure superconductivity hybridizes electron and hole bands. This is why coexistence quasiparticles occupying states within the Fermi sea can't scatter to states above the Fermi sea, which can be seen in Figure 2.12 (e) & (f). In the case of pure superconductivity, and SC + Nematicity, and pure SDW analytic solutions to the coherence factor are known. The coherence factor in the case of pure SC is:

$$|C_{ij}^{\text{SC}}(\mathbf{k}, \mathbf{k}')|^2 = \frac{\delta_{ij}}{2} \left(1 + \frac{\xi_{\mathbf{k}} \xi_{\mathbf{k}'} - \Delta_{\mathbf{k}} \Delta_{\mathbf{k}'}}{E_{\mathbf{k}}^{\text{SC}} E_{\mathbf{k}'}^{\text{SC}}} \right) \quad (2.61)$$

Similarly, the SC + Nematicity coexistence state has effectively the same coherence factor, due to being a superconducting state with an electronic state modified by nematicity:

$$|C_{ij}^{\text{SC+Nem}}(\mathbf{k}, \mathbf{k}')|^2 = \frac{\delta_{ij}}{2} \left(1 + \frac{\tilde{\xi}_{\mathbf{k}} \tilde{\xi}_{\mathbf{k}'} - \Delta_{\mathbf{k}} \Delta_{\mathbf{k}'}}{E_{\mathbf{k}}^{(\text{SC+Nem})} E_{\mathbf{k}'}^{(\text{SC+Nem})}} \right) \quad (2.62)$$

where it can be seen that the interband coherence factors for these superconducting states will always be zero, while the intraband coherence factors can be nonzero. The SDW state is different however, as both the interband and intraband coherence factors can be nonzero. While some coherence factors can be found analytically, the SC + SDW coexistence coherence factors are difficult to obtain and have been calculated numerically within this work. Now that the coherence factors are known either analytically or numerically, Fermi's golden rule can finally be used to find the rate at which particles scatter from one state to another off of impurities. Fermi's golden rule can be rewritten in the Nambu basis as:

$$w_{\mathbf{k}, \mathbf{k}'} = \frac{2\pi}{\hbar} V^2 |C_{ij}(\mathbf{k}, \mathbf{k}')|^2 \delta(E_{\mathbf{k}}^{(i)} - E_{\mathbf{k}'}^{(j)}) \quad (2.63)$$

From Fermi's golden rule, which is merely the rate at which quasiparticles scatter off a single impurity to one state of momentum \mathbf{k}' , one can multiply by the density of impurities (N_{imp}) and integrate over all possible \mathbf{k}' states that can be scattered to in order to obtain the quasiparticle scattering rate:

$$\tau_{ij}^{-1}(\mathbf{k}) = N_{\text{imp}} V^2 \frac{2\pi}{\hbar} \int \frac{d^2 k'}{(2\pi)^2} |C_{ij}(\mathbf{k}, \mathbf{k}')|^2 \delta(E_{\mathbf{k}}^{(i)} - E_{\mathbf{k}'}^{(j)}) \quad (2.64)$$

where the unknown $N_{\text{imp}} V^2$ can be eliminated in favor of the normal state quasiparticle relaxation times; $\tau_n^{-1} = N_{\text{imp}} V^2 \frac{2\pi}{\hbar} N_F$ where N_F is the density of states at the Fermi level in the normal state. The interband quasiparticle scattering rates in the SC + Nematic state specifically can be reduced to:

$$\tau_{\text{SC+Nem}}^{-1}(\mathbf{k}) = \frac{2\pi}{\hbar} N_{\text{imp}} V^2 \int_{-\infty}^{\infty} d\tilde{\xi}_{\mathbf{k}'} \int \frac{dk_l}{|\mathbf{v}_F|} |C_{11}^{(\text{SC+Nem})}(\mathbf{k}, \mathbf{k}')|^2 \delta(E_{\mathbf{k}'}^{(\text{SC+Nem})} - E_{\mathbf{k}}^{(\text{SC+Nem})}) \quad (2.65)$$

where the $\tilde{\xi}_{\mathbf{k}} \tilde{\xi}_{\mathbf{k}'}$ term in the coherence factor will integrate to 0 by symmetry and can be neglected. The δ -function in terms of $E_{\mathbf{k}}^{(\text{SC+Nem})}$ can be rewritten in terms of $\tilde{\xi}_{\mathbf{k}}$ by defining $f(\tilde{\xi}_{\mathbf{k}'}) = E_{\mathbf{k}}^{(\text{SC+Nem})} - \sqrt{\tilde{\xi}_{\mathbf{k}'}^2 + \Delta_{\mathbf{k}'}^2}$ and using the equation:

$$\delta\left(E_{\mathbf{k}}^{(\text{SC+Nem})} - \sqrt{\tilde{\xi}_{\mathbf{k}'}^2 + \Delta_{\mathbf{k}'}^2}\right) = \sum_{\tilde{\xi}_{\mathbf{k}',0}} \left| \frac{\partial f(\tilde{\xi}_{\mathbf{k}'})}{\partial \tilde{\xi}_{\mathbf{k}'}} \right|_{\tilde{\xi}_{\mathbf{k}',0}}^{-1} \delta\left(\tilde{\xi}_{\mathbf{k}'} - \tilde{\xi}_{\mathbf{k}',0}\right) \quad (2.66)$$

where $\tilde{\xi}_{\mathbf{k}',0}$ can be found by setting $f(\tilde{\xi}_{\mathbf{k}'}) = 0$ and results in two solutions $\tilde{\xi}_{\mathbf{k}',0}^{\pm} = \pm \sqrt{(E_{\mathbf{k}}^{(\text{SC+Nem})})^2 - \Delta_{\mathbf{k}'}^2}$. From this, it can be shown that:

$$\sum_{\tilde{\xi}_{\mathbf{k}',0}} \left| \frac{\partial f(\tilde{\xi}_{\mathbf{k}'})}{\partial \tilde{\xi}_{\mathbf{k}'}} \right|_{\tilde{\xi}_{\mathbf{k}',0}}^{-1} = 2 \frac{\sqrt{(E_{\mathbf{k}}^{(\text{SC+Nem})})^2 - \Delta_{\mathbf{k}'}^2}}{E_{\mathbf{k}}^{(\text{SC+Nem})}} \quad (2.67)$$

Furthermore, using this and integrating the δ -function, it can be shown that:

$$\tau_{\text{SC+Nem}}^{-1} = \frac{2\pi}{\hbar} N_{\text{imp}} V^2 \int \frac{dk_l}{|\mathbf{v}_F|} \left(\frac{E_{\mathbf{k}}^{(\text{SC+Nem})}}{\sqrt{(E_{\mathbf{k}}^{(\text{SC+Nem})})^2 + \Delta_{\mathbf{k}'}^2}} - \frac{\Delta_{\mathbf{k}}}{E_{\mathbf{k}}^{(\text{SC+Nem})}} \frac{\Delta_{\mathbf{k}'}}{\sqrt{(E_{\mathbf{k}}^{(\text{SC+Nem})})^2 + \Delta_{\mathbf{k}'}^2}} \right) \quad (2.68)$$

which can be further simplified by defining the normal and anomalous quasiparticle self-energies for nematic superconductors respectively as:

$$\begin{aligned} g(E_{\mathbf{k}}^{(\text{SC+Nem})}) &= -\frac{i}{\tilde{N}_F} \sum_{\mathbf{k}'} \frac{E_{\mathbf{k}}^{(\text{SC+Nem})}}{(E_{\mathbf{k}}^{(\text{SC+Nem})})^2 - (E_{\mathbf{k}'}^{(\text{SC+Nem})})^2} \\ h(E_{\mathbf{k}}^{(\text{SC+Nem})}) &= -\frac{i}{\tilde{N}_F} \sum_{\mathbf{k}'} \frac{\Delta_{\mathbf{k}}}{(E_{\mathbf{k}}^{(\text{SC+Nem})})^2 - (E_{\mathbf{k}'}^{(\text{SC+Nem})})^2} \end{aligned} \quad (2.69)$$

this simplifies the quasiparticle scattering rate equation to:

$$\tau_{\text{SC+Nem}}^{-1} = \tau_{\text{NF}}^{-1} \left(\text{Re}(g(E_{\mathbf{k}}^{(\text{SC+Nem})})) - \frac{\Delta_{\mathbf{k}}}{E_{\mathbf{k}}^{(\text{SC+Nem})}} \text{Re}(h(E_{\mathbf{k}}^{(\text{SC+Nem})})) \right) \quad (2.70)$$

where τ_{NF}^{-1} is the quasiparticle scattering rate at the Fermi level in the nematic state, and is defined by $\tau_{\text{NF}}^{-1} = \frac{2\pi}{\hbar} N_{\text{imp}} V^2 \tilde{N}_F$ and \tilde{N}_F is the DOS at the Fermi level in the nematic state.

Strong Scattering Limit

In the strong scattering limit, more than a single interaction between an impurity and the quasiparticles need to be considered for the probability for a quasiparticle to scatter between a state with momentum \mathbf{k} and \mathbf{k}' . In order to account for this, the scattering potential \hat{T} needs to be calculated from[1] the Lippmann-Schwinger equation:

$$\hat{T} = \hat{\mathcal{H}}_{\mathbf{k}}^{\text{imp}} + \hat{\mathcal{H}}_{\mathbf{k}}^{\text{imp}} \sum_{\mathbf{k}'} \hat{G}_{\mathbf{k}'}(E_{\mathbf{k}}) \hat{T} \quad (2.71)$$

where $\hat{\mathcal{H}}_{\mathbf{k}}^{\text{imp}} = V\hat{\tau}_3$ is the impurity potential for scattering off a single impurity (and was

solely used as the impurity potential in the Born limit), $\hat{\tau}_3$ is the Pauli matrix, and $\hat{G}_{\mathbf{k}}(E)$ is the single-particle Green's function in the absence of impurities, defined by[52]:

$$\hat{G}_{\mathbf{k}'}(E_{\mathbf{k}}) = \frac{1}{E_{\mathbf{k}}^2 - E_{\mathbf{k}'}^2} \begin{pmatrix} E_{\mathbf{k}} + \tilde{\xi}_{\mathbf{k}'} & -\Delta_{\mathbf{k}'} \\ -\Delta_{\mathbf{k}'} & E_{\mathbf{k}} - \tilde{\xi}_{\mathbf{k}'} \end{pmatrix} \rightarrow \sum_{\mathbf{k}'} \hat{G}_{\mathbf{k}'}(E_{\mathbf{k}}) = -i\tilde{N}_F \begin{pmatrix} g(E_{\mathbf{k}}) & -h(E_{\mathbf{k}}) \\ -h(E_{\mathbf{k}}) & g(E_{\mathbf{k}}) \end{pmatrix} \quad (2.72)$$

In general, this can be calculated for a normal state electron dispersion ($\xi_{\mathbf{k}}$), but in this work was only calculated for a nematic electron dispersion ($\tilde{\xi}_{\mathbf{k}}$). From this it can be shown that the T -matrix is of the form:

$$\hat{T} = \frac{V\hat{\tau}_3 + iV^2\tilde{N}_F(g(E_{\mathbf{k}})\hat{I}_{2x2} + h(E_{\mathbf{k}})\hat{\tau}_1)}{1 + V^2\tilde{N}_F^2(|g(E_{\mathbf{k}})|^2 - |h(E_{\mathbf{k}})|^2)} \quad (2.73)$$

which can be reduced in the Unitary limit, using the approximation that $V\tilde{N}_F \gg 1$, to the simpler form:

$$\hat{T} = \frac{i(g(E_{\mathbf{k}})\hat{I}_{2x2} + h(E_{\mathbf{k}})\hat{\tau}_1)}{\tilde{N}_F(|g(E_{\mathbf{k}})|^2 - |h(E_{\mathbf{k}})|^2)} \quad (2.74)$$

It should be noted that the Born limit can be recovered from this equation with the approximation that $V\tilde{N}_F \ll 1$ in the weak impurity scattering limit. In order to derive the scattering probability from a state with momentum \mathbf{k} to a state \mathbf{k}' in the unitary limit for the nematic state coexisting with superconductivity, $|t_{\mathbf{k},\mathbf{k}'}|^2 = \left| \langle E_{\mathbf{k}}^{(\text{SC+Nem})} | \hat{T} | E_{\mathbf{k}'}^{(\text{SC+Nem})} \rangle \right|^2$ must be found.

$$\begin{aligned} |t_{\mathbf{k},\mathbf{k}'}|^2 = & \frac{1}{2\tilde{N}_F^2} \left[a \left(1 + \frac{\Delta_{\mathbf{k}}\Delta_{\mathbf{k}'}}{E_{\mathbf{k}}^{(\text{SC+Nem})}E_{\mathbf{k}'}^{(\text{SC+Nem})}} \right) \right. \\ & \left. + b \frac{\tilde{\xi}_{\mathbf{k}}\tilde{\xi}_{\mathbf{k}'}}{E_{\mathbf{k}}^{(\text{SC+Nem})}E_{\mathbf{k}'}^{(\text{SC+Nem})}} + 2c \left(\frac{\Delta_{\mathbf{k}}}{E_{\mathbf{k}}^{(\text{SC+Nem})}} + \frac{\Delta_{\mathbf{k}'}}{E_{\mathbf{k}'}^{(\text{SC+Nem})}} \right) \right] \end{aligned} \quad (2.75)$$

where

$$a = \frac{\left|g(E_{\mathbf{k}}^{(\text{SC+Nem})})\right|^2 + \left|h(E_{\mathbf{k}}^{(\text{SC+Nem})})\right|^2}{\left(\left|g(E_{\mathbf{k}}^{(\text{SC+Nem})})\right|^2 - \left|h(E_{\mathbf{k}}^{(\text{SC+Nem})})\right|^2\right)^2} \quad (2.76)$$

$$b = \frac{\left|g(E_{\mathbf{k}}^{(\text{SC+Nem})})\right|^2 - \left|h(E_{\mathbf{k}}^{(\text{SC+Nem})})\right|^2}{\left(\left|g(E_{\mathbf{k}}^{(\text{SC+Nem})})\right|^2 - \left|h(E_{\mathbf{k}}^{(\text{SC+Nem})})\right|^2\right)^2} \quad (2.77)$$

$$c = \frac{\text{Re}\left(g(E_{\mathbf{k}}^{(\text{SC+Nem})})h^*(E_{\mathbf{k}}^{(\text{SC+Nem})})\right)}{\left(\left|g(E_{\mathbf{k}}^{(\text{SC+Nem})})\right|^2 - \left|h(E_{\mathbf{k}}^{(\text{SC+Nem})})\right|^2\right)^2} \quad (2.78)$$

The quasiparticle scattering rates in the Unitary limit can also be derived from Fermi's Golden Rule, but with the impurity potential \hat{T} instead of $\hat{\mathcal{H}}_{\mathbf{k}}^{\text{imp}}$, this results in the equation:

$$\tau_{\text{SC+Nem}}^{-1}(\mathbf{k}) = \frac{2\pi}{\hbar} N_{\text{imp}} \int_{-\infty}^{\infty} d\tilde{\xi}_{\mathbf{k}'} \int \frac{dk_l}{|\mathbf{v}_F|} |t_{\mathbf{k},\mathbf{k}'}|^2 \delta(E_{\mathbf{k}'}^{(\text{SC+Nem})} - E_{\mathbf{k}}^{(\text{SC+Nem})}) \quad (2.79)$$

where the $\tilde{\xi}_{\mathbf{k}}\tilde{\xi}_{\mathbf{k}'}$ term again integrates to 0 by symmetry. The δ -function can again be rewritten in terms of $\tilde{\xi}_{\mathbf{k}'}$ instead of $E_{\mathbf{k}'}^{(\text{SC+Nem})}$ and integrated out in order to come to the equation:

$$\begin{aligned} \tau_{\text{SC+Nem}}^{-1} = \frac{2\pi}{\hbar} \frac{N_{\text{imp}}}{\tilde{N}_F^2} \int \frac{dk_l}{|\mathbf{v}_F|} \left[a \left(\frac{E_{\mathbf{k}}^{(\text{SC+Nem})}}{\sqrt{(E_{\mathbf{k}}^{(\text{SC+Nem})})^2 + \Delta_{\mathbf{k}'}^2}} + \frac{\Delta_{\mathbf{k}}}{E_{\mathbf{k}}^{(\text{SC+Nem})}} \frac{\Delta_{\mathbf{k}'}}{\sqrt{(E_{\mathbf{k}}^{(\text{SC+Nem})})^2 + \Delta_{\mathbf{k}'}^2}} \right) \right. \\ \left. + 2c \left(\frac{\Delta_{\mathbf{k}}}{E_{\mathbf{k}}^{(\text{SC+Nem})}} \frac{E_{\mathbf{k}}^{(\text{SC+Nem})}}{\sqrt{(E_{\mathbf{k}}^{(\text{SC+Nem})})^2 + \Delta_{\mathbf{k}'}^2}} + \frac{\Delta_{\mathbf{k}'}}{\sqrt{(E_{\mathbf{k}}^{(\text{SC+Nem})})^2 + \Delta_{\mathbf{k}'}^2}} \right) \right] \end{aligned} \quad (2.80)$$

and can be rewritten in terms of the normal, $g(E_{\mathbf{k}})$, and anomalous, $h(E_{\mathbf{k}})$, self-energies.

$$\begin{aligned} \tau_{\text{SC+Nem}}^{-1} = \tau_{\text{NF}}^{-1} & \left(a \left[\text{Re}(g(E_{\mathbf{k}}^{(\text{SC+Nem})})) + \frac{\Delta_{\mathbf{k}}}{E_{\mathbf{k}}^{(\text{SC+Nem})}} \text{Re}(h(E_{\mathbf{k}}^{(\text{SC+Nem})})) \right] \right. \\ & \left. + 2c \left[\frac{\Delta_{\mathbf{k}}}{E_{\mathbf{k}}^{(\text{SC+Nem})}} \text{Re}(g(E_{\mathbf{k}}^{(\text{SC+Nem})})) + \text{Re}(h(E_{\mathbf{k}}^{(\text{SC+Nem})})) \right] \right) \end{aligned} \quad (2.81)$$

where τ_{NF}^{-1} is the quasiparticle scattering rate of the nematic state in the Unitary limit here and is defined as $\tau_{\text{NF}}^{-1} = \frac{2\pi}{\hbar} N_{\text{imp}} / \tilde{N}_F$. The normal and anomalous self-energies can be defined[47] as:

$$\begin{aligned} g(E_{\mathbf{k}}) &= -\frac{i}{\tilde{N}_F} \sum_{\mathbf{k}'} \frac{E_{\mathbf{k}}}{E_{\mathbf{k}}^2 - E_{\mathbf{k}'}^2} \\ h(E_{\mathbf{k}}) &= -\frac{i}{\tilde{N}_F} \sum_{\mathbf{k}'} \frac{\Delta_{\mathbf{k}'}}{E_{\mathbf{k}}^2 - E_{\mathbf{k}'}^2} \end{aligned} \quad (2.82)$$

These self-energies can be rewritten as complex integrals over \mathbf{k}' -space:

$$\begin{aligned} g(E_{\mathbf{k}}) &= -\frac{i}{\tilde{N}_F} \int \frac{dk'_l}{|\mathbf{v}_F|} \int d\xi_{\mathbf{k}'} \frac{E_{\mathbf{k}}}{E_{\mathbf{k}}^2 - E_{\mathbf{k}'}^2} \\ h(E_{\mathbf{k}}) &= -\frac{i}{\tilde{N}_F} \int \frac{dk'_l}{|\mathbf{v}_F|} \int d\xi_{\mathbf{k}'} \frac{\Delta_{\mathbf{k}'}}{E_{\mathbf{k}}^2 - E_{\mathbf{k}'}^2} \end{aligned} \quad (2.83)$$

which can be simplified with the residue theorem. In order to do this, they must first be rewritten to reveal where their poles are:

$$\begin{aligned} g(E_{\mathbf{k}}) &= -\frac{i}{\tilde{N}_F} \int \frac{dk'_l}{|\mathbf{v}_F|} \int d\xi_{\mathbf{k}'} \frac{E_{\mathbf{k}}}{(\xi_{\mathbf{k}'} + \Phi f_{\mathbf{k}'} + \sqrt{E_{\mathbf{k}} - \Delta_{\mathbf{k}'}})(\xi_{\mathbf{k}'} + \Phi f_{\mathbf{k}'} - \sqrt{E_{\mathbf{k}} - \Delta_{\mathbf{k}'}})} \\ h(E_{\mathbf{k}}) &= -\frac{i}{\tilde{N}_F} \int \frac{dk'_l}{|\mathbf{v}_F|} \int d\xi_{\mathbf{k}'} \frac{\Delta_{\mathbf{k}'}}{(\xi_{\mathbf{k}'} + \Phi f_{\mathbf{k}'} + \sqrt{E_{\mathbf{k}} - \Delta_{\mathbf{k}'}})(\xi_{\mathbf{k}'} + \Phi f_{\mathbf{k}'} - \sqrt{E_{\mathbf{k}} - \Delta_{\mathbf{k}'}})} \end{aligned} \quad (2.84)$$

which have the poles: $\xi_{\mathbf{k}'}^{\pm} = -\Phi f_{\mathbf{k}} \pm \sqrt{E_{\mathbf{k}}^2 - \Delta_{\mathbf{k}'}^2}$. In order to apply residue theorem to these integrals, the function $f(\xi_{\mathbf{k}'})$ can be defined:

$$f(\xi_{\mathbf{k}'}) = \frac{1}{(\xi_{\mathbf{k}'} + 2\Phi f_{\mathbf{k}'} + \xi_{\mathbf{k}'}^+) (\xi_{\mathbf{k}'} + 2\Phi f_{\mathbf{k}'} + \xi_{\mathbf{k}'}^-)} \quad (2.85)$$

which has the residue:

$$\text{Res}\{f(\xi_{\mathbf{k}'})\}_{\xi_{\mathbf{k}'}=\xi_{\mathbf{k}'}^+} = \text{Res}\{f(\xi_{\mathbf{k}'})\}_{\xi_{\mathbf{k}'}=\xi_{\mathbf{k}'}^-} = \frac{1}{2\sqrt{E_{\mathbf{k}}^2 - \Delta_{\mathbf{k}'}^2}} \quad (2.86)$$

This simplifies the equations for the normal and anomalous self-energies to:

$$\begin{aligned} g(E_{\mathbf{k}}) &= \frac{1}{\tilde{N}_F} \int \frac{dk'_l}{|\mathbf{v}_F|} \frac{E_{\mathbf{k}}}{\sqrt{E_{\mathbf{k}}^2 - \Delta_{\mathbf{k}'}^2}} \\ h(E_{\mathbf{k}}) &= \frac{1}{\tilde{N}_F} \int \frac{dk'_l}{|\mathbf{v}_F|} \frac{\Delta_{\mathbf{k}'}}{\sqrt{E_{\mathbf{k}}^2 - \Delta_{\mathbf{k}'}^2}} \end{aligned} \quad (2.87)$$

Interestingly, $\text{Re}\{g(E_{\mathbf{k}})\}$ is the DOS of the superconducting state normalized by \tilde{N}_F . Additionally, as $T \rightarrow 0$, the nematic order parameter goes to zero ($\Phi \rightarrow 0$) and \tilde{N}_F goes to N_F , the DOS on the normal state FS. Additionally, as $T \rightarrow T_c$ and $\Delta \rightarrow 0$, $g(E_{\mathbf{k}}) \rightarrow 1$ and $h(E_{\mathbf{k}}) \rightarrow 0$.

Boltzmann Thermal Conductivity

The thermal flux, Φ_q , through a surface can be written in terms of the negative temperature gradient across a material and the thermal conductivity tensor, κ :

$$\Phi_q = -\kappa \nabla T \quad (2.88)$$

The thermal flux carried by non-equilibrium excitations is given by[47]:

$$\Phi_q(\mathbf{r}) = 2 \int \frac{d^2k}{(2\pi)^2} E_{\mathbf{k}}(\mathbf{r}) \mathbf{v}_{\mathbf{k}}(\mathbf{r}) f_{\mathbf{k}}(\mathbf{r}) \quad (2.89)$$

where $E_{\mathbf{k}}$ is the quasiparticle excitation energy, $\mathbf{v}_{\mathbf{k}}$ is the quasiparticle velocity, and $f_{\mathbf{k}}$ is the non-equilibrium distribution function for quasiparticles interacting with impurities. The distribution function satisfies the Boltzmann kinetic equation:

$$\frac{\partial f_{\mathbf{k}}}{\partial t} + \nabla_{\mathbf{k}} E_{\mathbf{k}} \cdot \nabla f_{\mathbf{k}} - \nabla E_{\mathbf{k}} \cdot \nabla_{\mathbf{k}} f_{\mathbf{k}} = \left(\frac{\partial f_{\mathbf{k}}}{\partial t} \right)_{\text{imp}} \quad (2.90)$$

where $\left(\frac{\partial f_{\mathbf{k}}}{\partial t} \right)_{\text{imp}}$ is the collision integral due to impurities. The kinetic equation can be simplified in the case of a stationary thermal flow and a distribution function close to the equilibrium distribution function. The non-equilibrium distribution function can be approximated as a linear perturbation from the equilibrium Fermi-Dirac distribution $f_{\mathbf{k}} \approx f_{\mathbf{k}}^{(0)} + \delta f_{\mathbf{k}}$. The collision integral vanishes for the equilibrium distribution function, and the small, linear non-equilibrium distribution term can be neglected on the left side of the Boltzmann kinetic equation (therefore $\frac{\partial f_{\mathbf{k}}}{\partial t} = \frac{\partial f_{\mathbf{k}}^{(0)}}{\partial t} = 0$). The Boltzmann kinetic equation can be further simplified by rewriting the second and third terms as:

$$\begin{aligned} \nabla_{\mathbf{k}} E_{\mathbf{k}} \cdot \nabla f_{\mathbf{k}}^{(0)} - \nabla E_{\mathbf{k}} \cdot \nabla_{\mathbf{k}} f_{\mathbf{k}}^{(0)} &= \nabla_{\mathbf{k}} E_{\mathbf{k}} \cdot \frac{\partial f_{\mathbf{k}}^{(0)}}{\partial E_{\mathbf{k}}} T \left(\frac{1}{T} \nabla E_{\mathbf{k}} - \frac{E_{\mathbf{k}}}{T^2} \nabla T \right) - \nabla E_{\mathbf{k}} \cdot \frac{\partial f_{\mathbf{k}}^{(0)}}{\partial E_{\mathbf{k}}} \nabla_{\mathbf{k}} E_{\mathbf{k}} \\ &= -\frac{E_{\mathbf{k}}}{T} \frac{\partial f_{\mathbf{k}}^{(0)}}{\partial E_{\mathbf{k}}} \nabla_{\mathbf{k}} E_{\mathbf{k}} \cdot \nabla T \end{aligned} \quad (2.91)$$

In the case of weak disorder, the collision integral can be found by multiplying the contribution of a single impurity by the concentration of impurities:

$$\left(\frac{\partial f_{\mathbf{k}}}{\partial t} \right)_{\text{imp}} = N_{\text{imp}} \int \frac{d^2k'}{(2\pi)^2} w_{\mathbf{k},\mathbf{k}'} (\delta f_{\mathbf{k}'} - \delta f_{\mathbf{k}}) \quad (2.92)$$

where $w_{\mathbf{k},\mathbf{k}'}$ is again the quasiparticle scattering rate from the state with momentum \mathbf{k} to the state with momentum \mathbf{k}' and can be found from Fermi's Golden Rule. Substituting these back into the Boltzmann kinetic equation, we get:

$$\begin{aligned}\tau_{\mathbf{k}}^{-1}\delta f_{\mathbf{k}} - N_{\text{imp}} \int \frac{d^2k'}{(2\pi)^2} w_{\mathbf{k},\mathbf{k}'} \delta f_{\mathbf{k}'} &= \frac{E_{\mathbf{k}}}{T} \frac{\partial f_{\mathbf{k}}^{(0)}}{\partial E_{\mathbf{k}}} \nabla_{\mathbf{k}} E_{\mathbf{k}} \cdot \nabla T \\ \delta f_{\mathbf{k}} &= \tau_{\mathbf{k}} N_{\text{imp}} \int \frac{d^2k'}{(2\pi)^2} w_{\mathbf{k},\mathbf{k}'} \delta f_{\mathbf{k}'} + \tau_{\mathbf{k}} E_{\mathbf{k}} \frac{\partial f_{\mathbf{k}}^{(0)}}{\partial E_{\mathbf{k}}} \mathbf{v}_{\mathbf{k}} \cdot \frac{\nabla T}{T}\end{aligned}\tag{2.93}$$

where $\tau_{\mathbf{k}}^{-1} = N_{\text{imp}} \int \frac{d^2k'}{(2\pi)^2} w_{\mathbf{k},\mathbf{k}'}$ is the quasiparticle scattering rate off impurities and $\mathbf{v}_{\mathbf{k}} = \nabla_{\mathbf{k}} E_{\mathbf{k}}$ is the quasiparticle velocity. The quasiparticle scattering rate ($w(\mathbf{k},\mathbf{k}')$) is invariant under particle-hole exchange ($\xi_{\mathbf{k}} \rightarrow -\xi_{\mathbf{k}}$) while the deviation from the Fermi-Dirac distribution ($\delta f_{\mathbf{k}}$) and the quasiparticle velocity are odd under particle-hole exchange, therefore the $\tau_{\mathbf{k}} N_{\text{imp}} \int \frac{d^2k'}{(2\pi)^2} w_{\mathbf{k},\mathbf{k}'} \delta f_{\mathbf{k}'}$ term must go to 0, therefore:

$$\delta f_{\mathbf{k}} = \tau_{\mathbf{k}} E_{\mathbf{k}} \frac{\partial f_{\mathbf{k}}^{(0)}}{\partial E} \mathbf{v}_{\mathbf{k}} \cdot \frac{\nabla T}{T}\tag{2.94}$$

Knowing how the quasiparticle distribution function deviates from the Fermi-Dirac distribution is crucial to understanding the thermal flux, as this is the only nonzero term:

$$\Phi_q = 2 \int \frac{d^2k'}{(2\pi)^2} E_{\mathbf{k}} \mathbf{v}_{\mathbf{k}} \delta f_{\mathbf{k}}\tag{2.95}$$

Performing this substitution results in the following equation:

$$(\Phi_q)_i = 2 \frac{(\nabla T)_j}{T} \int \frac{d^2k}{(2\pi)^2} \frac{\partial f_{\mathbf{k}}^{(0)}}{\partial E} E_{\mathbf{k}}^2 (\mathbf{v}_{\mathbf{k}})_i (\mathbf{v}_{\mathbf{k}})_j \tau_{\mathbf{k}}\tag{2.96}$$

which can be used to determine the thermal conductivity tensor from the equation $\Phi_q = -\kappa \nabla T$:

$$(\Phi_q)_i = -\kappa_{ij}(\nabla T)_j \rightarrow \kappa_{ij} = -\frac{2}{T} \int \frac{d^2k}{(2\pi)^2} \frac{\partial f_{\mathbf{k}}^{(0)}}{\partial E} E_{\mathbf{k}}^2 (\mathbf{v}_{\mathbf{k}})_i (\mathbf{v}_{\mathbf{k}})_j \tau_{\mathbf{k}} \quad (2.97)$$

NUMERICAL METHODS

k-space Integration Grids

The electronic thermal conductivity derived within Boltzmann kinetic theory written as:

$$\kappa_{ij} = -\frac{2}{T} \sum_{n=1}^2 \int \frac{d^2k}{(2\pi)^2} (E_{\mathbf{k}}^{(n)})^2 (\mathbf{v}_{\mathbf{k}}^{(n)})_i (\mathbf{v}_{\mathbf{k}}^{(n)})_j \frac{\partial f_{\mathbf{k}}^0}{\partial E} (\tau_{n1}^{-1} + \tau_{n2}^{-1})^{-1} \quad (3.1)$$

calculated numerically would seem to imply that a simple Cartesian integration grid was utilized in which boxes are created in (k_x, k_y) -space and the integrand of κ_{ij} is evaluated within each of these boxes then summed up to evaluate the integral via a simple Riemann sum. While this approach will converge with dense enough integration grids, its use is computationally expensive and becomes unviable as $T \rightarrow 0$ and thermal transport becomes increasingly dominated by low-energy quasiparticles which occupy isolated pockets in \mathbf{k} -space. This can be mitigated by implementing a cutoff quasiparticle energy, E_c , above which points in \mathbf{k} -space are simply discarded and their contribution to the κ_{ij} integral in Equation (3.1) is approximated to be zero. This is an accurate approximation due to the $\frac{\partial f_{\mathbf{k}}^0}{\partial E}$ in the integrand, which is the energy derivative of the equilibrium Fermi-Dirac distribution, $f_{\mathbf{k}}^0 = \frac{1}{1+e^{E_{\mathbf{k}}/T}}$, so the energy derivative of this function is:

$$\frac{\partial f_{\mathbf{k}}^0}{\partial E} = -\frac{1}{4T} \frac{1}{\cosh^2(E_{\mathbf{k}}/2T)}. \quad (3.2)$$

This behaves similarly to a Gaussian function centered at the Fermi energy ($E_{\mathbf{k}} = 0$) whose width decreases with T . Ultimately as $T \rightarrow 0$ this function becomes a δ -function at the Fermi energy. This is intuitive because the Fermi-Dirac distribution becomes a Heaviside function where states are occupied below the Fermi level and unoccupied above it when $T \rightarrow 0$, and the energy derivative of that is a δ -function centered at the Fermi energy.

This method of calculating Equation (3.1) with a Cartesian Riemann sum in \mathbf{k} -space and removing any \mathbf{k} -points with quasiparticle energies over some carefully considered E_c has been shown[60] to produce good results, however these come at a considerable computational cost requiring the use of the Nautilus supercomputer cluster and only accurately calculate Equation (3.1) down to $T = .05T_N$ (here T_N is the Néel temperature and is equivalent to the SDW transition temperature T_{SDW}). It can be seen that the function $\frac{\partial f_{\mathbf{k}}^0}{\partial E}$ when $\xi_{\mathbf{k}} < E_c$ is poorly captured by a (k_x, k_y) -grid as described above. This calculation can be improved by more carefully choosing the integration grid based on polar coordinates $(\theta_{\mathbf{k}})$ in \mathbf{k} -space and curves of constant quasiparticle energy, either lines of constant $\xi_{\mathbf{k}}$ in the normal state or $E_{\mathbf{k}}$ in a broken symmetry state such as SC or SDW, depending on whether the calculation is being performed at high or low T . To create a grid of this type, the polar $k(\xi, \theta_{\mathbf{k}})$ value was found at every $(\xi, \theta_{\mathbf{k}})$ -value chosen by self-consistently solving the equation:

$$0 = \xi + t_1 \cos(2k \cos \theta_{\mathbf{k}}) + t_1 \cos(2k \sin \theta_{\mathbf{k}}) + t_2 \cos(2k \cos \theta_{\mathbf{k}}) \cos(2k \sin \theta_{\mathbf{k}}) \quad (3.3)$$

where $k_x = k(\xi, \theta_{\mathbf{k}}) \cos \theta_{\mathbf{k}}$ and $k_y = k(\xi, \theta_{\mathbf{k}}) \sin \theta_{\mathbf{k}}$. This method can be applied to any closed FS tight-binding dispersion relation (and open FS dispersion with minimal modifications), but was applied to the $\xi_{\mathbf{k}}^{(1)}$ dispersion relation in Equation (3.3). In order to accommodate an integration grid of this type the κ_{ij} integral can be rewritten as

$$\kappa_{ij} = -\frac{2}{T} \sum_{n=1}^2 \int_{-E_c}^{E_c} d\xi \int_0^{2\pi} \frac{d\theta_{\mathbf{k}}}{2\pi} N(\xi, \theta_{\mathbf{k}}) (E_{\mathbf{k}}^{(n)})^2 (\mathbf{v}_{\mathbf{k}}^{(n)})_i (\mathbf{v}_{\mathbf{k}}^{(n)})_j \frac{\partial f_{\mathbf{k}}^0}{\partial E} (\tau_{n1}^{-1} + \tau_{n2}^{-1})^{-1} \quad (3.4)$$

where $N(\xi, \theta_{\mathbf{k}})$ is the local density of states in the normal state and is equal to:

$$N(\xi, \theta_{\mathbf{k}}) = \frac{1}{|\nabla_{\mathbf{k}} \xi_{\mathbf{k}}|} \frac{dk_l(\theta_{\mathbf{k}})}{d\theta_{\mathbf{k}}}, \quad \frac{dk_l(\theta_{\mathbf{k}})}{d\theta_{\mathbf{k}}} = \frac{k d\theta_{\mathbf{k}}}{\cos d\theta_{\mathbf{k}}}. \quad (3.5)$$

Integrating over $\theta_{\mathbf{k}}$ in Equation (3.4) results in integrating over a curve of constant ξ and integrating over $\xi_{\mathbf{k}}$ results in integrating over quasiparticle energy in the normal state. Integration grids of this type can be seen in Figure 3.1(a) with a low enough grid density to emphasize the pattern of the \mathbf{k} -points. Despite this illustration having a comically low N_{ξ} in order to make the constant ξ curves recognizable, it can be seen that this grid does a much better job of capturing the function $\frac{\partial f_{\mathbf{k}}^0}{\partial E}$ along the FS than the (k_x, k_y) -grid did.

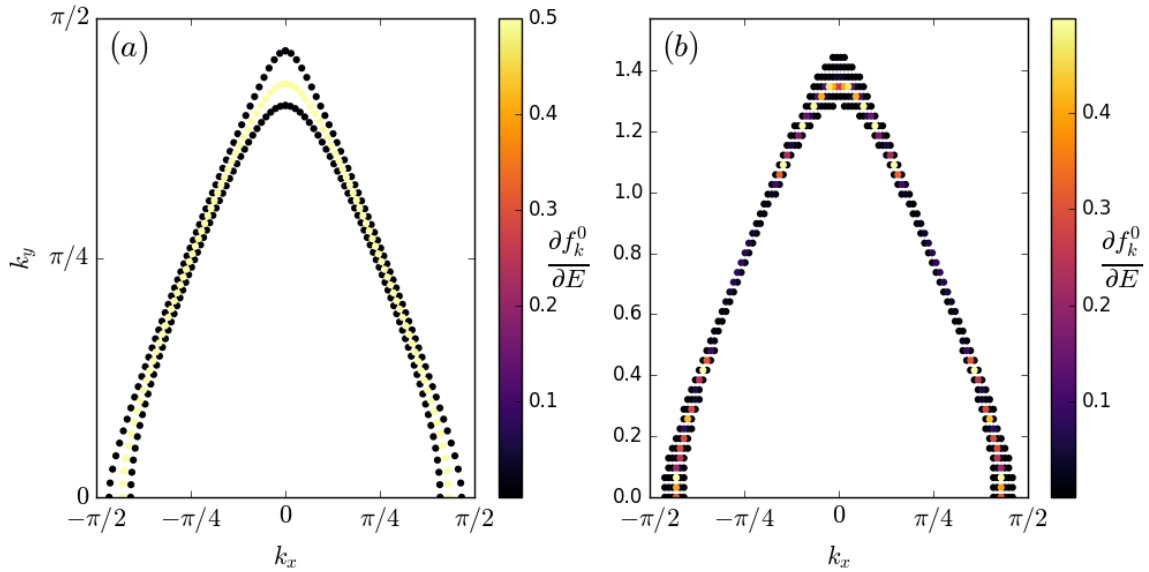


Figure 3.1: Heatmaps of $\frac{\partial f_{\mathbf{k}}^0}{\partial E}$ when $T = .5T_N$ plotted on integration grids for the $\xi_{\mathbf{k}}^{(1)}$ FS when $t_1 = 100T_N$, $t_2 = 10T_N$, and $E_c = 7.5T_N$. (a) $(\xi, \theta_{\mathbf{k}})$ -grid where $N_{\xi} = 3$ and $N_{\theta_{\mathbf{k}}} = 100$, so the total number of \mathbf{k} -points in the grid is $N_{grid} = 300$. (b) (k_x, k_y) -grid where $N_x = 100$ and $N_y = 50$, however a majority of the grid points were cutoff due to being below E_c leaving $N_{grid} = 330$ \mathbf{k} -points in this grid. It should be noted that these are purely for illustration and only grids like those in (a), albeit with a larger N_{ξ} , were used in calculations.

As one would expect from the illustrations of these grids, the $(\xi, \theta_{\mathbf{k}})$ -grid does a significantly better job at capturing the κ_{ij} integral than the (k_x, k_y) -grid. In order to demonstrate this, the electronic thermal conductivity in the normal state was calculated at

$T = .5T_N$. The normal state conductivity is a simplification of Equation (3.4) and can be written as:

$$\kappa^n = -\frac{2}{T} \int_{-E_c}^{E_c} d\xi \int_0^{2\pi} \frac{d\theta_{\mathbf{k}}}{2\pi} N(\xi, \theta_{\mathbf{k}}) (\xi_{\mathbf{k}})^2 v_x^2 \frac{\partial f_{\mathbf{k}}^0}{\partial E} \tau_n \quad (3.6)$$

This was calculated as a function of the total number of \mathbf{k} -points in both grids (N_{grid}) that were included in the κ^n calculation until convergence was reached. Typically, N_{ξ} and $N_{\theta_{\mathbf{k}}}$ are nearly the same, however N_{ξ} is chosen to be odd in order to ensure the grid includes the FS.

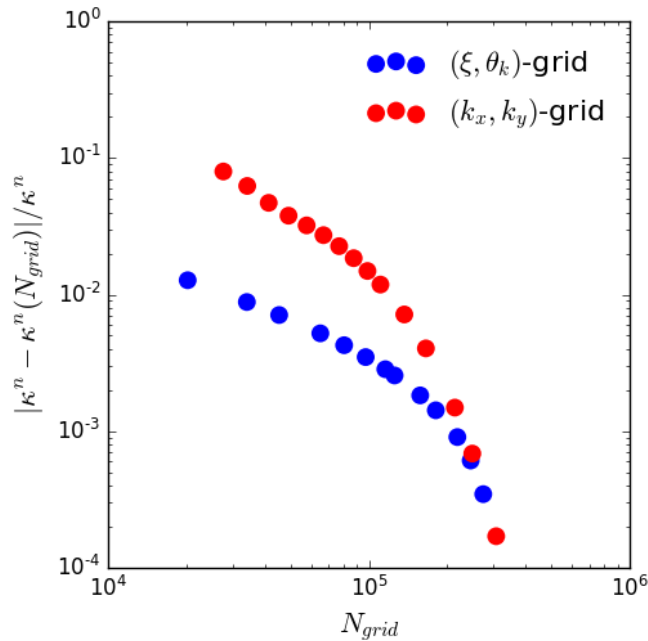


Figure 3.2: Convergence of the κ^n integral on the $(\xi, \theta_{\mathbf{k}})$ -grid (blue) and the (k_x, k_y) -grid (red), where it can be seen that given the same number of points the $(\xi, \theta_{\mathbf{k}})$ -grid tends to be an order of magnitude more accurate for this simple calculation.

Calculations of κ^n for varying values of N_{grid} for both grids found that the $(\xi, \theta_{\mathbf{k}})$ -grid tended to be an order of magnitude closer to the converged thermal conductivity value in the normal state compared to the (k_x, k_y) -grid, until $N_{grid} \sim 2 \cdot 10^5$ at which point both grids reach nearly identical convergence. However, it should be noted that a grid density of $N_{grid} \sim 2 \cdot 10^5$ would

take a very long time to calculate thermal conductivities below $T = T_c$ due to the time it takes to calculate the quasiparticle lifetimes.

Similarly, a simple (k_x, k_y) -grid was found to have insufficient convergence for calculations on FSs distorted by a nematic phase. Rather than implementing a $(\xi, \theta_{\mathbf{k}})$ -grid for this situation, a $(\tilde{\xi}, k_x)$ -grid was chosen due to the distorted FS becoming open in the k_x -direction, so parameterizing the grid in terms of k_x led to better convergence than parameterizing in terms of $\theta_{\mathbf{k}}$.

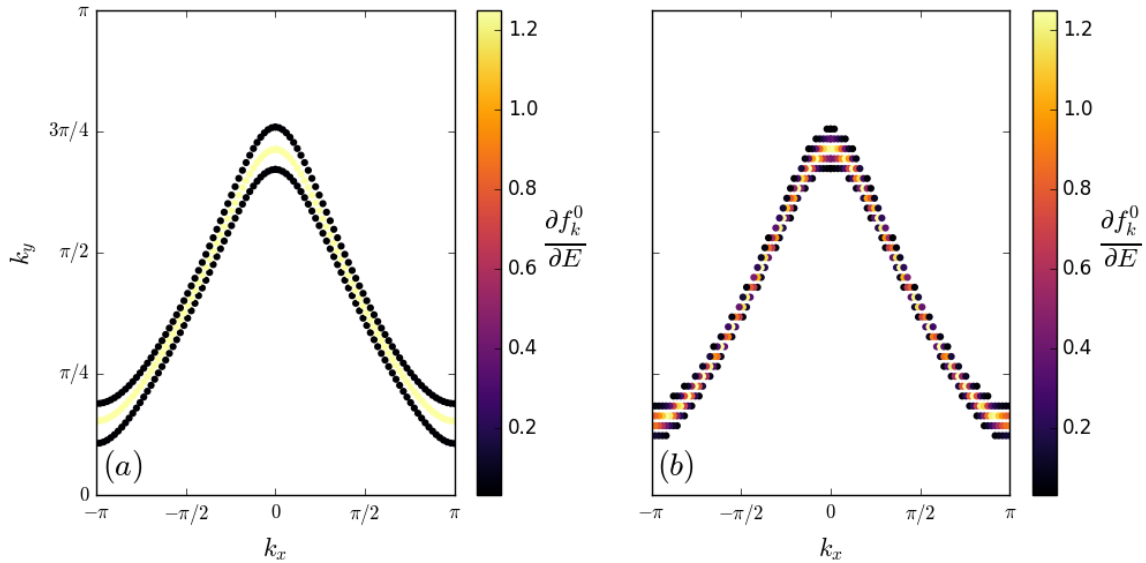


Figure 3.3: Heatmaps of $\frac{\partial f_{\mathbf{k}}^0}{\partial E}$ when $T = .2T_S$ plotted on integration grids for the $\xi_{\mathbf{k}}^{(3)}$ FS distorted by a nematic phase when $\mu = -4.8T_S$, $t_1 = 6T_S$, $t_2 = -1T_S$, $\Phi = 1.38T_S$, and $E_c = 8T_S$. (a) (\tilde{x}, k_x) -grid where $N_{\tilde{\xi}} = 3$ and $N_{\theta_{\mathbf{k}}} = 50$, so the total number of \mathbf{k} -points in the grid is $N_{grid} = 150$. (b) (k_x, k_y) -grid where $N_x = 100$ and $N_y = 50$, however a majority of the grid points were cutoff due to being below E_c leaving $N_{grid} = 168$ \mathbf{k} -points in this grid. It should be noted that these are purely for illustration and only grids like those in (a), albeit with a larger $N_{\tilde{\xi}}$, were used in calculations.

A comparison of the $(\tilde{\xi}, k_x)$ -grid to the simpler (k_x, k_y) -grid for nematically distorted FSs can be seen in Figure 3.3. Grids of this type can be generated by solving for k_y as a function of $\tilde{\xi}$ and k_x , for the $\xi_{\mathbf{k}}^{(3)}$ electron dispersion this led to the equation:

$$k_y = \frac{1}{a} \cos^{-1} \left(- \frac{\tilde{\xi} + \mu + 2t_1 \cos k_x a - \Phi \cos k_x a}{2t_1 + 4t_2 \cos k_x a + \Phi} \right) \quad (3.7)$$

where the grid can be created from this equation with evenly spaced values of $\tilde{\xi}$ and k_x . Grids of this type were used to calculate the thermal conductivity in the nematic phase:

$$\kappa_{ij}^N = -\frac{2}{T} \int_{-E_c}^{E_c} d\xi \int_0^{2\pi} \frac{d\theta_{\mathbf{k}}}{2\pi} \tilde{N}(\xi, \theta_{\mathbf{k}}) (\tilde{\xi}_{\mathbf{k}})^2 \mathbf{v}_i \mathbf{v}_j \frac{\partial f_{\mathbf{k}}^0}{\partial E} \tau_n \quad (3.8)$$

which is similar calculation to normal state thermal conductivity, but with the electron dispersion modified by nematicity. Performing this calculation on both the $(\tilde{\xi}, k_x)$ -grid and (k_x, k_y) -grid (seen in Figure 3.4) revealed that the $(\tilde{\xi}, k_x)$ -grid had nearly an order of magnitude better convergence until $N_{grid} \sim 5 \cdot 10^4$. It should be noted that the (k_x, k_y) -grid performed noticeably better for the nematically distorted tight-binding FS due to the fact that the FS became elongated along a Cartesian direction, however it still fails to reach a reasonable convergence at low enough N_{grid} -values to be computationally viable for more difficult calculations.

The $(\xi, \theta_{\mathbf{k}})$ -grid was used to calculate the normal state thermal conductivity, $\kappa^n(T)$ and the pure SDW thermal conductivity components $\kappa_{ij}^{\text{SDW}}(T)$ at high- T . However, it was found to be insufficient for calculating the pure SDW conductivity and the SC + SDW coexistence state conductivity at low- T due to missing the FS reconstruction caused by the SDW order in a similar fashion to how the (k_x, k_y) -grid missed the normal state tight-binding FS in Figure 3.1(b). In order to resolve this, a new grid can be produced in a very similar fashion to Equation (3.3) but with the SDW eigenvalues $E_{\mathbf{k}}^{(\alpha)}$ and $E_{\mathbf{k}}^{(\beta)}$, this will be referred to as the $(E^{(\alpha, \beta)}, \theta_{\mathbf{k}})$ -grid. The pure SDW eigenvalues are:

$$E_{\mathbf{k}}^{(\alpha)} = \xi_{\mathbf{k}}^+ + \sqrt{(\xi_{\mathbf{k}}^-)^2 + M^2}, \quad E_{\mathbf{k}}^{(\beta)} = \xi_{\mathbf{k}}^+ - \sqrt{(\xi_{\mathbf{k}}^-)^2 + M^2} \quad (3.9)$$

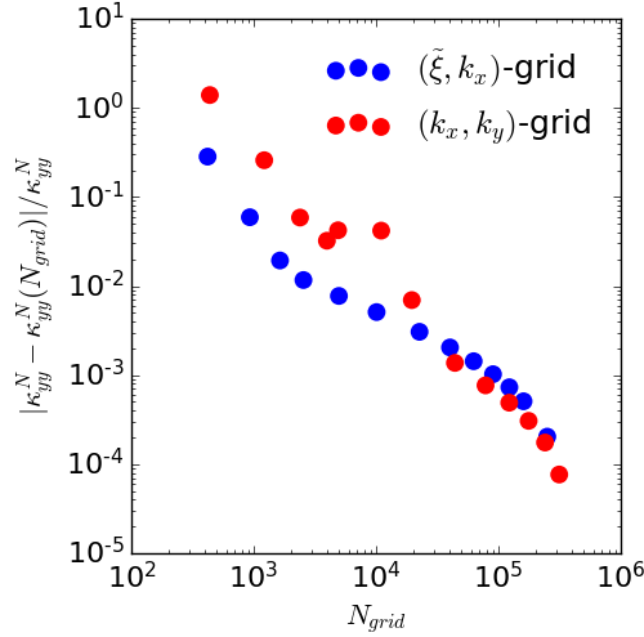


Figure 3.4: Convergence of the κ^N integral on the $(\tilde{\xi}, k_x)$ -grid (blue) and the (k_x, k_y) -grid (red), where it can be seen that given the same number of points the $(\tilde{\xi}, k_x)$ -grid tends to be nearly an order of magnitude more accurate for this calculation.

where $\xi_{\mathbf{k}}^{\pm} = \frac{1}{2}(\xi_{\mathbf{k}} \pm \xi_{\mathbf{k}+\mathbf{Q}})$. In materials where the SDW state is commensurate with the lattice, we can simplify the equations for $\xi_{\mathbf{k}}^{\pm}$ to:

$$\xi_{\mathbf{k}}^{+} = -t_2 \cos 2k_x \cos 2k_y, \quad \xi_{\mathbf{k}}^{-} = -t_1 \cos 2k_x - t_1 \cos 2k_y \quad (3.10)$$

for the $\xi_{\mathbf{k}}^{(1)}$ normal state dispersion relation. The $(E^{(\alpha,\beta)}, \theta_{\mathbf{k}})$ -grid can be constructed from these eigenvalues in a similar manner to how the $(\xi, \theta_{\mathbf{k}})$ -grid was constructed by self-consistently solving for $k(E^{(\alpha,\beta)}, \theta_{\mathbf{k}})$ for both $E_{\mathbf{k}}^{(\alpha)}$ and $E_{\mathbf{k}}^{(\beta)}$ from the equations:

$$0 = E - E_{\mathbf{k}}^{(\alpha)} : \quad 0 = E + t_2 \cos(2k \cos \theta_{\mathbf{k}}) \cos(2k \sin \theta_{\mathbf{k}}) - \sqrt{(t_1 \cos(2k \cos \theta_{\mathbf{k}}) + t_1 \cos(2k \sin \theta_{\mathbf{k}}))^2 + M^2} \quad (3.11)$$

$$0 = E - E_{\mathbf{k}}^{(\beta)} : 0 = E + t_2 \cos(2k \cos \theta_{\mathbf{k}}) \cos(2k \sin \theta_{\mathbf{k}}) + \sqrt{(t_1 \cos(2k \cos \theta_{\mathbf{k}}) + t_1 \cos(2k \sin \theta_{\mathbf{k}}))^2 + M^2} \quad (3.12)$$

where again $k_x = k(E^{(\alpha,\beta)}, \theta_{\mathbf{k}}) \cos \theta_{\mathbf{k}}$ and $k_y = k(E^{(\alpha,\beta)}, \theta_{\mathbf{k}}) \sin \theta_{\mathbf{k}}$. However, unlike the $(\xi, \theta_{\mathbf{k}})$ -grid, not every $(E^{(\alpha,\beta)}, \theta_{\mathbf{k}})$ combination has a $k(E^{(\alpha,\beta)}, \theta_{\mathbf{k}})$ solution, as can be seen in Figure 3.5(a). In fact, the $E_{\mathbf{k}}^{(\alpha)}$ portion of the $(E, \theta_{\mathbf{k}})$ -grid contains no solutions below $E^{(\alpha)} = M$, and has a negligible contribution to thermal transport at low- T (below $T \sim .3T_N$). Due to the $E_{\mathbf{k}}^{(2)}$ portion of the $(E, \theta_{\mathbf{k}})$ -grid being more important to the low- T transport, it's the only grid shown in Figure 3.5(a) which is being compared to the $(\xi, \theta_{\mathbf{k}})$ -grid in Figure 3.5(b).

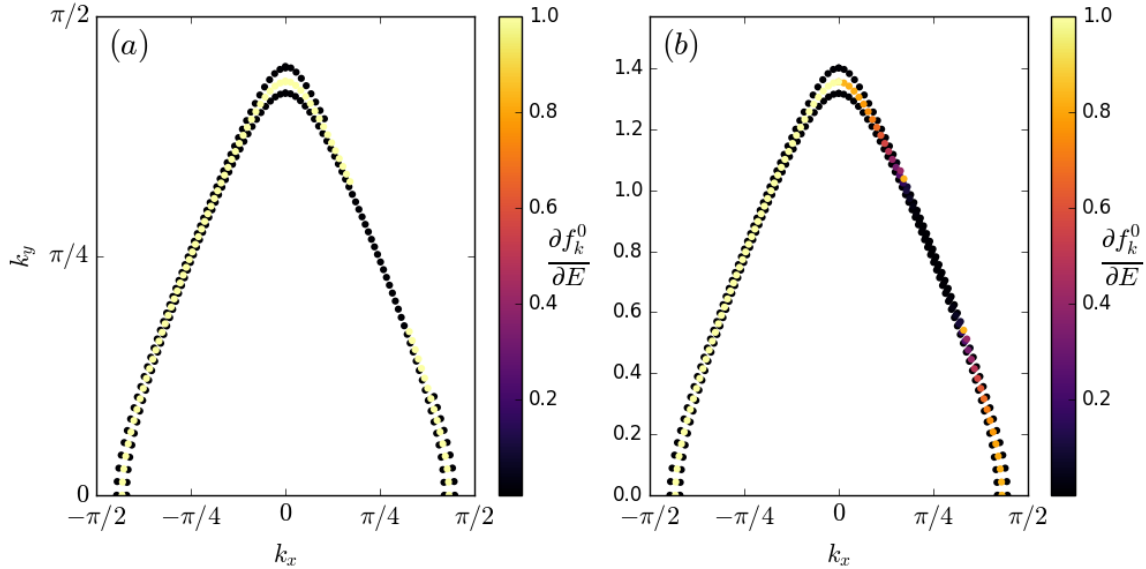


Figure 3.5: Heatmaps of $\frac{\partial f_{\mathbf{k}}^0}{\partial E}$ when $T = .25T_N$ plotted on integration grids for the $E_{\mathbf{k}}^{(2)}$ reconstructed FS when $\mathbf{Q} = (\pi/2, \pi/2)$ and $M = 2T_N$ for the $\xi_{\mathbf{k}}^{(1)}$ normal state dispersion with band parameters $t_1 = 100T_N$, $t_2 = 10T_N$, and $E_c = 3.25T_N$. (a) $(E^{(\beta)}, \theta_{\mathbf{k}})$ -grid where $N_E = 3$ and $N_{\theta_{\mathbf{k}}} = 100$, and the total number of \mathbf{k} -points in the grid is $N_{grid} = 250$ ($N_{grid} \neq N_E N_{\theta_{\mathbf{k}}}$ since not every $(E^{(\beta)}, \theta_{\mathbf{k}})$ combination has a solution). (b) $(\xi, \theta_{\mathbf{k}})$ -grid where $N_{\xi} = 3$ and $N_{\theta_{\mathbf{k}}} = 100$, so $N_{grid} = 300$. It should be noted that these are purely for illustration and much higher grid densities were used for actual calculations.

It can also be seen that the $(E^{(\alpha,\beta)}, \theta_{\mathbf{k}})$ -grid provides an improvement to the convergence of κ_{xy}^{SDW} over the $(\xi, \theta_{\mathbf{k}})$ -grid. While this isn't as good of an improvement as the $(\xi, \theta_{\mathbf{k}})$ -grid was over the (k_x, k_y) -grid, any improvement to the convergence is welcome in order to reduce the computational cost of this calculation due to how much time it takes to calculate the quasiparticle lifetimes in the SC + SDW coexistence phase on the GPU.

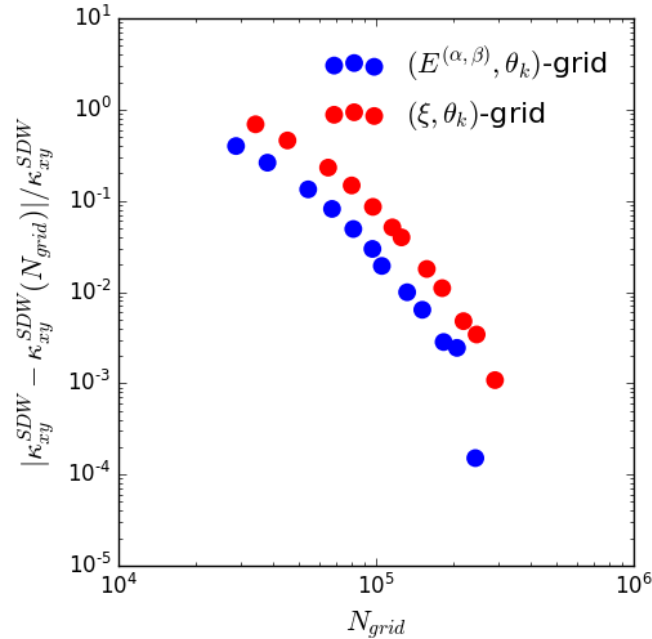


Figure 3.6: Convergence of the κ_{xy}^{SDW} integral at $T = 0.02T_N$ on the $(E, \theta_{\mathbf{k}})$ -grid (blue) and the $(\xi, \theta_{\mathbf{k}})$ -grid (red), where it can be seen that given the same number of points the $(E, \theta_{\mathbf{k}})$ -grid is a slight, but noticeable improvement over the $(\xi, \theta_{\mathbf{k}})$ -grid.

While the $(E^{(\alpha,\beta)}, \theta_{\mathbf{k}})$ -grid may seem like it could be capable of capturing all the details of the SC + SDW coexistence phase because it captures the details of the reconstructed FS (knowing that all symmetry nodes are an intersection of nodal lines and the FS), When the SC gap function is even under translations of \mathbf{Q} (i.e. $\Delta_{\mathbf{k}+\mathbf{Q}} = \Delta_{\mathbf{k}}$) additional mixing nodes appear near the FS reconstruction. To account for this in the integration grid, curves of equal energy can be solved for around these mixing nodes and embedded into the pre-existing $(E^{(\alpha,\beta)}, \theta_{\mathbf{k}})$ -grid which would otherwise wholly miss these nodes which can be crucial

to low- T electronic thermal transport. In order to create grids of this type, the coexistence phase eigenvalues are first considered

$$\begin{aligned} E_{\mathbf{k}}^{(1)} &= \sqrt{\Gamma_{\mathbf{k}} + 2\Lambda_{\mathbf{k}}} \\ E_{\mathbf{k}}^{(2)} &= \sqrt{\Gamma_{\mathbf{k}} - 2\Lambda_{\mathbf{k}}} \end{aligned} \quad (3.13)$$

$$\begin{aligned} \Gamma_{\mathbf{k}} &= (\xi_{\mathbf{k}}^+)^2 + (\xi_{\mathbf{k}}^-)^2 + (\Delta_{\mathbf{k}}^+)^2 + (\Delta_{\mathbf{k}}^-)^2 + M^2 \\ \Lambda_{\mathbf{k}} &= \sqrt{(\xi_{\mathbf{k}}^+ \xi_{\mathbf{k}}^- + \Delta_{\mathbf{k}}^+ \Delta_{\mathbf{k}}^-)^2 + M^2((\xi_{\mathbf{k}}^+)^2 + (\Delta_{\mathbf{k}}^+)^2)} \end{aligned}$$

and similar to the definitions of $\xi_{\mathbf{k}}^{\pm}$, $\Delta_{\mathbf{k}}^{\pm} = \frac{1}{2}(\Delta_{\mathbf{k}} \pm \Delta_{\mathbf{k}+\mathbf{Q}})$. These eigenvalues can be simplified if the symmetry of the SC gap is known under translations of \mathbf{Q} , here we will consider both the even and odd cases for completeness but only the even case will be relevant to generating a grid around the additional mixing node. When the SC gap is odd under translations of \mathbf{Q} and $\Delta_{\mathbf{k}+\mathbf{Q}} = -\Delta_{\mathbf{k}}$, $\Delta_{\mathbf{k}}^+ = 0$ and $\Delta_{\mathbf{k}}^- = \Delta_{\mathbf{k}}$. Similarly, when the SC gap is even under translations of \mathbf{Q} and $\Delta_{\mathbf{k}+\mathbf{Q}} = \Delta_{\mathbf{k}}$, $\Delta_{\mathbf{k}}^+ = \Delta_{\mathbf{k}}$ and $\Delta_{\mathbf{k}}^- = 0$. This reduces the eigenvalues of the SC + SDW coexistence phase to:

$$E_{\mathbf{k}}^{(1,2;E,O)} = \sqrt{\Gamma_{\mathbf{k}} \pm 2\Lambda_{\mathbf{k}}^{(E,O)}} \quad (3.14)$$

$$\begin{aligned} \Gamma_{\mathbf{k}} &= (\xi_{\mathbf{k}}^+)^2 + (\xi_{\mathbf{k}}^-)^2 + \Delta_{\mathbf{k}}^2 + M^2 \\ \Lambda_{\mathbf{k}}^{(E)} &= \sqrt{(\xi_{\mathbf{k}}^+ \xi_{\mathbf{k}}^-)^2 + M^2((\xi_{\mathbf{k}}^+)^2 + \Delta_{\mathbf{k}}^2)} \\ \Lambda_{\mathbf{k}}^{(O)} &= \sqrt{(\xi_{\mathbf{k}}^+ \xi_{\mathbf{k}}^-)^2 + M^2(\xi_{\mathbf{k}}^+)^2} \end{aligned}$$

where the (E) and (O) subscripts denote when the SC gap is even or odd under translations

of the SDW nesting vector respectively. The mixing nodes can be solved for when $E_{\mathbf{k}}^{(2;E)} = 0$, which results in both the conditions $\xi_{\mathbf{k}}^- = 0$ and $E_{\mathbf{k}}^{(2;E)} = M - \sqrt{(\xi_{\mathbf{k}}^+)^2 + \Delta_{\mathbf{k}}^2} = 0$ needing to be satisfied. In general, this can be easily solved for self-consistently for arbitrary $\Delta_{\mathbf{k}}$ SC gaps which are even under translations of \mathbf{Q} . The \mathbf{k} -space solutions to these equations will be called (k_x^{mix}, k_y^{mix}) , and it should be noted that two solutions exist for each flat region of the tight-binding FS that becomes reconstructed by the SDW order. This means that for SDW orders with anisotropic transport properties like were studied in this work, there exist four (k_x^{mix}, k_y^{mix}) -solutions. However, for the $\mathbf{Q} = (\pi/2, \pi/2)$ only the first two quadrants of \mathbf{k} -space needed to be integrated to capture the essential physics of these materials by symmetry so only two of these solutions can be seen in Figure 3.7(a).

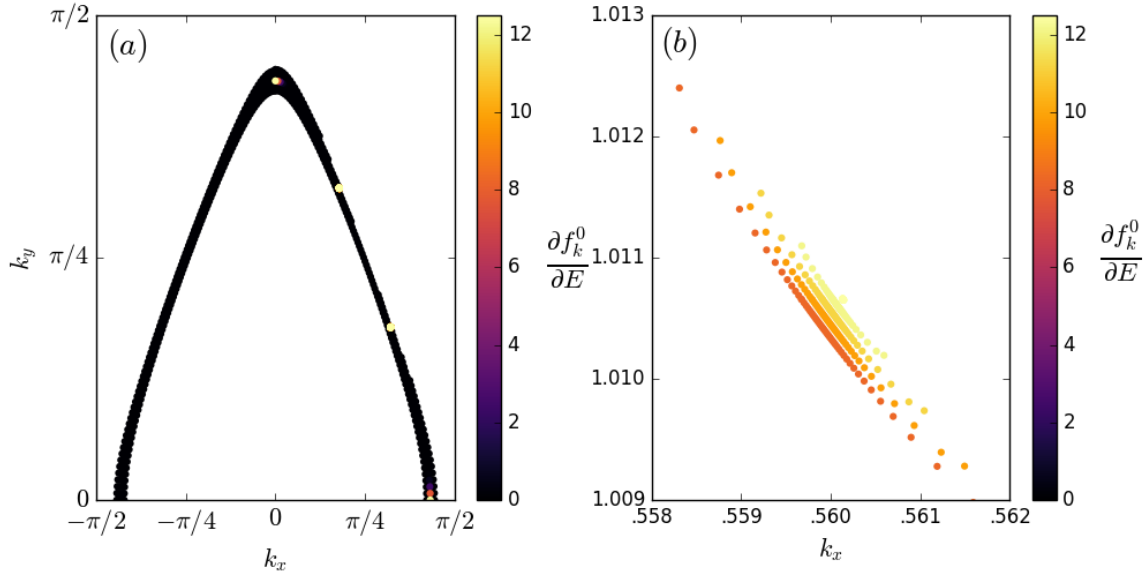


Figure 3.7: Heatmaps of $\frac{\partial f_{\mathbf{k}}^0}{\partial E}$ when $T = .02T_N$ plotted on the integration grid for the $E_{\mathbf{k}}^{(2)}$ reconstructed FS when the $\mathbf{Q} = (\pi/2, \pi/2)$ SDW state coexists with d_{xy} superconductivity. Due to the fact that this is a $d^{(E)}$ -wave SC state, additional mixing nodes besides the typical d -wave symmetry nodes appear in the region of the FS reconstruction. (a) The $(E^{(\alpha,\beta)}, \theta_{\mathbf{k}})$ -grid combined with the $(E^{(2;E)}, \theta_{\mathbf{k}})$ -grid in order to properly capture the behavior of the additional mixing nodes, as just the $(E^{(\alpha,\beta)}, \theta_{\mathbf{k}})$ -grid tends to miss these points at low- T . (b) Zoomed in plot of the $(E^{(2;E)}, \theta_{\mathbf{k}})$ -grid at one of the mixing nodes.

A specialized grid may be constructed around these (k_x^{mix}, k_y^{mix}) -solutions in order to better

capture their contributions to the electronic thermal conductivity. This is required at very low- T due to the fact that the $(E^{(\alpha,\beta)}, \theta_{\mathbf{k}})$ -grid does a poor job of capturing these nodes as they occupy a significantly smaller region of \mathbf{k} -space relative to d -wave symmetry nodes (which were the only other type of node studied in this work). This newest mixing node grid will be referred to as the $(E^{(2;E)}, \theta_{\mathbf{k}})$ -grid, and rather than simply replacing the $(E^{(\alpha,\beta)}, \theta_{\mathbf{k}})$ -grid with it at low- T the two grids were "stitched" together. This was accomplished by removing any points of the $(E^{(\beta)}, \theta_{\mathbf{k}})$ -grid that would fall within the confines of the $(E^{(2;E)}, \theta_{\mathbf{k}})$ -grid. The purpose of this is to capture the effects of both these additional mixing nodes, which are important at low- T , and the effects of the \mathbf{k} -points along the reconstructed FS, which become important as $T \rightarrow T_c$, in a continuous manner. The $(E^{(2;E)}, \theta_{\mathbf{k}})$ -grid constructed around one of these (k_x^{mix}, k_y^{mix}) -solutions present in Figure 3.7(a) was zoomed in on in Figure 3.7(b) to emphasize what these mixing node grids looks like. The $(E^{(2;E)}, \theta_{\mathbf{k}})$ -grid was constructed by solving the self-consistency equation:

$$0 = E - E_{\mathbf{k}=(k_x^{mix}+k \cos \theta_{\mathbf{k}}, k_y^{mix}+k \sin \theta_{\mathbf{k}})}^{(2;E)} \quad (3.15)$$

Where for a given $(E^{(2;E)}, \theta_{\mathbf{k}})$ -value in the grid, $k(E^{(2;E)}, \theta_{\mathbf{k}})$ can be solved for and the (k_x, k_y) -values of the $(E^{(2;E)}, \theta_{\mathbf{k}})$ -grid can be solved for from the equations $k_x = k_x^{mix} + k(E^{(2;E)}, \theta_{\mathbf{k}}) \cos \theta_{\mathbf{k}}$ and $k_y = k_y^{mix} + k(E^{(2;E)}, \theta_{\mathbf{k}}) \sin \theta_{\mathbf{k}}$. An integration grid of this type produces concentric curves of equal $E^{(2;E)}$ -values around the additional mixing nodes. In order to demonstrate how much better the $(E^{(2;E)}, \theta_{\mathbf{k}})$ -grid captures the behavior of these mixing nodes over the more general $(E, \theta_{\mathbf{k}})$ -grid, $\kappa_{xy}^{d(E)}$ was calculated at very low- T due to the fact that the d -wave symmetry nodes only contribute to the $\kappa_{xx}^{d(E)}$ and $\kappa_{yy}^{d(E)}$ thermal conductivity elements for the $\mathbf{Q} = (\pi/2, \pi/2)$ SDW state due to the quasiparticle states at those nodes having Fermi velocities either purely in the k_x or k_y directions and don't contribute to the $\kappa_{xy}^{d(E)}$ tensor element. Therefore, only the mixing nodes which have Fermi

velocities with equal components in both the k_x and k_y directions contribute to $\kappa_{xy}^{d(E)}$.

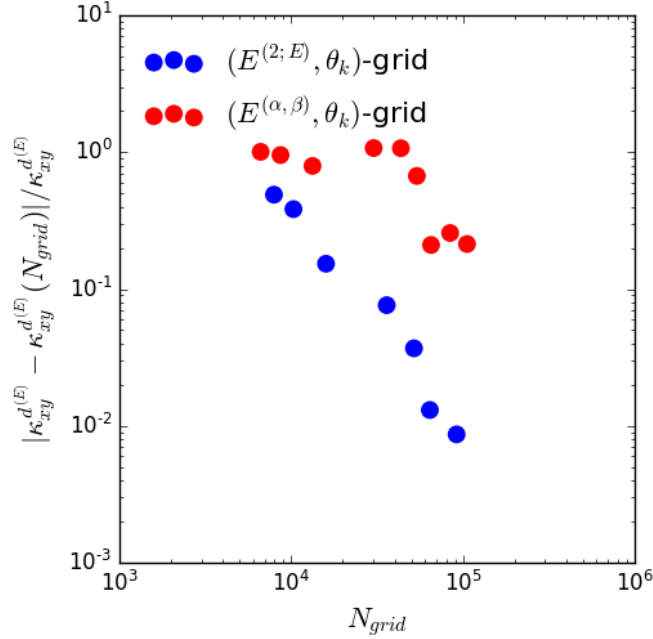


Figure 3.8: Convergence of the $\kappa_{xy}^{d(E)}$ integral at $T = 0.02T_N$ on the $(E^{(2;E)}, \theta_{\mathbf{k}})$ -grid (blue) and the $(E^{(\alpha,\beta)}, \theta_{\mathbf{k}})$ -grid (red), where it can be seen that given the same number of points the $(E^{(2;E)}, \theta_{\mathbf{k}})$ -grid is a noticeable improvement over the $(E, \theta_{\mathbf{k}})$ -grid due to actually picking up the mixing nodes properly.

In Figure 3.8 it can be seen that without the inclusion of the $(E^{(2;E)}, \theta_{\mathbf{k}})$ -grid to capture the behavior of the additional mixing nodes, the SC + SDW thermal conductivity element $\kappa_{xy}^{d(E)}$ doesn't drop below 10% error for a reasonable N_{grid} -value. However, once the $(E^{(2;E)}, \theta_{\mathbf{k}})$ -grid is included it can be seen that this thermal conductivity element can be easily calculated within 1% convergence.

The most computationally expensive component in the thermal conductivity integral to properly calculate was by far the quasiparticle lifetimes ($\tau_{\mathbf{k}}$). In order to mitigate this computational cost, the quasiparticle lifetimes were calculated on GPUs which are capable of parallelizing the calculation. It can be seen from Figure 3.9 that calculating $\tau_{\mathbf{k}}$ on the GPU allowed for the use of grids with ten times the number of points while still maintaining

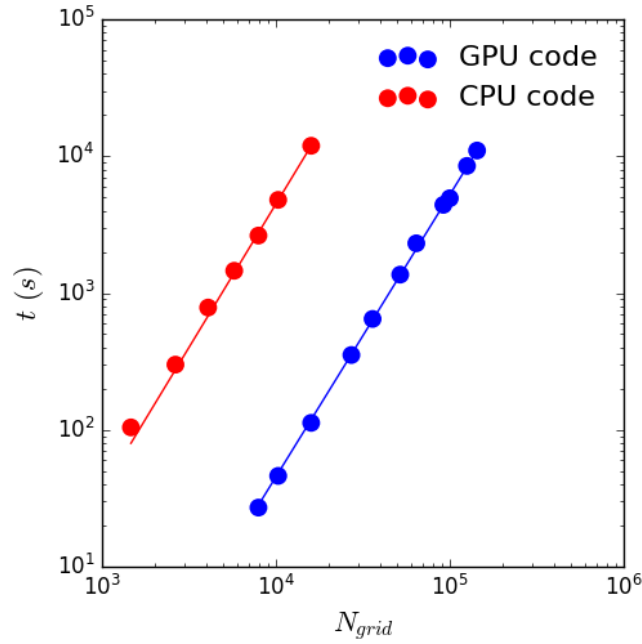


Figure 3.9: Time taken to calculate all the quasiparticle lifetimes $\tau_{\mathbf{k}}$ in the SC + SDW coexistence phase when run on a GPU (Nvidia GeForce RTX 2060 Mobile) and a CPU (Intel i7-10750H).

the same computational cost of running this calculation on the CPU. It should also be noted that this CPU calculation was in fact compiled with jit from the numba python package and that an uncompiled version of this CPU code was so slow that it would've been unfeasible to go beyond $N_{grid} \sim 2 \cdot 10^3$, a grid density nowhere near convergence for any values shown in the convergence plots from this section. The time complexity of the $\tau_{\mathbf{k}}$ calculation was also found for both the GPU and CPU code by fitting $t(N_{grid})$ to the power law $t(N_{grid}) = a \cdot 10^{b \cdot N_{grid}}$. The fit parameters were found to be: $a_{GPU} = 2.589 \cdot 10^{-7} s$, $b_{GPU} = 2.061$, $a_{CPU} = 1.836 \cdot 10^{-5}$, and $b_{CPU} = 2.097$. This means that both the GPU and CPU code have time complexities of order $\mathcal{O}(N^2)$. This is to be expected given that increasing N_{grid} increases the number of $\tau_{\mathbf{k}}$ values that need to be calculated for the κ_{ij} integral and increases the number of points in the grid for the $\tau_{\mathbf{k}}$ calculation, since that integral is calculated on the same grid that the conductivity integral is calculated.

Normal and Anomalous Self-energy Calculations

In the nematic phase the normal, $g(E_{\mathbf{k}})$, and anomalous, $h(E_{\mathbf{k}})$, self-energies can be calculated from the complex integrals:

$$\begin{aligned} g(E_{\mathbf{k}}) &= \frac{1}{\tilde{N}_F} \int \frac{dk'_l}{|\mathbf{v}_F|} \frac{E_{\mathbf{k}}}{\sqrt{E_{\mathbf{k}}^2 - \Delta_{\mathbf{k}'}^2}} \\ h(E_{\mathbf{k}}) &= \frac{1}{\tilde{N}_F} \int \frac{dk'_l}{|\mathbf{v}_F|} \frac{\Delta_{\mathbf{k}'}}{\sqrt{E_{\mathbf{k}}^2 - \Delta_{\mathbf{k}'}^2}} \end{aligned} \quad (3.16)$$

In order to accurately calculate these integrals, they must be separated into their real and imaginary components. This can be accomplished by solving for when $E_{\mathbf{k}}^2 - \Delta_{\mathbf{k}'}^2 = 0$, in order to determine the \mathbf{k}' -points at which these integrands go from being real to imaginary. Since this calculation is performed along the nematically deformed FS, which is defined by $\xi_{\mathbf{k}} + \Phi f_{\mathbf{k}} = 0$, k_y can be solved as a function of k_x for a particular electron dispersion relation (here $\xi_{\mathbf{k}}^{(3)}$ was used):

$$k_y = \frac{1}{a} \cos^{-1} \left(- \frac{\mu + 2t_1 \cos k_x a - \Phi \cos k_x a}{2t_1 + 4t_2 \cos k_x a + \Phi} \right) \quad (3.17)$$

In order to simplify the algebra required to solve for when these integrands go from real to imaginary, $\Delta_{\mathbf{k}'} = \pm E_{\mathbf{k}}$ was solved instead. Doing this results in the following solutions:

$$\begin{aligned}
k_x^{(1)} &= \frac{1}{a} \cos^{-1} \left(\frac{-\beta_1 + \sqrt{\beta_1^2 - 4\alpha\gamma_1}}{2\alpha} \right) \\
k_x^{(2)} &= \frac{1}{a} \cos^{-1} \left(\frac{-\beta_2 + \sqrt{\beta_2^2 - 4\alpha\gamma_2}}{2\alpha} \right) \\
k_x^{(3)} &= \frac{1}{a} \cos^{-1} \left(\frac{-\beta_1 - \sqrt{\beta_1^2 - 4\alpha\gamma_1}}{2\alpha} \right) \\
k_x^{(4)} &= \frac{1}{a} \cos^{-1} \left(\frac{-\beta_2 - \sqrt{\beta_2^2 - 4\alpha\gamma_2}}{2\alpha} \right)
\end{aligned} \tag{3.18}$$

where

$$\begin{aligned}
\alpha &= 4rt_2 \\
\beta_1 &= 4t_2 + 4rt_1 + 4E_{\mathbf{k}}t_2\sqrt{1+r^2}/\Delta \\
\beta_2 &= 4t_2 + 4rt_1 - 4E_{\mathbf{k}}t_2\sqrt{1+r^2}/\Delta \\
\gamma_1 &= 2t_1 + \Phi + r\mu + 2E_{\mathbf{k}}t_1\sqrt{1+r^2}/\Delta + E_{\mathbf{k}}\Phi\sqrt{1+r^2}/\Delta \\
\gamma_2 &= 2t_1 + \Phi + r\mu - 2E_{\mathbf{k}}t_1\sqrt{1+r^2}/\Delta - E_{\mathbf{k}}\Phi\sqrt{1+r^2}/\Delta
\end{aligned} \tag{3.19}$$

$k_x^{(1)}$ and $k_x^{(2)}$ correspond to the case when $r > 0$ and when $\Delta_{\mathbf{k}'} = E_{\mathbf{k}}$ and $\Delta_{\mathbf{k}'} = -E_{\mathbf{k}}$ respectively. Whereas $k_x^{(3)}$ and $k_x^{(4)}$ correspond to the case when $r < 0$ and when $\Delta_{\mathbf{k}'} = E_{\mathbf{k}}$ and $\Delta_{\mathbf{k}'} = -E_{\mathbf{k}}$.

Solving for these allowed for the real and imaginary regimes of $g(E_{\mathbf{k}})$ and $h(E_{\mathbf{k}})$ to be integrated separately, allowing for a better convergence of these integrals compared to integrating over the entire FS with no regard for these boundaries. This can be seen in Figure 3.10 where integrating the real and imaginary regions of $g(E_{\mathbf{k}})$ separately results in nearly an order of magnitude improvement to the convergence at high integration grid densities.

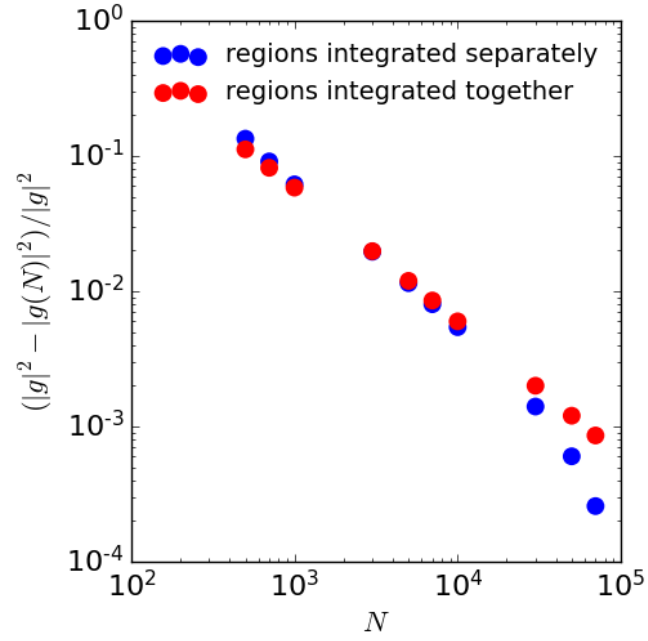


Figure 3.10: Convergence of $|g(E_{\mathbf{k}})|^2$ calculated on the nematically deformed $\xi_{\mathbf{k}}^{(3)}$ FS when $\mu = -4.8T_S$, $t_1 = 6T_S$, $t_2 = -T_S$, $\Phi = 1.34T_S$, $\Delta = 0.18T_S$, $r = 0.6$, and $E_{\mathbf{k}} = .015T_S$, chosen to ensure that both $k_x^{(1)}$ and $k_x^{(2)}$ are well defined and the integrand of $g(E_{\mathbf{k}})$ has three separate regions.

DETERMINATION OF ANISOTROPY CONSTANTS VIA FITTING OF MAGNETIC
HYSTERESIS TO NUMERICAL CALCULATION OF STONER-WOHLFARTH MODEL

Contribution of Authors and Co-Authors

Manuscript in following chapter

Author: [S F Peterson]

Contributions: [Developed an algorithmic method to compute magnetic hysteresis loops using the Stoner-Wohlfarth model for thin-films with uniaxial or cubic anisotropy. Used numerical Stoner-Wohlfarth calculation with a least-squares fitting algorithm to fit magnetic hysteresis of $\text{Fe}_x\text{Co}_y\text{Mn}_z$ previously measured on a Vibrating Sample Magnetometer (VSM) to determine the cubic anisotropy constants (K_1). Compared K_1 -values determined via this method to previously published values in order to establish this as a viable method of determining anisotropy constants through VSM measurements as opposed to angle-resolved Ferromagnetic Resonance and Torque Magnetometry measurements which are more time intensive, thus limiting their application. Authored paper and handled review process, including correspondence after publication.]

Author: [Y U Idzerda]

Contributions: [Principle Investigator. Posed original problem and its broader importance to the field. Provided pre-existing magnetic hysteresis data of $\text{Fe}_x\text{Co}_y\text{Mn}_z$ thin-film samples measured via VSM. Proofread and edited text of paper. Assisted in submission process.]

Manuscript Information

[S. F. Peterson and Y. U. Idzerda]

[AIP Advances]

Status of Manuscript:

Prepared for submission to a peer-reviewed journal

Officially submitted to a peer-reviewed journal

Accepted by a peer-reviewed journal

Published in a peer-reviewed journal

[American Institute of Physics]

[April 6, 2021]

[August 5, 2021]

[AIP Advances **11**]

[<https://doi.org/10.1063/5.0051454>]

Determination of anisotropy constants via fitting of magnetic hysteresis to numerical calculation of Stoner–Wohlfarth model

Cite as: AIP Advances 11, 085111 (2021); doi: 10.1063/5.0051454
 Submitted: 6 April 2021 • Accepted: 28 July 2021 •
 Published Online: 5 August 2021



S. F. Peterson^{a)}  and Y. U. Idzerda^{b)} 

AFFILIATIONS

Department of Physics, Montana State University, Bozeman, Montana 59717, USA

^{a)}Author to whom correspondence should be addressed: seanpeterson9@montana.edu

^{b)}Electronic mail: idzerda@montana.edu

ABSTRACT

Anisotropy constants of magnetic materials are typically determined through angle-resolved Ferromagnetic Resonance (ar-FMR) and torque magnetometry, which can be time consuming measurements, thus limiting their utility. The Stoner–Wohlfarth model can be used to numerically fit measured magnetic hysteresis curves to more easily determine these anisotropy constants. To demonstrate this, 10 nm bct Fe_xCo_yMn_z single-crystal films grown by molecular beam epitaxy on MgO(001) substrates were investigated. The hysteresis behavior measured by vibrating sample magnetometry was least-squares fit against numerically calculated hysteresis curves generated from the Stoner–Wohlfarth model to extract the anisotropy constants. The cubic anisotropy of different compositions of FeCoMn films was at $\sim 10^4$ J/m³, which is on the same order of magnitude of bct Fe and Co thin films measured by ar-FMR and torque magnetometry techniques.

© 2021 Author(s). All article content, except where otherwise noted, is licensed under a Creative Commons Attribution (CC BY) license (<http://creativecommons.org/licenses/by/4.0/>). <https://doi.org/10.1063/5.0051454>

I. INTRODUCTION

Anisotropic magnetic materials have applications in many forms of magnetic memory, ranging from hard drive technologies to magnetic RAM (MRAM).^{1,2} The stability of a bit to thermal fluctuations depends on its total moment, its total magnetic anisotropy, and any fringing magnetic fields from nearby bits. The information density of magnetic memory storage devices can be increased by enhancing the magnetization density of the bit material or by increasing the strength of that material's magnetic anisotropy.³ Recently, single-crystal bct films of FeCoMn have been synthesized, which greatly increases the magnetization density beyond the Slater-Pauling limit,⁴ but the magnetic anisotropy of these ternary films is yet to be fully explored.

Historically, the strength of the magnetic anisotropy was determined by either performing angle-resolved Ferromagnetic Resonance (ar-FMR)⁵ or by torque magnetometry.⁶ Unfortunately, such measurements are time intensive and not suitable to combinatoric methods where large sample composition ranges can be explored and appropriately mapped as a function of composition. Hysteresis loops measured using the surface magneto-optical Kerr Effect

(SMOKE) have been successfully used in a combinatorics study to identify the ferromagnetic region of the ternary phase diagram for sputtered polycrystalline FeCoV films.⁷ Similarly, combinatoric synthesis coupled with Vibrating Sample Magnetometry (VSM) has been used to map the coercive field variation over the ternary composition space of FeCoW⁸ and FeCoNb⁹ films for applications as low-cost alternatives to rare-earth permanent magnets. Although the primary focus of these combinatoric studies was controlling the coercive field values through the alloys' composition, it was found that the coercive field was also dependent on extrinsic surface/interface roughness.^{10,11}

Intrinsic anisotropy constants could be a more useful measure of the magnetic utility and can be determined directly from a comparison of the magnetic hysteresis with calculated loops predicted within the Stoner–Wohlfarth (SW) model. This process could be further improved by using the data from existing combinatorics studies to train a machine-learning algorithm¹² to predict alloys with more desirable material parameters, such as higher magnetization densities and anisotropy constants (as was carried out to predict larger magnetic moments through the addition of Pt and Ir to FeCo alloys¹³).

II. MODEL GEOMETRY

The Stoner–Wohlfarth (SW) model is applicable to any sample geometry, but the fitting algorithm can be greatly simplified by selecting particular measurement geometries that exploit the dominant anisotropy within the material (from crystalline or shape anisotropy). By restricting the applied field to be coincident with selected crystallographic directions, specific anisotropy constants can be more easily determined. In the general case (or where there is no dominant anisotropy), vector magnetometry can be used to simultaneously determine all anisotropy constants from numerically fitting multiple hysteresis loops.

The samples in this work are single-crystal 10–20 nm thick bcc $\text{Fe}_x\text{Co}_y\text{Mn}_z$ thin films deposited on MgO(001) by Molecular Beam Epitaxy (MBE) and capped with 3 nm of Al to prevent oxidation. These films have a large perpendicular anisotropy, confining the magnetization to be within the film plane. Restricting the applied field to the film plane allows for determination of the in-plane cubic anisotropy constants.

The focus of this work is on the first-order cubic anisotropy term, K_1 , but the second-order term, K_2 (typically smaller by an order of magnitude), can be likewise determined. By depositing these films on a MgO(001) substrate, the epitaxial nature of the films and the in-plane geometry of the applied field eliminate the contribution of the second-order term. The second-order term does become important for field sweeps taken out of the film plane, especially for field sweeps along the [111] direction.¹⁴ Even in those cases where the magnetization canted out of the film plane, it has been shown¹⁵ that the effect of the K_2 term on the magnetic hysteresis loop is minimal unless K_2 is orders of magnitude larger than K_1 .

III. STONER-WOHLFARTH MODEL

Using the geometry seen in Fig. 1, it is possible to construct an energy that incorporates the in-plane cubic anisotropy and the coupling between the applied magnetic field and the magnetization.

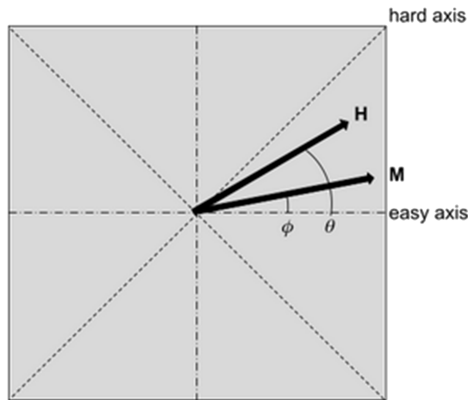


FIG. 1. Thin film magnet with an in-plane cubic anisotropy and $K_1 > 0$. ϕ is the angle between the x-axis and the magnetization direction, and θ is the angle between the x-axis and the applied magnetic field direction.

Using the macroscopic spin approximation, the film magnetization is viewed as a single magnetic domain with a constant magnitude but variable direction. This approximation works well for thin film single-crystal samples that have been previously magnetized to their saturation magnetization. The dominant terms of the energy for such a system are

$$E = K_1 \sin^2 \phi \cos^2 \phi - \mu_0 \vec{H} \cdot \vec{M}, \quad (1)$$

where the first term is the first-order cubic anisotropy energy of constant K_1 and the second is the Zeeman energy. As discussed above, the second-order cubic anisotropy constant, K_2 , has been neglected but can be similarly determined if hysteresis measurements are taken in (or near) the [111] plane. This can be rewritten in terms of the reduced energy Γ , by normalizing E by K_1 ,

$$\Gamma = \sin^2 \phi \cos^2 \phi - 2\vec{h} \cdot \vec{M}/M_S, \quad (2)$$

where the reduced field $\vec{h} = \frac{\vec{H}}{H_K}$, $H_K = \frac{2K_1}{\mu_0 M}$, \vec{M} is the magnetization vector, and M_S is the saturation magnetization. The most energetically favorable orientation for the magnetization direction, ϕ , is determined from $\frac{\partial \Gamma}{\partial \phi} = 0$ and $\frac{\partial^2 \Gamma}{\partial \phi^2} > 0$ at every value of the normalized applied magnetic field (h) and at a particular sweep field direction (θ), which is held constant.

These energy minima for the magnetization direction as a function of the applied magnetic field strength can be seen in Fig. 2 as red shaded curves. The blue shaded curves have negative second-derivatives and are unstable energy maxima. The normalized hysteresis loop is simply the cosine of the angle between the applied magnetic field and the magnetization [$\vec{h} \cdot \vec{M}/M_S = \cos(\phi - \theta)$] and is shown in Fig. 3.

The minor loops present in the model hysteresis are indicative of a two-step hysteresis, an effect which was measured experimentally by Daboo.¹⁶ These minor loops were theoretically treated by

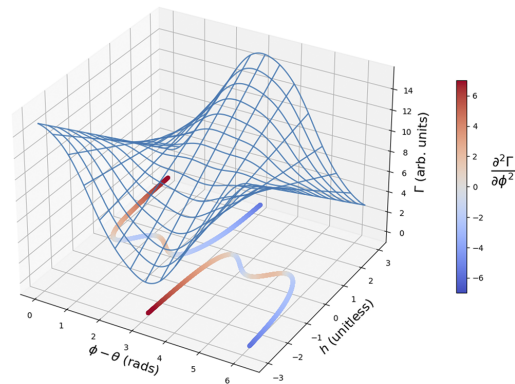


FIG. 2. Normalized energy surface for Eq. (2) at a constant $\theta = \frac{\pi}{12}$, with $\phi(h)$ when $\frac{\partial \Gamma}{\partial \phi} = 0$ is plotted on the bottom plane and shaded proportional to $\frac{\partial^2 \Gamma}{\partial \phi^2}$.

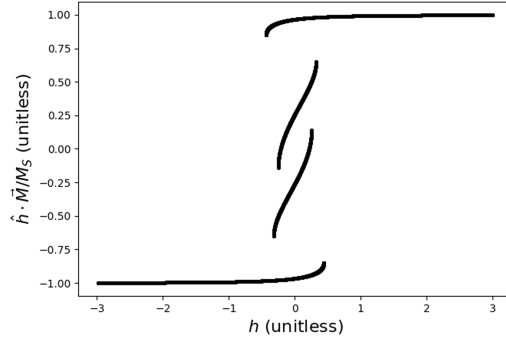


FIG. 3. Magnetic hysteresis of the thin film magnet when $\theta = \frac{\pi}{12}$, with two-step hysteresis, which gets removed when fitting to data.

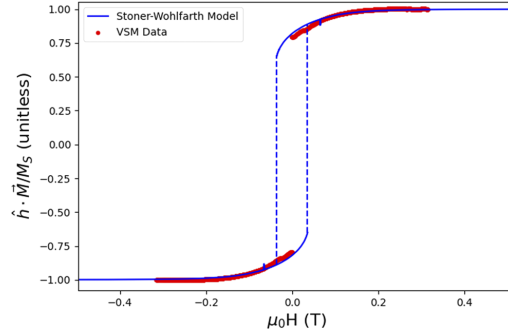


FIG. 4. Stoner-Wohlfarth model best fit to magnetic hysteresis data.

Usov¹⁷ for bulk materials with cubic anisotropies with three equivalent crystalline directions (x , y , and z) whereas the samples considered in this work only have two magnetically equivalent directions due to a tetragonal distortion and the thin film magnetic shape anisotropy, which violate the cubic symmetry in the z -direction.

Historically, the agreement between the Stoner-Wohlfarth model hysteresis loop (using known magnetization and magnetic anisotropy constants) and the measured hysteresis loop was used to validate the SW model.¹⁸ This model can be applied to any sample geometry, as has been carried out for fcc Co nanoparticles¹⁹ and magnetic spin valves,¹⁸ the latter of which include an additional energy term for the magnetic interaction between two magnetic layers of the spin-valve. The process used to validate the SW model can also be inverted to determine the magnetization and magnetic anisotropy constants through a least-squares fitting method. Measured hysteresis loops are the projection of the magnetization vector along the analysis direction. If the analysis direction coincides with the applied field direction (as is typically carried out), the normalized hysteresis loop is again the cosine of the angle between the applied magnetic field and the magnetization.

IV. RESULTS

Residuals between the calculated Stoner-Wohlfarth model magnetizations for a given θ and H_K are found and used in a least-squares fitting algorithm to fit to the model parameters. A typical fit of this type can be seen in Fig. 4. The cubic anisotropy constant can be calculated with the definition of $H_K = \frac{2K_1}{\mu_0 M}$. This procedure was performed on the hysteresis loops of several $\text{Fe}_x\text{Co}_y\text{Mn}_z$ films with different compositions. Details of the growth and composition determination are reported elsewhere.⁴ The hysteresis loops were acquired using the VSM option of the Quantum Design Physical Properties Measurement System (PPMS) calibrated by the NIST Pd standard. The hysteresis had a linear, diamagnetic background removed (from the MgO substrate) and was smoothed with a Gaussian filter. The results of these fits are presented in Table I.

These values are on the same order as epitaxial bcc Fe(100) on GaAs(100),²⁰ epitaxial bcc Co on GaAs(110),²¹ and epitaxial bcc Co on GaAs(001)²² cubic anisotropies, which were found by ar-FMR to

TABLE I. Cubic anisotropy constant K_1 from fitting Stoner-Wohlfarth model calculated hysteresis loops to VSM measured hysteresis loops for bcc $\text{Fe}_x\text{Co}_y\text{Mn}_z$ films.

x	y	z	$M(10^{-7} \text{ A m}^2)$	$K_1(10^4 \text{ J/m}^3)$
0.33	0.60	0.07	1.1 ± 0.1	2.7 ± 0.1
0.43	0.47	0.10	1.3 ± 0.1	2.3 ± 0.1
0.43	0.46	0.11	2.3 ± 0.1	6.3 ± 0.3
0.47	0.42	0.12	1.7 ± 0.1	3.9 ± 0.2
0.40	0.42	0.18	2.4 ± 0.1	4.1 ± 0.2

be $2.4 \cdot 10^4 \text{ J/m}^3$, $-6.6 \cdot 10^4 \text{ J/m}^3$, and $2.6 \cdot 10^4 \text{ J/m}^3$, respectively. The anisotropy constants in these cases were found to depend on film thickness.

V. CONCLUSIONS

The Stoner-Wohlfarth model calculated hysteresis loops computationally coupled with a least-squares fitting algorithm and some simple data filtering techniques create a viable method for determining anisotropy constants from magnetic hysteresis data. Not only can cubic anisotropy constants be determined but a similar technique can also be applied to more complicated energies to predict their hysteresis behavior as well (including higher order anisotropy terms, surface/interface anisotropy contributions, fringe field interactions, etc.). For example, second-order, K_2 , cubic anisotropy could be considered for hysteresis loops measured near the [111] crystal plane. This also opens the possibility of quantifying effects that contribute to a hysteresis other than these anisotropies including interlayer coupling between a free layer and a pinned layer magnetization¹⁸ with a single fitting procedure.

This technique has been shown to extract cubic anisotropy constants, in good agreement with known first-order cubic anisotropies presented in the literature. However, it is not without its limitations; square hysteresis loops acquired along the easy axis cannot be used. Experience shows that hysteresis data taken at angles near the central angle between the easy and hard axes of the sample achieve the best results for the extraction of the fit parameters.

The sample must have reached its saturation magnetization from a sufficiently large applied magnetic field so that the macroscopic spin approximation is valid. Simultaneously fitting hysteresis loops taken at a few angles for the same sample could improve the anisotropy determination further. Despite requiring hysteresis measurements to be taken at several angles, this technique would require data to be taken at far fewer angles than ar-FMR techniques, which typically require data to be taken roughly every 5°.

In previous combinatorics studies,⁷⁻⁹ the anisotropy constants of many alloys have only been characterized qualitatively in favor of easily studying measurement of magnetic properties such as the coercive field and the saturation magnetization. These are typically determined from the hysteresis of the sample measured either with a VSM or a MOKE magnetometer, the data of which can be retroactively used to determine magnetic anisotropy constants as well. However, determining the anisotropy constants of these materials may require modifications of the energy equation to include different orders of anisotropy, such as uniaxial anisotropy (both perpendicular shape anisotropy and in-plane uniaxial anisotropy generated from details of the film growth) or second-order cubic terms; fortunately, the analysis process would remain relatively unchanged. Coupled with a machine-learning algorithm,^{12,13} these data and the relevant composition data of the samples could be used to predict new magnetic materials.

ACKNOWLEDGMENTS

This work was supported by the National Science Foundation through Grant No. 1809846. We would like to thank Collin Crites and Frank Schooner for useful discussions and suggesting corrections to this manuscript.

DATA AVAILABILITY

The data that support the findings of this study are available from the corresponding author upon reasonable request.

REFERENCES

- ¹B. Tudu *et al.*, "Recent developments in perpendicular magnetic anisotropy thin films for data storage applications," *Vacuum* **146**, 329 (2017).
- ²W. Kang *et al.*, "Modeling and exploration of the voltage-controlled magnetic anisotropy effect for the next-generation low-power and high-speed MRAM applications," *IEEE Trans. Nanotechnol.* **16**, 387 (2017).

- ³T. Burkert *et al.*, "Giant magnetic anisotropy in tetragonal FeCo alloys," *Phys. Rev. Lett.* **93**, 027203 (2004).
- ⁴R. J. Snow *et al.*, "Large moments in bcc Fe_xCo_yMn_z ternary alloy thin films," *Appl. Phys. Lett.* **112**, 072403 (2018).
- ⁵G. A. Prinz, "Magnetic anisotropy in epitaxial metal films," *Ultramicroscopy* **47**, 346 (1992).
- ⁶J. Rigue *et al.*, "A torque magnetometer for thin films applications," *J. Magn. Magn. Mater.* **324**, 1561 (2012).
- ⁷S. W. Fackler *et al.*, "Combinatorial study of Fe-Co-V hard magnetic thin films," *Sci. Technol. Adv. Mater.* **18**, 231 (2017).
- ⁸T. R. Gao *et al.*, "Combinatorial exploration of rare-earth-free permanent magnets: Magnetic and microstructural properties of Fe-Co-W thin films," *Appl. Phys. Lett.* **102**, 022419 (2013).
- ⁹V. Alexandrakis *et al.*, "Combinatorial development of Fe-Co-Nb thin film magnetic nanocomposites," *ACS Comb. Sci.* **17**, 698 (2015).
- ¹⁰S. Vilain *et al.*, "Surface roughness and composition effects on the magnetic properties of electrodeposited Ni-Co alloys," *J. Magn. Magn. Mater.* **157-158**, 274 (1996).
- ¹¹Y. P. Zhao *et al.*, "Effect of surface roughness on magnetic domain wall thickness, domain size and coercivity," *J. Appl. Phys.* **89**, 1325 (2001).
- ¹²A. G. Kusne *et al.*, "On-the-fly machine-learning for high-throughput experiments: Search for rare-earth-free permanent magnets," *Sci. Rep.* **4**, 6367 (2014).
- ¹³Y. Iwasaki *et al.*, "Machine learning autonomous identification of magnetic alloys beyond the Slater-Pauling limit," *Commun. Mater.* **2**, 31 (2021).
- ¹⁴J. Geshev *et al.*, "Dependence of the magnetization and remanence of single-domain particles on the second cubic anisotropy constant," *J. Appl. Phys.* **90**, 6243 (2001).
- ¹⁵J. Garcia-Otero *et al.*, "Influence of the cubic anisotropy constants on the hysteresis loops of single-domain particles: A Monte Carlo study," *J. Appl. Phys.* **85**, 2287 (1999).
- ¹⁶C. Daboo *et al.*, "Anisotropy and orientational dependence of magnetization reversal process in epitaxial ferromagnetic thin films," *Phys. Rev. B* **51**, 15964 (1995).
- ¹⁷N. A. Usov and S. E. Peschany, "Theoretical hysteresis loops for single-domain particles with cubic anisotropy," *J. Magn. Magn. Mater.* **174**, 247 (1997).
- ¹⁸M. Labrune *et al.*, "Magnetization rotation in spin-valve multilayers," *J. Magn. Magn. Mater.* **171**, 1 (1997).
- ¹⁹W. Wernsdorfer *et al.*, "Magnetisation reversal by uniform rotation (Stoner-Wohlfarth model) in FCC cobalt nanoparticles," *J. Magn. Magn. Mater.* **242-245**, 132 (2002).
- ²⁰J. Krebs *et al.*, "Properties of Fe single-crystal films grown on (100)GaAs by molecular-beam epitaxy," *J. Appl. Phys.* **61**, 2596 (1987).
- ²¹G. A. Prinz *et al.*, "FMR of cubic cobalt grown by molecular beam epitaxy on GaAs," *J. Appl. Phys.* **57**, 3672 (1985).
- ²²S. J. Blundell *et al.*, "Structure induced magnetic anisotropy behavior in Co/GaAs(001) films," *J. Appl. Phys.* **73**, 5948 (1993).

THERMAL TRANSPORT IN TWO-DIMENSIONAL NEMATIC SUPERCONDUCTORS

Contribution of Authors and Co-Authors

Manuscript in following chapter

Author: [Sourav Sen Choudhury]

Contributions: [Theory lead of project. Posed problem as continuation of work from: *Phys. Rev. B*, 103:104501, 2021. Where an electronic nematic phase coexisting with superconductivity was considered instead of a $\mathbf{Q} = (\pi, \pi)$ SDW phase coexisting with superconductivity. Provided theoretical framework of problem as applied to previous superconducting states as a background for theoretical work in this paper.]

Author: [Sean Peterson]

Contributions: [Computational lead of project. Wrote all relevant code and ran it on Nautilus cluster in order to collect data and produce figures for this work. Applied theoretical framework from previous works to derive equations vital to the calculations done in this work.]

Author: [Yves Idzerda]

Contributions: [Principle Investigator.]

Manuscript Information

[Sourav Sen Choudhury, Sean Peterson, Yves Idzerda]

[Phys. Rev. B]

Status of Manuscript:

Prepared for submission to a peer-reviewed journal

Officially submitted to a peer-reviewed journal

Accepted by a peer-reviewed journal

Published in a peer-reviewed journal

[American Physical Society]

[May 4, 2022]

[June 21, 2022]

[Phys. Rev. B **105**]

[<https://doi.org/10.1103/PhysRevB.105.214515>]

Thermal transport in two-dimensional nematic superconductors

Sourav Sen Choudhury, Sean Peterson , and Yves Idzerda
Department of Physics, Montana State University, Bozeman, Montana 59717, USA

 (Received 4 May 2022; revised 9 June 2022; accepted 13 June 2022; published 21 June 2022)

We study the thermal transport in a two-dimensional system with coexisting superconducting (SC) and nematic orders. We analyze the nature of the coexistence phase in a tight-binding square lattice where the nematic state is modelled as a d -wave Pomeranchuk-type instability and the feedback of the symmetry breaking nematic state on the SC order is accounted for by mixing of the s , d pairing interaction. The electronic thermal conductivity is computed within the framework of Boltzmann kinetic theory where the impurity scattering collision integral is treated in the Born and unitary limits. We present qualitative, analytical, and numerical results that show that the heat transport properties of SC states emerging from a nematic background are quite distinct and depend on the degree of anisotropy of the SC gap induced by nematicity. We describe the influence of the Fermi surface topology, the van Hove singularities, and the presence or absence of zero-energy excitations in the coexistence phase on the low-temperature behavior of the thermal conductivity. Our main conclusion is that the interplay of nematic and SC orders has visible signatures in the thermal transport, which can be used to infer SC gap structure in the coexistence phase.

DOI: [10.1103/PhysRevB.105.214515](https://doi.org/10.1103/PhysRevB.105.214515)

I. INTRODUCTION

Low-temperature transport properties of normal metals are primarily determined by the scattering of electrons by impurities. For heat transport, the linear T dependence of the thermal conductivity $\kappa_n(T)$ can be explained using semiclassical transport theory based on the Boltzmann kinetic equation [1], which has also been used to explain heat transport properties of conventional superconductors [2]. The advent of unconventional superconductors like heavy fermions [3], cuprates [4–7], and iron-based superconductors [8–10], lead to new questions regarding the low-temperature transport properties of such systems since the unconventional superconductors significantly differ from the uniformly gapped conventional superconductors and their gap structure may contain nodal points [i.e., points on the Fermi surface (FS) where the superconducting gap is zero]. The small energy gap surrounding the nodal points allows quasiparticles to be easily excited and hence these nodal quasiparticles dominate the heat transport properties at low temperatures. Thermal transport in unconventional superconductors has been previously studied theoretically by various authors with different levels of sophistication [11–16], and thermal conductivity measurements are a useful probe of the gap structure of unconventional superconductors [17,18].

Unconventional superconductors possess complex phase diagrams with multiple broken symmetry phases coexisting with superconductivity. Often these multiple phases appear at similar ordering temperatures when material properties (like dopant concentration) are varied over wide ranges. While it is fairly common for unconventional superconductors to have proximate magnetic and superconducting orders [19–23], only in recent years have nematic states been reported for

both iron-based superconductors [24–26] as well as cuprates [27–32]. (Here nematic order means electronic nematicity, where the electronic state has the same translational symmetry as the underlying crystal, but a lower rotational symmetry.) Studies on the origin of the nematic state [33] argue that in iron-based superconductors, nematic order is driven by either spin fluctuations [34,35] (in the case of pnictides) or orbital fluctuations [36–38] (in the case of chalcogenides). For cuprates it has been proposed that the nematicity arises from fluctuations of stripe order [39,40] or from the instability of the Fermi surface (Pomeranchuk instability) [41–44]. Further the superconducting instability in a nematic electron fluid has been studied using renormalization group (RG) techniques [45]. It has been shown that fluctuations of the nematic order parameter at the quantum critical point eventually leads to the superconducting pairing instability.

Regardless of the origin of the nematic state, the influence of nematicity on the emerging superconducting state can change the character of the superconducting order from s -wave to d -wave pairing [46]. Additionally, since the anisotropy of the superconducting state correlates with the Fermi surface deformation of the nematic state, the competition or cooperation between the SC and nematic orders is found to depend on the nematic distortion of the Fermi surface relative to the anisotropy of the superconducting gap function [47].

Nematic superconductors themselves may display interesting thermal transport behavior. For instance, the nematic to isotropic quantum phase transition deep within the d -wave superconducting phase of a two-dimensional tetragonal crystal are predicted, within the framework of the Boltzmann equation, to display a logarithmic enhancement of the thermal conductivity at the nematic critical point [48]. Other

theoretical studies, performed using the quasiclassical formalism, show that the oscillations of the thermal conductivity in multiband superconductors with an anisotropic gap under a rotating magnetic field, change sign at low temperatures and fields and can be used to distinguish between nodes and minima in the energy gap of iron-based superconductors [49,50].

Recent experimental studies have examined the structure of the SC gap in iron-based nematic superconductors. Using specific heat measurements, it was found that the electronic specific heat was linear in T for $T < T_c$, indicating the presence of line nodes [51] while angle-resolved photo-emission spectroscopy (ARPES) [52] observed spontaneous breaking of the rotational symmetry of the SC gap amplitude as well as the unidirectional distortion of the Fermi pockets. (It should be noted that this latter study indicated that in the compound LiFeAs, nematicity could occur below T_c and speculated that superconducting state develops a spontaneous nematic order at T_c .)

The gap structure of nematic superconductors have also been probed by thermal conductivity experiments [53,54] demonstrating that in the $T \rightarrow 0$ limit, the residual linear term $\kappa(T)/T$ is extremely small, indicating nodeless superconductivity in FeSe. Finally in the case of cuprate superconductors [28,29] and strontium ruthenate materials [55], transport measurements show large strongly temperature-dependent anisotropies in these otherwise isotropic electronic systems.

Motivated by these experimental studies and in complement to previous theoretical studies, this paper investigates the thermal transport properties of a nematic system, where the superconducting phase arises out of a nematic background (i.e., the onset of SC order occurs at a lower temperature than the nematic order). To treat the nematic and SC orders on equal footing, we introduce a mean-field Hamiltonian and determine how the interaction between these coexisting phases impacts the heat transport properties of the system. We emphasize that in this paper we study a single-band electronic system with a tight binding dispersion $\xi_{\mathbf{k}}$. We do not consider the effects arising from the multiplicity of bands and therefore neglect orbital degrees of freedom. Thus our analysis is not directly applicable to iron pnictide superconductors (where multi orbital mixing plays a significant role), but is more relevant for cuprate superconductors. Nevertheless, we believe that the analysis given below provides important insights regarding the interplay of superconducting and nematic orders and their impact of thermal transport properties of such systems, particularly in the coexistence phase.

For our transport calculations we use the quasiparticle Boltzmann equation (which is physically more transparent than calculations based on the Green's function or quasiclassical methods), and calculate the thermal conductivity for the case where the dominant scattering process of quasiparticles is by nonmagnetic impurities. Within Boltzmann theory, we only consider the case of small phase shifts (i.e., the Born approximation) and phase shifts close to $\pi/2$ (i.e., the unitary limit). The quasiparticle Boltzmann approach fails at low temperatures when low-energy quasiparticles cannot be well established due to impurity broadening. In the following we assume that a quasiparticle description applies [56].

The organization of the paper is as follows. In Sec II A, we discuss the model Hamiltonian and the formalism we

have employed. The self-consistent approach to determining coexisting nematic and SC order parameters is presented in Sec. II B and the kinetic formalism is described in Sec. II C. Numerical results for heat conductivity are discussed in Sec. III. Section IV is a brief conclusion.

II. MODEL AND FORMALISM

A. Hamiltonian

For our model we consider a 2D system with a single band with an inversion symmetric dispersion $\xi_{\mathbf{k}} (= \xi_{-\mathbf{k}})$ given by

$$H_0 = \sum_{\mathbf{k}, \sigma = \pm 1} \xi_{\mathbf{k}} c_{\mathbf{k}\sigma}^\dagger c_{\mathbf{k}\sigma}, \quad (1)$$

where

$$\xi_{\mathbf{k}} = -2[t_1(\cos k_x + \cos k_y) + 2t_2 \cos k_x \cos k_y] - \mu.$$

This describes the nearest-neighbor and next-nearest-neighbor hopping on a 2D square lattice with lattice spacing $a = 1$. The nematic state is modelled through an additional mean-field Hamiltonian [57]

$$H_{\text{nem}} = \sum_{\mathbf{k}, \sigma} \Phi f_{\mathbf{k}} c_{\mathbf{k}\sigma}^\dagger c_{\mathbf{k}\sigma}, \quad \Phi = -V_{\text{nem}} \sum_{\mathbf{k}} f_{\mathbf{k}} (c_{\mathbf{k}}^\dagger c_{\mathbf{k}}), \quad (2)$$

where Φ is the nematic order parameter and $f_{\mathbf{k}} = (\cos k_x - \cos k_y)$. This additional term causes a deformation of the Fermi surface (FS), which elongates it along the k_x axis and shrinks it along the k_y axis as is illustrated in Fig. 1. Thus in the nematic state (when $\Phi \neq 0$) the deformed FS does not have the same point group symmetry of the underlying 2D lattice and can capture the effect of symmetry-breaking FS deformations on the SC state [47]. In this paper, only the case where the nematic transition temperature is greater than the superconducting critical temperature ($T_N > T_c$) is considered (i.e., superconductivity arises inside the nematic state).

The effect of the symmetry-broken nematic state on the development of the SC order can be accounted for by using a SC order parameter of the form [47]

$$\Delta_{\mathbf{k}} = \Delta \mathcal{Y}_{\mathbf{k}}$$

where $\mathcal{Y}_{\mathbf{k}} = (1 + r f_{\mathbf{k}}) / \sqrt{1 + r^2}$ ($\mathcal{Y}_{\mathbf{k}}$ is normalized by $\sqrt{1 + r^2}$ to ensure that $\int \frac{d^2k}{(2\pi)^2} |\mathcal{Y}_{\mathbf{k}}|^2 = 1$) and $\Delta_{\mathbf{k}} = \Delta_{-\mathbf{k}}$. Here r is a phenomenological anisotropy parameter and is a measure of the degree of anisotropy caused by the coexisting nematic order. (The anisotropy parameter r is proportional Φ and when Φ is zero, the SC interaction reduces to pure s wave.) This form of the order parameter encapsulates the mixing of the s and d -wave components induced by nematicity (it is assumed that superconductivity only exists in the spin singlet channel). While $r \propto \Phi$, it should be noted that it also depends on details of the electronic structure [47] that are beyond the scope of this paper (hence r is treated as a phenomenological parameter). In the nematic state, $r \neq 0$ and can be either positive or negative.

In Fig. 2, the nonuniform SC gap amplitude is illustrated as a colored band bordering the deformed FS for different values of the anisotropy parameter r . As shown in the figure, the direction of the SC gap maximum relative to the direction FS elongation (induced by the nematic order) depends on whether

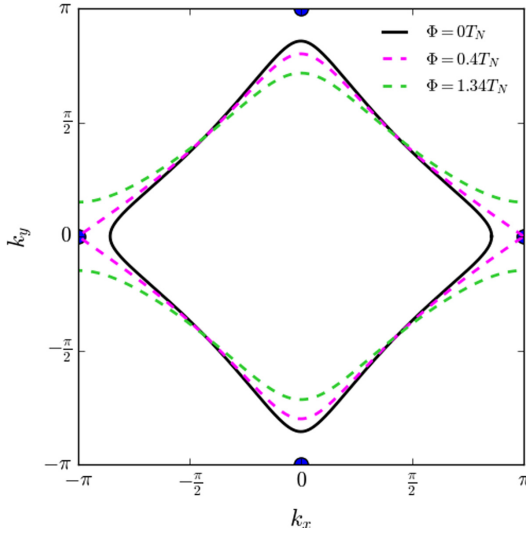


FIG. 1. Evolution of the Fermi surface shape under nematic distortion at different temperatures. Closed FS ($\mu = -4.8T_N$) at $T > T_N$ (black curve), at $T = 0.97T_N$ (magenta curve) and $T = 0$ (green curve). The blue dots indicate the locations of the saddle points in the band structure that lead to van Hove singularities in the bare DOS (see Fig. 5). It can be seen that the magenta curves pass through the saddle points at $(\pi, 0)$. The band parameters are $t_1 = 6T_N$ and $t_2 = -T_N$.

r is positive or negative. Thus, the superconducting part of the mean-field Hamiltonian can be written as

$$H_{SC} = \frac{1}{2} \sum_{\mathbf{k}, \sigma} \sigma \Delta \mathcal{Y}_{\mathbf{k}} (c_{\mathbf{k}\sigma}^\dagger c_{-\mathbf{k}-\sigma}^\dagger + \text{H.c.}),$$

$$\Delta = -V_{SC} \sum_{\mathbf{k}} \mathcal{Y}_{\mathbf{k}} (c_{-\mathbf{k}, \downarrow} c_{\mathbf{k}, \uparrow}), \quad (3)$$

and the full mean-field Hamiltonian for intertwined nematic and superconducting orders given by

$$H = H_0 + H_{\text{nem}} + H_{SC}$$

can be recast into a matrix form for particular spin orientations $\sigma = \pm 1(\uparrow, \downarrow)$

$$H^{(\sigma)} = \frac{1}{2} \sum_{\mathbf{k}} \hat{\Psi}_{\mathbf{k}, \sigma}^\dagger \hat{\mathcal{H}}_{\mathbf{k}}^{(\sigma)} \hat{\Psi}_{\mathbf{k}, \sigma},$$

$$\hat{\mathcal{H}}_{\mathbf{k}}^{(\sigma)} = \begin{pmatrix} \xi_{\mathbf{k}} + \Phi f_{\mathbf{k}} & \sigma \Delta_{\mathbf{k}} \\ \sigma \Delta_{\mathbf{k}} & -\xi_{\mathbf{k}} - \Phi f_{\mathbf{k}} \end{pmatrix}, \quad (4)$$

where $\hat{\Psi}_{\mathbf{k}, \sigma}^\dagger = (c_{\mathbf{k}\sigma}^\dagger, c_{-\mathbf{k}-\sigma})$ is the Nambu vector. The leading factor of $1/2$ is from the particle-hole doubling of the bands in superconductivity. The eigenvalues of $\hat{\mathcal{H}}_{\mathbf{k}}^{(\sigma)}$ give the quasi-particle energies, $\pm E_{\mathbf{k}}$, where

$$E_{\mathbf{k}} = \sqrt{(\xi_{\mathbf{k}} + \Phi f_{\mathbf{k}})^2 + \Delta_{\mathbf{k}}^2}. \quad (5)$$

As noted earlier, the nature of the spectrum critically depends on the value of the anisotropy parameter, r . When $r > 0$,

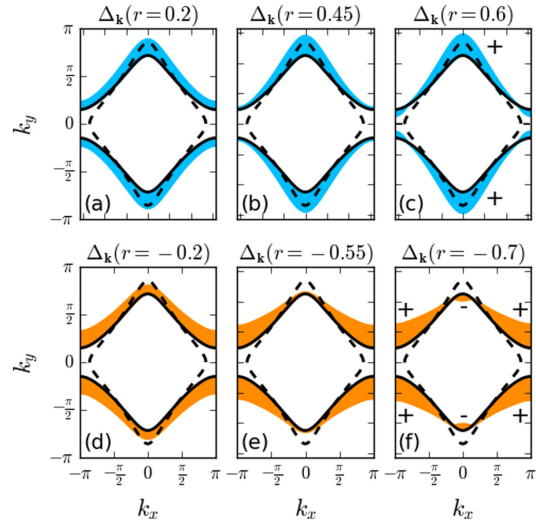


FIG. 2. A qualitative illustration of the superconducting gap amplitude for different values of the anisotropy parameter r along the FS deformed by the nematic order (dotted line indicates original FS, solid line indicates deformed FS). For positive values of r , the direction of the the SC gap maximum (cyan) is antialigned with the FS elongation. For negative values of r , the direction of the the SC gap maximum (orange) is aligned with the FS elongation. The parameters used for the illustration are $\mu = -4.8T_N$, $t_1 = 6T_N$, $t_2 = -T_N$, $\Delta = 0.2T_N$, and $\Phi = 1.34T_N$.

the spectrum has nodes (i.e., points on the nematic FS for which $E_{\mathbf{k}} = 0$) only if the parameter r exceeds a critical value $r > r_c^+$ where $r_c^+ = -\frac{2t_1 t_2 + t_2 \Phi - 4t_2^2}{4t_2^2 + t_2 \mu - 4t_1 t_2}$. When $r < 0$, the spectrum has nodes only if the parameter r is below a critical value $r < r_c^-$ where $r_c^- = -\frac{2t_1 t_2 + t_2 \Phi + 4t_2^2}{4t_2^2 + t_2 \mu + 4t_1 t_2}$. These critical values r_c^\pm can be determined from the condition $E_{\mathbf{k}} = 0$, which occurs only when $\xi_{\mathbf{k}} \equiv \xi_{\mathbf{k}} + \Phi f_{\mathbf{k}}$ and $\Delta_{\mathbf{k}}$ simultaneously vanish. To find the location of the nodes we set

$$\tilde{\xi}_{\mathbf{k}} = 0 \Rightarrow k_y^* = \cos^{-1} \left(-\frac{\mu + 2t_1 \cos k_x - \Phi \cos k_x}{2t_1 + 4t_2 \cos k_x + \Phi} \right), \quad (6)$$

which gives us the k_y coordinates of all points along the nematically deformed FS on the upper half of the BZ as a function of k_x . To find the locations of the nodes on the deformed FS, we set

$$\Delta_{(k_x, k_y^*)} = 0 \Rightarrow k_x^\pm = \cos^{-1} \left(\frac{-t_2 - r t_1 \pm p}{2r t_2} \right),$$

$$p = \sqrt{t_2^2 + r^2 t_1^2 - r t_2 \Phi - r^2 \mu t_2}. \quad (7)$$

In Fig. 3(a) we display k_x^\pm as a function of r , which identifies the critical values r_c^\pm and shows that nodes only exist at k_x^+ when r is positive and at k_x^- when r is negative. The location of these nodes depends on the value of the parameter r . Figure 3(b) shows the range of locations of the point nodes on the deformed FS as r takes values in the

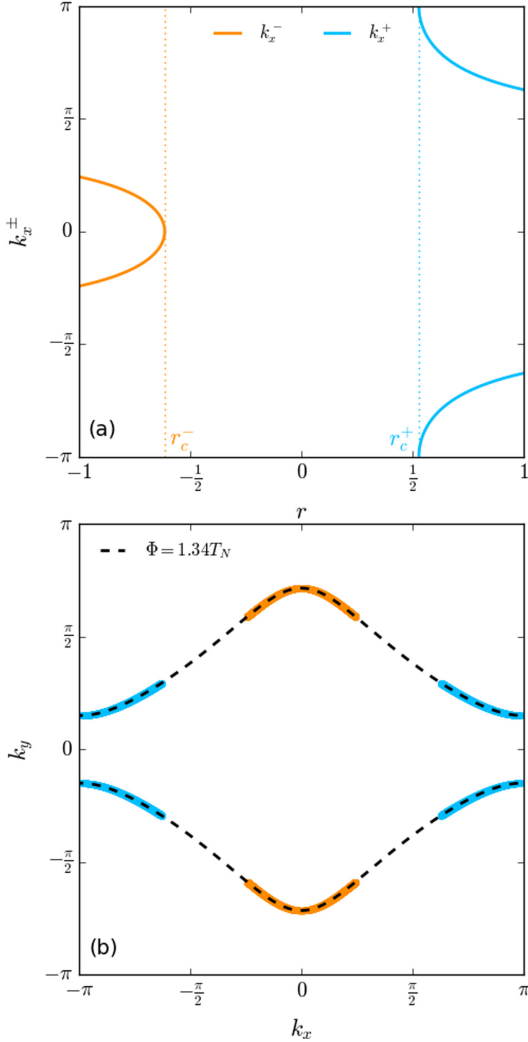


FIG. 3. (a) Equation (7) has solutions k_x^+ only when $r > r_c^+$ (cyan curve) and k_x^- only when $r < r_c^-$ (orange curve). With the parameters $\mu = -4.8T_N$, $t_1 = 6T_N$, $t_2 = -T_N$, and $\Phi = 1.34T_N$, the critical r values are $r_c^+ \approx 0.52866$ and $r_c^- \approx -0.61447$. The dotted-vertical lines emphasize that there are no solutions to Eq. (7) when r is in the range $r_c^- < r < r_c^+$. (b) Range of locations $(\pm k_x^+, \pm k_y^*)$ of the nodes when $r_c^+ < r < 1$ (shaded in cyan) and $(\pm k_x^-, \pm k_y^*)$ when $-1 < r < r_c^-$ (shaded in orange). A particular r value only corresponds to point nodes located either in the cyan regions or in the orange regions.

range $r_c^+ < r < 1$ (region shaded in cyan) and $-1 < r < r_c^-$ (region shaded in orange). It should be emphasized that at any given r value only a single point node exists in each quadrant of the BZ, the shaded regions only represent the range of locations.

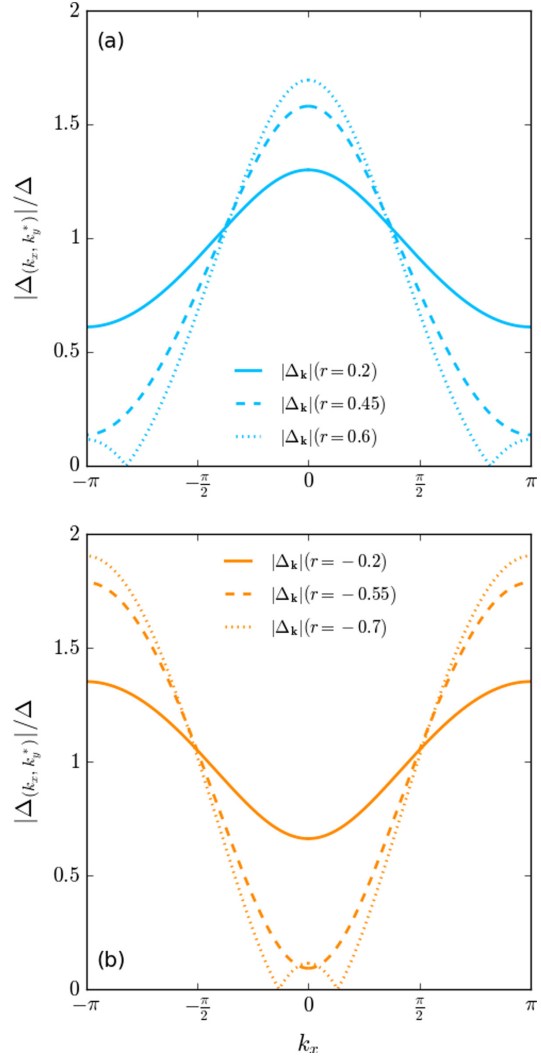


FIG. 4. Gap amplitude $|\Delta_{\mathbf{k}}|$ in the coexistence phase along the nematically deformed FS ($\tilde{\xi}_{\mathbf{k}} = 0$) at $T = 0$ with parameters $\mu = -4.8T_N$, $t_1 = 6T_N$, $t_2 = -T_N$, $r_c^+ \approx 0.52866$, and $r_c^- \approx -0.61447$. (a) Low-energy excitations when $0 < r < r_c^+$ occur at $(\pm\pi, \pm k_y^*)$ in the BZ before the appearance of nodes. When $r > r_c^+$ secondary local maxima of the SC gap amplitude appear at $(\pm\pi, \pm k_y^*)$. (b) Low-energy excitations when $r_c^- < r < 0$ occur at $(0, \pm k_y^*)$ in the BZ before the appearance of nodes. When $r < r_c^-$ secondary local maxima of the SC gap amplitude appear at $(0, \pm k_y^*)$.

In Fig. 4 we plot the $|\Delta_{\mathbf{k}}|$ along the deformed FS. We see that for $0 < r < r_c^+$, $|\Delta_{\mathbf{k}}|$ has minima at $(\pm\pi, \pm k_y^*)$, whereas for $r_c^- < r < 0$, the minima occur at $(0, \pm k_y^*)$. Therefore, these also indicate the locations of the excitations with the lowest energies. However, once the nodes form (i.e., for

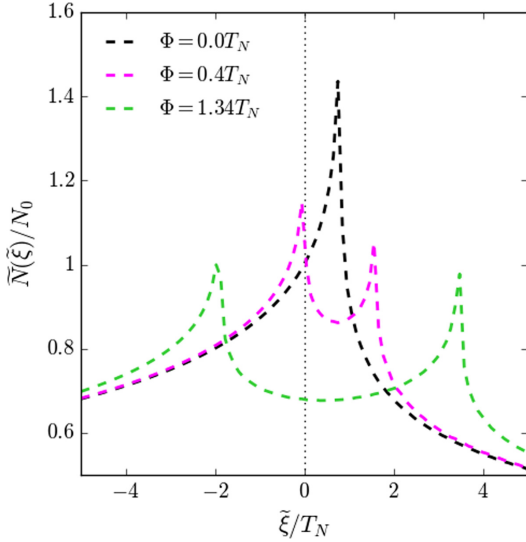


FIG. 5. Evolution of the bare DOS under the nematic order at different temperatures for a closed ($\mu = -4.8T_N$) FS. The DOS at $T > T_N$ and at $T = 0$ are given by the black and green curves in. The van Hove singularities in the bare DOS cross the Fermi level at $T = 0.97T_N$ (magenta curve). This occurs when the deformed FS passes through the saddle point located at $(\pi, 0)$ as seen in Fig. 1 (see text for details).

$r > r_c^+$ or $r < r_c^-$), $|\Delta_{\mathbf{k}}|$ has a secondary local maxima at these same locations in the BZ. The location of the low-energy excitations (before the formation of nodes) and the appearance of these secondary maxima of the gap amplitude (after the formation of nodes) have a significant effect on the heat transport properties of the system (see Sec. III).

While the presence of the nodes plays a dominant role in determining the transport properties in the coexistence phase at low temperatures (as will be discussed later in Sec. III), the existence of van Hove singularities is an important feature that influences transport properties for $T > T_c$ when the system is in the purely nematic phase. The dispersion relation in the nematic phase ($\tilde{\xi}_{\mathbf{k}} = \xi_{\mathbf{k}} + \Phi f_{\mathbf{k}}$) has saddle points ($|\nabla_{\mathbf{k}} \tilde{\xi}_{\mathbf{k}}| = 0$) close to the FS at $(k_x, k_y) = (\pi, 0)$ and $(0, \pi)$, which can be seen in Fig. 1 as the blue points. These saddle points cause van Hove singularities to occur in the bare density of states at energies $\tilde{\xi}_{\mathbf{k}}^{vH} = -\mu + 4t_2 \pm 2\Phi$. Furthermore, as can be seen in Fig. 1, the nematic FS passes through these saddle points when the closed FS transitions to an open FS along the \hat{k}_x axis.

In the absence of nematicity, the saddle points at $(k_x, k_y) = (\pi, 0)$ and $(0, \pi)$ lead to van Hove singularities in the bare DOS at the same energy [57] ($\xi_{\mathbf{k}}^{vH} = -\mu + 4t_2$) as seen in the black curve in Fig. 5. However as the nematic order parameter becomes nonzero, the saddle points at $(\pi, 0)$ and $(0, \pi)$ lead to van Hove singularities in the bare DOS at different energies $\tilde{\xi}_{\mathbf{k}}^{vH} = \xi_{\mathbf{k}}^{vH} - 2\Phi$ and $\tilde{\xi}_{\mathbf{k}}^{vH} = \xi_{\mathbf{k}}^{vH} + 2\Phi$ respectively. This can be seen from the two singularities present in both the magenta

and green curves in Fig. 5. When the nematic order parameter reaches the critical value $\Phi_c = |-\frac{\mu}{2} + 2t_2|$, the van Hove singularities cross the Fermi level as indicated in the magenta curves in Fig. 5. The van Hove singularities crossing the Fermi level [58] has an impact on the transport properties of the system when $T > T_c$ and will be discussed in Sec. III.

B. Self-consistent equations for nematicity and superconductivity

The self-consistent equations for Φ and Δ are obtained by calculating the averages in (2) and (3), respectively [47]

$$\Phi = V_{\text{nem}} \sum_{\mathbf{k}} \frac{f_{\mathbf{k}}}{2} \left[\frac{\xi_{\mathbf{k}} + \Phi f_{\mathbf{k}}}{E_{\mathbf{k}}} \tanh \frac{E_{\mathbf{k}}}{2T} - 1 \right], \quad (8)$$

$$\Delta = -V_{\text{sc}} \Delta \sum_{\mathbf{k}} \frac{\mathcal{Y}_{\mathbf{k}}^2}{2E_{\mathbf{k}}} \tanh \frac{E_{\mathbf{k}}}{2T}. \quad (9)$$

The equation for Φ in the pure nematic phase is obtained by setting $\Delta = 0$ in Eq. (8) and leads to the following self-consistent equation:

$$\Phi = V_{\text{nem}} \sum_{\mathbf{k}} \frac{f_{\mathbf{k}}}{2} \left[\tanh \frac{\xi_{\mathbf{k}} + \Phi f_{\mathbf{k}}}{2T} - 1 \right]. \quad (10)$$

The equation that determines the nematic transition temperature T_N is obtained by setting $\Phi \rightarrow 0$ as $T \rightarrow T_N$ in Eq. (10), yielding

$$1 = \frac{V_{\text{nem}}}{2} \sum_{\mathbf{k}} \frac{f_{\mathbf{k}}^2}{2T_N} \left[\text{sech}^2 \frac{\xi_{\mathbf{k}}}{2T_N} \right]. \quad (11)$$

The superconducting transition temperature in the absence of nematicity (T_c^0) can be determined from Eq. (9)

$$1 = -V_{\text{sc}} \sum_{\mathbf{k}} \frac{\mathcal{Y}_{\mathbf{k}}^2}{2\xi_{\mathbf{k}}} \tanh \frac{\xi_{\mathbf{k}}}{2T_c^0}. \quad (12)$$

Note that in all the cases considered in this paper, T_c^0 has been set to $0.4T_N$. However, the superconducting transition temperature (T_c) in the presence of the nematic order is different from T_c^0 as can be seen in Fig. 6.

1. Numerical solution of self-consistent equations

Equations (8) and (9) can be solved self-consistently. For clarity, the parameters V_{nem} and V_{sc} are eliminated in favor of T_N and T_c^0 using Eqs. (11) and (12). Similarly, $\Phi_0(T)$ (the nematic order parameter in the absence of SC) can also be solved self-consistently from Eq. (10) where V_{nem} was again eliminated in favor of T_N using Eq. (11). The solutions $\Phi(T)$ and $\Delta(T)$ for $r = \pm 0.2$ are shown in Fig. 6. It can be seen that in the presence of SC, the nematic order parameter is slightly diminished from its value in the absence of SC [i.e., $\Phi(T) < \Phi_0(T)$ when $\Delta(T) \neq 0$]. The SC transition temperature is also lower in the presence of nematicity ($T_c = 0.211T_N$ for $r = 0.2$, $T_c = 0.317T_N$ for $r = -0.2$, and $T_c^0 = 0.4T_N$), which is indicative of competing nematic and SC orders [47]. This was found to be the case for all parameter combinations studied in this paper.

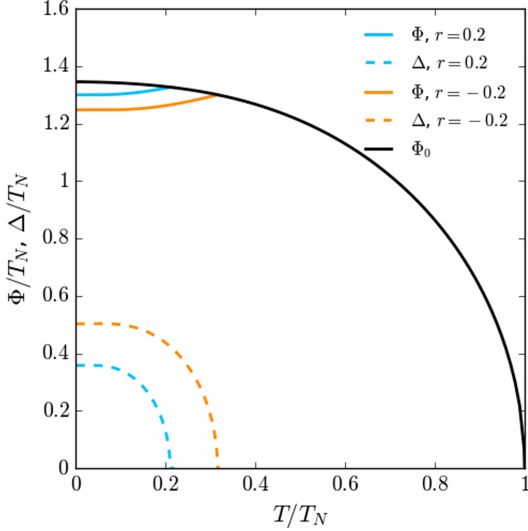


FIG. 6. Self-consistent solutions for $\Phi(T)$ and $\Delta(T)$ on the closed ($\mu = -4.8T_N$) tight-binding Fermi surface when $r = 0.2$ (cyan curves), $r = -0.2$ (orange curves), and $T_c^0 = 0.4T_N$. Also pictured is $\Phi_0(T)$, the nematic order in the absence of superconductivity (black curve). The band parameters are $t_1 = 6T_N$ and $t_2 = -T_N$.

C. Kinetic method for heat conductivity

We use the Boltzmann kinetic equation approach to calculate the thermal conductivity for the system with intertwined orders. This method was widely used to compute thermal conductivity, both in s -wave superconductors [2,59], as well as in unconventional superconductors [11,48,60,61]. The expression for the thermal conductivity for a superconductor in the Boltzmann kinetic approach is given by the expression [60]

$$\kappa_{ij} = -\frac{2}{T} \int \frac{d^2k}{(2\pi)^2} E_{\mathbf{k}}^2 v_{\mathbf{k},i} v_{\mathbf{k},j} \frac{\partial f_{\mathbf{k}}^0}{\partial E} \tau_{\mathbf{k}} \quad (13)$$

where $f_{\mathbf{k}}^0 = \frac{1}{e^{\epsilon_{\mathbf{k}}/T} + 1}$ is the equilibrium Fermi-Dirac distribution function. The quasiparticle velocity is defined as

$$\mathbf{v}_{\mathbf{k}} = \nabla_{\mathbf{k}} E_{\mathbf{k}} \quad (14)$$

and the quasiparticle relaxation time is given by [11]

$$\tau_{\mathbf{k}}^{-1} = N_{\text{imp}} \frac{2\pi}{\hbar} \int \frac{d^2k'}{(2\pi)^2} |t_{\mathbf{k},\mathbf{k}'}|^2 \delta(E_{\mathbf{k}} - E_{\mathbf{k}'}) \quad (15)$$

where $t_{\mathbf{k},\mathbf{k}'}$ is the amplitude for a single impurity to scatter a quasiparticle from the state with momentum \mathbf{k} and energy $E_{\mathbf{k}}$ to the state with momentum \mathbf{k}' and energy $E_{\mathbf{k}'}$ and N_{imp} is the density of impurities.

In order to determine the amplitude $t_{\mathbf{k},\mathbf{k}'}$, we first write the impurity scattering Hamiltonian in the same Nambu basis as Eq. (4):

$$H_{\text{imp}} = v_{\text{imp}} \sum_{\mathbf{k},\mathbf{k}',\sigma} c_{\mathbf{k}'\sigma}^\dagger c_{\mathbf{k}\sigma} = \frac{1}{2} \sum_{\mathbf{k},\mathbf{k}'} \hat{\Psi}_{\mathbf{k}'\sigma}^\dagger \hat{v} \hat{\Psi}_{\mathbf{k}\sigma}, \quad (16)$$

$$\hat{v} = v_{\text{imp}} \hat{\tau}_3,$$

where $\hat{\tau}_3$ is the Pauli matrix in Nambu space and v_{imp} is a nonmagnetic isotropic impurity potential. The operators $c_{\mathbf{k},\sigma}^\dagger$ and $c_{\mathbf{k},\sigma}$, which create and destroy normal state particles, are related to the superconducting state quasiparticles $a_{\mathbf{k},\sigma}^\dagger$ and $a_{\mathbf{k},\sigma}$ by the Bogoliubov transformation

$$\hat{\Psi}_{\mathbf{k},\sigma} = \hat{B}_{\mathbf{k}}^{(\sigma)} \hat{A}_{\mathbf{k}}, \quad (17)$$

$$\hat{B}_{\mathbf{k}}^{(\sigma)} = \begin{pmatrix} u_{\mathbf{k}} & -v_{\mathbf{k}} \\ v_{\mathbf{k}} & u_{\mathbf{k}} \end{pmatrix}, \quad (18)$$

where $u_{\mathbf{k}} = \frac{E_{\mathbf{k}} + \xi_{\mathbf{k}}}{\sqrt{(E_{\mathbf{k}} + \xi_{\mathbf{k}})^2 + \Delta_{\mathbf{k}}^2}}$, $v_{\mathbf{k}} = \frac{\sigma \Delta_{\mathbf{k}}}{\sqrt{(E_{\mathbf{k}} + \xi_{\mathbf{k}})^2 + \Delta_{\mathbf{k}}^2}}$, and $\hat{A}_{\mathbf{k}}^\dagger = (a_{\mathbf{k},\sigma'}^\dagger, a_{-\mathbf{k},-\sigma'})$. Upon performing the Bogoliubov transformation (18) on the Nambu vectors, we get

$$H_{\text{imp}} = \frac{1}{2} \sum_{\mathbf{k},\mathbf{k}'} \hat{A}_{\mathbf{k}}^\dagger \hat{D}_{\mathbf{k},\mathbf{k}'} \hat{A}_{\mathbf{k}}, \quad (19)$$

where the matrix $\hat{D}_{\mathbf{k},\mathbf{k}'}$ is given by

$$\hat{D}_{\mathbf{k},\mathbf{k}'} = (\hat{B}_{\mathbf{k}'}^{(\sigma')})^\dagger \hat{v} \hat{B}_{\mathbf{k}}^{(\sigma)}. \quad (20)$$

Using this formalism, we can now determine some important terms. From the ordering of the $\hat{A}_{\mathbf{k}}^\dagger$ vector, the amplitude $t_{\mathbf{k},\mathbf{k}'}$ in the Born approximation is given by

$$t_{\mathbf{k},\mathbf{k}'} = (\hat{D}_{\mathbf{k},\mathbf{k}'})_{11}. \quad (21)$$

To get the amplitude in the unitary limit, we replace \hat{v} in Eq. (20) by the T matrix for impurity scattering

$$\hat{D}_{\mathbf{k},\mathbf{k}'} = (\hat{B}_{\mathbf{k}'}^{(\sigma')})^\dagger \hat{T} \hat{B}_{\mathbf{k}}^{(\sigma)}. \quad (22)$$

The T matrix can be obtained from [11] the Lippmann-Schwinger equation

$$\hat{T} = \hat{v} + \hat{v} \sum_{\mathbf{k}} \hat{G}_{\mathbf{k}}(E) \hat{T} \quad (23)$$

where $\hat{G}_{\mathbf{k}}(E)$ is the single-particle Green's function for the superconductor in the absence of impurities, and is given by

$$\hat{G}_{\mathbf{k}}(E) = \frac{1}{E^2 - E_{\mathbf{k}}^2} \begin{pmatrix} E + \xi_{\mathbf{k}} & \sigma \Delta_{\mathbf{k}} \\ \sigma \Delta_{\mathbf{k}} & E - \xi_{\mathbf{k}} \end{pmatrix}. \quad (24)$$

Using Eq. (24) in Eq. (23), we get

$$\hat{T} = \frac{v_{\text{imp}} \hat{\tau}_3 + i v_{\text{imp}}^2 \tilde{N}_0 (g \hat{I}_{2 \times 2} + h \hat{\tau}_1)}{1 + v_{\text{imp}}^2 \tilde{N}_0^2 (|g|^2 - |h|^2)}. \quad (25)$$

The functions $g(E_{\mathbf{k}})$ and $h(E_{\mathbf{k}})$ are given by

$$g(E_{\mathbf{k}}) = -\frac{i}{\tilde{N}_0} \sum_{\mathbf{k}'} \frac{E_{\mathbf{k}}}{E_{\mathbf{k}}^2 - E_{\mathbf{k}'}^2}, \quad (26)$$

$$h(E_{\mathbf{k}}) = -\frac{i}{\tilde{N}_0} \sum_{\mathbf{k}'} \frac{\Delta_{\mathbf{k}'}}{E_{\mathbf{k}}^2 - E_{\mathbf{k}'}^2}, \quad (27)$$

where $\tilde{N}_0 \equiv N(\xi_{\mathbf{k}} = 0)$ is the density of states on the FS deformed due to nematicity and therefore depends on $\Phi(T)$. As $T \rightarrow T_N$, $\tilde{N}_0 = N_0$ where $N_0 \equiv N(\xi_{\mathbf{k}} = 0)$, which is the density of states on the original tight-binding FS. When $\Delta \rightarrow 0$, $g(E_{\mathbf{k}}) = 1$ and $h(E_{\mathbf{k}}) = 0$. The functions $g(E_{\mathbf{k}})$ and $h(E_{\mathbf{k}})$ are the normal and anomalous part of the quasiparticle self-energy respectively [60]. The real part of the function $g(E_{\mathbf{k}})$ is proportional to the quasiparticle density of states and the imaginary

part corresponds to dispersive corrections to the quasiparticle self-energy.

The function $h(E_{\mathbf{k}})$ goes to zero for all superconducting states with the order parameters corresponding to nonidentity representations of the crystal symmetry group (for example, the $d_{x^2-y^2}$ and d_{xy} pairing states [11,60]). In our case $h(E_{\mathbf{k}}) \neq 0$ due to the feedback from the symmetry broken nematic state on the SC order. The T matrix in Eq. (25) is directly parameterized in terms of the strength of the impurity potential v_{imp} , however it can also be equivalently parameterized in terms of the normal state scattering phase shift δ_N [11]. In this paper we only consider two limiting cases: weak impurity potential ($v_{\text{imp}}\tilde{N}_0 \ll 1 \Rightarrow \delta_N \ll \pi/2$), which puts us in the limit where the Born approximation is valid, whereas a strong impurity potential ($v_{\text{imp}}\tilde{N}_0 \gg 1 \Rightarrow \delta_N = \pi/2$) puts us in the unitary limit. In the Born and unitary limits, the T matrix in Eq. (25) reduces to

$$\hat{T}_{\text{Born}} = t_N^{\text{Born}} \hat{\tau}_3, \quad (28)$$

$$\hat{T}_{\text{Unitary}} = \frac{t_N^{\text{Unitary}}}{|g|^2 - |h|^2} (g\hat{t}_{2 \times 2} + h\hat{\tau}_1), \quad (29)$$

where $t_N^{\text{Born}} = v_{\text{imp}}$ and $t_N^{\text{Unitary}} = i/\tilde{N}_0$. Using Eqs. (21), (22), (28), and (29) we can compute the amplitude $t_{\mathbf{k},\mathbf{k}'}$ in the Born and unitary limits, respectively:

$$|t_{\mathbf{k},\mathbf{k}'}|^2 = \frac{|t_N^{\text{Born}}|^2}{2} \left(1 + \frac{\xi_{\mathbf{k}} \xi_{\mathbf{k}'} - \Delta_{\mathbf{k}} \Delta_{\mathbf{k}'}}{E_{\mathbf{k}} E_{\mathbf{k}'}} \right), \quad (30)$$

$$|t_{\mathbf{k},\mathbf{k}'}|^2 = \frac{|t_N^{\text{Unitary}}|^2}{2} \left[a \left(1 + \frac{\Delta_{\mathbf{k}} \Delta_{\mathbf{k}'}}{E_{\mathbf{k}} E_{\mathbf{k}'}} \right) + b \frac{\xi_{\mathbf{k}} \xi_{\mathbf{k}'}}{E_{\mathbf{k}} E_{\mathbf{k}'}} + 2c \left(\frac{\Delta_{\mathbf{k}}}{E_{\mathbf{k}}} + \frac{\Delta_{\mathbf{k}'}}{E_{\mathbf{k}'}} \right) \right], \quad (31)$$

where a , b , and c are defined as

$$a = \frac{|g|^2 + |h|^2}{\| |g|^2 - |h|^2 \|^2}, \quad (32)$$

$$b = \frac{|g|^2 - |h|^2}{\| |g|^2 - |h|^2 \|^2}, \quad (33)$$

$$c = \frac{\text{Re}(gh^*)}{\| |g|^2 - |h|^2 \|^2}. \quad (34)$$

Using Eqs. (30) and (31) in Eq. (15), the scattering rates in both the Born and unitary limits respectively are found to be

$$\tau_{\mathbf{k}}^{-1} = \tau_{NF}^{-1} \left(\text{Re}(g(E_{\mathbf{k}})) - \frac{\Delta_{\mathbf{k}}}{E_{\mathbf{k}}} \text{Re}(h(E_{\mathbf{k}})) \right), \quad (35)$$

$$\tau_{\mathbf{k}}^{-1} = \tau_{NF}^{-1} \left\{ a \left[\text{Re}(g(E_{\mathbf{k}})) + \frac{\Delta_{\mathbf{k}}}{E_{\mathbf{k}}} \text{Re}(h(E_{\mathbf{k}})) \right] + 2c \left[\frac{\Delta_{\mathbf{k}}}{E_{\mathbf{k}}} \text{Re}(g(E_{\mathbf{k}})) + \text{Re}(h(E_{\mathbf{k}})) \right] \right\}, \quad (36)$$

where τ_{NF}^{-1} is the scattering rate on the nematically deformed FS in the absence of the SC order and is defined as $\tau_N^{-1}(\xi_{\mathbf{k}}) = \frac{2\pi}{\hbar} N_{\text{imp}} |t_N|^2 \tilde{N}(\xi_{\mathbf{k}})$, $\tau_{NF}^{-1} = \tau_N^{-1}(\xi_{\mathbf{k}} = 0)$. In the Born and unitary limits t_N has been defined after Eq. (29) as t_N^{Born} and t_N^{Unitary} . Note that when $\Delta = 0$, $a = b = 1$, and $c = 0$, and we find $\tau_{\mathbf{k}}^{-1} = \tau_{NF}^{-1}$ in both the Born and unitary limits. Further,

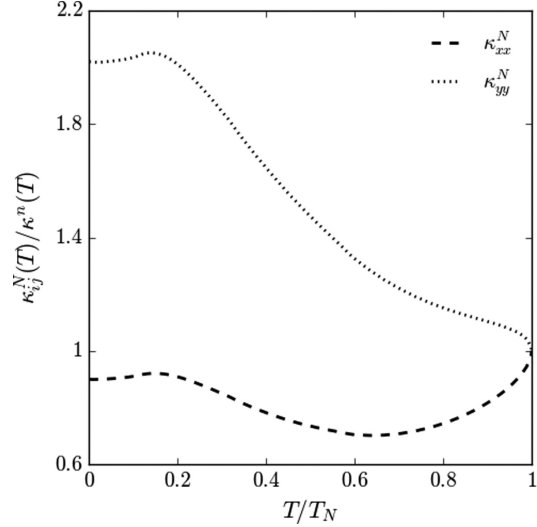


FIG. 7. Heat conductivity components $[\kappa_{ij}^N(T)]$ of the nematically deformed closed FS with band parameters $t_1 = 6T_N$, $t_2 = -T_N$, and $\mu = -4.8T_N$ in the absence of SC order. $\kappa_{ij}^N(T)$ is normalized by the conductivity $[\kappa^n(T)]$ of the normal state (originalFS, $\Phi = 0$). The normal state conductivity is T linear, $\kappa^n(T) = \text{constant} \times T$.

when $\Phi \rightarrow 0 \Rightarrow r \rightarrow 0 \Rightarrow \Delta_{\mathbf{k}} = \Delta$ and $\tilde{N}_0 = N_0$, $\tau_n = \tau_n$, $\text{Re}(g(E_{\mathbf{k}})) = N_{sc}(E_{\mathbf{k}})/N_0$, $h(E_{\mathbf{k}}) = \frac{\Delta}{E_{\mathbf{k}}} g(E_{\mathbf{k}})$, where $N_{sc}(E_{\mathbf{k}})$ is the quasiparticle DOS in the superconducting state. This reduces the quasiparticle scattering rate in Eq. (35) to $\tau_{\mathbf{k}}^{-1} = \tau_n^{-1} \frac{N_{sc}(E_{\mathbf{k}})}{N_0} (1 - \frac{\Delta^2}{E_{\mathbf{k}}^2})$, which is the usual expression for an s -wave superconductor in the Born limit [2,60]. Again in the case when $\Phi \rightarrow 0 \Rightarrow r \rightarrow 0$ and $\Delta_{\mathbf{k}}$ has $d_{x^2-y^2}$ symmetry, $h(E_{\mathbf{k}}) = 0$, which implies $a = 1/|g|^2$ and $c = 0$. Therefore Eq. (35) reduces to the well-known expression [11,60], $\tau_{\mathbf{k}}^{-1} = \tau_n^{-1} \frac{N_{sc}(E_{\mathbf{k}})}{N_0}$, for the scattering rate of the $d_{x^2-y^2}$ pairing state in the Born limit. Furthermore Eq. (36) reduces to, $\tau_{\mathbf{k}}^{-1} = \tau_n^{-1} \frac{N_{sc}(E_{\mathbf{k}})}{N_0} \frac{1}{|g(E_{\mathbf{k}})|^2}$, which is the scattering rate for the $d_{x^2-y^2}$ pairing state in the unitary limit [11,60]. Using Eqs. (35) and (36) we numerically compute the thermal conductivity tensor $\kappa_{ij}(T)$ from Eq. (13) in both the Born and unitary limits. We also compute the conductivity in the purely nematic state $\kappa_N(T)$ by setting $\Delta = 0$ in Eq. (13), thus eliminating the unknowns N_{imp} and v_{imp} in favor of the nematic state relaxation time τ_N .

III. NUMERICAL RESULTS AND DISCUSSION

A. Pure nematic phase: $\Phi \neq 0$, $\Delta = 0$

We begin our discussion by calculating the thermal conductivity of the pure nematic state for our tight-binding model with an initially closed Fermi surface. The components of the thermal conductivity tensor are normalized by the normal state ($\Phi = 0$ and $\Delta = 0$) conductivity $[\kappa^n(T)]$. The results are shown in Fig. 7, where we have treated the impurity scattering within the Born approximation.

It can be seen that the κ_{xx}^N and κ_{yy}^N components of the thermal conductivity tensor are no longer equal, as is the case for the original ($\Phi = 0$) tight-binding Fermi surface (i.e., $\kappa_{xx}^n = \kappa_{yy}^n = \kappa^n$ in the normal state). This is due to the fact that the nematic deformation has enhanced the quasiparticle velocities in the y direction while diminishing the velocities in the x direction (see Fig. 10). This results in κ_{yy}^N always being greater than κ_{xx}^N . Despite these modifications to the quasiparticle velocities, the κ_{xy}^N components still vanish due to the symmetry inherent in the velocities on the deformed FS.

While the effect of the nematic deformation on the Fermi velocities is an important characteristic, it cannot explain all the features of the thermal conductivity in Fig. 7. If the nematic deformation only impacted the velocities as explained above, it would cause κ_{yy}^N to increase by the same amount that κ_{xx}^N decreases from κ^n , leading to a symmetric splitting in the κ_{xx}^N and κ_{yy}^N components.

The asymmetric splitting in Fig. 7 is due to the fact that the particle lifetimes in the nematic state are different from the normal state. The particle lifetime in the nematic state is $\tau_N(\xi_{\mathbf{k}}) \propto 1/\tilde{N}(\xi_{\mathbf{k}})$ [defined below Eq. (36)]. In Fig. 5 it can be seen that as the van Hove singularities approach the Fermi level, $\tilde{N}(\xi_{\mathbf{k}})$ near the Fermi level increases, which causes $\tau_N(\xi_{\mathbf{k}})$ near the Fermi level to decrease. Thus, near T_N (the van Hove singularities cross the Fermi level when $T = 0.97T_N$) κ_{xx}^N decreases much more quickly than κ_{yy}^N increases. However after the van Hove singularity passes through the Fermi level, the DOS $\tilde{N}(\xi_{\mathbf{k}})$ near the Fermi level begins to decrease (see Fig. 5), causing τ_N to increase. This results in long-lived, high velocity quasiparticles, which conduct heat more efficiently, forcing κ_{yy}^N to increase rather rapidly.

Simultaneously, although the velocity of the quasiparticles moving in the x direction are reduced, the lifetimes are increased (which more than compensates for the velocity reduction), causing κ_{xx}^N to also increase, but at a much slower rate than κ_{yy}^N . Finally, near $T = 0$, $\Phi(T)$ has reached saturation and remains at a constant value resulting in both the particle velocities and lifetimes becoming nearly constant at low T . This results in the usual metallic state with a conductivity that is linear in T . Thus, van Hove singularities crossing the Fermi level [58] (due to FS deformations caused by nematicity) have a significant effect on the heat transport properties properties of the system when it is in the pure nematic phase.

B. Pure superconducting phase: $\Phi = 0$, $\Delta \neq 0$

In Fig. 8 we have calculated the thermal conductivity of the pure SC states for our tight binding model. For the various pairing states, namely, s , $d_{x^2-y^2}$, the values of $\Delta(T)$ are obtained by self consistently solving the weak coupling gap equation. In the Born limit, we see the characteristic exponential fall in the thermal conductivity of the isotropic fully gapped s -wave superconductor [2].

The general behavior of $\kappa(T)/T$ in the Born limit, for the $d_{x^2-y^2}$ state also agrees with earlier calculations [11,16,62], where the low- T regime is dominated by the nodal quasiparticles, producing a finite residual κ/T . The $d_{x^2-y^2}$ pairing has nodes on flat parts of the FS with large Fermi velocity and smaller DOS. By gapping the corners of the FS with large DOS, the scattering rate is significantly reduced,

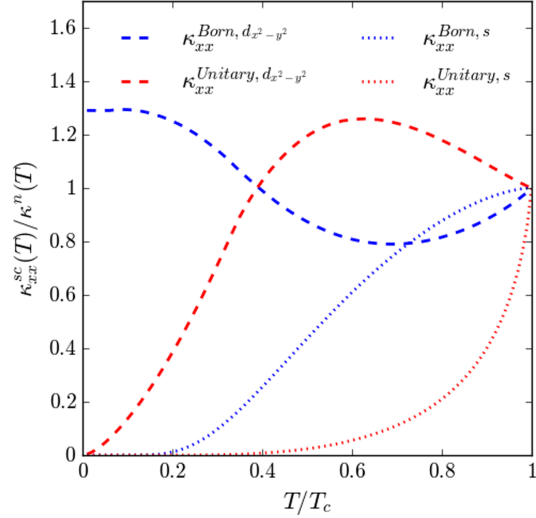


FIG. 8. Thermal conductivity components of the closed FS with band parameters $\mu = -48T_c$, $t_1 = 60T_c$, and $t_2 = -10T_c$ in the pure $d_{x^2-y^2}$ and s -wave superconducting states in both the Born and unitary limits.

producing longer-lived high-velocity nodal quasiparticles that result in heat conductivity exceeding that of the normal state. The scattering rate in the pure s -wave state is given by the expression [60] [see discussion below Eq. (36)], $\tau_{\mathbf{k}}^{-1} = \tau_N^{-1} \frac{N_{sc}(E_{\mathbf{k}})}{N_0} (1 - \frac{\Delta^2}{E_{\mathbf{k}}^2})$. However, in the case of the pure $d_{x^2-y^2}$ state [60], $\tau_{\mathbf{k}}^{-1} = \tau_N^{-1} \frac{N_{sc}(E_{\mathbf{k}})}{N_0}$.

Comparing the coherence factors for various states, one can notice that near their transition temperatures the effective relaxation time for the s -wave state is greater than the $d_{x^2-y^2}$ state. This results in the observed different slopes near T_c in Fig. 8 for the Born limit.

In Fig. 8 we have also plotted thermal conductivity in the unitary limit for both s and $d_{x^2-y^2}$ pairing states. Again the general behavior of $\kappa(T)/T$ in the unitary limit agrees with previously published results [11,16]. The unitary limit result for the $d_{x^2-y^2}$ pairing state is in better agreement with experimental data for cuprates, than the Born approximation result. It has been found experimentally that at low temperatures $\kappa(T)$ has a power-law like temperature dependence with an exponent greater than unity and that $\kappa(T) > \kappa_n(T)$ for intermediate temperatures [63,64].

C. Coexistence phase: $\Phi \neq 0$, $\Delta \neq 0$

In this section and what follows, to study the effects of SC order emerging from a nematic background, we discuss the components of the thermal conductivity tensor and thermal transport in the coexistence phase, where the SC order and the nematic order are simultaneously nonzero. To illustrate important aspects of our results and emphasize the fact that κ_{yy} is always greater than κ_{xx} when $\Phi \neq 0$, we have chosen to normalize $\kappa_{yy}(T)$ and $\kappa_{xx}(T)$ by the nematic state

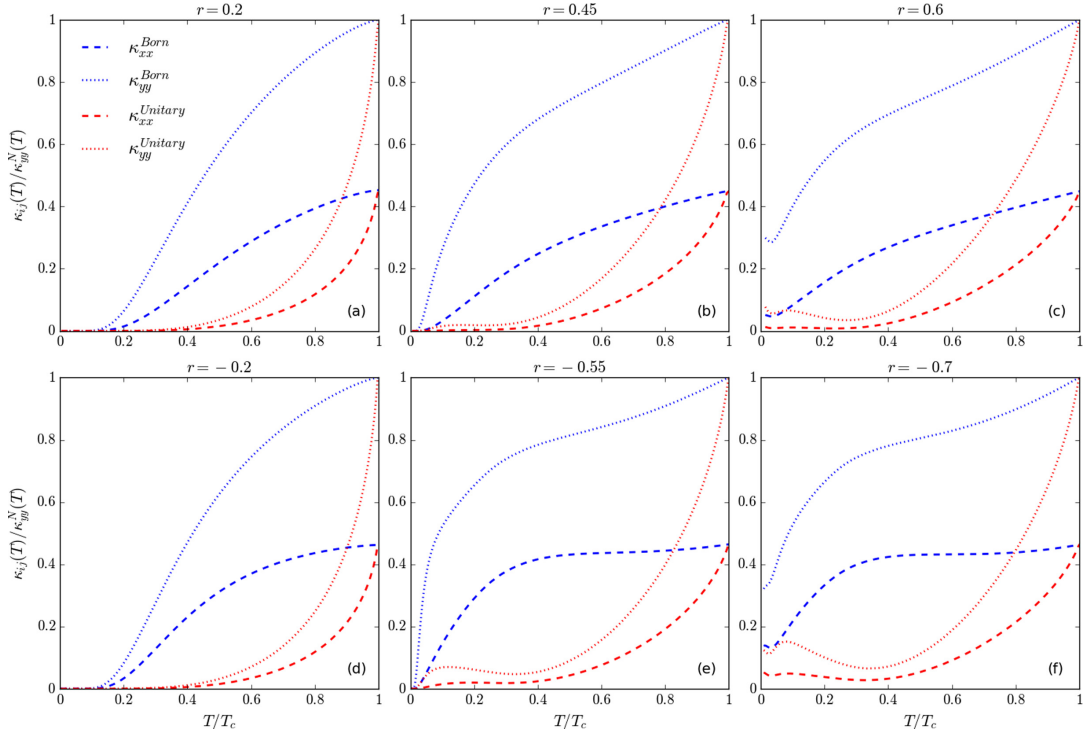


FIG. 9. Thermal conductivity components (κ_{xx} and κ_{yy}) in the coexistence phase in both the Born (blue curves) and unitary (red curves) limits normalized by the $\kappa_{yy}^N(T)$ component in the pure nematic phase when (a) $r = 0.2$ with $T_c = 0.211T_N$, (b) $r = 0.45$ with $T_c = 0.158T_N$, (c) $r = 0.6$ with $T_c = 0.140T_N$, (d) $r = -0.2$ with $T_c = 0.317T_N$, (e) $r = -0.55$ with $T_c = 0.332T_N$, and (f) $r = -0.7$ with $T_c = 0.323T_N$. The parameters used are $\mu = -4.8T_N$, $t_1 = 6T_N$, $t_2 = -T_N$, and $\Phi = 1.34T_N$. The critical r values are $r_c^+ \approx 0.52866$ and $r_c^- \approx -0.61447$. Thus the FS (at $T = 0$) in the coexistence phase corresponds to the green curve in Fig. 1).

thermal conductivity component $\kappa_{yy}^N(T)$, as a result of which $\kappa_{yy}(T) = 1$ at $T = T_c$. Apart from the the distortion of the FS, the nematic order parameter $\Phi(T)$ has another important consequence, which pertains to the coexistence phase. As previously discussed, the feedback from the symmetry broken nematic phase on the SC order leads to the mixing of the s -wave and d -wave channels. The degree of this mixing is determined by the parameter $r \propto \Phi(T)$. Therefore, we categorize our study of thermal transport into three cases: weak mixing ($|r| \ll |r_c^\pm|$), moderate mixing ($|r| \lesssim |r_c^\pm|$), and strong mixing ($|r| > |r_c^\pm|$), all displayed in Fig. 9. As before, we have computed the thermal conductivity using the Boltzmann transport equation method and treated the impurity scattering in both the Born and unitary limits (as outlined in Sec. II C).

There are certain common features in all the plots shown in Fig. 9. The conductivity components in the Born limit either fall to zero [Figs. 9(a), 9(b), 9(d), and 9(e)] or to a residual value [Figs. 9(c) and 9(f)]. These changes occur significantly more slowly than the corresponding components in the unitary limit due to the fact that, in the unitary limit (which corresponds to strong scattering centers), the quasiparticles are significantly more short-lived than the Born limit (which

corresponds to weak scattering centers). These longer-lived quasiparticles in the Born limit conduct heat more efficiently than those in the unitary limit at lower temperatures.

Another common feature in Fig. 9 is that when $r > 0$, $\kappa_{yy}^{\text{Born}}(T)$ falls roughly at the same rate as $\kappa_{xx}^{\text{Born}}(T)$ as T decreases from T_c relative to the conductivity in the pure nematic phase [see Figs. 9(a)–9(c)]. The slight difference in slope is because the Fermi velocity in the x and y directions are not equal. For the case when $r < 0$, $\kappa_{xx}^{\text{Born}}(T)$ falls noticeably more slowly than $\kappa_{yy}^{\text{Born}}(T)$ for $T < T_c$ [see Figs. 9(d)–9(f)] due to the correlation between the locations of the low-energy excitations in the BZ (when $r > 0$ as compared to when $r < 0$) and the Fermi velocities ($\tilde{v}_{F,x}$ and $\tilde{v}_{F,y}$) in the x and y directions along the nematically deformed FS.

When $r > 0$, the low-energy excitations are located near $(\pm\pi, \pm k_y^*)$ whereas they are located near $(0, \pm k_x^*)$ for $r < 0$ [compare Fig. 4(a) with Fig. 4(b)]. These low-energy excitations are primarily responsible for carrying the heat current in the coexistence phase. The quasiparticle velocities in the coexistence phase are $\mathbf{v}_k \approx \tilde{\mathbf{v}}_F \frac{\tilde{E}_k}{E_k}$, where $\tilde{\mathbf{v}}_F$ is the Fermi velocity corresponding to the nematically deformed FS. In the regions around low-energy excitations for both $r > 0$ and

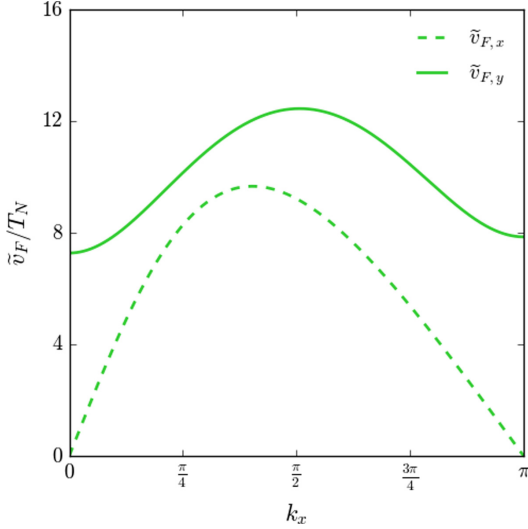


FIG. 10. Quasiparticle velocity in the pure nematic state plotted along the nematically deformed FS ($\tilde{v}_F = \nabla_{\mathbf{k}} \tilde{\xi}_{(k_x, k_y^*)}$) when $T = 0$ with band parameters $\mu = -4.8T_N$, $t_1 = 6T_N$, and $t_2 = -T_N$.

$r < 0$, $\tilde{v}_{F,y}$ are roughly equal and greater than $\tilde{v}_{F,x}$, resulting in $\kappa_{yy}^{\text{Born}}$ being always greater than $\kappa_{xx}^{\text{Born}}$ with the slope of $\kappa_{yy}^{\text{Born}}$ being roughly equal for both $r > 0$ and $r < 0$. However, as seen in (see Fig. 10) the Fermi velocities in the x direction are greater around the point $(0, \pm k_y^*)$ compared to $(\pm\pi, k_y^*)$, resulting in faster quasiparticles for $r > 0$ values compared to when $r < 0$. This results in $\kappa_{xx}^{\text{Born}}(T)$ to decrease more slowly near T_c for $r < 0$ when compared to $r > 0$.

1. Weak mixing: $|r| \ll |r_c^\pm|$

At low values of r the SC gap is weakly anisotropic (for $r = 0.2$: $|\Delta_{\mathbf{k}}^{\text{min}}|/|\Delta_{\mathbf{k}}^{\text{max}}| = 0.46$ and for $r = -0.2$: $|\Delta_{\mathbf{k}}^{\text{min}}|/|\Delta_{\mathbf{k}}^{\text{max}}| = 0.48$) and thus differs only slightly from the case of the uniformly gapped s -wave superconductor [see Figs. 2(a) and 2(d)]. Therefore, in the case of weak mixing [$r = \pm 0.2$, see Figs. 9(a) and 9(d)] the thermal conductivity profiles for both the components κ_{xx} and κ_{yy} are similar to the well known results for s -wave pairing [2,60] [compare Figs. 9(a) and 9(d) to Fig. 8]. Since $0.2 \ll r_c^+$ and $-0.2 \gg r_c^-$ for our chosen band parameters, no nodes exist in these cases and the FS is fully-gapped by the SC order. Therefore, there are only gapped excitations in the coexistence phase, leading to an exponential reduction at low T for both the Born and unitary limits in Figs. 9(a) and 9(d).

2. Moderate mixing: $|r| \lesssim |r_c^\pm|$

As the magnitude of s -wave and d -wave mixing is allowed to increase to $r = 0.45$ ($|\Delta_{\mathbf{k}}^{\text{min}}|/|\Delta_{\mathbf{k}}^{\text{max}}| = 0.08$) and $r = -0.55$ ($|\Delta_{\mathbf{k}}^{\text{min}}|/|\Delta_{\mathbf{k}}^{\text{max}}| = 0.05$), the SC gap develops deep minima on the FS [see Figs. 2(b) and 2(e) and Fig. 4] with the resulting thermal conductivity profiles are displayed in Figs. 9(b) and 9(e). The d -wave component in the SC

order parameter becomes stronger as we transition from weak ($r = \pm 0.2$) to moderate ($r = 0.45, r = -0.55$) mixing, resulting in the effective relaxation time to decrease near T_c in the Born limit, as explained previously in Sec. III B. This change is reflected in the slopes near T_c in Fig. 9 (for the Born limit). Further, as the nonuniformity in the order parameter increases, the Fermi surface is no longer efficiently gapped by the SC order, which results in the presence of excitations with lower energy than in the weak mixing case. Thus both thermal conductivity tensor components fall to 0 at much lower temperatures compared to the weak mixing case. Unlike the d -wave state, κ_{ij} components eventually fall to 0 at low T in the Born limit. This is a direct consequence of the fact that the system is still fully-gapped by the SC order (because $|r| \lesssim |r_c^\pm|$).

In the unitary limit (see Fig. 11), the lifetime $\tau_{\mathbf{k}}$ at the FS begins to increase at low energies due to the stronger anisotropy in the SC gap and κ_{ij} has a slight upturn before falling to zero at low T . Since the real part of $g(E)$ corresponds to the density of states in the coexistence phase, $\text{Re}(g(E)) = 0$ for $E < |\Delta_{\mathbf{k}}^{\text{min}}|$, as there can be no excitations below the minimum value of the energy gap. Further, there is a coherence peak in the density of states at $E = |\Delta_{\mathbf{k}}^{\text{max}}|$. As $E \rightarrow |\Delta_{\mathbf{k}}^{\text{min}}|$ both the $\text{Re}(g(E))$ and $\text{Re}(h(E))$ decrease, whereas $\text{Im}(g(E))$ and $\text{Im}(h(E))$ increase, causing the parameters a and c to increase [see Eq. (34)]. This results in a reduction $\tau_{\mathbf{k}}^{-1}$ [see Eq. (36)] and a consequent increase in the quasiparticle lifetime in the unitary limit as $E \rightarrow |\Delta_{\mathbf{k}}^{\text{min}}|$.

3. Strong mixing: $|r| > |r_c^\pm|$

Finally, as $|r| > |r_c^\pm|$, the SC gap collapses at the nodal points on the FS. The nonuniformity of the gap results in smaller secondary SC gap maxima $|\Delta_{\mathbf{k}}^{\text{max},(-)}|$ on the FS (see Figs. 4 and 2), corresponding to the negative sign of the SC gap function. The corresponding thermal conductivity profiles are presented in Figs. 9(c) and 9(f). In comparison with the moderate mixing case [Figs. 9(b) and 9(e)], there is now a residual thermal conductivity at $T = 0$ (an obvious consequence of the existence of zero-energy excitations at the nodes).

Furthermore, in both the Born and unitary limits, the residual κ_{yy} values are roughly the same for $r < 0$ and $r > 0$, (see Figs. 9(c) and 9(f)). This is again because the y velocities of the quasiparticles are roughly the same at the locations of the nodes. However, in both the Born and unitary limits, the residual values of κ_{xx} when $r < 0$ are greater than when $r > 0$. When $r < r_c^- < 0$ the nodes appear around $(0, \pm k_y^*)$ whereas when $r > r_c^+ > 0$, the nodes appear around $(\pm\pi, k_y^*)$ [see Fig. 3(b)]. As seen in (see Fig. 10) the Fermi velocities in the x direction are greater around the point $(0, \pm k_y^*)$ compared to $(\pm\pi, k_y^*)$, resulting in faster nodal quasiparticles for negative r values, which conduct heat more efficiently.

Unlike the pure nodal $d_{x^2-y^2}$ pairing state (see Fig. 8), the components of κ_{ij} in the unitary limit no longer go to 0 as $T \rightarrow 0$ because the quasiparticle lifetimes on the Fermi surface diverge at low energies (see Fig. 12). In addition, the real part of $g(E)$ and $h(E)$ go to zero as $E \rightarrow 0$ causing the lifetime $\tau_{\mathbf{k}}$ to diverge as $E \rightarrow 0$ for both the Born and unitary limits.

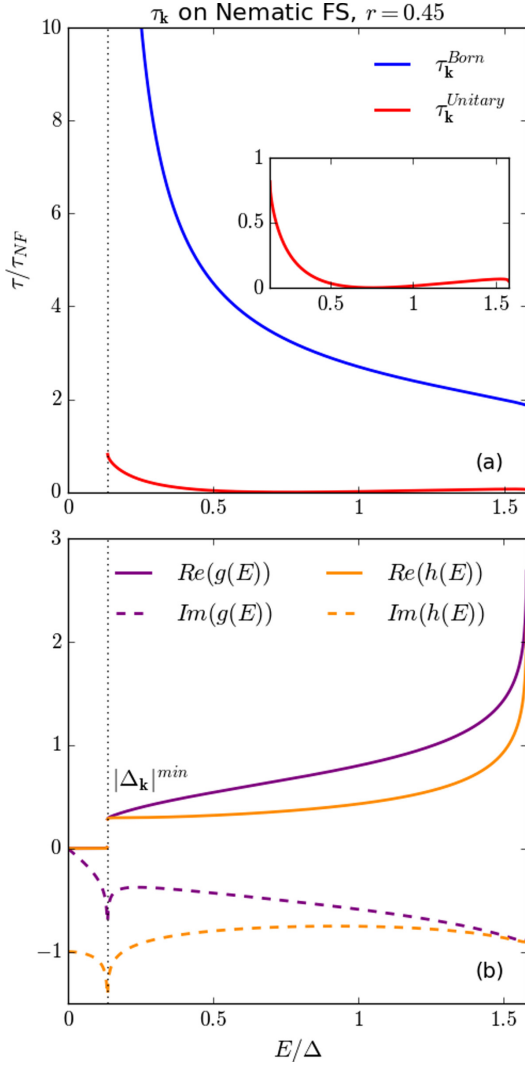


FIG. 11. (a) Quasiparticle lifetimes in the coexistence phase in the Born (blue curves) and unitary (red curves) limits on the nematic FS, normalized by the quasiparticle lifetimes on the FS (τ_{NF}) in the pure nematic state. The inset is an expanded display of the lifetime in the unitary limit. E ranges from zero to $|\Delta_{\mathbf{k}}|^{\max}$, the maximum value of the gap amplitude on the FS. The black dotted line indicates the minimum value of the gap amplitude on the FS, $|\Delta_{\mathbf{k}}|^{\min}$. (b) The real and imaginary parts of $g(E)$ and $h(E)$ plotted over the same energies to illustrate their effects on the quasiparticle lifetimes.

The singularity in the quasiparticle lifetime in the Born limit in Fig. 12(a) occurs due to the coherence peak in the SC DOS [see Fig. 12(b)] that appears at the energy corresponding to the smaller secondary SC gap maxima $|\Delta_{\mathbf{k}}|^{\max,(-)}$ on the

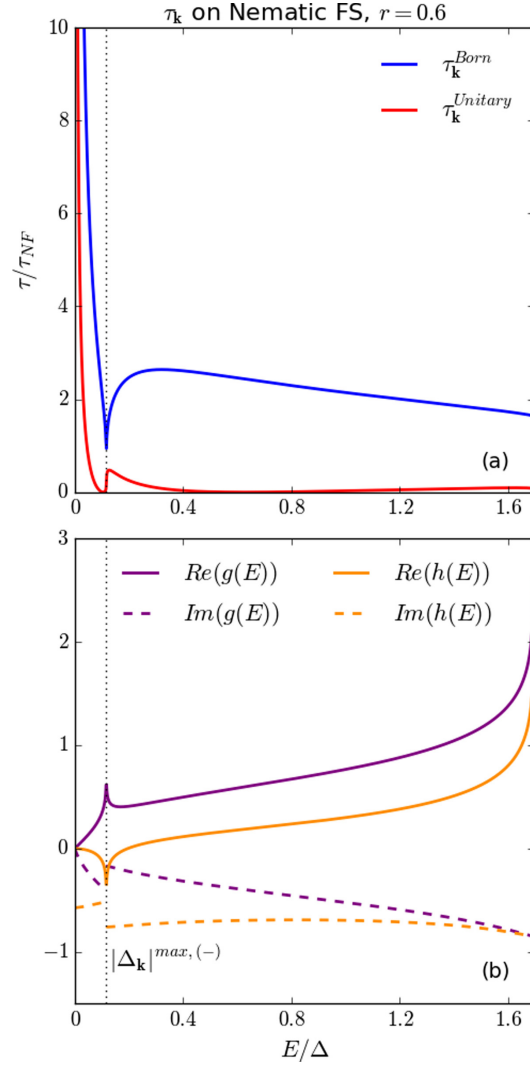


FIG. 12. (a) Quasiparticle lifetimes in the coexistence phase in the Born (blue curves) and unitary (red curves) limits on the nematic FS, normalized by the quasiparticle lifetimes on the FS (τ_{NF}) in the pure nematic state. E ranges from zero to $|\Delta_{\mathbf{k}}|^{\max,(+)}$, the maximum value of the gap amplitude on the FS. The black line indicates the secondary, negative gap maximum on the FS $|\Delta_{\mathbf{k}}|^{\max,(-)}$. (b) The real and imaginary parts of $g(E)$ and $h(E)$ plotted over the same energies to illustrate their effects on the quasiparticle lifetimes.

FS (see Figs. 2 and 4). Finally, at $E = |\Delta_{\mathbf{k}}|^{\max,(-)}$, $|g| \approx |h|$, which causes $\tau_{\mathbf{k}}^{-1}$ to diverge and therefore the quasiparticle lifetime $\tau_{\mathbf{k}}$ vanishes at that energy in the unitary limit.

In closing, we mention that for each of the cases studied above, the lifetimes for the anisotropic pairing states with

positive values of r are the roughly the same as those with negative values of r because the spectrum of low-energy excitations of the quasiparticles are nearly the same for both (see Fig. 4). At the location of these low-energy excitations (i.e., near the gap minima or nodes), the magnitude of the Fermi velocities are roughly the same, implying that the local density of states at those locations are also nearly equal. As a result the quasiparticle lifetimes corresponding to SC pairing states with either positive or negative values of the anisotropy parameter r do not differ much from one another. We have therefore not included the lifetime plots for negative values of r .

IV. CONCLUSIONS

We have considered a single band electronic system where a spin singlet superconducting order appears inside a nematic phase. In the above analysis we do not consider effects arising from multiplicity of bands and hence the results are more applicable to cuprates rather than the iron pnictide superconductors. We treat both the orders at the mean-field level in a tight-binding square lattice with the nematic order being modelled as a d -wave Pomeranchuk-type instability. The feedback from the symmetry-broken nematic phase on the SC order was accounted for through a mixing of the s -wave and d -wave channels, which is controlled by a constant, phenomenological anisotropy parameter r . Depending on the value of r , the gap function can display a deep minima (in the case of moderate mixing) or nodes (in the case of strong mixing).

By determining the amplitudes of the SC and the nematic orders self-consistently for all temperatures, the nature of the low-energy excitations could be analysed showing that for $r > r_c^+(\Phi)$ or $r < r_c^-(\Phi)$, the spectrum has nodes, which create a nonuniformity in the SC gap (a direct outcome of the interplay of the FS distortion due to nematicity). This nonuniformity results in inequivalent gap maxima at $|\Delta_{\mathbf{k}}|^{\max.(-)}$ and $|\Delta_{\mathbf{k}}|^{\max.(+)}$.

Temperature dependence of the electronic heat conductivity in the mixed SC and Nematic system was computed using the Boltzmann transport equation method, where the impurity scattering collision integral and quasiparticle lifetime were determined in both the Born and unitary limits. We conclude that the nematic deformation of the FS results in $\kappa_{xx}(T) \neq \kappa_{yy}(T)$ and that there are significant differences in the thermal conductivity behavior in the coexistence phase that can distinguish between deep minima or nodes in the anisotropic SC gap structure. In the case of the SC gap having deep minima on the FS, $\kappa \rightarrow 0$ as $T \rightarrow 0$ in both the Born and unitary limits. In the case when the SC gap function has nodes, low-energy excitations lead to a finite residual κ/T in the $T \rightarrow 0$ in both the Born and unitary limits.

ACKNOWLEDGMENTS

This research was primarily supported by the National Science Foundation under Grant No. DMR-1809846 and through the MonArk Quantum Foundry, an NSF supported quantum foundry, under Award No. DMR-1906383.

- [1] J. Ziman, *Electrons and Phonons* (Clarendon Press, Oxford, 1960).
- [2] J. Bardeen, G. Rickayzen, and L. Tewordt, *Phys. Rev.* **113**, 982 (1959).
- [3] C. Pfleiderer, *Rev. Mod. Phys.* **81**, 1551 (2009).
- [4] D. J. Van Harlingen, *Rev. Mod. Phys.* **67**, 515 (1995).
- [5] C. C. Tsuei and J. R. Kirtley, *Rev. Mod. Phys.* **72**, 969 (2000).
- [6] L. Taillefer, *Annu. Rev. Condens. Matter Phys.* **1**, 51 (2010).
- [7] D. F. Agterberg, J. S. Davis, S. D. Edkins, E. Fradkin, D. J. Van Harlingen, S. A. Kivelson, P. A. Lee, L. Radzihovsky, J. M. Tranquada, and Y. Wang, *Annu. Rev. Condens. Matter Phys.* **11**, 231 (2020).
- [8] H.-H. Wen and S. Li, *Annu. Rev. Condens. Matter Phys.* **2**, 121 (2011).
- [9] G. R. Stewart, *Rev. Mod. Phys.* **83**, 1589 (2011).
- [10] A. Chubukov, *Annu. Rev. Condens. Matter Phys.* **3**, 57 (2012).
- [11] B. Arfi and C. J. Pethick, *Phys. Rev. B* **38**, 2312 (1988).
- [12] P. Hirschfeld, D. Vollhardt, and P. Wölfle, *Solid State Commun.* **59**, 111 (1986).
- [13] K. Scharnberg, D. Walker, H. Monien, L. Tewordt, and R. A. Klemm, *Solid State Commun.* **60**, 535 (1986).
- [14] H. Monien, K. Scharnberg, and D. Walker, *Solid State Commun.* **63**, 535 (1987).
- [15] A. C. Durst and P. A. Lee, *Phys. Rev. B* **62**, 1270 (2000).
- [16] M. J. Graf, S.-K. Yip, J. A. Sauls, and D. Rainer, *Phys. Rev. B* **53**, 15147 (1996).
- [17] Y. Matsuda, K. Izawa, and I. Vekhter, *J. Phys.: Condens. Matter* **18**, R705 (2006).
- [18] H. Shakeripour, C. Petrovic, and L. Taillefer, *New J. Phys.* **11**, 055065 (2009).
- [19] B. Lake, H. M. Rønnow, N. B. Christensen, G. Aeppli, K. Lefmann, D. F. McMorrow, P. Vorderwisch, P. Smeibidl, N. Mangkorntong, T. Sasagawa *et al.*, *Nature (London)* **415**, 299 (2002).
- [20] N. D. Mathur, F. M. Grosche, S. R. Julian, I. R. Walker, D. M. Freye, R. K. W. Haselwimmer, and G. G. Lonzarich, *Nature (London)* **394**, 39 (1998).
- [21] S. Badoux, W. Tabis, F. Laliberté, G. Grissonnanche, B. Vignolle, D. Vignolles, J. Béard, D. A. Bonn, W. N. Hardy, R. Liang *et al.*, *Nature (London)* **531**, 210 (2016).
- [22] D. Y. Kim, S.-Z. Lin, F. Weickert, M. Kenzelmann, E. D. Bauer, F. Ronning, J. D. Thompson, and R. Movshovich, *Phys. Rev. X* **6**, 041059 (2016).
- [23] N. Doiron-Leyraud, P. Auban-Senzier, S. René de Cotret, C. Bourbonnais, D. Jérôme, K. Bechgaard, and L. Taillefer, *Phys. Rev. B* **80**, 214531 (2009).
- [24] T.-M. Chuang, M. P. Allan, J. Lee, Y. Xie, N. Ni, S. L. Bud'ko, G. S. Boebinger, P. C. Canfield, and J. C. Davis, *Science* **327**, 181 (2010).
- [25] A. E. Böhrer and C. Meingast, *C. R. Phys.* **17**, 90 (2016).
- [26] J.-H. Chu, H.-H. Kuo, J. G. Analytis, and I. R. Fisher, *Science* **337**, 710 (2012).
- [27] S. Nakata, M. Horio, K. Koshiishi, K. Hagiwara, C. Lin, M. Suzuki, S. Ideta, K. Tanaka, D. Song, Y. Yoshida *et al.*, *npj Quantum Mater.* **6**, 86 (2021).
- [28] Y. Ando, K. Segawa, S. Komiya, and A. N. Lavrov, *Phys. Rev. Lett.* **88**, 137005 (2002).

- [29] V. Hinkov, D. Haug, B. Fauqué, P. Bourges, Y. Sidis, A. Ivanov, C. Bernhard, C. T. Lin, and B. Keimer, *Science* **319**, 597 (2008).
- [30] Y. Sato, S. Kasahara, H. Murayama, Y. Kasahara, E.-G. Moon, T. Nishizaki, T. Loew, J. Porras, B. Keimer, T. Shibauchi *et al.*, *Nat. Phys.* **13**, 1074 (2017).
- [31] O. Cyr-Choinière, G. Grissonnanche, S. Badoux, J. Day, D. A. Bonn, W. N. Hardy, R. Liang, N. Doiron-Leyraud, and L. Taillefer, *Phys. Rev. B* **92**, 224502 (2015).
- [32] J. Wu, A. T. Bollinger, X. He, and I. Božović, *Nature (London)* **547**, 432 (2017).
- [33] R. M. Fernandes, A. V. Chubukov, and J. Schmalian, *Nat. Phys.* **10**, 97 (2014).
- [34] J. Hu and C. Xu, *Physica C: Superconductivity* **481**, 215 (2012).
- [35] R. M. Fernandes, A. E. Böhmer, C. Meingast, and J. Schmalian, *Phys. Rev. Lett.* **111**, 137001 (2013).
- [36] A. E. Böhmer, F. Hardy, F. Eilers, D. Ernst, P. Adelman, P. Schweiss, T. Wolf, and C. Meingast, *Phys. Rev. B* **87**, 180505(R) (2013).
- [37] Y. Yamakawa, S. Onari, and H. Kontani, *Phys. Rev. X* **6**, 021032 (2016).
- [38] L. Fanfarillo, L. Benfatto, and B. Valenzuela, *Phys. Rev. B* **97**, 121109(R) (2018).
- [39] S. A. Kivelson, I. P. Bindloss, E. Fradkin, V. Oganesyan, J. M. Tranquada, A. Kapitulnik, and C. Howald, *Rev. Mod. Phys.* **75**, 1201 (2003).
- [40] E. Fradkin, S. A. Kivelson, M. J. Lawler, J. P. Eisenstein, and A. P. Mackenzie, *Annu. Rev. Condens. Matter Phys.* **1**, 153 (2010).
- [41] H. Yamase and W. Metzner, *Phys. Rev. B* **73**, 214517 (2006).
- [42] V. Oganesyan, S. A. Kivelson, and E. Fradkin, *Phys. Rev. B* **64**, 195109 (2001).
- [43] Y.-J. Kao and H.-Y. Kee, *Phys. Rev. B* **72**, 024502 (2005).
- [44] C. J. Halboth and W. Metzner, *Phys. Rev. Lett.* **85**, 5162 (2000).
- [45] I. Mandal, *Phys. Rev. B* **94**, 115138 (2016).
- [46] R. M. Fernandes and A. J. Millis, *Phys. Rev. Lett.* **111**, 127001 (2013).
- [47] X. Chen, S. Maiti, R. M. Fernandes, and P. J. Hirschfeld, *Phys. Rev. B* **102**, 184512 (2020).
- [48] L. Fritz and S. Sachdev, *Phys. Rev. B* **80**, 144503 (2009).
- [49] A. B. Vorontsov and I. Vekhter, *Phys. Rev. Lett.* **105**, 187004 (2010).
- [50] A. V. Chubukov and I. Eremin, *Phys. Rev. B* **82**, 060504(R) (2010).
- [51] F. Hardy, M. He, L. Wang, T. Wolf, P. Schweiss, M. Merz, M. Barth, P. Adelman, R. Eder, A.-A. Haghighirad, and C. Meingast, *Phys. Rev. B* **99**, 035157 (2019).
- [52] Y. S. Kushnirenko, D. V. Evtushinsky, T. K. Kim, I. Morozov, L. Harnagea, S. Wurmehl, S. Aswartham, B. Büchner, A. V. Chubukov, and S. V. Borisenko, *Phys. Rev. B* **102**, 184502 (2020).
- [53] J. K. Dong, T. Y. Guan, S. Y. Zhou, X. Qiu, L. Ding, C. Zhang, U. Patel, Z. L. Xiao, and S. Y. Li, *Phys. Rev. B* **80**, 024518 (2009).
- [54] P. Bourgeois-Hope, S. Chi, D. A. Bonn, R. Liang, W. N. Hardy, T. Wolf, C. Meingast, N. Doiron-Leyraud, and L. Taillefer, *Phys. Rev. Lett.* **117**, 097003 (2016).
- [55] R. A. Borzi, S. A. Grigera, J. Farrell, R. S. Perry, S. J. S. Lister, S. L. Lee, D. A. Tennant, Y. Maeno, and A. P. Mackenzie, *Science* **315**, 214 (2007).
- [56] E.-A. Kim, M. J. Lawler, P. Oreto, S. Sachdev, E. Fradkin, and S. A. Kivelson, *Phys. Rev. B* **77**, 184514 (2008).
- [57] H. Yamase, V. Oganesyan, and W. Metzner, *Phys. Rev. B* **72**, 035114 (2005).
- [58] A. Kreisel, C. A. Marques, L. C. Rhodes, X. Kong, T. Berlijn, R. Fittipaldi, V. Granata, A. Vecchione, P. Wahl, and P. J. Hirschfeld, *npj Quantum Mater.* **6**, 100 (2021).
- [59] B. T. Geilikman, *JETP* **7**, 721 (1958).
- [60] V. P. Mineev and K. Samokin, *Introduction to Unconventional Superconductivity* (Gordon and Breach, Amsterdam, 1998).
- [61] B. Arfi, *Phys. Rev. B* **47**, 523 (1993).
- [62] S. S. Choudhury and A. B. Vorontsov, *Phys. Rev. B* **103**, 104501 (2021).
- [63] R. C. Yu, M. B. Salamon, J. P. Lu, and W. C. Lee, *Phys. Rev. Lett.* **69**, 1431 (1992).
- [64] D. Ginsberg, *Physical Properties of High Temperature Superconductors III* (World Scientific, Singapore, 1998), Chap. 3, pp. 159–283.

ANISOTROPIC THERMAL TRANSPORT IN SUPERCONDUCTORS WITH
COEXISTING SPIN DENSITY WAVES

Contribution of Authors and Co-Authors

Manuscript in following chapter

Author: [Sean F Peterson]

Contributions: [Computational lead of project. Wrote all relevant code and ran it on an Nvidia GPU in order to collect data and produce figures for this work. Applied theoretical framework from previous works to derive equations vital to the calculations done in this work.]

Author: [Sourav Sen Choudhury]

Contributions: [Theory lead of project. Posed problem as continuation of work from: *Phys. Rev. B*, 103:104501, 2021. Where a $\mathbf{Q} = (\pi/2, \pi/2)$ and $\mathbf{Q} = (\pi, 0)$ SDW phase coexisting with superconductivity was considered instead of a $\mathbf{Q} = (\pi, \pi)$ SDW phase coexisting with superconductivity. Provided theoretical framework of problem as applied to previous superconducting states as a background for theoretical work in this paper.]

Author: [Yves Idzerda]

Contributions: [Principle Investigator.]

Manuscript Information

[Sean F Peterson, Sourav Sen Choudhury, Yves Idzerda]

[Phys. Rev. B]

Status of Manuscript:

Prepared for submission to a peer-reviewed journal

Officially submitted to a peer-reviewed journal

Accepted by a peer-reviewed journal

Published in a peer-reviewed journal

[American Physical Society]

[April 12, 2023]

[July 17, 2022]

[Phys. Rev. B **108**]

[<https://doi.org/10.1103/PhysRevB.108.054503>]

Anisotropic thermal transport in superconductors with coexisting spin density waves

Sean F. Peterson , Sourav Sen Choudhury, and Yves Idzerda 

Department of Physics, Montana State University, Bozeman, Montana 59717, USA

 (Received 12 April 2023; revised 25 June 2023; accepted 17 July 2023; published 2 August 2023)

Thermal conductivity measurements can provide key and experimentally verifiable insight into the electronic transport of unconventional superconductors. In this paper, electronic thermal transport of two-dimensional tight-binding metallic systems with coexisting d -wave superconducting (SC) and antiferromagnetic spin density wave (SDW) orders with nesting vector $\mathbf{Q} = (\pi/2, \pi/2)$ or $(\pi, 0)$ are considered. The coexisting SC and SDW orders are modeled at the mean-field level. Thermal conductivities are numerically calculated within Boltzmann kinetic theory in the weak impurity scattering (Born) limit. These SDW nesting vectors are chosen for their unique property of reconstructing the Fermi surface parallel to \mathbf{Q} and preserving the metallic FS perpendicular to \mathbf{Q} . This leads to anisotropic electronic thermal conductivities parallel and perpendicular to \mathbf{Q} , which also depend on the presence or absence of additional gapless excitations exclusive to the coexistence phase. It was found that the $\mathbf{Q} = (\pi/2, \pi/2)$ and $(\pi, 0)$ SDW systems exhibit equivalent electron transport relative to \mathbf{Q} . These systems also had equivalent electron transport when coexisting with a d -wave SC gap when $\Delta_{\mathbf{k}}$ had the same symmetry class under translations of \mathbf{Q} .

DOI: [10.1103/PhysRevB.108.054503](https://doi.org/10.1103/PhysRevB.108.054503)

I. INTRODUCTION

Among the most studied candidates for high-temperature superconductors (SCs) are cuprates [1], iron pnictides [2], and iron chalcogenides [3]. A common feature for these families of materials is that they have quasi-two-dimensional sheets of transition-metal atoms (either Cu or Fe) in a square lattice resulting in cylindrical Fermi surfaces [4,5] (FSs) that can be treated as two-dimensional systems (since they are largely k_z independent). Due to the layered structure of these quasi-two-dimensional sheets, it is possible to grow single superconducting layers on a substrate and study superconductivity strictly in two dimensions [6–8]. It is important to note that many of these high- T_c SCs are unconventional in nature.

Unconventional SCs often have phase diagrams with multiple broken symmetry phases which depend on material properties such as electron or hole doping concentration [9,10]. One of the more common broken-symmetry states that superconductivity can coexist with is an antiferromagnetic (AFM) state which couples quasiparticle states in different parts of the Brillouin zone by a nesting vector, \mathbf{Q} , forming a spin density wave (SDW) state [11–14]. While in this paper only the interplay between SDW and SC orders will be investigated, the SDW state will often be preceded by a structural transition from a tetragonal to an orthorhombic [15] or a monoclinic [16] lattice, thus breaking the fourfold rotational symmetry $C(4)$ of the crystal. This structural transition can result in an Ising nematic phase [17] and its effects on electronic thermal transport in SC systems has been previously discussed [18]. Including effects of a structural transition with SDW and SC ordering is beyond the scope of this paper. While it is assumed here that the $C(4)$ symmetry of the underlying structural square lattice is preserved, the magnetic structure imposed on the lattice by the existence of striped AFM order-

ing reduces the $C(4)$ symmetry of the unit cell [1] to that of a twofold rotational symmetry $C(2)$ in the magnetic cell. This broken symmetry is often reflected in the transport properties of such materials [19].

To better understand these unconventional SCs, thermal conductivity measurements are an invaluable tool for probing the transport properties of materials [20,21]. In normal metals, the electronic thermal conductivity at low temperatures is dominated by electron scattering of impurities and results in a linear temperature dependence which is well understood within the framework of semiclassical transport theory based on the Boltzmann kinetic equation [22]. In conventional SCs, the entire FS is gapped and the thermal conductivity is known to decrease exponentially [23] as $T \rightarrow 0$. However, in unconventional SCs (such as d -wave SCs) the thermal conductivity is known to have a linear T dependence at low- T in the limit of weak impurity scattering, similar to a normal metal due to the existence of zero-energy quasiparticle excitations (nodes) on the FS [24,25]. The band topology in the vicinity of these nodes is of utmost importance as it determines the quasiparticle velocities, which can drastically change the transport properties of a material. For example, it has been shown [26] that two types of d -wave SC (d_{xy} vs $d_{x^2-y^2}$) have very different thermal conductivities on tight-binding FSs due to different Fermi velocities and local densities of states at the nodes. Electron transport within SDW materials was observed [27] to follow suppressed Fermi liquid behavior, and as such has an electronic thermal conductivity that is linear in T but diminished from the normal metallic state thermal conductivity [28,29]. Thermal transport in d -wave superconducting materials with density waves, such as charge density waves or SDWs, which reduce the $C(4)$ rotational symmetry to a $C(2)$ rotational symmetry, have been shown to exhibit anisotropic thermal transport at low- T [30,31].

In the cuprates, the superconducting gap is known to have d -wave symmetry [32]. Superconductivity can be preceded by a commensurate SDW order with nesting vector $\mathbf{Q} = (\pi, \pi)$ [11,12,33] (also known as the AFM1 state [34]). This reconstructs [35,36] the metallic FS with quasiparticle pockets located at the M points in the BZ [37] while preserving the d -wave SC symmetry nodes which are the main contributors to the transport properties in the clean limit [29]. The d -wave SC state was also found to coexist with the $\mathbf{Q} = (\pi, 0)$ SDW state in the underdoped region of a two-dimensional Hubbard model [38], which is often used to model the cuprates. In thin-film cuprates [6,8], the behavior of the bulk phase was preserved in monolayers, including the high- T_c value at optimal doping, indicating that SC in the cuprates is inherently a two-dimensional phenomena. Some cuprate materials have been measured to exhibit anisotropic in-plane electronic thermal conductivities, where electrons preferentially travel along one crystallographic direction over another [39,40] due to electronic inhomogeneities. Additionally, quasi-one-dimensional electronic thermal transport mediated by spin fluctuations was also observed in the cuprates [41].

In the iron pnictides, an unconventional superconducting gap may emerge out of a commensurate SDW state with nesting vector $\mathbf{Q} = (\pi, 0)$ [16,42–45] (also known as the AFM2 state [34]). This results in a striped AFM which reduces the $C(4)$ symmetry of the crystal lattice to a magnetic cell with $C(2)$ symmetry [46]. In such materials, it has been shown that the DC electric conductivity within the Drude model is highly anisotropic between the conductivity parallel and perpendicular to \mathbf{Q} (i.e. $\sigma_{xx} \neq \sigma_{yy}$) [19].

While SC often arises out of an AFM state in cuprates and iron pnictides, iron chalcogenides lack AFM ordering [47] in bulk. However, FeSe monolayers can exhibit SDW ordering when grown on substrates that increase the spacing between Fe atoms due to epitaxial strain [14]. These strained FeSe monolayers have been measured [7] to have greatly enhanced transition temperatures (T_c), when compared to those measured in bulk [3]. High- T_c superconductivity in these strained FeSe monolayers is likely due to the presence of SDWs in the material enhancing the SC state [14]. In some iron chalcogenides, the SDW nesting vector was found to be the commensurate nesting vector $\mathbf{Q} = (\pi/2, \pi/2)$ [48,49] (also known as the AFM3 state [34]).

In this paper, the single band electronic transport properties of two cases are considered. The first being a collinear commensurate SDW state with nesting vector $\mathbf{Q} = (\pi/2, \pi/2)$ (AFM3) coexisting with the d -wave singlet pairing SC states: $d_{x^2-y^2}$ and d_{xy} . The second case is a similar collinear commensurate SDW state, but with a nesting vector of $\mathbf{Q} = (\pi, 0)$ (AFM2) coexisting with the same d -wave singlet SC pairing states. The effects arising from the multiplicity of bands were not considered and therefore orbital degrees of freedom were neglected. Thus, the present analysis is not directly applicable to iron-based SCs (where orbital mixing plays a significant role) but is more relevant for cuprate SCs which can be accurately modeled with a single band model [50,51]. Nevertheless, the analysis given below provides important insights regarding the interplay of SC and SDW orders and their impact on thermal transport properties of such systems, particularly in the coexistence phase.

II. MODEL AND FORMALISM

A. Hamiltonian

In this paper, the normal-state metallic tight-binding Hamiltonian will be considered,

$$H_0 = \sum_{\mathbf{k}, \sigma} \xi_{\mathbf{k}} \hat{a}_{\mathbf{k}\sigma}^\dagger \hat{a}_{\mathbf{k}\sigma}, \quad (1)$$

with the 2D inversion-symmetric ($\xi_{\mathbf{k}} = \xi_{-\mathbf{k}}$) dispersion relations

$$\begin{aligned} \xi_{\mathbf{k}}^{(1)} &= \mu - t_1(\cos 2k_x + \cos 2k_y) - t_2 \cos 2k_x \cos 2k_y \\ \xi_{\mathbf{k}}^{(2)} &= \mu - t_1(\cos(k_x - k_y) + \cos(k_x + k_y)) \\ &\quad - t_2 \cos(k_x - k_y) \cos(k_x + k_y), \end{aligned} \quad (2)$$

where μ is the chemical potential, t_1 is the nearest-neighbor hopping, and t_2 is the next-nearest-neighbor hopping on a two-dimensional square lattice of the spacing one ($a = 1$), all of which are in units of the Néel temperature (T_N). The chemical potential was set to zero ($\mu = 0$) and the hopping parameters were set to $t_1 = 100 T_N$ and $t_2 = 10 T_N$ for both dispersion relations, consistent with previous calculations [52,53] and experiments [54,55] in literature. For $\xi_{\mathbf{k}}^{(1)}$, this results in the weak metallic FS ($\xi_{\mathbf{k}}^{(1)} = 0$) with quasiparticle pockets centered at the Γ and M points in the first Brillouin zone (FBZ) which can be seen as the black curves in Fig. 1(a). For $\xi_{\mathbf{k}}^{(2)}$, this results in a metallic FS ($\xi_{\mathbf{k}}^{(2)} = 0$) with a quasiparticle pocket centered around the Γ point in the FBZ which can be seen as the black curve in Fig. 1(b). The first dispersion relation, $\xi_{\mathbf{k}}^{(1)}$, represents a system where the FS is translated by the SDW nesting vector $\mathbf{Q} = (\pi/2, \pi/2)$ and overlaps with the original FS at the edge of the reduced Brillouin Zone (RBZ) as can be seen in Fig. 1(a). The second dispersion relation, $\xi_{\mathbf{k}}^{(2)}$, represents a SDW nesting vector $\mathbf{Q} = (\pi, 0)$, as can be seen in Fig. 1(b).

The emergence of SDW ordering in these metallic systems occurs below the Néel temperature and is the result of a striped AFM system. This broken symmetry is also reflected in the shape of the RBZ which can be seen as the blue dashed lines in Fig. 1. Due to this reduced rotational symmetry, the $\xi_{\mathbf{k}}$ and $\xi_{\mathbf{k}+\mathbf{Q}}$ FSs only overlap in the direction parallel to the nesting vector \mathbf{Q} , leading to a FS reconstruction parallel to \mathbf{Q} while preserving the normal state tight-binding FS perpendicular to \mathbf{Q} . This reconstructed FS can be seen by the black curve in Fig. 2.

To begin studying thermal transport in a system with coexisting SDW and SC orders, the Hamiltonian is modeled at the mean-field level [52]:

$$\begin{aligned} H &= H_0 + H_{\text{SDW}} + H_{\text{SC}}, \\ H_{\text{SDW}} &= \frac{1}{2} \sum_{\mathbf{k}, \sigma} \sigma M (\hat{a}_{\mathbf{k}, \sigma}^\dagger \hat{a}_{\mathbf{k}+\mathbf{Q}, \sigma} + \text{H.c.}), \\ H_{\text{SC}} &= \frac{1}{2} \sum_{\mathbf{k}, \sigma} \sigma \Delta \mathcal{Y}_{\mathbf{k}} (\hat{a}_{\mathbf{k}, \sigma}^\dagger \hat{a}_{-\mathbf{k}, -\sigma}^\dagger + \text{H.c.}), \end{aligned} \quad (3)$$

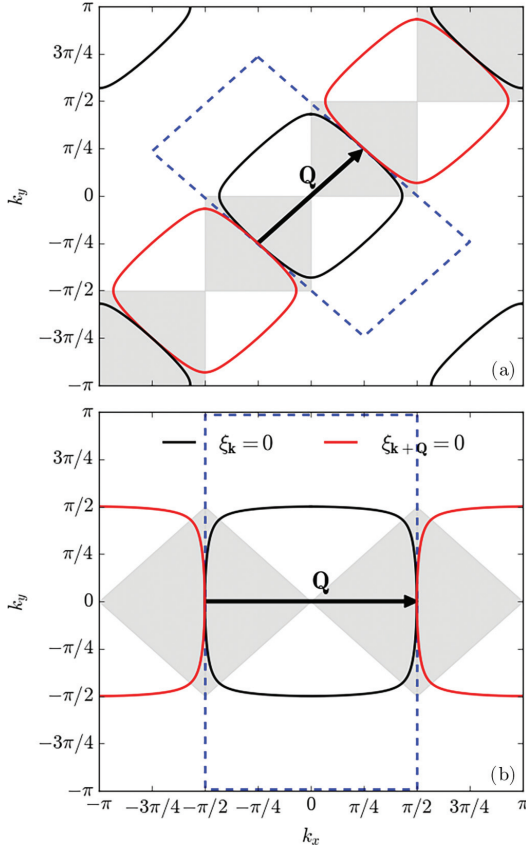


FIG. 1. Fermi surface nesting between tight-binding FSs (black curves) and the FSs translated by \mathbf{Q} (red curves) for SDW orders with the nesting vector: (a) $\mathbf{Q} = (\pi/2, \pi/2)$ and (b) $\mathbf{Q} = (\pi, 0)$, where the FS reconstruction due to SDW ordering occurs in the gray regions and the normal state FS is preserved in the white regions. These SDW states also result in magnetic cells which are larger than the unit cells of the underlying lattice; this results in the periodicity in \mathbf{k} space being reduced from the square FBZ to the reduced Brillouin zone seen as the blue dashed curves.

where the mean-field order parameters are defined by

$$M = -\frac{V_{\text{SDW}}}{2} \sum_{\mathbf{k}, \sigma} \sigma \langle \hat{a}_{\mathbf{k}+\mathbf{Q}, \sigma}^\dagger \hat{a}_{\mathbf{k}, \sigma} \rangle, \quad (4)$$

$$\Delta = -V_{\text{SC}} \sum_{\mathbf{k}} \mathcal{Y}_{\mathbf{k}} (\hat{a}_{-\mathbf{k}, \downarrow}^\dagger \hat{a}_{\mathbf{k}, \uparrow}^\dagger).$$

These order parameters were found self-consistently by a method outlined in Appendix A and superconductivity was assumed to arise out of the SDW ordering ($T_N > T_c$), consistent with phase diagrams for iron-based [56,57] and cuprate [58] SCs. The results of these self-consistency calculations for the order parameters can be seen in Fig. 8. Here a collinear sinusoidal SDW system was considered with a spatial mag-

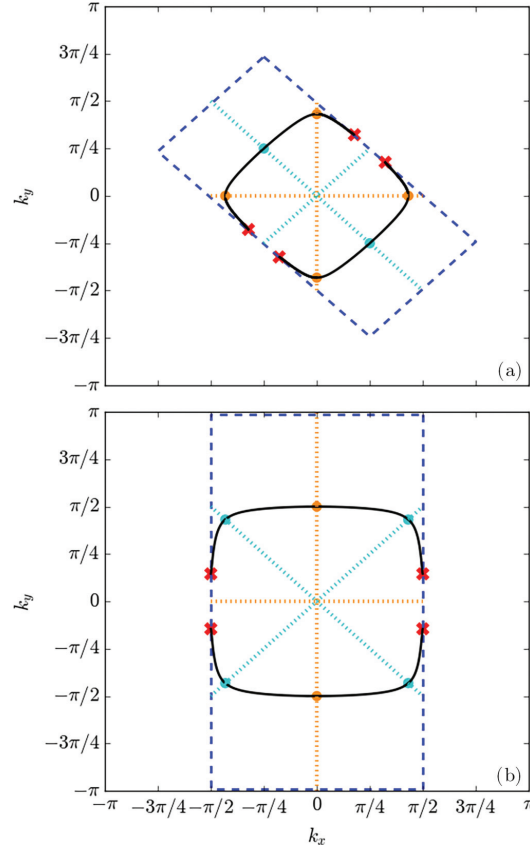


FIG. 2. FSs reconstructed by SDW ordering (solid black curves) when $M = 2T_N$ for the nesting vectors (a) $\mathbf{Q} = (\pi/2, \pi/2)$ and (b) $\mathbf{Q} = (\pi, 0)$. The d -wave nodal lines are represented with dotted cyan and orange lines for $d_{x^2-y^2}$ and d_{xy} respectively. Cyan and orange points represent the locations of the $d_{x^2-y^2}$ and d_{xy} nodes, respectively, when their nodal lines cross the reconstructed FS. Red X's show the locations of additional mixing nodes that occur only when the SC gap is even under translations of \mathbf{Q} ($\Delta_{\mathbf{k}+\mathbf{Q}} = \Delta_{\mathbf{k}}$).

netization of $\mathbf{m}(\mathbf{r}) = 2M\hat{z} \cos \mathbf{Q} \cdot \mathbf{r}$. SDW ordering couples electron states of parallel spins whose momenta differ by the nesting vector \mathbf{Q} . For the SC order, only singlet electron pairing is considered and $\Delta_{\mathbf{k}} = \Delta \mathcal{Y}_{\mathbf{k}}$, where $\mathcal{Y}_{\mathbf{k}}$ is a basis function compatible with the square symmetry inherent to the lattice. The basis functions considered were $d_{x^2-y^2}$ ($\mathcal{Y}_{\mathbf{k}} \propto \cos k_x - \cos k_y$) and d_{xy} ($\mathcal{Y}_{\mathbf{k}} \propto \sin k_x \sin k_y$), and qualitative illustrations of these SC gap structures can be seen in Fig. 3 on the two normal state FSs.

The mean-field Hamiltonian for $T < T_c$ and $\Delta \neq 0$ can be written in matrix form in the Nambu basis as

$$H^{(\sigma)} = \frac{1}{2} \sum_{\mathbf{k}} (\Psi_{\mathbf{k}}^n)^\dagger \hat{\mathcal{H}}_{\mathbf{k}}^{(\sigma)} \Psi_{\mathbf{k}}^n,$$

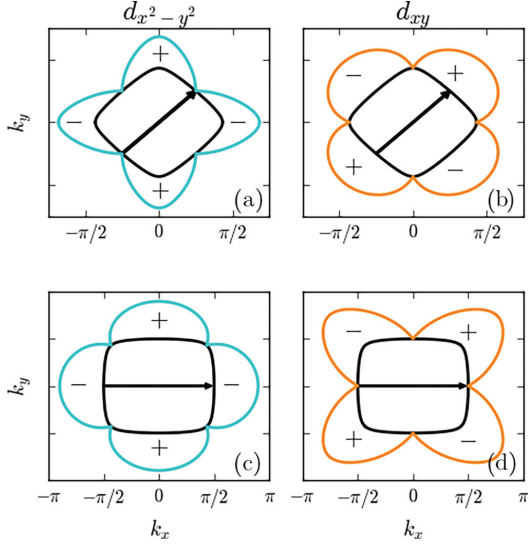


FIG. 3. Qualitative illustration of the amplitude and sign of the superconducting gap along the normal state tight-binding FSs (band parameters $t_1 = 100T_N$ and $t_2 = 10T_N$) to show the symmetry of the SC gap under translations of the \mathbf{Q} vector. (a) $d_{x^2-y^2}$ SC pairing on the $\xi_{\mathbf{k}}^{(1)}$ FS, (b) d_{xy} pairing on the $\xi_{\mathbf{k}}^{(1)}$ FS, (c) $d_{x^2-y^2}$ SC pairing on the $\xi_{\mathbf{k}}^{(2)}$ FS, and (d) d_{xy} pairing on the $\xi_{\mathbf{k}}^{(2)}$ FS.

the spin-dependent Hamiltonian matrix in the regions of the RBZ where the FS reconstructs due to SDW ordering (see gray shaded regions in Fig. 1) can be written as

$$\hat{\mathcal{H}}_{\mathbf{k}}^{(\sigma)} = \begin{pmatrix} \xi_{\mathbf{k}} & \sigma \Delta_{\mathbf{k}} & \sigma M & 0 \\ \sigma \Delta_{\mathbf{k}} & -\xi_{\mathbf{k}} & 0 & \sigma M \\ \sigma M & 0 & \xi_{\mathbf{k}+\mathbf{Q}} & \sigma \Delta_{\mathbf{k}+\mathbf{Q}} \\ 0 & \sigma M & \sigma \Delta_{\mathbf{k}+\mathbf{Q}} & -\xi_{\mathbf{k}+\mathbf{Q}} \end{pmatrix}, \quad (5)$$

and reduces to a pure SC Hamiltonian in regions where the normal state FS is preserved (see unshaded regions in Fig. 1),

$$\hat{\mathcal{H}}_{\mathbf{k}}^{(\sigma)} = \begin{pmatrix} \xi_{\mathbf{k}} & \sigma \Delta_{\mathbf{k}} & 0 & 0 \\ \sigma \Delta_{\mathbf{k}} & -\xi_{\mathbf{k}} & 0 & 0 \\ 0 & 0 & \xi_{\mathbf{k}+\mathbf{Q}} & \sigma \Delta_{\mathbf{k}+\mathbf{Q}} \\ 0 & 0 & \sigma \Delta_{\mathbf{k}+\mathbf{Q}} & -\xi_{\mathbf{k}+\mathbf{Q}} \end{pmatrix}, \quad (6)$$

where $(\hat{\Psi}_{\mathbf{k}}^n)^\dagger = (\hat{a}_{\mathbf{k},\sigma}^\dagger, \hat{a}_{-\mathbf{k},-\sigma}, \hat{a}_{\mathbf{k}+\mathbf{Q},\sigma}^\dagger, \hat{a}_{-\mathbf{k}-\mathbf{Q},-\sigma})$ is the Nambu vector for the normal state. The eigenvalues of $\hat{\mathcal{H}}_{\mathbf{k}}$ in the shaded regions when SC and SDW orders coexist are the quasiparticle energies $\pm E_{\mathbf{k}}^{(1,2)}$,

$$\begin{aligned} E_{\mathbf{k}}^{(1)} &= \sqrt{\Gamma_{\mathbf{k}} + 2\Lambda_{\mathbf{k}}}, & E_{\mathbf{k}}^{(2)} &= \sqrt{\Gamma_{\mathbf{k}} - 2\Lambda_{\mathbf{k}}}, \\ \Gamma_{\mathbf{k}} &= (\xi_{\mathbf{k}}^+)^2 + (\xi_{\mathbf{k}}^-)^2 + (\Delta_{\mathbf{k}}^+)^2 + (\Delta_{\mathbf{k}}^-)^2 + M^2, & (7) \\ \Lambda_{\mathbf{k}} &= \sqrt{(\xi_{\mathbf{k}}^+ \xi_{\mathbf{k}}^- + \Delta_{\mathbf{k}}^+ \Delta_{\mathbf{k}}^-)^2 + M^2((\xi_{\mathbf{k}}^+)^2 + (\Delta_{\mathbf{k}}^+)^2)}, \end{aligned}$$

TABLE I. Symmetry class of the SC basis function, $\mathcal{J}_{\mathbf{k}}$, under translations of the SDW nesting vector \mathbf{Q} .

\mathbf{Q}	$d^{(O)}$ wave	$d^{(E)}$ wave
$(\pi/2, \pi/2)$	$d_{x^2-y^2}$	d_{xy}
$(\pi, 0)$	d_{xy}	$d_{x^2-y^2}$

where $\xi_{\mathbf{k}}^\pm = (\xi_{\mathbf{k}} \pm \xi_{\mathbf{k}+\mathbf{Q}})/2$ and $\Delta_{\mathbf{k}}^\pm = (\Delta_{\mathbf{k}} \pm \Delta_{\mathbf{k}+\mathbf{Q}})/2$. In the regions where the normal state FS is preserved perpendicular to \mathbf{Q} , the eigenvalues reduce to the typical pure SC eigenvalues:

$$E_{\mathbf{k}}^{(1)} = \sqrt{\xi_{\mathbf{k}}^2 + \Delta_{\mathbf{k}}^2}, \quad E_{\mathbf{k}}^{(2)} = \sqrt{\xi_{\mathbf{k}+\mathbf{Q}}^2 + \Delta_{\mathbf{k}+\mathbf{Q}}^2}. \quad (8)$$

When $T > T_c$ and $\Delta = 0$, the eigenvalues in the regions where the $\xi_{\mathbf{k}}$ and $\xi_{\mathbf{k}+\mathbf{Q}}$ FSs overlap and the FS reconstructs reduce to the pure SDW eigenvalues:

$$\begin{aligned} E_{\mathbf{k}}^{(1)} &= E_{\mathbf{k}}^{(\alpha)} = \xi_{\mathbf{k}}^+ + \sqrt{(\xi_{\mathbf{k}}^-)^2 + M^2}, \\ E_{\mathbf{k}}^{(2)} &= E_{\mathbf{k}}^{(\beta)} = \xi_{\mathbf{k}}^+ - \sqrt{(\xi_{\mathbf{k}}^-)^2 + M^2}. \end{aligned} \quad (9)$$

The eigenvalues in the region where the normal-state FS is preserved reduce to $E_{\mathbf{k}}^{(1)} = \xi_{\mathbf{k}}$ and $E_{\mathbf{k}}^{(2)} = \xi_{\mathbf{k}+\mathbf{Q}}$. Furthermore, the FS of this system is reconstructed from the black curves in Fig. 1 to the black curves in Fig. 2 when $T < T_N$, where it can be seen that sections of the FS parallel to \mathbf{Q} become gapped by the SDW order.

B. Symmetry classes of the SC order parameters

The coexistence of the SDW and SC order parameters M and Δ depends on the symmetry of the SC order parameter translated by the SDW nesting vector. If translations of the SC order parameter by \mathbf{Q} are even ($\Delta_{\mathbf{k}+\mathbf{Q}} = \Delta_{\mathbf{k}}$), denoted by (E), then the order parameters are competitive with each other and the existence of SC order suppresses the SDW order and the SC transition temperature (T_c) [52], which can be seen from the orange curves in Fig. 8. Whereas if the SC order parameter is odd under translations of the nesting vector ($\Delta_{\mathbf{k}+\mathbf{Q}} = -\Delta_{\mathbf{k}}$), denoted by (O), then the order parameters are cooperative with each other and the existence of SC order enhances the SDW on-site magnetization and T_c [52], which can be seen from the cyan curves in Fig. 8.

As can be seen from Fig. 3, for the SDW state with nesting vector $\mathbf{Q} = (\pi/2, \pi/2)$, the SC gap is even under translations of \mathbf{Q} for d_{xy} and odd for $d_{x^2-y^2}$. However, for the SDW state with $\mathbf{Q} = (\pi, 0)$, the $d_{x^2-y^2}$ SC pairing state is even under translations of \mathbf{Q} and d_{xy} is odd under these same translations (these symmetry classifications are listed in Table I). This switching between the d -wave symmetry classes under translations of \mathbf{Q} is a direct result of both the \mathbf{Q} vectors and the $d_{x^2-y^2}$ and d_{xy} SC basis functions ($\mathcal{J}_{\mathbf{k}}$) being rotated by $\theta_{\mathbf{k}} = \pi/4$ relative to each other. Therefore, to maintain the same symmetry in $\Delta_{\mathbf{k}}$ under translations of \mathbf{Q} , the d -wave basis functions are switched when \mathbf{Q} is rotated.

The nature of the zero-energy excitations critically depends on the symmetry of the SC gap under translations of the nesting vector [26]. When this symmetry is even, $\Delta_{\mathbf{k}+\mathbf{Q}} = \Delta_{\mathbf{k}}$

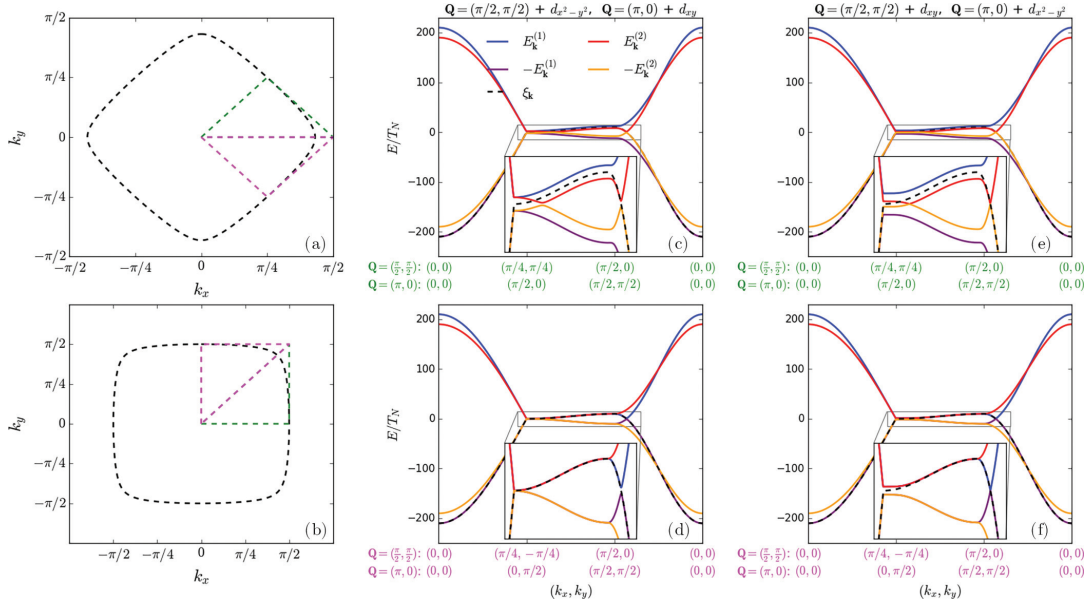


FIG. 4. (a) Band paths relative to the $\xi_{\mathbf{k}}^{(1)}$ FS for the $\mathbf{Q} = (\pi/2, \pi/2)$ SDW systems both parallel to \mathbf{Q} (green) and perpendicular to \mathbf{Q} (magenta). (b) Band paths relative to the $\xi_{\mathbf{k}}^{(2)}$ FS for the $\mathbf{Q} = (\pi, 0)$ SDW systems both parallel to \mathbf{Q} (green) and perpendicular to \mathbf{Q} (magenta). (c) Band structure for the d -wave SC gap which is odd under translations of \mathbf{Q} plotted along the band paths parallel to \mathbf{Q} for both nesting vectors (green paths). (d) Band structure for the d -wave SC gap which is odd under translations of \mathbf{Q} plotted along the band paths perpendicular to \mathbf{Q} for both nesting vectors (magenta paths). (e) Band structure for the d -wave SC gap which is even under translations of \mathbf{Q} plotted along the band paths parallel to \mathbf{Q} for both nesting vectors (green paths). (f) Band structure for the d -wave SC gap which is even under translations of \mathbf{Q} plotted along the band paths perpendicular to \mathbf{Q} for both nesting vectors (magenta paths).

so $\Delta_{\mathbf{k}}^+ = \Delta_{\mathbf{k}}$ and $\Delta_{\mathbf{k}}^- = 0$. Similarly, when this symmetry is odd, $\Delta_{\mathbf{k}+\mathbf{Q}} = -\Delta_{\mathbf{k}}$ so $\Delta_{\mathbf{k}}^+ = 0$ and $\Delta_{\mathbf{k}}^- = \Delta_{\mathbf{k}}$. This simplifies the eigenvalues when both Δ and M are nonzero in Eq. (7) to

$$\begin{aligned}
 E_{\mathbf{k}}^{(1,2;E,O)} &= \sqrt{\Gamma_{\mathbf{k}} \pm 2\Lambda_{\mathbf{k}}^{(E,O)}}, \\
 \Gamma_{\mathbf{k}} &= (\xi_{\mathbf{k}}^+)^2 + (\xi_{\mathbf{k}}^-)^2 + \Delta_{\mathbf{k}}^2 + M^2, \\
 \Lambda_{\mathbf{k}}^{(E)} &= \sqrt{(\xi_{\mathbf{k}}^+ \xi_{\mathbf{k}}^-)^2 + M^2((\xi_{\mathbf{k}}^+)^2 + \Delta_{\mathbf{k}}^2)}, \\
 \Lambda_{\mathbf{k}}^{(O)} &= \sqrt{(\xi_{\mathbf{k}}^+ \xi_{\mathbf{k}}^-)^2 + M^2(\xi_{\mathbf{k}}^+)^2}. \quad (10)
 \end{aligned}$$

For even symmetry, nodal points exist in addition to the SC symmetry nodes near the edge of the RBZ where $\xi_{\mathbf{k}}^- = 0$ and when $E_{\mathbf{k}}^{(2;E)} = M - \sqrt{(\xi_{\mathbf{k}}^+)^2 + \Delta_{\mathbf{k}}^2} = 0$. The locations of these nodes can be seen as the red crosses in Fig. 2. In the odd symmetry cases, these additional nodes are absent. Furthermore, two of the d -wave symmetry nodes with odd translational symmetry are gapped by the SDW order due to their nodal lines aligning with \mathbf{Q} . This can be seen from the cyan $d_{x^2-y^2}$ and orange d_{xy} nodal lines parallel to \mathbf{Q} in Figs. 2(a) and 2(b), respectively.

The resulting band structures are shown in Fig. 4, where the first two panels, Figs. 4(a) and 4(b), illustrate the band paths relative to the normal state FSs. The middle two panels, Figs. 4(c) and 4(d), display the calculated band structure for both SDW states coexisting with the d -wave SC gaps which

are odd under translations of \mathbf{Q} along the indicated paths. The final two panels, Figs. 4(e) and 4(f), display the calculated band structure for both SDW states coexisting with the d -wave SC gaps which are even under translations of \mathbf{Q} again along the indicated paths. For $\mathbf{Q} = (\pi/2, \pi/2)$, the odd d -wave state is the $d_{x^2-y^2}$ pairing and for $\mathbf{Q} = (\pi, 0)$ the odd state is the d_{xy} pairing state. In Fig. 4(c), the bands shown are those in the region where SDW ordering reconstructs the FS parallel to \mathbf{Q} along the green paths. The SC node typically present in the vicinity of $\mathbf{k} = (\pi/4, \pi/4)$ [for $\mathbf{Q} = (\pi/2, \pi/2)$] or near $\mathbf{k} = (\pi/2, 0)$ [for $\mathbf{Q} = (\pi, 0)$] becomes gapped by the SDW. This again corresponds to the cyan $d_{x^2-y^2}$ and orange d_{xy} nodal lines in Figs. 2(a) and 2(b), respectively. In Fig. 4(d), the bands determined along the magenta paths in Figs. 4(a) and 4(b) are shown where the normal state FS is preserved perpendicular to \mathbf{Q} , resulting in the pure SC bands and the d -wave symmetry nodes in the vicinity of $\mathbf{k} = (\pi/4, -\pi/4)$ [for $\mathbf{Q} = (\pi/2, \pi/2)$] or near $\mathbf{k} = (0, \pi/2)$ [for $\mathbf{Q} = (\pi, 0)$] are preserved.

In Figs. 4(e) and 4(f), the band structure is shown for the SDW states coexisting with the d -wave SC gaps with even symmetry when translated by \mathbf{Q} . For the $\mathbf{Q} = (\pi/2, \pi/2)$ SDW state, this is the d_{xy} pairing state and for the $\mathbf{Q} = (\pi, 0)$ SDW state this is the $d_{x^2-y^2}$ pairing state. The quasiparticle bands parallel to \mathbf{Q} along the green paths in Figs. 4(a) and 4(b) are shown in Fig. 4(e). The typical d -wave nodes occurring in the vicinity of $\mathbf{k} = (\pi/2, 0)$ [for $\mathbf{Q} = (\pi/2, \pi/2)$] or $\mathbf{k} =$

$(\pi/2, \pi/2)$ [for $\mathbf{Q} = (\pi, 0)$] remain intact when both SC and SDW coexist. In addition to the d -wave symmetry nodes, additional nodes appear parallel to \mathbf{Q} near $\mathbf{k} = (\pi/4, \pi/4)$ [when $\mathbf{Q} = (\pi/2, \pi/2)$] or near $\mathbf{k} = (\pi/2, 0)$ [when $\mathbf{Q} = (\pi, 0)$]. These additional nodes correspond to the red crosses in Fig. 2. Figure 4(f) displays the band structure along the magenta band paths in Figs. 4(a) and 4(b), where the normal state FS is preserved, again resulting in the pure SC bands.

C. Kinetic method for heat conductivity

From these band structures, the electronic thermal conductivity was calculated using the Boltzmann kinetic equation similar to calculations for the thermal conductivities of both s -wave and unconventional SCs. Within the Boltzmann kinetic approach, the thermal conductivity tensor is given by the equation [59]

$$\kappa_{ij} = -\frac{2}{T} \sum_{n=1}^2 \int \frac{d^2k}{(2\pi)^2} (E_{\mathbf{k}}^{(n)})^2 (\mathbf{v}_{\mathbf{k}}^{(n)})_i (\mathbf{v}_{\mathbf{k}}^{(n)})_j \frac{\partial f_{\mathbf{k}}^0}{\partial E} \times (\tau_{n1}^{-1} + \tau_{n2}^{-1})^{-1}, \quad (11)$$

where $f_{\mathbf{k}}^0 = \frac{1}{e^{\beta E_{\mathbf{k}}} + 1}$ is the equilibrium Fermi-Dirac distribution function, $\mathbf{v}_{\mathbf{k}}^{(n)} = \nabla_{\mathbf{k}} E_{\mathbf{k}}^{(n)}$ is the quasiparticle velocity, and τ_{nm} is the quasiparticle relaxation time defined as

$$\tau_{nm}^{-1}(\mathbf{k}) = N_{\text{imp}} V^2 \frac{2\pi}{\hbar} \int \frac{d^2k'}{(2\pi)^2} |C_{nm}(\mathbf{k}, \mathbf{k}')|^2 \delta(E_{\mathbf{k}}^{(n)} - E_{\mathbf{k}'}^{(m)}), \quad (12)$$

where $C_{nm}(\mathbf{k}, \mathbf{k}')$ is known as the coherence factor and is the amplitude for a single impurity to scatter a quasiparticle from the state with momentum \mathbf{k} and energy $E_{\mathbf{k}}^{(n)}$ to a state with momentum \mathbf{k}' and energy $E_{\mathbf{k}'}^{(m)}$ within the Born limit [26]. N_{imp} is the density of impurities and V is the isotropic scattering amplitude, where $N_{\text{imp}}V \ll 1$ in the limit of weak impurity scattering. The quasiparticle relaxation time integral was calculated numerically with the unknown $N_{\text{imp}}V^2$ eliminated in favor of the normal-state quasiparticle relaxation times; $\tau_n^{-1} = N_{\text{imp}}V^2 \frac{2\pi}{\hbar} N_F$, where N_F is the density of states (DOS) at the Fermi level in the normal state. Furthermore, τ_n^{-1} cancels out for the choice of normalization used in this paper, $\kappa(T)/\kappa(T_N)$.

The coherence factors can be calculated from the impurity scattering Hamiltonian:

$$H_{\text{imp}} = V \sum_{\mathbf{k}, \mathbf{k}', \sigma} \hat{a}_{\mathbf{k}', \sigma}^\dagger \hat{a}_{\mathbf{k}, \sigma} = \sum_{\mathbf{k}, \mathbf{k}', \sigma} (\hat{\Psi}_{\mathbf{k}'}^n)^\dagger \hat{\mathcal{H}}_{\mathbf{k}}^{\text{imp}} \hat{\Psi}_{\mathbf{k}}^n, \quad (13)$$

where $\hat{\mathcal{H}}_{\mathbf{k}}^{\text{imp}}$ is the impurity scattering Hamiltonian in the Nambu basis, and can be written as

$$\hat{\mathcal{H}}_{\mathbf{k}}^{\text{imp}} = \frac{V}{4} \begin{pmatrix} 1 & 0 & 0 & 0 \\ 0 & -1 & 0 & 0 \\ 0 & 0 & 1 & 0 \\ 0 & 0 & 0 & -1 \end{pmatrix}, \quad (14)$$

which can be rewritten in the basis of the coexistence state Nambu vector to reveal the matrix of coherence factors:

$$H_{\text{imp}} = \sum_{\mathbf{k}, \mathbf{k}', \sigma} \hat{\Psi}_{\mathbf{k}'}^\dagger \hat{D}(\mathbf{k}, \mathbf{k}') \hat{\Psi}_{\mathbf{k}}, \quad (15)$$

where $\hat{\Psi}_{\mathbf{k}}^\dagger = (\hat{c}_{1, \mathbf{k}, \sigma}^\dagger, \hat{c}_{1, -\mathbf{k}, -\sigma}^\dagger, \hat{c}_{2, \mathbf{k}, \sigma}^\dagger, \hat{c}_{2, -\mathbf{k}, -\sigma}^\dagger)$ is the Nambu state vector for the coexistence quasiparticle bands (this can be generalized to accommodate Nambu vectors for the SDW and SC quasiparticles since M and Δ aren't always nonzero depending on T and \mathbf{k}). Quasiparticles occupying states in the $E_{\mathbf{k}}^{(1)}$ band with momentum \mathbf{k} are defined by $\hat{c}_{1, \mathbf{k}, \sigma}^\dagger |0\rangle$ and quasiparticles occupying states in the $E_{\mathbf{k}}^{(2)}$ band with momentum \mathbf{k} are defined by $\hat{c}_{2, \mathbf{k}, \sigma}^\dagger |0\rangle$, where $|0\rangle$ is the vacuum state with no quasiparticles. Performing the Bogoliubov transformation on the impurity scattering Hamiltonian yields the matrix of coherence factors for the quasiparticle and quasihole bands, $\hat{D}(\mathbf{k}, \mathbf{k}')$,

$$\hat{D}(\mathbf{k}, \mathbf{k}') = \hat{B}_{\mathbf{k}'} \hat{\mathcal{H}}_{\mathbf{k}}^{\text{imp}} \hat{B}_{\mathbf{k}}^\dagger, \quad (16)$$

where $\hat{B}_{\mathbf{k}}$ is the Bogoliubov transformation matrix, the structure of which depends on whether or not Δ and/or M is nonzero and the symmetry class of the SC gap function. The details of the Bogoliubov transformation matrices have been worked out in Appendix B. The intraband quasiparticle band coherence factors are

$$C_{11}(\mathbf{k}, \mathbf{k}') = D_{11}(\mathbf{k}, \mathbf{k}'), \quad C_{22}(\mathbf{k}, \mathbf{k}') = D_{33}(\mathbf{k}, \mathbf{k}') \quad (17)$$

and the interband quasiparticle band coherence factors are

$$C_{12}(\mathbf{k}, \mathbf{k}') = D_{13}(\mathbf{k}, \mathbf{k}'), \quad C_{21}(\mathbf{k}, \mathbf{k}') = D_{31}(\mathbf{k}, \mathbf{k}'), \quad (18)$$

where the $-E_{\mathbf{k}}^{(1)}$ and $-E_{\mathbf{k}}^{(2)}$ bands have been neglected due to quasiparticle-quasihole symmetry in the model. The calculation of the coherence factors from $\hat{\mathcal{H}}_{\mathbf{k}}^{\text{imp}}$ and the Bogoliubov transformation matrices was performed numerically.

A more simple case to consider analytically is that of superconductivity in the absence of a coexistence state, such as SDWs. In the Born limit, the coherence factor is known [59] to be

$$|C^{\text{SC}}(\mathbf{k}, \mathbf{k}')|^2 = \frac{1}{2} \left(1 + \frac{\xi_{\mathbf{k}} \xi_{\mathbf{k}'} - \Delta_{\mathbf{k}} \Delta_{\mathbf{k}'}}{E_{\mathbf{k}} E_{\mathbf{k}'}} \right), \quad (19)$$

where the quasiparticle energy for a SC is defined as $E_{\mathbf{k}} = \sqrt{\xi_{\mathbf{k}}^2 + \Delta_{\mathbf{k}}^2}$. The $\xi_{\mathbf{k}} \xi_{\mathbf{k}'}$ term in this coherence factor integrates to 0 by symmetry in Eq. (12). For a d -wave SC gap, the $\Delta_{\mathbf{k}} \Delta_{\mathbf{k}'}$ term also integrates to 0 due to having symmetric positive and negative $\Delta_{\mathbf{k}}$ values on the bare tight-binding FS. Thus, the quasiparticle lifetimes of the d -wave state in the Born limit is inversely proportional to the DOS of the superconducting quasiparticle states [59,60], $N(E_{\mathbf{k}})$; $\tau_{\mathbf{k}}^d = \tau_n N_F / N(E_{\mathbf{k}})$. However, on symmetry-broken tight-binding FSs this term doesn't necessarily integrate to 0, as was the case when integrated on a distorted FS due to nematicity [18]. Another case which can be discussed analytically is that of the SDW state in the absence of superconductivity. The intraband coherence factors of this state can be written [26] as

$$|C_{11}^{\text{SDW}}(\mathbf{k}, \mathbf{k}')|^2 = |C_{22}^{\text{SDW}}(\mathbf{k}, \mathbf{k}')|^2 = \frac{1}{2} \left(1 + \frac{\xi_{\mathbf{k}}^- \xi_{\mathbf{k}'}^- + M^2}{\zeta_{\mathbf{k}} \zeta_{\mathbf{k}'}} \right) \quad (20)$$

and the interband coherence factors can be written [26] as

$$|C_{12}^{\text{SDW}}(\mathbf{k}, \mathbf{k}')|^2 = |C_{21}^{\text{SDW}}(\mathbf{k}, \mathbf{k}')|^2 = \frac{1}{2} \left(1 - \frac{\xi_{\mathbf{k}}^- \xi_{\mathbf{k}'}^- + M^2}{\zeta_{\mathbf{k}} \zeta_{\mathbf{k}'}} \right), \quad (21)$$

where $\zeta_{\mathbf{k}} = \sqrt{(\xi_{\mathbf{k}}^-)^2 + M^2}$. While in the limit of a perfectly nested SDW state ($t_2 = 0$), the $\xi_{\mathbf{k}}^- \xi_{\mathbf{k}'}^-$ can be shown to integrate to 0 and the quasiparticle lifetimes become $\tau_{11}^{\text{SDW}} = \tau_n N_F / N(E_{\mathbf{k}}^{(\alpha)})(1 + M^2 / (E_{\mathbf{k}}^{(\alpha)})^2)^{-1}$, $\tau_{22}^{\text{SDW}} = \tau_n N_F / N(E_{\mathbf{k}}^{(\beta)})(1 + M^2 / (E_{\mathbf{k}}^{(\beta)})^2)^{-1}$, and $\tau_{12}^{\text{SDW}} = \tau_{21}^{\text{SDW}} = 0$ [26], however, such symmetry arguments cannot be made away from perfect nesting and the lifetimes need to be calculated numerically.

III. NUMERICAL RESULTS AND DISCUSSION

The Cartesian components of the thermal conductivity tensor $\kappa_{xx}(T)$, $\kappa_{yy}(T)$, and $\kappa_{xy}(T)$ [$\kappa_{yx}(T) = \kappa_{xy}(T)$] were numerically calculated in the RBZ. However, the frame-of-reference of the nesting vector \mathbf{Q} diagonalizes the thermal conductivity tensor, and is therefore the more natural frame to study thermal transport. This is straightforwardly accomplished by rotating the coordinate system by $\theta = \pi/4$ for the case when $\mathbf{Q} = (\pi/2, \pi/2)$. The rotated conductivity tensor $\hat{\kappa}' = \hat{R}(\theta = \pi/4) \hat{\kappa} \hat{R}^T(\theta = \pi/4)$ is

$$\begin{pmatrix} \kappa_{\perp} & 0 \\ 0 & \kappa_{\parallel} \end{pmatrix} = \frac{1}{2} \begin{pmatrix} 1 & -1 \\ 1 & 1 \end{pmatrix} \begin{pmatrix} \kappa_{xx} & \kappa_{xy} \\ \kappa_{xy} & \kappa_{xx} \end{pmatrix} \begin{pmatrix} 1 & 1 \\ -1 & 1 \end{pmatrix}, \quad (22)$$

which was simplified by using the inherent symmetries ($\kappa_{xx} = \kappa_{yy}$, $\kappa_{yx} = \kappa_{xy}$) in the case when $\mathbf{Q} = (\pi/2, \pi/2)$, and leads to the diagonalized thermal conductivity components $\kappa_{\perp} = \kappa_{xx} - \kappa_{xy}$ and $\kappa_{\parallel} = \kappa_{xx} + \kappa_{xy}$. In the SDW system with $\mathbf{Q} = (\pi, 0)$, no rotation is needed and κ_{xy} integrates to 0, resulting in a diagonal thermal conductivity tensor.

Appropriately integrating the band structure generates the electronic DOS for both SC + SDW coexistence states. One important aspect of the nodal structures is the variation in the DOS just above the Fermi level (which occurs when $E = 0$) for the two SC + SDW coexistence states (shown in Fig. 5). The enhancement occurring just above the Fermi level has important consequences for the low- T behavior of the thermal conductivity elements.

The electronic thermal conductivity calculated on the normal state tight-binding FS was found to have a linear dependence on temperature. To accentuate the deviation from the normal state thermal conductivity, the conductivity elements in Figs. 6 and 7(a) had their linear T -dependence removed by plotting $\kappa(T)/T$ and were normalized by $\kappa(T_N)/T_N$. In Fig. 7(b), the conductivity elements were normalized by $\kappa(T_N)$ on a log-log scale to emphasize which conductivity elements preserve this linear T dependence and which ones deviate from it as $T \rightarrow 0$.

A. Pure d -wave SC thermal conductivity

The thermal conductivity of a d -wave SC in the absence of a coexistence state on a tight-binding electronic dispersion ($\xi_{\mathbf{k}} = \mu - t_1 \cos k_x - t_1 \cos k_y - t_2 \cos k_x \cos k_y$) has been previously calculated in literature [18,26]. This has also been

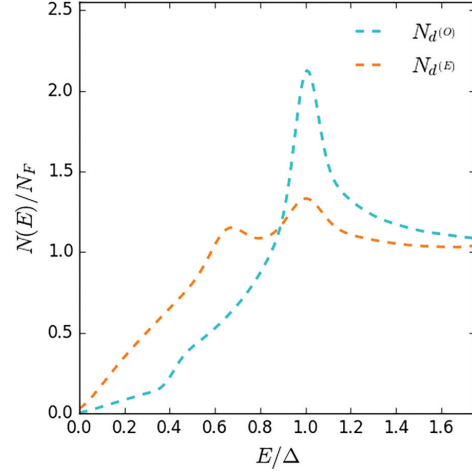


FIG. 5. Density of states normalized by the normal state DOS at the Fermi level (N_F) for SDW + d -wave SC order with odd symmetry under translations of \mathbf{Q} (cyan) and SDW + d -wave SC order with even symmetry under translations of \mathbf{Q} (orange) plotted versus energy normalized by the SC gap maxima on the FS (Δ).

calculated in this paper (see Fig. 6) to compare the thermal conductivity of the SC + SDW coexistence states to. Since the $C(4)$ rotational symmetry of the tight-binding FS is preserved for the pure superconducting state, $\kappa_{xx} = \kappa_{yy}$ and $\kappa_{xy} = \kappa_{yx} = 0$ by symmetry.

For d -wave SCs, the quasiparticle lifetimes can be shown to only depend inversely on the quasiparticle DOS [59,60] [$\tau_{\mathbf{k}}^d = \tau_n N_F / N(E_{\mathbf{k}})$]. The quasiparticle lifetimes for the $d_{x^2-y^2}$

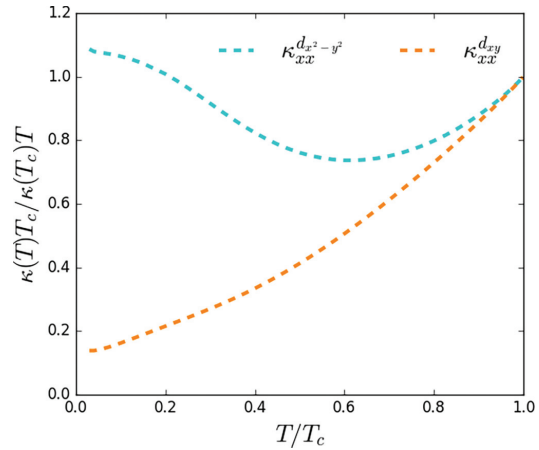


FIG. 6. Thermal conductivity $\kappa_{xx}(T)/T$ calculated for a tight-binding dispersion $\xi_{\mathbf{k}} = \mu - t_1 \cos k_x - t_1 \cos k_y - t_2 \cos k_x \cos k_y$ (where $\mu = 0$, $t_1 = 100T_c$, and $t_2 = 10T_c$) with $d_{x^2-y^2}$ (cyan) and d_{xy} (orange) SC gaps normalized by $\kappa_{xx}(T_c)/T_c$ to remove the T linearity.

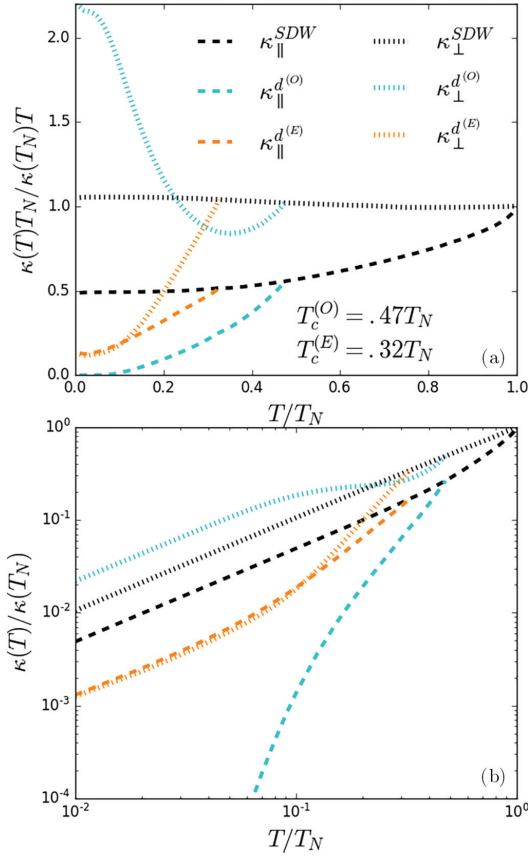


FIG. 7. Diagonalized thermal conductivity tensor elements parallel (dashed curves) and perpendicular (dotted curves) to the SDW nesting vector \mathbf{Q} in the pure SDW state (black), SDW + d -wave SC state with odd translational symmetry (cyan), and SDW + d -wave SC state with even translational symmetry (orange). (a) $\kappa(T)T_N/\kappa(T_N)T$ plotted to remove linear T dependence and emphasize deviations from normal state conductivity. (b) $\kappa(T)/\kappa(T_N)$ plotted on a log-log scale to emphasize low- T linearity.

and d_{xy} states are very different due to the difference in the local DOS of their respective nodal quasiparticle states. The difference in the local DOS at the nodes of these d -wave SC states is due to the curvature of the FS where these nodes occur; flat regions of the FS result in a low local DOS and curved regions of the FS result in a high local DOS. The $d_{x^2-y^2}$ SC gap has nodal quasiparticle states with a low local DOS, and therefore longer lifetimes, and high Fermi velocities whereas, the d_{xy} SC gap leads to nodal quasiparticle states with a high local DOS, and therefore short lifetimes, and low Fermi velocities. Therefore, the low- T thermal transport of these d -wave states is profoundly different, as the $d_{x^2-y^2}$ SC gap has nodal quasiparticles which are both long-lived and high velocity, while the d_{xy} SC gap has nodal quasiparticles which are both short-lived and low-velocity. This leads to

the low- T thermal conductivity for the $d_{x^2-y^2}$ SC gap being slightly enhanced relative to the normal state, and the low- T thermal conductivity for a d_{xy} SC gap being greatly diminished relative to the normal state (see Fig. 6).

B. Pure SDW thermal conductivity

In the pure SDW case, the electronic thermal conductivities were calculated numerically in the directions parallel and perpendicular to the nesting vector \mathbf{Q} (see the black curves of Fig. 7). Parallel to the nesting vector, the thermal conductivity $\kappa_{\parallel}^{SDW}(T)$ falls sharply when compared to that of the normal state, which is often seen in thermal conductivity measurements of SDW antiferromagnets [27,28,61]. This fall in conductivity can be attributed to a growing gap in the reconstructed FS as T decreases from T_N , which can be seen in Fig. 2. As the on-site magnetization, $M(T)$, reaches its maximum value, $\kappa_{\parallel}^{SDW}(T)/T$ becomes a constant, diminished from the normal-state conductivity. This result is comparable to the pure SDW thermal conductivity for the case when $\mathbf{Q} = (\pi, \pi)$ with a nearly half electron filling for similar band parameters [26]. Perpendicular to \mathbf{Q} in these SDW systems, the normal state tight-binding FS is preserved and $\kappa_{\perp}^{SDW}(T)$ is essentially that of the normal state thermal conductivity. However, as $T \rightarrow 0$, this thermal conductivity becomes slightly enhanced due to the gap in the FS generated by the SDW order, which reduces the available states at the Fermi level, increasing the quasiparticle lifetimes resulting in a slightly enhanced thermal conductivity.

C. SDW + d -wave SC thermal conductivity

When the propagation direction of the SDW is aligned (parallel case) with a d -wave nodal line, the FS reconstruction destroys two of the d -wave symmetry nodes [e.g., this occurs for the $\mathbf{Q} = (\pi/2, \pi/2)$ SDW and the $d_{x^2-y^2}$ SC gap or $\mathbf{Q} = (\pi, 0)$ SDW and the d_{xy} SC gap], while the symmetry nodes perpendicular to the SDW propagation direction are unaffected. This can be seen by the cyan lines in Fig. 2(a) and the orange lines in Fig. 2(b), where the remaining nodes occur on the low local DOS regions (flat regions) of the FS. These two coexistence phases have SC gaps which are odd under translations of their respective \mathbf{Q} vectors (i.e., $\Delta_{\mathbf{k}+\mathbf{Q}} = -\Delta_{\mathbf{k}}$) [see Figs. 3(a) and 3(d)]. More so, these systems have equivalent band structures along their respective band paths [see Figs. 4(c) and 4(d)]. Due to these similarities these coexistence states have equivalent transport properties relative to their \mathbf{Q} vectors, which will be referred to as the $d^{(O)}$ -wave state (odd symmetry state).

The $\mathbf{Q} = (\pi/2, \pi/2)$ SDW state coexisting with the d_{xy} SC gap and the $\mathbf{Q} = (\pi, 0)$ SDW state coexisting with the $d_{x^2-y^2}$ SC gap have symmetry nodes on the high local DOS regions (curved regions) of their respective normal state FSs, all of which remain unchanged by the FS reconstruction [note the orange points in Figs. 2(a) and the cyan points in Fig. 2(b)]. These coexistence states both have SC gaps which are even under translations of \mathbf{Q} [see Figs. 3(b) and 3(c)]. Due to this translational symmetry, additional mixing nodes appear near the FS reconstruction, which can be seen as the red crosses in Fig. 2. Furthermore, these coexistence states have

equivalent band structures along their respective band paths [see Figs. 4(e) and 4(f)] which lead to them having equivalent transport properties relative to \mathbf{Q} . These states will be referred to as the $d^{(E)}$ -wave state (even symmetry state).

1. SDW + $d^{(O)}$ -wave SC thermal conductivity

Perpendicular to \mathbf{Q} , this system behaves like a pure d -wave SC system, similar to the previously discussed $d_{x^2-y^2}$ SC gap on a tight-binding FS. However, only half the symmetry nodes typically present in similar d -wave SC systems survive the FS reconstruction, so the DOS just above the Fermi level ($E = 0$) is approximately half that of the pure d -wave system with the same band parameters (note the reduction in the DOS just above the Fermi level for $d^{(O)}$ in Fig. 5). With half the available states to scatter just above the Fermi level, there is a doubling in the quasiparticle lifetimes at the remaining nodes relative to the lifetimes of quasiparticles occupying nodal states in similar d -wave SCs without coexisting SDWs. Since the remaining symmetry nodes contain quasiparticles with Fermi velocities purely perpendicular to \mathbf{Q} with lifetimes approximately twice that of their pure SC counterparts, the residual $\kappa_{\perp}(T \rightarrow 0)/T$ is therefore roughly twice the residual $\kappa(T \rightarrow 0)/T$ for a pure d -wave SC with nodes located on the flat parts of a tight-binding FS [26] [compare cyan curves in Figs. 6–7(a)]. The thermal conductivity perpendicular to \mathbf{Q} is linear in T [see Fig. 7(b)], and therefore behaves like a SC with line nodes in this direction [25]. The thermal conductivity parallel to \mathbf{Q} decreases exponentially as $T \rightarrow 0$ since the nodal quasiparticle states which would have Fermi velocities parallel to \mathbf{Q} for SCs with similar nodal lines have been gapped by the FS reconstruction, and therefore the system behaves like a fully gapped SC in this direction [23].

2. SDW + $d^{(E)}$ -wave SC thermal conductivity

Since none of these d -wave symmetry nodes become gapped by the FS reconstruction and additional mixing nodes appear due to the SC gap being even under translations of \mathbf{Q} , the DOS just above the Fermi level for $d^{(E)}$ is relatively large (see Fig. 5) and results in short-lived quasiparticles. The majority of the states just above the Fermi level are located in the vicinity of the d -wave symmetry nodes rather than the mixing nodes, which results in the symmetry nodes dominating low- T thermal transport. Quasiparticles occupying states at the symmetry nodes have Fermi velocities with equal magnitude components perpendicular and parallel to \mathbf{Q} and contribute equally to the low- T transport in both directions. However, quasiparticles occupying states at the mixing nodes have Fermi velocities parallel to \mathbf{Q} and only contribute to κ_{\parallel} , thus leading to a system with weakly anisotropic thermal transport where $\kappa_{\parallel}(T \rightarrow 0) > \kappa_{\perp}(T \rightarrow 0)$ [see the orange curves in Fig. 6(a)].

The residual $\kappa(T \rightarrow 0)/T$ thermal conductivity elements in these cases are much smaller than $\kappa_{\perp}(T \rightarrow 0)/T$ in the previously discussed d -wave system due to the quasiparticles at these d -wave symmetry nodes having significantly lower Fermi velocities and lifetimes. Furthermore, these residual $\kappa(T \rightarrow 0)/T$ values both parallel and perpendicular to \mathbf{Q} are nearly identical to those for the similar d_{xy} SC gap on a tight-binding FS [compare orange curves in Figs. 6–7(a)].

This is due to the fact that the d -wave symmetry nodes for the $d^{(E)}$ -wave case are largely unaffected by their coexistence with the SDW state, but this does introduce additional mixing nodes which slightly enhance $\kappa_{\parallel}(T)/T$ above the pure SC value. While the quasiparticles occupying the states at the mixing nodes have high Fermi velocities parallel to \mathbf{Q} , the relative dearth of available states means they don't play a significant role in thermal transport. This d -wave SC state decreases linearly with T at low T as can be seen in Fig. 7(b) both parallel and perpendicular to \mathbf{Q} , and therefore behaves like a SC with line nodes in both directions [25].

IV. CONCLUSION

While this paper ignores the effects of band multiplicity, these results are still useful in determining the nodal structures of commensurate SDW systems with nesting vectors $\mathbf{Q} = (\pi/2, \pi/2)$ and $\mathbf{Q} = (\pi, 0)$ coexisting with singlet d -wave SC pairings. Commensurate SDW systems of type AFM3 and AFM2 were considered on two-dimensional tight-binding square lattices and found to have equivalent transport properties within Boltzmann kinetic theory in the weak impurity scattering (Born) limit relative to their nesting vectors. Parallel to their nesting vectors these systems behave similar to a suppressed metal, where the electronic thermal conductivity is linear in T but diminished from the normal state thermal conductivity. However, perpendicular to their nesting vectors, the transport properties of these systems are almost identical to that of the normal metallic state, except they are slightly enhanced as $T \rightarrow 0$ due to the FS reconstruction parallel to \mathbf{Q} creating a gap in the FS and reducing N_F , thus enhancing the quasiparticle lifetimes.

The d -wave SC states coexisting with the $\mathbf{Q} = (\pi/2, \pi/2)$ and $\mathbf{Q} = (\pi, 0)$ nesting vectors have equivalent transport properties, with the $d_{x^2-y^2}$ and d_{xy} states swapped between the nesting vectors. The d -wave symmetry nodes are located on regions of the tight-binding FS with the same relatively small local DOS and have equivalent band structures when the $\mathbf{Q} = (\pi/2, \pi/2)$ SDW state coexists with the $d_{x^2-y^2}$ SC gap and the $\mathbf{Q} = (\pi, 0)$ SDW state coexists with the d_{xy} SC gap (these are the odd-symmetry $d^{(O)}$ -wave states in this paper). Similarly, the d -wave nodes occur on regions of the tight-binding FS with the same relatively large local DOS and have equivalent band structures when the $\mathbf{Q} = (\pi/2, \pi/2)$ SDW state coexists with the d_{xy} SC gap and the $\mathbf{Q} = (\pi, 0)$ SDW state coexists with the $d_{x^2-y^2}$ SC gap (these are the even-symmetry $d^{(E)}$ -wave states in this paper).

The electron transport properties of these commensurate SDW systems were also studied when SC singlet pairing arises ($T_N > T_c$) out of it. The electronic thermal conductivity for a $d^{(O)}$ -wave SC gap measured parallel to \mathbf{Q} was found to decrease exponentially with T , consistent with results for fully gapped SCs [23]. Perpendicular to \mathbf{Q} , the conductivity was found to decrease linearly with T , consistent with SCs with line nodes [25]. Furthermore, the residual $\kappa_{\perp}(T \rightarrow 0)/T$ value was found to be roughly twice that of pure d -wave SCs containing nodal quasiparticle states situated on the flat regions of a tight-binding FS. Therefore, the effect of SDW states with $C(2)$ rotational symmetry on d -wave SC states such as these is that it gaps the nodal quasiparticle states

in the direction of SDW propagation, greatly reducing thermal transport in that direction, and doubles the lifetimes of quasiparticles traveling perpendicular to the SDW propagation direction, thus greatly enhancing thermal transport in that direction. This results in a system with highly anisotropic electron transport where fast long-lived quasiparticles tend to travel perpendicular to \mathbf{Q} .

When the d -wave SC gap is even under translations of \mathbf{Q} ($d^{(E)}$ wave), the SC symmetry nodes are preserved as none of them appear in the region of the FS which is reconstructed by the SDW order. Due to the translational symmetry of the SC gap, additional mixing nodes appear in the vicinity of the FS reconstruction parallel to \mathbf{Q} . The electronic thermal conductivity both parallel and perpendicular to \mathbf{Q} were found to decrease linearly with T . In fact, $\kappa_{\parallel}(T \rightarrow 0)/T$ and $\kappa_{\perp}(T \rightarrow 0)/T$ were nearly identical due to quasiparticles occupying states at the d -wave symmetry nodes contributing equally to thermal transport in both directions. However, thermal transport parallel to \mathbf{Q} was slightly enhanced since quasiparticles occupying states at the mixing nodes enhanced transport in that direction. The coexistence of SDW states with $C(2)$ d -wave SC gaps such as these leaves thermal transport of such systems largely unaffected due to the nodal quasiparticle states remaining mostly unchanged by the FS reconstruction, however, it does introduce additional mixing nodes which slightly enhance thermal transport in the direction of SDW propagation. Therefore, this results in a system with weakly anisotropic thermal transport, where slow short-lived quasiparticles travel both parallel and perpendicular to \mathbf{Q} , but slightly prefer to travel parallel to \mathbf{Q} .

These results could be relevant in determining the nature of the d -wave gap in cuprates with commensurate SDW orders of nesting vectors: $\mathbf{Q} = (\pi/2, \pi/2)$ or $\mathbf{Q} = (\pi, 0)$. If the thermal conductivity is measured both parallel and perpendicular to \mathbf{Q} and the nesting vector is known, weakly or strongly anisotropic thermal transport at low T could be used to determine whether the SC gap is $d_{x^2-y^2}$ or d_{xy} in nature. Additionally, these results could be relevant to understanding the nature of anisotropic in-plane electronic thermal transport

measured in some cuprate samples [39–41]. One study found quasi-one-dimensional electronic thermal transport at low T mediated by spin excitations [41], similar to the $d^{(O)}$ wave result in this paper which had a residual thermal conductivity perpendicular to \mathbf{Q} as $T \rightarrow 0$, but not parallel to \mathbf{Q} . However, other studies [39,40] found that electronic thermal transport was supported in both directions, but still favored a particular direction due to electronic inhomogeneities. This effect could either be due to the fact that these samples weren't monolayers and the SDW nesting vectors for each layer weren't all parallel, or the anisotropic transport in these materials is due to a nematic phase which was discussed in a previous work [18].

ACKNOWLEDGMENTS

This work was conducted at the NSF MonArk Quantum Foundry which is supported from the NSF Q-AMASE-I program Award No. DMR1906383. The authors would like to thank A. Vorontsov for the initial suggestion of the problem.

APPENDIX A: ORDER PARAMETER SELF-CONSISTENCY

The mean-field order parameters M and Δ can be self-consistently solved for from the Green's function method [26,52,62–64]. This can be obtained from the bare Matsubara Green's function which can be found from the Dyson equation

$$\hat{G}_{\mathbf{k}}(\omega_n) = (i\omega_n \hat{I} - \hat{H}_{\mathbf{k}})^{-1}, \quad (\text{A1})$$

where $\omega_n = 2\pi T(n + 1/2)$ is the Matsubara frequency. The relevant Green's functions for Δ are contained in the diagonal blocks, whereas the relevant Green's functions for M are contained in the off-diagonal blocks. Calculating the relevant Green's functions from the Dyson equation and substituting them into the definitions of the mean-field order parameters Δ and M yields two systems of equations for when the SC gap is odd or even under translations of \mathbf{Q} . When the SC gap is odd under translations of \mathbf{Q} , $1/V_{\text{SC}}$ and $1/V_{\text{SDW}}$ when Δ and M are nonzero can be written as

$$\begin{aligned} \frac{1}{V_{\text{SC}}} &= T \sum_{\omega_n} \sum_{\mathbf{k}}^{E_c} \frac{\mathcal{Y}_{\mathbf{k}}^2}{D_{\mathbf{k}}^{(O)}(\omega_n)} (\omega_n^2 + (\xi_{\mathbf{k}}^-)^2 + (\xi_{\mathbf{k}}^+)^2 + M^2 + \Delta_{\mathbf{k}}^2), \\ \frac{1}{V_{\text{SDW}}} &= T \sum_{\omega_n} \sum_{\mathbf{k}}^{E_B} \frac{1}{D_{\mathbf{k}}^{(O)}(\omega_n)} (\omega_n^2 + (\xi_{\mathbf{k}}^-)^2 - (\xi_{\mathbf{k}}^+)^2 + M^2 + \Delta_{\mathbf{k}}^2), \\ D_{\mathbf{k}}^{(O)} &= (\omega_n^2 + (\xi_{\mathbf{k}}^-)^2 + (\xi_{\mathbf{k}}^+)^2 + \Delta_{\mathbf{k}}^2 + M^2)^2 - 4(\xi_{\mathbf{k}}^+)^2((\xi_{\mathbf{k}}^-)^2 + M^2) = (\omega_n^2 + (E_{\mathbf{k}}^{(1:O)})^2)(\omega_n^2 + (E_{\mathbf{k}}^{(2:O)})^2), \end{aligned} \quad (\text{A2})$$

and $1/V_{\text{SC}}$ and $1/V_{\text{SDW}}$ when the SC gap is even under translations of \mathbf{Q} when both Δ and M are nonzero can be written as

$$\begin{aligned} \frac{1}{V_{\text{SC}}} &= T \sum_{\omega_n} \sum_{\mathbf{k}}^{E_c} \frac{\mathcal{Y}_{\mathbf{k}}^2}{D_{\mathbf{k}}^{(E)}(\omega_n)} (\omega_n^2 + (\xi_{\mathbf{k}}^-)^2 + (\xi_{\mathbf{k}}^+)^2 - M^2 + \Delta_{\mathbf{k}}^2), \\ \frac{1}{V_{\text{SDW}}} &= T \sum_{\omega_n} \sum_{\mathbf{k}}^{E_B} \frac{1}{D_{\mathbf{k}}^{(E)}(\omega_n)} (\omega_n^2 + (\xi_{\mathbf{k}}^-)^2 - (\xi_{\mathbf{k}}^+)^2 + M^2 - \Delta_{\mathbf{k}}^2), \\ D_{\mathbf{k}}^{(E)} &= (\omega_n^2 + (\xi_{\mathbf{k}}^-)^2 + (\xi_{\mathbf{k}}^+)^2 + \Delta_{\mathbf{k}}^2 + M^2)^2 - 4(\xi_{\mathbf{k}}^+)^2((\xi_{\mathbf{k}}^-)^2 + M^2) - 4M^2\Delta_{\mathbf{k}}^2 = (\omega_n^2 + (E_{\mathbf{k}}^{(1:E)})^2)(\omega_n^2 + (E_{\mathbf{k}}^{(2:E)})^2), \end{aligned} \quad (\text{A3})$$

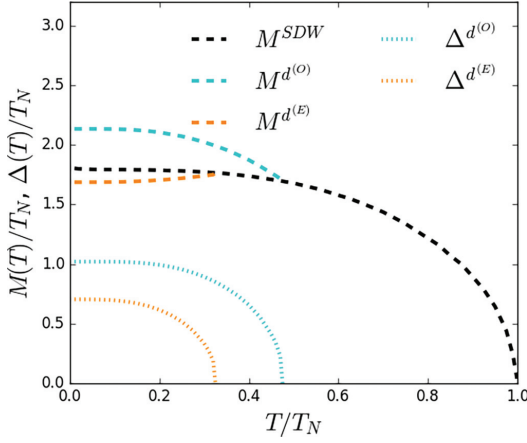


FIG. 8. Self-consistently calculated M and Δ order parameters in the absence of superconductivity (black), when spin density waves coexist with a d -wave SC gap which is odd under translations of \mathbf{Q} (cyan), and when spin density waves coexist with a d -wave SC gap which is even under translations of \mathbf{Q} (orange).

where $E_c = 2\pi T(n_c + 1/2)$ and $E_B = 2\pi T(n_B + 1/2)$ are the cutoff energies for the SC and SDW Matsubara sums, respectively; $n_c = 30T_N/T$ and $n_B = 175T_N/T$ were used in this paper. The natural choice of energy scale for these equations is T_N , since T_c depends on the value of M . To self-consistently solve for the order parameters, Δ and M , the SC and SDW interaction potentials can be eliminated by subtracting Eq. (A4) from Eq. (A2) or Eq. (A3),

$$\frac{1}{V_{\text{SC}}} = T_c^0 \sum_{\omega_n} \frac{\mathcal{Y}_{\mathbf{k}}^2 (\omega_n^2 + (\xi_{\mathbf{k}}^-)^2 + (\xi_{\mathbf{k}}^+)^2)}{(\omega_n^2 + (\xi_{\mathbf{k}}^-)^2 + (\xi_{\mathbf{k}}^+)^2)^2 - 4(\xi_{\mathbf{k}}^- \xi_{\mathbf{k}}^+)^2},$$

$$\frac{1}{V_{\text{SDW}}} = T_N \sum_{\omega_n} \frac{(\omega_n^2 + (\xi_{\mathbf{k}}^-)^2 + (\xi_{\mathbf{k}}^+)^2)}{(\omega_n^2 + (\xi_{\mathbf{k}}^-)^2 + (\xi_{\mathbf{k}}^+)^2)^2 - 4(\xi_{\mathbf{k}}^- \xi_{\mathbf{k}}^+)^2}, \quad (\text{A4})$$

and T_c^0 is the superconducting transition temperature in the absence of SDWs. In this paper, $T_c^0 = .35T_N$ was used for both symmetry classes, but the actual superconducting transition temperatures were found to be $T_c^{(O)} = .47T_N$ and $T_c^{(E)} =$

$.32T_N$ from self-consistency. The order parameters Δ and M can be seen as a function of temperature for both the odd and even symmetry classes in Fig. 8.

APPENDIX B: TWO-STEP DIAGONALIZATION

A two-step process can be employed to simplify the calculation of the Bogoliubov transformation which diagonalizes the Hamiltonian when M and Δ are simultaneously nonzero [65]. The first step in this procedure is to diagonalize the Hamiltonian when $M \neq 0$ and $\Delta = 0$. It can be shown that the Bogoliubov transformation matrix in this case is $\hat{B}_{\mathbf{k}}^{\text{SDW}}$, which can be used to define the states for the $E_{\mathbf{k}}^{(\alpha)}$ and $E_{\mathbf{k}}^{(\beta)}$ quasiparticle bands, respectively, as $\hat{\alpha}_{\mathbf{k},\sigma}^\dagger |0\rangle$ and $\hat{\beta}_{\mathbf{k},\sigma}^\dagger |0\rangle$,

$$\hat{\Psi}_{\mathbf{k}}^{\text{SDW}} = \hat{B}_{\mathbf{k}}^{\text{SDW}} \hat{\Psi}_{\mathbf{k}}^n = \begin{pmatrix} \hat{\alpha}_{\mathbf{k},\sigma} \\ \hat{\alpha}_{-\mathbf{k},-\sigma}^\dagger \\ \hat{\beta}_{\mathbf{k},\sigma} \\ \hat{\beta}_{-\mathbf{k},-\sigma}^\dagger \end{pmatrix} = \begin{pmatrix} u_{\mathbf{k}} & 0 & v_{\mathbf{k}} & 0 \\ 0 & u_{\mathbf{k}} & 0 & -v_{\mathbf{k}} \\ -v_{\mathbf{k}} & 0 & u_{\mathbf{k}} & 0 \\ 0 & v_{\mathbf{k}} & 0 & u_{\mathbf{k}} \end{pmatrix} \begin{pmatrix} \hat{a}_{\mathbf{k},\sigma} \\ \hat{a}_{-\mathbf{k},-\sigma}^\dagger \\ \hat{a}_{\mathbf{k}+\mathbf{Q},\sigma} \\ \hat{a}_{-\mathbf{k}-\mathbf{Q},-\sigma}^\dagger \end{pmatrix}, \quad (\text{B1})$$

where $u_{\mathbf{k}} = \sqrt{\frac{1}{2}(1 + \frac{\xi_{\mathbf{k}}}{\zeta_{\mathbf{k}}})}$, $v_{\mathbf{k}} = \sqrt{\frac{1}{2}(1 - \frac{\xi_{\mathbf{k}}}{\zeta_{\mathbf{k}}})}$, and $\zeta_{\mathbf{k}} = \sqrt{(\xi_{\mathbf{k}}^-)^2 + M^2}$. The transformation matrix $\hat{B}_{\mathbf{k}}^{\text{SDW}}$ is used to calculate the coherence matrix in Eq. (16) when $T > T_c$ in the regions of \mathbf{k} space in which the FS reconstruction occurs. However, this transformation matrix can also be used to rewrite the Hamiltonian, $\hat{\mathcal{H}}_{\mathbf{k}}$, when both M and Δ are nonzero in the basis of the SDW Nambu vector, $\hat{\Psi}_{\mathbf{k}}^{\text{SDW}}$, as $\hat{\mathcal{H}}_{\mathbf{k}}'$:

$$H = \frac{1}{2} \sum_{\mathbf{k}} (\hat{\Psi}_{\mathbf{k}}^{\text{SDW}})^\dagger \hat{\mathcal{H}}_{\mathbf{k}}' \hat{\Psi}_{\mathbf{k}}^{\text{SDW}}. \quad (\text{B2})$$

Performing this change of basis on the coexistence Hamiltonian without loss of generality results in a Hamiltonian with intraband coupling terms, which couple the $E_{\mathbf{k}}^{(\alpha,\beta)}$ bands with the $-E_{\mathbf{k}}^{(\alpha,\beta)}$ bands, and interband coupling terms, which couple the $E_{\mathbf{k}}^{(\alpha,\beta)}$ bands with the $-E_{\mathbf{k}}^{(\beta,\alpha)}$ bands:

$$\hat{\mathcal{H}}_{\mathbf{k}}' = \hat{B}_{\mathbf{k}}^{\text{SDW}} \hat{\mathcal{H}}_{\mathbf{k}} (\hat{B}_{\mathbf{k}}^{\text{SDW}})^\dagger = \begin{pmatrix} E_{\mathbf{k}}^{(\alpha)} & \Delta_{\mathbf{k}} |u_{\mathbf{k}}|^2 - \Delta_{\mathbf{k}+\mathbf{Q}} |v_{\mathbf{k}}|^2 & 0 & 2\Delta_{\mathbf{k}}^+ u_{\mathbf{k}} v_{\mathbf{k}} \\ \Delta_{\mathbf{k}} |u_{\mathbf{k}}|^2 - \Delta_{\mathbf{k}+\mathbf{Q}} |v_{\mathbf{k}}|^2 & -E_{\mathbf{k}}^{(\alpha)} & -2\Delta_{\mathbf{k}}^+ u_{\mathbf{k}} v_{\mathbf{k}} & 0 \\ 0 & -2\Delta_{\mathbf{k}}^+ u_{\mathbf{k}} v_{\mathbf{k}} & E_{\mathbf{k}}^{(\beta)} & -\Delta_{\mathbf{k}} |v_{\mathbf{k}}|^2 + \Delta_{\mathbf{k}+\mathbf{Q}} |u_{\mathbf{k}}|^2 \\ 2\Delta_{\mathbf{k}}^+ u_{\mathbf{k}} v_{\mathbf{k}} & 0 & -\Delta_{\mathbf{k}} |v_{\mathbf{k}}|^2 + \Delta_{\mathbf{k}+\mathbf{Q}} |u_{\mathbf{k}}|^2 & -E_{\mathbf{k}}^{(\beta)} \end{pmatrix}. \quad (\text{B3})$$

Analytically diagonalizing the general equation for the Hamiltonian in the $\hat{\Psi}_{\mathbf{k}}^{\text{SDW}}$ basis is a difficult task, however, it can be simplified in the cases of SC gaps with even and odd symmetries under translations of \mathbf{Q} . The simplest case to con-

sider is the odd case, where $\Delta_{\mathbf{k}+\mathbf{Q}} = -\Delta_{\mathbf{k}}$, which simplifies the intraband coupling terms to $\pm \Delta_{\mathbf{k}} (|u_{\mathbf{k}}|^2 + |v_{\mathbf{k}}|^2) = \pm \Delta_{\mathbf{k}}$. This also reduces the interband coupling terms to 0, decoupling the $E_{\mathbf{k}}^{(\alpha)}$ and $E_{\mathbf{k}}^{(\beta)}$ SDW bands entirely. Therefore, the

Hamiltonian in the $\hat{\Psi}_{\mathbf{k}}^{\text{SDW}}$ basis when the SC gap is odd under translations of \mathbf{Q} reduces to

$$\hat{\mathcal{H}}'_{\mathbf{k}} = \begin{pmatrix} E_{\mathbf{k}}^{(\alpha)} & \Delta_{\mathbf{k}} & 0 & 0 \\ \Delta_{\mathbf{k}} & -E_{\mathbf{k}}^{(\alpha)} & 0 & 0 \\ 0 & 0 & E_{\mathbf{k}}^{(\beta)} & -\Delta_{\mathbf{k}} \\ 0 & 0 & -\Delta_{\mathbf{k}} & -E_{\mathbf{k}}^{(\beta)} \end{pmatrix}, \quad (\text{B4})$$

which can be diagonalized by two separate Bogoliubov transformations with dispersion relations $\epsilon_{\mathbf{k}}^{(1;O)} = \sqrt{(E_{\mathbf{k}}^{(\alpha)})^2 + \Delta_{\mathbf{k}}^2}$ and $\epsilon_{\mathbf{k}}^{(2;O)} = \sqrt{(E_{\mathbf{k}}^{(\beta)})^2 + \Delta_{\mathbf{k}}^2}$, which can be shown [26] to be equivalent to $E_{\mathbf{k}}^{(1;O)}$ and $E_{\mathbf{k}}^{(2;O)}$. These Bogoliubov transformations can also be used to define the states for the $E_{\mathbf{k}}^{(1)}$ and $E_{\mathbf{k}}^{(2)}$ as $\hat{c}_{1,\mathbf{k},\sigma}^{\dagger} |0\rangle$ and $\hat{c}_{2,\mathbf{k},\sigma}^{\dagger} |0\rangle$, respectively, by performing the transformation on $\hat{\Psi}_{\mathbf{k}}^{\text{SDW}}$,

$$\hat{\Psi}_{\mathbf{k}}^{(O)} = \hat{B}_{\mathbf{k}}^{(O)} \hat{\Psi}_{\mathbf{k}}^{\text{SDW}} = \begin{pmatrix} \hat{c}_{1,\mathbf{k},\sigma} \\ \hat{c}_{1,-\mathbf{k},-\sigma}^{\dagger} \\ \hat{c}_{2,\mathbf{k},\sigma} \\ \hat{c}_{2,-\mathbf{k},-\sigma}^{\dagger} \end{pmatrix} = \begin{pmatrix} u_{\mathbf{k}}^{(1;O)} & v_{\mathbf{k}}^{(1;O)} & 0 & 0 \\ -v_{\mathbf{k}}^{(1;O)} & u_{\mathbf{k}}^{(1;O)} & 0 & 0 \\ 0 & 0 & u_{\mathbf{k}}^{(2;O)} & -v_{\mathbf{k}}^{(2;O)} \\ 0 & 0 & v_{\mathbf{k}}^{(2;O)} & u_{\mathbf{k}}^{(2;O)} \end{pmatrix} \begin{pmatrix} \hat{\alpha}_{\mathbf{k},\sigma} \\ \hat{\alpha}_{-\mathbf{k},-\sigma}^{\dagger} \\ \hat{\beta}_{\mathbf{k},\sigma} \\ \hat{\beta}_{-\mathbf{k},-\sigma}^{\dagger} \end{pmatrix}, \quad (\text{B5})$$

where $u_{\mathbf{k}}^{(1,2;O)} = \sqrt{\frac{1}{2} \left(1 + \frac{E_{\mathbf{k}}^{(\alpha,\beta)}}{E_{\mathbf{k}}^{(1,2;O)}} \right)}$ and $v_{\mathbf{k}}^{(1,2;O)} = \sqrt{\frac{1}{2} \left(1 - \frac{E_{\mathbf{k}}^{(\alpha,\beta)}}{E_{\mathbf{k}}^{(1,2;O)}} \right)}$. $\hat{B}_{\mathbf{k}}^{(O)} = \hat{B}_{\mathbf{k}}^{(O)} \hat{B}_{\mathbf{k}}^{\text{SDW}}$ is used to calculate the coherence factor in Eq. (16) when \mathbf{k} is in the region where the FS becomes reconstructed, $\Delta \neq 0$, and $\Delta_{\mathbf{k}}$ is odd under translations of \mathbf{Q} . The $\hat{B}_{\mathbf{k}}^{(O)}$ transformation matrix

calculated here is consistent with previous calculations in literature for the cuprates [66] if the order of the Nambu vector elements are properly accounted for. When the SC gap is even under translations of \mathbf{Q} , $\hat{\mathcal{H}}'_{\mathbf{k}}$ can't be simplified generally beyond setting $\Delta_{\mathbf{k}+\mathbf{Q}} = \Delta_{\mathbf{k}}$, and $\hat{\mathcal{H}}'_{\mathbf{k}}$ needs to be diagonalized numerically to calculate $\hat{B}_{\mathbf{k}}^{(E)}$.

- [1] L. Taillefer, *Annu. Rev. Condens. Matter Phys.* **1**, 51 (2010).
- [2] H.-H. Wen and S. Li, *Annu. Rev. Condens. Matter Phys.* **2**, 121 (2011).
- [3] F.-C. Hsu, J.-Y. Luo, K.-W. Yeh, T.-K. Chen, T.-W. Huang, P. M. Wu, Y.-C. Lee, Y.-L. Huang, Y.-Y. Chu, D.-C. Yan *et al.*, *Proc. Natl. Acad. Sci. USA* **105**, 14262 (2008).
- [4] S. Lebegue, *Phys. Rev. B* **75**, 035110 (2007).
- [5] D. J. Singh and M.-H. Du, *Phys. Rev. Lett.* **100**, 237003 (2008).
- [6] Y. Yu, L. Ma, P. Cai, R. Zhong, C. Ye, J. Shen, G. D. Gu, X. H. Chen, and Y. Zhang, *Nature (London)* **575**, 156 (2019).
- [7] J.-F. Ge, Z.-L. Liu, C. Liu, C.-L. Gao, D. Qian, Q.-K. Xue, Y. Liu, and J.-F. Jia, *Nat. Mater.* **14**, 285 (2015).
- [8] A. T. Bollinger and I. Bozovic, *Supercond. Sci. Technol.* **29**, 103001 (2016).
- [9] D. N. Basov and A. V. Chubukov, *Nat. Phys.* **7**, 272 (2011).
- [10] S. Sachdev, *Physica C* **470**, S4 (2010).
- [11] B. Lake, G. Aeppli, K. N. Clausen, D. F. McMorrow, K. Lefmann, N. E. Hussey, N. Mangkorntong, M. Nohara, H. Takagi, T. E. Mason, and A. Schröder, *Science* **291**, 1759 (2001).
- [12] E. Demler, S. Sachdev, and Y. Zhang, *Phys. Rev. Lett.* **87**, 067202 (2001).
- [13] N. Harrison and S. E. Sebastian, *Phys. Rev. B* **80**, 224512 (2009).
- [14] S. Tan, Y. Zhang, M. Xia, Z. Ye, F. Chen, X. Xie, R. Peng, D. Xu, Q. Fan, H. Xu *et al.*, *Nat. Mater.* **12**, 634 (2013).
- [15] M. A. McGuire, A. D. Christianson, A. S. Sefat, B. C. Sales, M. D. Lumsden, R. Jin, and E. A. Payzant, D. Mandrus, Y. Luan, V. Keppens, V. Varadarajan, J. W. Brill, R. P. Hermann, M. T. Sougrati, F. Grandjean, and G. J. Long *et al.*, *Phys. Rev. B* **78**, 094517 (2008).
- [16] C. de la Cruz, Q. Huang, J. W. Lynn, J. Li, W. Ratcliff II, J. L. Zarestky, H. A. Mook, G. F. Chen, J. L. Luo, N. L. Wang *et al.*, *Nature (London)* **453**, 899 (2008).
- [17] L. Nie, A. V. Maharaj, E. Fradkin, and S. A. Kivelson, *Phys. Rev. B* **96**, 085142 (2017).
- [18] S. Sen Choudhury, S. Peterson, and Y. Idzerda, *Phys. Rev. B* **105**, 214515 (2022).
- [19] Y. Ran, F. Wang, H. Zhai, A. Vishwanath, and D. H. Lee, *Phys. Rev. B* **79**, 014505 (2009).
- [20] H. Shakeripour, C. Petrovic, and L. Taillefer, *New J. Phys.* **11**, 055065 (2021).
- [21] K. Hashimoto, M. Yamashita, S. Kasahara, Y. Senshu, N. Nakata, S. Tonegawa, K. Ikada, A. Serafini, A. Carrington, T. Terashima *et al.*, *Phys. Rev. B* **81**, 220501(R) (2010).
- [22] J. Ziman, *Electrons and Phonons* (Clarendon Press, Oxford, 1960).
- [23] J. Bardeen, G. Rickayzen, and L. Tewordt, *Phys. Rev.* **113**, 982 (1959).
- [24] B. Arfi and C. J. Pethick, *Phys. Rev. B* **38**, 2312 (1988).
- [25] M. J. Graf, S.-K. Yip, J. A. Sauls, and D. Rainer, *Phys. Rev. B* **53**, 15147 (1996).
- [26] S. S. Choudhury and A. B. Vorontsov, *Phys. Rev. B* **103**, 104501 (2021).
- [27] M. S. Kim, Z. P. Yin, L. L. Zhao, E. Morosan, G. Kotliar, and M. C. Aronson, *Phys. Rev. B* **84**, 075112 (2011).
- [28] F. Steckel, S. Rodan, R. Hermann, C. G. F. Blum, S. Wurmehl, B. Buchner, and C. Hess, *Phys. Rev. B* **90**, 134411 (2014).
- [29] S. Chatterjee, S. Sachdev, and A. Eberlein, *Phys. Rev. B* **96**, 075103 (2017).
- [30] A. C. Durst and S. Sachdev, *Phys. Rev. B* **80**, 054518 (2009).
- [31] P. R. Schiff and A. C. Durst, *Phys. Rev. B* **81**, 054504 (2010).

- [32] A. Damascelli, Z. Hussain, and S. Z.-X., *Rev. Mod. Phys.* **75**, 473 (2003).
- [33] J. M. Tranquada, B. J. Sternlieb, J. D. Axe, Y. Nakamura, and S. Uchida, *Nature (London)* **375**, 561 (1995).
- [34] C. Fang, B. A. Bernevig, and J. Hu, *Europhys. Lett.* **86**, 67005 (2009).
- [35] F. Laliberté, J. Chang, N. Doiron-Leyraud, E. Hassinger, R. Daou, M. Rondeau, B. J. Ramshaw, R. Liang, D. A. Bonn, W. N. Hardy *et al.*, *Nat. Commun.* **2**, 432 (2011).
- [36] T. Helm, M. V. Kartsovnik, M. Bartkowiak, N. Bittner, M. Lambacher, A. Erb, J. Wosnitzer, and R. Gross, *Phys. Rev. Lett.* **103**, 157002 (2009).
- [37] E. G. Moon and S. Sachdev, *Phys. Rev. B* **80**, 035117 (2009).
- [38] B.-H. Zheng, C.-M. Chung, P. Corboz, G. Ehlers, M.-P. Qin, R. M. Noack, H. Shi, S. R. White, S. Zhang, and G. K.-L. Chan, *Science* **358**, 1155 (2017).
- [39] J. L. Cohn and J. Karpinski, *Phys. Rev. B* **58**, 14617 (1998).
- [40] X. F. Sun, S. Ono, Y. Abe, S. Komiya, K. Segawa, and Y. Ando, *Phys. Rev. Lett.* **96**, 017008 (2006).
- [41] A. V. Sologubenko, E. Felder, K. Gianno, H. R. Ott, A. Vietkine, and A. Revcolevschi, *Phys. Rev. B* **62**, R6108 (2000).
- [42] J. Zhao, Q. Huang, C. de la Cruz, S. Li, J. W. Lynn, Y. Chen, M. A. Green, G. F. Chen, G. Li, Z. Li *et al.*, *Nat. Mater.* **7**, 953 (2008).
- [43] Y. Chen, J. W. Lynn, J. Li, G. Li, G. F. Chen, J. L. Luo, N. L. Wang, P. Dai, C. de la Cruz, and H. A. Mook, *Phys. Rev. B* **78**, 064515 (2008).
- [44] S. A. J. Kimber, D. N. Argyriou, F. Yokaichiya, K. Habicht, S. Gerischer, T. Hansen, T. Chatterji, R. Klingeler, C. Hess, G. Behr *et al.*, *Phys. Rev. B* **78**, 140503(R) (2008).
- [45] Q. Huang, Y. Qiu, W. Bao, M. A. Green, J. W. Lynn, Y. C. Gasparovic, T. Wu, G. Wu, and X. H. Chen, *Phys. Rev. Lett.* **101**, 257003 (2008).
- [46] J. Zhao, W. Ratcliff II, J. W. Lynn, G. F. Chen, J. L. Luo, N. L. Wang, J. Hu, and P. Dai, *Phys. Rev. B* **78**, 140504(R) (2008).
- [47] Y. Mizuguchi and Y. Takano, *J. Phys. Soc. Jpn.* **79**, 102001 (2010).
- [48] Y. Qiu, W. Bao, Y. Zhao, C. Broholm, V. Stanev, Z. Tesanovic, Y. C. Gasparovic, S. Chang, J. Hu, B. Qian *et al.*, *Phys. Rev. Lett.* **103**, 067008 (2009).
- [49] S. Li, C. de la Cruz, Q. Huang, Y. Chen, J. W. Lynn, J. Hu, Y. L. Huang, F. C. Hsu, K. W. Yeh, M. K. Wu, and P. Dai, *Phys. Rev. B* **79**, 054503 (2009).
- [50] A. Foley, S. Verret, A. M. S. Tremblay, and D. Senechal, *Phys. Rev. B* **99**, 184510 (2019).
- [51] H. Xu, H. Shi, E. Vitali, M. Qin, and S. Zhang, *Phys. Rev. Res.* **4**, 013239 (2022).
- [52] M. Kato and K. Machida, *Phys. Rev. B* **37**, 1510 (1988).
- [53] O. K. Anderson, A. I. Liechtenstein, O. Jepsen, and F. Paulsen, *J. Phys. Chem. Solids* **56**, 1573 (1995).
- [54] W. Meevasana, F. Baumberger, K. Tanaka, F. Schmitt, W. R. Dunkel, D. H. Lu, S. K. Mo, H. Eisaki, and Z. X. Shen, *Phys. Rev. B* **77**, 104506 (2008).
- [55] A. A. Kordyuk, S. V. Borisenko, M. Knupfer, and J. Fink, *Phys. Rev. B* **67**, 064504 (2003).
- [56] X. F. Wang, T. Wu, G. Wu, R. H. Liu, H. Chen, Y. L. Xie, and X. H. Chen, *New J. Phys.* **11**, 045003 (2009).
- [57] J.-H. Chu, J. G. Analytis, C. Kucharczyk, and I. R. Fisher, *Phys. Rev. B* **79**, 014506 (2009).
- [58] D. Haug, V. Hinkov, Y. Sidis, P. Bourges, N. B. Christensen, A. Ivanov, T. Keller, C. T. Lin, and B. Keimer, *New J. Phys.* **12**, 105006 (2010).
- [59] V. P. Mineev and K. V. Samokin, *Introduction to Unconventional Superconductivity* (Gordon and Breach Science Publishers, Amsterdam, 1998).
- [60] P. A. Lee, *Phys. Rev. Lett.* **71**, 1887 (1993).
- [61] T. A. Sayles, W. M. Yuhasz, J. Paglione, T. Yanagisawa, J. R. Jeffries, M. B. Maple, Z. Henkie, A. Pietraszko, T. Cichorek, R. Wawryk *et al.*, *Phys. Rev. B* **77**, 144432 (2008).
- [62] K. Machida and M. Kato, *Phys. Rev. Lett.* **58**, 1986 (1987).
- [63] K. Machida, *J. Phys. Soc. Jpn.* **50**, 2195 (1981).
- [64] M. Kato and K. Machida, *J. Phys. Soc. Jpn.* **56**, 2136 (1987).
- [65] J.-P. Ismer, I. Eremin, E. Rossi, D. K. Morr, and G. Blumberg, *Phys. Rev. Lett.* **105**, 037003 (2010).
- [66] T. Das, R. S. Markiewicz, and A. Bansil, *Phys. Rev. B* **77**, 134516 (2008).

CONCLUSION

Broken symmetries inherent to a material's lattice or magnetic state tend to manifest themselves in the symmetries of the material's other properties as well. In this work these broken-symmetry properties were investigated as the cubic magneto-anisotropy for tetragonal thin-film ferromagnets which have an in-plane cubic symmetry in their lattice. The broken-symmetry inherent to the transport properties of nematic superconductors and antiferromagnetic superconductors were also investigated. The transport properties of both these materials were found to have $C(2)$ rotational symmetry due to the nematic deformation of the FS and the rotational symmetry of the magnetizations of the AFM2 and AFM3 states.

Cubic Anisotropy Constants

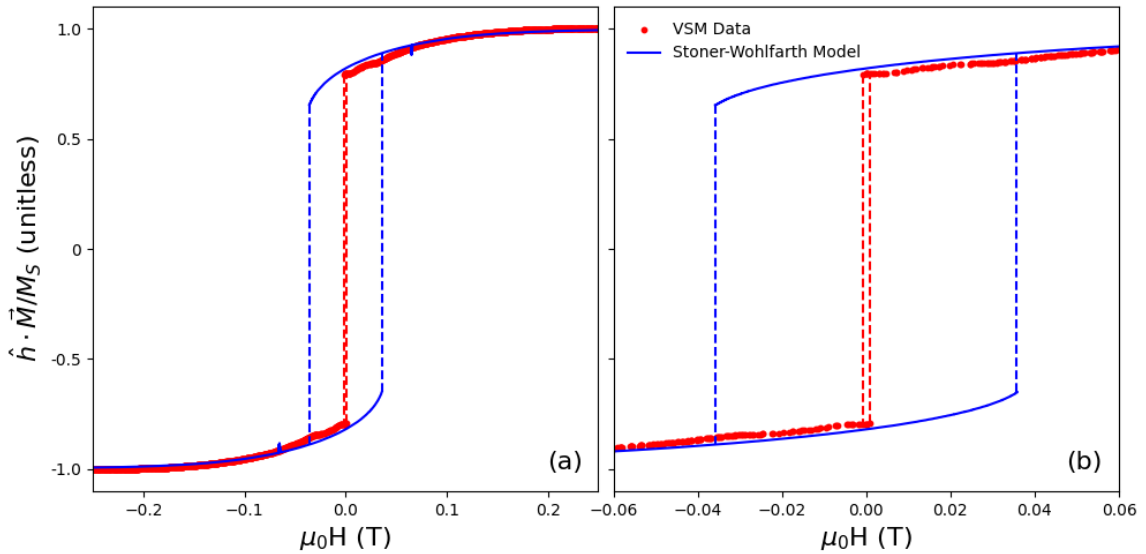


Figure 7.1: (a) Stoner-Wohlfarth Model best fit (blue curve) to FeCoMn magnetic hysteresis data measured by VSM (red curve), (b) enlarged to visualize hysteresis in the raw data which has a coercive applied magnetic field value of around 1mT.

Residuals between the calculated Stoner-Wohlfarth Model magnetizations for a given θ

and H_K are found and used in a least-squares fitting algorithm to fit to the model parameters. A typical fit of this type can be seen in Figure 7.1. The cubic anisotropy constant can be calculated with the definition of $H_K = \frac{2K_1}{\mu_0 M}$. This procedure was performed on the hysteresis loops of several $\text{Fe}_x\text{Co}_y\text{Mn}_z$ films with different compositions. Details of the growth and composition determination are reported elsewhere[55]. The hysteresis loops were acquired using the VSM option of the Quantum Design Physical Properties Measurement System (PPMS) calibrated by a NIST Pd standard. The hysteresis had a linear, diamagnetic background removed (from the MgO substrate) and was smoothed with a gaussian filter. The results of these fits are presented in Table 7.1.

Table 7.1: Cubic anisotropy constants, $K_{\text{cubic}}^{(1)}$ from fitting Stoner-Wohlfarth model hysteresis loops to VSM measured hysteresis loops of bcc $\text{Fe}_x\text{Co}_y\text{Mn}_z$ films.

x	y	z	M (10^{-7}Am^2)	$K_{\text{cubic}}^{(1)}$
0.33	0.60	0.07	1.1 ± 0.1	2.7 ± 0.1
0.43	0.47	0.10	1.3 ± 0.1	2.3 ± 0.1
0.43	0.46	0.11	2.3 ± 0.1	6.3 ± 0.3
0.47	0.42	0.12	1.7 ± 0.1	3.9 ± 0.2
0.40	0.42	0.18	2.4 ± 0.1	4.1 ± 0.2

These values are on the same order as epitaxial bcc Fe(100) on GaAs(100)[32], epitaxial bcc Co on GaAs(110)[22], and epitaxial bcc Co on GaAs(001)[56] cubic anisotropies, which were found by ar-FMR to be $2.4 \cdot 10^4 J/m^3$, $-6.6 \cdot 10^4 J/m^3$, and $2.6 \cdot 10^4 J/m^3$, respectively. The anisotropy constants in these cases were found to depend on film thickness.

Thermal Transport in Nematic Superconductors

A two-dimensional tight-binding square-lattice metallic state distorted by an electronic nematic phase results in thermal transport measurements which are anisotropic along the Cartesian crystallographic directions. It can be seen that the κ_{xx}^N and κ_{yy}^N components of the thermal conductivity tensor are no longer equal, as is the case for the original ($\Phi = 0$) tight-binding Fermi surface (i.e. $\kappa_{xx}^n = \kappa_{yy}^n = \kappa^n$ in the normal state). This is due to the fact that the nematic deformation has enhanced the quasiparticle velocities in the y -direction while diminishing the velocities in the x -direction. This results in κ_{yy}^N always being greater than κ_{xx}^N . Despite these modifications to the quasiparticle velocities, the κ_{xy}^N components still vanish due to the symmetry inherent in the velocities on the deformed FS. The asymmetric splitting in Figure 7.2 is due to the fact that the particle lifetimes in the nematic state are different from the normal state. The particle lifetime in the nematic state is $\tau_N(\tilde{\xi}_{\mathbf{k}}) \propto 1/\tilde{N}(\tilde{\xi}_{\mathbf{k}})$. As the van Hove singularities approach the Fermi level, $\tilde{N}(\tilde{\xi}_{\mathbf{k}})$ near the Fermi level increases, which causes $\tau_N(\tilde{\xi}_{\mathbf{k}})$ near the Fermi level to decrease. Thus, near T_N (the van Hove singularities cross the Fermi level when $T = 0.97T_N$) κ_{xx}^N decreases much more quickly than κ_{yy}^N increases. However, after the van Hove singularity passes through the Fermi level the DOS $\tilde{N}(\tilde{\xi}_{\mathbf{k}})$ near the Fermi level begins to decrease, causing τ_N to increase. This results in long-lived, high velocity quasiparticles which conduct heat more efficiently, forcing κ_{yy}^N to increase rather rapidly.

A spin-singlet superconducting state arising out of an electronic nematic phase was considered on a two-dimensional tight-binding square-lattice, where both orders were treated at the mean-field level and the nematic order was modelled as a d -wave Pomeranchuk type instability. The feedback from the symmetry-broken nematic phase on the SC order was accounted for through a mixing of the s -wave and d -wave channels which is controlled by a constant, phenomenological anisotropy parameter, r . Depending on the value of r , the

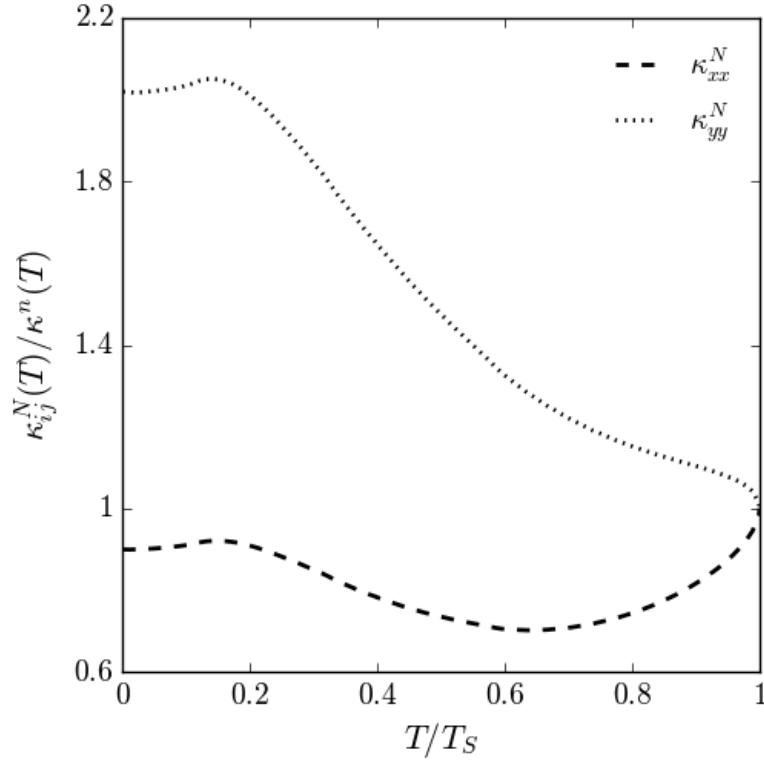


Figure 7.2: Heat conductivity components ($\kappa_{ij}^N(T)$) of the nematically deformed closed FS with band parameters $t_1 = 6T_S$, $t_2 = -T_S$, and $\mu = -4.8T_S$ in the absence of SC order. $\kappa_{ij}^N(T)$ is normalized by the conductivity ($\kappa^n(T)$) of the normal state (original FS, $\Phi = 0$). The normal state conductivity is T -linear, $\kappa^n(T) = \text{constant} \times T$.

gap function can display a deep minima (in the case of moderate mixing) or nodes (in the case of strong mixing). By determining the amplitudes of the SC and the nematic orders self-consistently for all temperatures, the nature of the low energy excitations could be analyzed showing that for $r > r_c^+(\Phi)$ or $r < r_c^-(\Phi)$, the spectrum has nodes which create a non-uniformity in the SC gap (a direct outcome of the interplay of the FS distortion due to nematicity). This non-uniformity results in inequivalent gap maxima at $|\Delta_{\mathbf{k}}|^{max,(-)}$ and $|\Delta_{\mathbf{k}}|^{max,(+)}$.

In the case of $|r| \ll |r_c^\pm|$ (such as the $r = \pm 0.2$ results), while the superconducting gap has a d -wave component due the feedback from the nematic phase on s -wave superconductivity, this component is small and is therefore effectively s -wave superconductivity. As an

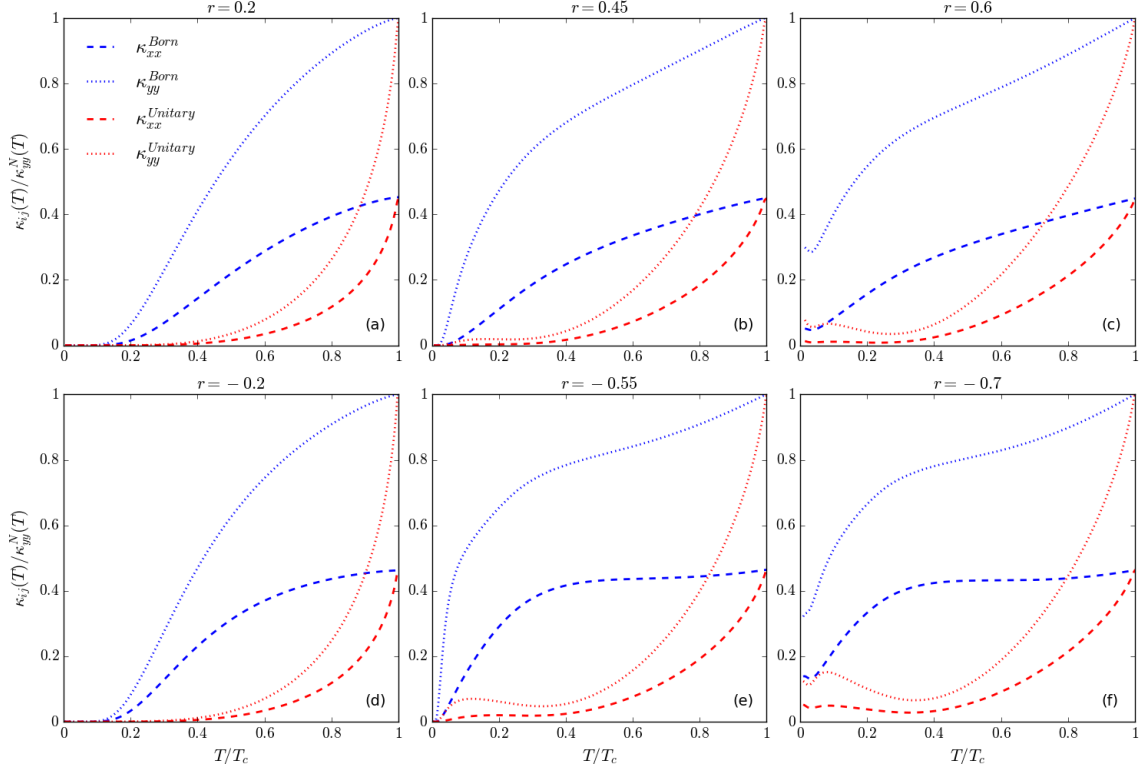


Figure 7.3: Thermal conductivity components (κ_{xx} and κ_{yy}) in the coexistence phase in both the Born (blue curves) and Unitary (red curves) limits normalized by the $\kappa_{yy}^N(T)$ component in the pure nematic phase when (a) $r = 0.2$ with $T_c = 0.211T_N$, (b) $r = 0.45$ with $T_c = 0.158T_N$, (c) $r = 0.6$ with $T_c = 0.140T_N$, (d) $r = -0.2$ with $T_c = 0.317T_N$, (e) $r = -0.55$ with $T_c = 0.332T_N$, and (f) $r = -0.7$ with $T_c = 0.323T_N$. The parameters used are $\mu = -4.8T_N$, $t_1 = 6T_N$, $t_2 = -T_N$, and $\Phi = 1.34T_N$. The critical r -values are $r_c^+ \approx 0.52866$ and $r_c^- \approx -0.61447$.

s -wave superconducting gaps doesn't result in nodes on the nematically distorted FS, the thermal conductivity elements in both the Born and Unitary scattering limits exponentially decrease at low- T , which can be seen in Figure 7.3 (a) and (d) as one would expect for a fully gapped superconductor[2, 47].

When $|r| \lesssim |r_c^\pm|$, deep minima in the superconducting gap appear as a result of the d -wave feedback on the s -wave gap becoming nearly the same magnitude as the s -wave component. These deep minima result in more long-lived quasiparticles which enhances the thermal conductivity tensor elements, which ultimately fall exponentially to zero at low- T

again due to the fully-gapped nature of the superconducting excitation spectrum. These results can be seen in Figure 7.3 (b) and (e).

When $|r| > |r_c^\pm|$, nodal quasiparticle states form on the nematically distorted FS. This resulted in the thermal conductivity in both the Born and Unitary limits no longer exponentially decreasing as $T \rightarrow 0$. While this is the expected result for nodal superconductors in the Born limit, the fact that the Unitary limit doesn't go to zero is unique to systems with a superconducting gap which has both s - and d -wave components due to the quasiparticle lifetime calculation in the Unitary limit.

Temperature dependence of the electronic heat conductivity in the mixed SC and Nematic system was computed using the Boltzmann transport equation method, where the impurity scattering collision integral and quasiparticle lifetime were determined in both the Born and Unitary limits. The nematic deformation of the FS results in $\kappa_{xx}(T) \neq \kappa_{yy}(T)$ and that there are significant differences in the thermal conductivity behavior in the coexistence phase that can distinguish between deep minima or nodes in the anisotropic SC gap structure. In the case of the SC gap having deep minima on the FS, $\kappa \rightarrow 0$ as $T \rightarrow 0$ in both the Born and Unitary limits. In the case when the SC gap function has nodes, low-energy excitations lead to a finite residual κ/T in the $T \rightarrow 0$ in both the Born and Unitary limits.

Thermal Transport in Symmetry-broken Antiferromagnetic Superconductors

Commensurate SDW systems of type AFM3 and AFM2 were considered on two-dimensional tight-binding square-lattices and found to have equivalent transport properties within Boltzmann kinetic theory in the weak impurity scattering (Born) limit relative to their nesting vectors. Parallel to their nesting vectors these systems behave similar to a suppressed metal, where the electronic thermal conductivity is linear in T but diminished from the normal state thermal conductivity. However, perpendicular to their nesting vectors, the transport properties of these systems are almost identical to that of the normal metallic

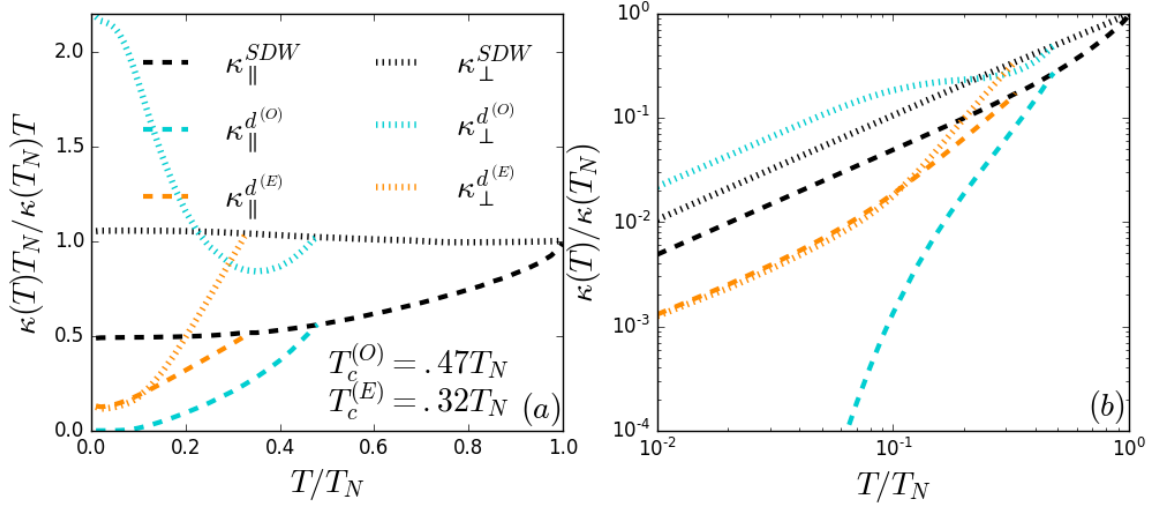


Figure 7.4: Diagonalized thermal conductivity tensor elements parallel (dashed curves) and perpendicular (dotted curves) to the SDW nesting vector \mathbf{Q} in the pure SDW state (black), SDW + d -wave SC state with odd translational symmetry (cyan), and SDW + d -wave SC state with even translational symmetry (orange). (a) $\kappa(T)T_N/\kappa(T_N)T$ plotted to remove linear T -dependence and emphasize deviations from normal state conductivity. (b) $\kappa(T)/\kappa(T_N)$ plotted on a log-log scale to emphasize low- T linearity.

state, except they are slightly enhanced as $T \rightarrow 0$ due to the FS reconstruction parallel to \mathbf{Q} creating a gap in the FS and reducing N_F , thus enhancing the quasiparticle lifetimes.

The d -wave SC states coexisting with the $\mathbf{Q} = (\pi/2, \pi/2)$ and $\mathbf{Q} = (\pi, 0)$ nesting vectors have equivalent transport properties, with the $d_{x^2-y^2}$ and d_{xy} states swapped between the nesting vectors. The d -wave symmetry nodes are located on regions of the tight-binding FS with the same relatively small local DOS and have equivalent band structures when the $\mathbf{Q} = (\pi/2, \pi/2)$ SDW state coexists with the $d_{x^2-y^2}$ SC gap and the $\mathbf{Q} = (\pi, 0)$ SDW state coexists with the d_{xy} SC gap (these are the odd symmetry, $d^{(O)}$ -wave state in this work). Similarly, the d -wave nodes occur on regions of the tight-binding FS with the same relatively large local DOS and have equivalent band structures when the $\mathbf{Q} = (\pi/2, \pi/2)$ SDW state coexists with the d_{xy} SC gap and the $\mathbf{Q} = (\pi, 0)$ SDW state coexists with the $d_{x^2-y^2}$ SC gap (these are the even symmetry, $d^{(E)}$ -wave state in this work).

The electron transport properties of these commensurate SDW systems were also studied when SC singlet pairing arises ($T_N > T_c$) out of it. The electronic thermal conductivity for a $d^{(O)}$ -wave SC gap measured parallel to \mathbf{Q} was found to decrease exponentially with T , consistent with results for fully-gapped SCs[2]. Perpendicular to \mathbf{Q} , the conductivity was found to decrease linearly with T , consistent with SCs with line nodes[25]. Furthermore, the residual $\kappa_{\perp}(T \rightarrow 0)/T$ value was found to be roughly twice that of pure d -wave SCs containing nodal quasiparticle states situated on the flat regions of a tight-binding FS. Therefore, the effect SDW states with $C(2)$ rotational symmetry on d -wave SC states such as these is that it gaps the nodal quasiparticle states in the direction of SDW propagation, greatly reducing thermal transport in that direction, and doubles the lifetimes of quasiparticles traveling perpendicular to the SDW propagation direction, thus greatly enhancing thermal transport in that direction. This results in a system with highly anisotropic electron transport where fast long-lived quasiparticles tend to travel perpendicular to \mathbf{Q} .

When the d -wave SC gap is even under translations of \mathbf{Q} ($d^{(E)}$ -wave), the SC symmetry nodes are preserved as none of them appear in the region of the FS which is reconstructed by the SDW order. Due to the translational symmetry of the SC gap, additional mixing nodes appear in the vicinity of the FS reconstruction parallel to \mathbf{Q} . The electronic thermal conductivity both parallel and perpendicular to \mathbf{Q} were found to decrease linearly with T . In fact, $\kappa_{\parallel}(T \rightarrow 0)/T$ and $\kappa_{\perp}(T \rightarrow 0)/T$ were nearly identical due to quasiparticles occupying states at the d -wave symmetry nodes contributing equally to thermal transport in both directions. However, thermal transport parallel to \mathbf{Q} was slightly enhanced since quasiparticles occupying states at the mixing nodes enhanced transport in that direction. The coexistence of SDW states with $C(2)$ d -wave SC gaps such as these leaves thermal transport of such systems largely unaffected due to the nodal quasiparticle states remaining mostly unchanged by the FS reconstruction, however it does introduce additional mixing

nodes which slightly enhance thermal transport in the direction of SDW propagation. Therefore, this results in a system with weakly anisotropic thermal transport, where slow short-lived quasiparticles travel both parallel and perpendicular to \mathbf{Q} , but slightly prefer to travel parallel to \mathbf{Q} .

These results could be relevant in determining the nature of the d -wave gap in cuprates with commensurate SDW orders of nesting vectors: $\mathbf{Q} = (\pi/2, \pi/2)$ or $\mathbf{Q} = (\pi, 0)$. If the thermal conductivity is measured both parallel and perpendicular to \mathbf{Q} and the nesting vector is known, weakly or strongly anisotropic thermal transport at low- T could be used to determine whether the SC gap is $d_{x^2-y^2}$ or d_{xy} in nature. Additionally, these results could be relevant to understanding the nature of anisotropic in-plane electronic thermal transport measured in some cuprate samples[11, 62, 64]. One study found quasi-one-dimensional electronic thermal transport at low- T mediated by spin excitations[62], similar to the $d^{(O)}$ -wave result in this work which had a residual thermal conductivity perpendicular to \mathbf{Q} as $T \rightarrow 0$, but not parallel to \mathbf{Q} . However, the other studies[11, 64] found that electronic thermal transport was supported in both directions, but still favored a particular direction due to electronic inhomogeneities. This effect could either be due to the fact that these samples weren't monolayers and the SDW nesting vectors for each layer weren't all parallel, or the anisotropic transport in these materials is due to a nematic phase which supports T -linear conductivity in both directions provided a strong enough mixing parameter r where nodal quasiparticle states appear in the superconducting quasiparticle energy spectrum. It is also interesting to consider that effects such as these could be due to the interplay between electronic nematic and SDW states, which could be pursued in future work.

REFERENCES CITED

- [1] B. Arfi and C. J. Pethick. Thermal conductivity and ultrasonic attenuation in heavy-fermion superconductors. *Phys. Rev. B*, 38:2312–2325, Aug 1988.
- [2] J. Bardeen, G. Rickayzen, and L. Tewordt. Theory of the Thermal Conductivity of Superconductors. *Phys. Rev.*, 113(4):982–994, 1959.
- [3] D. N. Basov and A. V. Chubukov. Manifesto for a higher T_c . *Nature Physics*, 7:272–276, 2011.
- [4] S. Blundell. *Magnetism in Condensed Matter*. Oxford University Press Inc., New York, 2001.
- [5] A. T. Bollinger and I. Bozovic. Two-dimensional superconductivity in the cuprates revealed by atomic-layer-by-layer molecular beam epitaxy. *Supercond. Sci. Technol.*, 29:103001, 2016.
- [6] S. Chatterjee, S. Sachdev, and A. Eberlein. Thermal and electrical transport in metals and superconductors across antiferromagnetic and topological quantum transitions. *Phys. Rev. B*, 96(7):075103, 2017.
- [7] Xiao Chen, S. Maiti, R. M. Fernandes, and P. J. Hirschfeld. Nematicity and superconductivity: Competition versus cooperation. *Phys. Rev. B*, 102:184512, Nov 2020.
- [8] Y. Chen, J. W. Lynn, J. Li, G. Li, G. F. Chen, J. L. Luo, N. L. Wang, P. Dai, C. de la Cruz, and H. A. Mook. Magnetic order of the iron spins in NdFeAsO. *Phys. Rev. B*, 78(6):064515, 2008.
- [9] J.-H. Chu, J. G. Analytis, K. De Greve, P. L. McMahon, I. Zahirul, Y. Yamamoto, and I. R. Fisher. In-plane resistivity anisotropy in an underdoped iron arsenide superconductor. *Science*, 329(5993):824–826, 2010.
- [10] A. Chubukov. Pairing Mechanism in Fe-based Superconductors. *Annu. Rev. Condens. Matter Phys.*, 3:57–92, 2012.
- [11] J. L. Cohn and J. Karpinski. Anisotropic in-plane thermal conductivity of single-crystal of YBa₂Cu₄O₈. *Phys. Rev. B*, 58(21):14617, 1998.
- [12] R. Coldea, S. M. Hayden, G. Aeppli, T. G. Perring, C. D. Frost, T. E. Mason, S.-W. Cheong, and Z. Fisk. Spin Waves and Electronic Interactions in La₂CuO₄. *Phys. Rev. Lett.*, 86(23):5377, 2001.
- [13] C. Daboo, R. J. Hicken, E. Gu, M. Gester, S. J. Gray, D. E. P. Eley, E. Ahmad, J. A. C. Bland, R. Ploessl, and J. N. Chapman. Anisotropy and orientational dependence of magnetization reversal process in epitaxial ferromagnetic thin films. *Phys. Rev. B*, 51:15964, 1995.

- [14] A. Damascelli, Z. Hussain, and Shen Z.-X. Angle-resolved photoemission studies of the cuprate superconductors. *Rev. Mod. Phys.*, 75(2):473–541, 2003.
- [15] C. de la Cruz, Q. Huang, J. W. Lynn, J. Li, W. Ratcliff II, J. L. Zarestky, H. A. Mook, G. F. Chen, J. L. Luo, N. L. Wang, and P. Dai. Magnetic order close to superconductivity in the iron-based layered $\text{LaO}_{1-x}\text{F}_x\text{FeAs}$ systems. *Nature*, 453:899–902, 2008.
- [16] E. Demler, S. Sachdev, and Y. Zhang. Spin-Ordering Quantum Transitions of Superconductors in a Magnetic Field. *Phys. Rev. Lett.*, 87:067202, 2001.
- [17] C. Fang, B. A. Bernevig, and J. Hu. Theory of magnetic order in $\text{Fe}_{1+y}\text{Te}_{1-x}\text{Se}_x$. *EPL*, 86:67005, 2009.
- [18] C. Fang, H Yao, W.-F. Tsai, J. Hu, and S. A. Kivelson. Theory of electron nematic order in lafeaso. *Phys. Rev. B*, 77(22):224509, 2008.
- [19] R. M. Fernandes, E. Abrahams, and J. Schmalian. Anisotropic in-plane resistivity in the nematic phase of the iron pnictides. *Phys. Rev. Lett.*, 107(21):217002, 2011.
- [20] R. M. Fernandes, A. V. Chubukov, and J. Schmalian. What drives nematic order in iron-based superconductors? *Nat. Phys.*, 10:97–104, Feb 2014.
- [21] E. Fradkin, S. A. Kivelson, M. J. Lawler, J. P. Eisenstein, and A. P. Mackenzie. Nematic fermi fluids in condensed matter physics. *Annu. Rev. Condens. Matter Phys.*, 1:153–178, 2010.
- [22] G. A. Prinz et. al. FMR of cubic cobalt grown by molecular beam epitaxy on GaAs. *J. Appl. Phys.*, 57:3672, 1985.
- [23] J.-F. Ge, Z.-L. Liu, C. Liu, C.-L. Gao, D. Qian, Q.-K. Xue, Y. Liu, and J.-F. Jia. Superconductivity above 100 K in single-layer FeSe films on doped SrTiO_3 . *Nature Mater.*, 14:285–289, 2015.
- [24] Mathias Getzlaff. *Fundamentals of Magnetism*. Springer-Verlag, Berlin, 2008.
- [25] M. J. Graf, S-K Yip, J. A. Sauls, and D. Rainer. Electronic thermal conductivity and the Wiedemann-Franz law for unconventional superconductors. *Phys. Rev. B*, 53(22):15147–15161, 1996.
- [26] N. Harrison and S. E. Sebastian. Dirac nodal pockets in the antiferromagnetic parent phase of FeAs superconductors. *Phys. Rev. B*, 80(22):224512, 2009.
- [27] T. Helm, M. V. Kartsovnik, M. Bartkowiak, N. Bittner, M. Lambacher, A. Erb, J. Wosnitza, and R. Gross. Measuring the gap in angle-resolved photoemission experiments on cuprates. *Phys. Rev. Lett.*, 103(15):157002, 2009.

- [28] F.-C. Hsu, J.-Y. Luo, K.-W. Yeh, T.-K. Chen, T.-W. Huang, P. M. Wu, Y.-C. Lee, Y.-L. Huang, Y.-Y. Chu, D.-C. Yan, and M.-K. Wu. Superconductivity in the PbO-type structure α -FeSe. *Proc. Natl Acad. Sci.*, 105:14262–14264, 2008.
- [29] J. Hu and C. Xu. Nematic orders in iron-based superconductors. *Physica C*, 481:215–222, 2012.
- [30] Q. Huang, Y. Qiu, W. Bao, M. A. Green, J. W. Lynn, Y. C. Gasparovic, T. Wu, G. Wu, and X. H. Chen. Neutron-Diffraction Measurements of Magnetic Order and a Structural Transition in the Parent BaFe_2As_2 Compound of FeAs-Based High-Temperature Superconductors. *Phys. Rev. Lett.*, 101(25):257003, 2008.
- [31] J.-P. Ismer, I. Eremin, E. Rossi, and et. al. Theory of Multiband Superconductivity in Spin-Density-Wave Metals. *Phys. Rev. Lett.*, 105(3):037003, 2010.
- [32] J. J. Krebs et. al. Properties of Fe single-crystal films grown on (100) GaAs by molecular-beam epitaxy. *J. Appl. Phys.*, 61:2596, 1987.
- [33] S. Kasahara, H. J. Shi, K. Hashimoto, S. Tonegawa, Y. Mizukami, T. Shibauchi, K. Sugimoto, T. Fukuda, T. Terashima, A. H. Nevidomskyy, and Y. Matsuda. Electronic nematicity above the structural and superconducting transition in $\text{bafe}_2(\text{as}_{1-x}\text{p}_x)_2$. *Nature*, 486:382–385, 2012.
- [34] M. Kato and K. Machida. Inherent Spin Density Wave Instability in Heavy-Fermion Superconductors. *Journal of the Physical Society of Japan*, 56(6):2136–2148, 1987.
- [35] M. Kato and K. Machida. Superconductivity and spin-density waves: Application to heavy-fermion materials. *Phys. Rev. B*, 37(4):1510–1519, 1988.
- [36] S. A. J. Kimber, D. N. Argyriou, F. Yokaichiya, K. Habicht, S. Gerischer, T. Hansen, T. Chatterji, R. Klingeler, C. Hess, G. Behr, A Kondrat, and B. Buchner. Magnetic ordering and negative thermal expansion in PrFeAsO . *Phys. Rev. B*, 78(14):140503(R), 2008.
- [37] M. Labrune, J. C. S. Kools, and A. Thiaville. Magnetization in spin-valve multilayers. *J. Magn. Magn. Mater.*, 171:1, 1997.
- [38] B. Lake, G. Aeppli, K. N. Clausen, D. F. McMorrow, K. Lefmann, N. E. Hussey, N. Mangkorntong, M. Nohara, H. Takagi, T. E. Mason, and A. Schröder. Spins in the Vortices of a High-Temperature Superconductor. *Science*, 291:1759–1762, 2001.
- [39] F. Laliberté, J. Chang, N. Doiron-Leyraud, E. Hassinger, R. Daou, M. Rondeau, B. J. Ramshaw, R. Liang, D. A. Bonn, W. N. Hardy, S. Pyon, T. Takayama, H. Takagi, I. Sheikin, L. Malone, C. Proust, K. Behnia, and L. Taillefer. Fermi-surface reconstruction by stripe order in cuprate superconductors. *Nat. Commun.*, 2:432, 2011.

- [40] S. Lebegue. Electronic structure and properties of the Fermi surface of the superconductor LaOFeP. *Phys. Rev. B*, 75(3):035110, 2007.
- [41] C.-C. Lee, W.-G. Yin, and W. Ku. Ferro-orbital order and strong magnetic anisotropy in the parent compounds of iron-pnictide superconductors. *Phys. Rev. Lett.*, 103(26):267001, 2009.
- [42] S. Li, C. de la Cruz, Q. Huang, Y. Chen, J. W. Lynn, J. Hu, Y. L. Huang, F. C. Hsu, K. W. Yeh, M. K. Wu, and P. Dai. First-order magnetic and structural phase transitions in $\text{Fe}_{1+y}\text{Se}_x\text{Te}_{1-x}$. *Phys. Rev. B*, 79(5):054503, 2009.
- [43] D. H. Lu, M. Yi, S.-K. Mo, A. S. Erickson, J. Analytis, J.-H. Chu, D. J. Singh, Z. Hussain, T. H. Geballe, I. R. Fisher, and Z.-X. Shen. Electronic structure of the iron-based superconductor laofep. *Nature*, 455:81–84, 2008.
- [44] K. Machida. Spin Density Wave and Superconductivity in Highly Anisotropic Materials. *Journal of the Physical Society of Japan*, 50(7):2195–2202, 1981.
- [45] K. Machida and M. Kato. Inherent Spin-Density-Wave Instability in Heavy-Fermion Superconductivity. *Phys. Rev. Lett.*, 58(19):1986–1988, 1987.
- [46] M. A. McGuire, A. D. Christianson, A. S. Sefat, B. C. Sales, M. D. Lumsden, R. Jin, and et. al. Phase transitions in LaFeAsO: Structural, magnetic, elastic, and transport properties, heat capacity and Mössbauer spectra. *Phys. Rev. B*, 78(9):094517, 2008.
- [47] V. P. Mineev and K. V. Samokin. *Introduction to Unconventional Superconductivity*. Gordon and Breach Science Publishers, Amsterdam, 1998.
- [48] Y. Mizuguchi and Y. Takano. Review of Fe Chalcogenides as the Simplest Fe-Based Superconductor. *Journal of the Physical Society of Japan*, 79:102001, 2010.
- [49] Robert C. O’Handley. *Modern Magnetic Materials Principles and Applications*. John Wiley & Sons, Inc., New York, 2000.
- [50] S. F. Peterson and Y. U. Idzerda. Determination of anisotropy constants via fitting of magnetic hysteresis to numerical calculation of Stoner-Wohlfarth model. *AIP Advances*, 11:085111, 2021.
- [51] S. F. Peterson, S. Sen Choudhury, and Y. Idzerda. Thermal transport in superconductors with coexisting spin density wave order. *Phys. Rev. B*, 108:054503, 2023.
- [52] C. J. Pethick and David Pines. Transport processes in heavy-fermion superconductors. *Phys. Rev. Lett.*, 57:118–121, Jul 1986.
- [53] G. A. Prinz. Magnetic anisotropy in epitaxial metal films. *Ultramicroscopy*, 47:346, 1992.

- [54] Y. Qiu, W. Bao, Y. Zhao, C. Broholm, V. Stanev, Z. Tesanovic, Y. C. Gasparovic, S. Chang, J. Hu, B. Qian, M. Fang, and Z. Mao. Spin Gap and Resonance at the Nesting Wave Vector in Superconducting $\text{FeSe}_{0.4}\text{Te}_{0.6}$. *Phys. Rev. Lett.*, 103(6):067008, 2009.
- [55] R. J. Snow et. al. Large moments in bcc $\text{Fe}_x\text{Co}_y\text{Mn}_z$ ternary alloy thin films. *Appl. Phys. Lett.*, 112:072403, 2018.
- [56] S. J. Blundell et. al. Structure induced magnetic anisotropy behavior in Co/GaAs(001) films. *J. Appl. Phys.*, 73:5948, 1993.
- [57] S. Sachdev. Quantum criticality and the phase diagram of the cuprates. *Physica C: Superconductivity and its Applications*, 470:S4–S6, 2010.
- [58] J. J. Sakurai and J. Napolitano. *Modern Quantum Mechanics*. Pearson Education, Inc., 1301 Sansome Street, San Francisco, CA 941 1 1, 1994.
- [59] S. Sen Choudhury, S. Peterson, and Y. Idzerda. Thermal transport in two-dimensional nematic superconductors. *Phys. Rev. B*, 105(21):214515, 2022.
- [60] S. Sen Choudhury and A. Vorontsov. Thermal transport in superconductors with coexisting spin density wave order. *Phys. Rev. B*, 103:104501, 2021.
- [61] D. J. Singh and M.-H. Du. Density Functional Study of $\text{LaFeAsO}_{1-x}\text{F}_x$: A Low Carrier Density Superconductor Near Itinerant Magnetism. *Phys. Rev. Lett.*, 100(23):237003, 2008.
- [62] A. V. Sologubenko, E. Felder, K. Gianno, H. R. Ott, A. Vietkine, and A. Revcolevschi. Thermal conductivity and specific heat of the linear chain cuprate Sr_2CuO_3 : Evidence for thermal transport via spinons. *Phys. Rev. B*, 62(10):R6108, 2000.
- [63] J. Stöhr and H. C. Siegmann. *Magnetism From Fundamentals to Nanoscale Dynamics*. Springer-Verlag, Berlin, 2006.
- [64] X. F. Sun, S. Ono, Y. Abe, S. Komiya, K. Segawa, and Y. Ando. Electronic Inhomogeneity and Breakdown of the Universal Thermal Conductivity of Cuprate Superconductors. *Phys. Rev. Lett.*, 96(1):017008, 2006.
- [65] L. Taillefer. Scattering and Pairing in Cuprate Superconductors. *Annu. Rev. Condens. Matter Phys.*, 1:51, 2010.
- [66] S. Tan, Y. Zhang, M. Xia, Z. Ye, F. Chen, X. Xie, R. Peng, D. Xu, Q. Fan, H. Xu, J. Jiang, T. Zhang, X. Lai, T. Xiang, J. Hu, B. Xie, and D. Feng. Interface-induced superconductivity and strain-dependent spin density waves in $\text{FeSe}/\text{SrTiO}_3$ thin films. *Nature Mater.*, 12:634–639, 2013.
- [67] Carsten Timm. *Theory of Superconductivity*. Institute of Theoretical Physics, 2012.

- [68] J. M. Tranquada, B. J. Sternlieb, J. D. Axe, Y. Nakamura, and S. Uchida. Evidence for stripe correlations of spins and holes in copper oxide superconductors. *Nature*, 375:561–563, 1995.
- [69] N. A. Usov and S. E. Peschany. Theoretical hysteresis loops for single-domain particles with cubic anisotropy. *J. Magn. Magn. Mater.*, 174:247, 1997.
- [70] H.-H. Wen and S. Li. Materials and Novel Superconductivity in Iron Pnictide Superconductors. *Annu. Rev. Condens. Matter Phys.*, 2:121, 2011.
- [71] H. Yamase, Y. Sakurai, M. Fujita, S. Wakimoto, and K. Yamada. Fermi surface in La-based cuprate superconductors from Compton scattering imaging. *Nat. Commun.*, 12:2223, 2021.
- [72] Hiroyuki Yamase, Vadim Oganesyan, and Walter Metzner. Mean-field theory for symmetry-breaking fermi surface deformations on a square lattice. *Phys. Rev. B*, 72:035114, Jul 2005.
- [73] Y. Yu, L. Ma, P. Cai, R. Zhong, C. Ye, J. Shen, G. D. Gu, X. H. Chen, and Y. Zhang. High-temperature superconductivity in monolayer $\text{Bi}_2\text{Sr}_2\text{CaCu}_2\text{O}_{8+\delta}$. *Nature*, 575:156–163, 2019.
- [74] J. Zhao, Q. Huang, C. de la Cruz, S. Li, J. W. Lynn, Y. Chen, M. A. Green, G. F. Chen, G. Li, Z. Li, J. L. Luo, N. L. Wang, and P. Dai. Structural and magnetic phase diagram of $\text{CeFeAsO}_{1-x}\text{F}_x$ and its relation to high-temperature superconductivity. *Nature Mater.*, 7:953–959, 2008.
- [75] B.-H. Zheng, C.-M. Chung, P. Corboz, G. Ehlers, M.-P. Qin, R. M. Noack, H. Shi, S. R. White, S. Zhang, and G. K.-L. Chan. Stripe order in the underdoped region of the two-dimensional Hubbard model. *Science*, 358:1155–1160, 2017.

APPENDIX

GITHUB REPOSITORIES

All code for the results of the papers used in this work was uploaded to github repositories in order to avoid including an unreasonable number of pages of code at the end of this work and have been organized in Table A.1.

Table A.1: Github repositories of code used in this work.

paper	Github repository
first paper[50]	seanpeterson9/hysteresisFitting
second paper[59]	seanpeterson9/thermalConductivitySCNem
third paper[51]	seanpeterson9/thermalConductivitySCSDW